Verification and Validation of Numerical Modelling Approaches Pertinent to Stomach Modelling

Xinying Liu

A thesis submitted in fulfilment of the requirements for the degree of

Doctor of Philosophy.

School of Chemical and Biomolecular Engineering

The University of Sydney

February 2023

Abstract

The digestive system is vital to the human body. Over many decades, scientists have been investigating the food breakdown mechanisms inside the stomach through *in vivo* human and animal studies and *in vitro* experiments. However, *in vivo* studies for gastric function are invasive and very difficult to perform, require strict ethics approval and specific technical skills, and it is hard to obtain detailed measurements. *In vitro* experiments are easier to perform, and more widely used, but further development is still required to better replicate the real stomach. Due to recent improvements in computing speed and algorithm development, computational modelling has become a viable option to investigate in-body processes. Such *in silico* models are more easily controlled to investigate individual variables, do not require invasive physical experiments, and can provide valuable insights into the local physics of gastric flow.

There is a huge potential for numerical approaches in stomach modelling as they can provide a comprehensive understanding of the complex flow and chemistry in the stomach. However, to make sure the numerical methods are accurate and reliable, rigorous verification and validation are essential as part of model development. A significant focus of this work was on verifying and validating the components of the established models. Peristalsis is a key aspect of the digestion process because of its important role in transporting and mixing gastric content. In this thesis, an evaluation of Smooth Particle Hydrodynamics (SPH) and Finite Volume Method (FVM) models of kinematically prescribed peristalsis-like flow in a tube was undertaken. The dependency of the net volumetric flow rate of fluid on the amplitude ratio of the wall deformation is available from an analytical study. Comparisons showed that both models could achieve a high level of accuracy provided solver parameters, especially in SPH, were chosen carefully. The impact of the numerical parameters in both models affecting solution stability and accuracy are presented in detail.

In the gastrointestinal tract system, the peristaltic waves are generated by the muscular fibres along the wall. To extend the study to peristaltic motion, a fluid-structure interaction (FSI) model was developed simulating wave propagation in a fluid-filled elastic tube. In the FSI model, FVM was used to perform the fluid flow analysis, finite element analysis (FEA) was used to conduct the structural analysis, and a coupling model was utilized to handle data transfer at the interface. According to the theoretical analysis, the wave propagation speed depends on the fluid properties and the wall material. The tube constraint has an influence on

the wave speed as well. The accuracy of the model was verified by comparing the calculated wave propagation speeds with theoretical values for many different parameter variations. Advice on the choice of structural element type was given and the axial stress and strain profiles of the structure were visualised.

Numerical approaches can not only be used to simulate the digestion process in a real stomach, but they can also be used to assist in designing *in vitro* experiments. A FSI model was developed in this thesis, based on the verified FSI methodology, to study an *in vitro* intestinal peristaltic system designed by Professor Timothy Langrish and his PhD student Chao Zhong from the University of Sydney. The *in vitro* system consists of an elastic, semi-transparent and deformable chamber that is made of thermoplastic polyurethane (TPU), and four oscillating pistons, that mimic the peristaltic motion. The chamber was filled with water initially and fluorescein dye was injected into the system. As the pistons compressed the chamber, the transportation of the dye was analyzed via the fluorescein concentration and image colour analysis. The FSI model simulated this system, with the consideration of the deformation and stress introduced by the moving pistons, the support of the system from the chamber's nearby bodies, and the fluid transport and mass transfer of the dye in the fluid. The dye concentration in the fluid was measured at different locations and the simulation results matched well with the experimental results in the base case. Further investigation is required for two other experimental cases, with different piston operating conditions, performed post-COVID, for which the simulation results match less well. The model results provide valuable insights into the dye mixing behaviour, velocity field and strain rate of the fluid, and von Mises stress in the elastic structure.

The study of mass transfer is essential in the food digestion process, especially when gastric acid interacts with food and nutrients dissolve in the gastric system. The same research group led by Professor Timothy Langrish investigated mass transfer in a tablet dissolution process in a beaker and stirrer system. In this thesis, a FVM model was built based on this *in vitro* study and provided a comprehensive understanding of the fluid flow and mass transfer in the system. The predicted mass transfer coefficients from the simulation aligned well with the experimental values. The effect of the type and rotation speed of the stirrers was also investigated. Mass transfer from the tablet was found to be closely related to the Reynolds number of the fluid and the shear stress acting on the tablet.

In the past two decades, various numerical approaches have been applied to simulate the digestion process in the stomach. A major limitation of the traditional grid based FVM is the need to change the location of every node in the mesh when the geometry is deformed significantly, as occurs in stomach modelling. This remeshing process is very time-consuming and has held back stomach model development. In recent years, researchers started to use particle-based methods, such as SPH, to simulate the digestion process in the stomach. The main advantages of the particle-based method are its efficiency in dealing with deforming walls, representing solids dynamically coupled to the fluid, and tracking material transport without numerical diffusion. Therefore, SPH was used in this thesis to further develop an existing stomach model that was developed at the CSIRO.

Firstly, a buoyancy-driven flow in a non-deforming stomach was simulated using the SPH method, embodied in the SPH code developed at the CSIRO. A FVM model was also developed, and its solution was used to compare with the SPH results. In the models, a water layer was placed above an oil layer initially. As the simulation started, the buoyancy effect driven by gravity caused the oil to float to the top layer and the water to sink to the bottom. The Rayleigh-Taylor Instability (RTI) was well-captured in the SPH model but not so clearly in the FVM model. However, numerical noise in the SPH is visible, together with incomplete phase separation. The different results between the two models were investigated and further improvement is required for both. However, both models show that the separation process happens rapidly (within 6 s) in the stomach geometry due to its special J shape.

The successfully developed approach for flow in the non-deforming stomach was then applied to a stomach with a moving wall and acid diffusion using SPH. The contraction waves were applied to the stomach surface as time-varying accelerations of the mesh nodes. The fluid inside was prescribed to have a neutral pH of 7 initially and a pH of ~3 was set at the wall. The fluid was divided into five horizontal layers initially and its mixing behaviour was investigated. As the contraction wave moved along the stomach wall, the fluid started mixing and the acid near the wall diffused into the fluid. The visualisation of the fluid mixing and the acid diffusion was captured. Several parameter variations were tested. The fluid viscosity was found to have a significant effect on both mixing and pH changes in the fluid. Analysis showed that the mass transfer was advection dominated even with the highest viscosity fluid. The acid diffusion coefficient controlled the acid flux at the wall and therefore had a strong impact on pH changes. A 50% change in the contraction wave speed did not affect either mixing or pH changes

significantly. This model has not been verified or validated rigorously and therefore further investigation is required.

In summary, the main contribution of this thesis is in the rigorous verification and validation of the two modelling approaches studied and the information provided on their strengths and weaknesses.

Acknowledgements

First and foremost, I would like to express my sincere gratitude to my primary supervisor, Professor David Fletcher, without whom the completion of this thesis would not have been possible. His immense knowledge and constant support have guided me throughout this project and inspired me tremendously along my PhD journey. I would also like to extend my thanks to my co-supervisor Dr Simon Harrison from CSIRO Data61, for his valuable insights and support in the project.

I would like to thank Dr Paul Cleary, in particular, for his expert input and helpful feedback on the project. Thanks also need to be extended to Dr Matt Sinnott and Dr Shouryadipta Ghosh for their support and input.

I wish to acknowledge the experimental data and valuable discussions provided by Chao Zhong and Professor Timothy Langrish from the Drying and Process Technology Research Group, without whom the comparison studies between experiment and simulation would not have been completed.

The help and assistance provided by Dr Jindong Yang, Dave Hyde, Dr Luke Mosse, and Dr Peter Brand from LEAP Australia on the use of the Ansys software is also greatly appreciated.

I would like to acknowledge the Research Training Program Stipend Scholarship provided by the Australian Government and the supplementary scholarship received from the Centre for Advanced Food Engineering (CAFÉ).

I also want to acknowledge the use of the National Computational Infrastructure (NCI) which is supported by the Australian Government, access through the Sydney Informatics Hub HPC Allocation Scheme, which is supported by the Deputy Vice-Chancellor (Research), University of Sydney, and the computing resources provided by the CSIRO HPC.

I wish to express my deepest appreciation to my family and friends for their encouragement, understanding and support. I also want to thank all my colleagues in the office for their kindness and advice. Special thanks to Liam, for all your patience and encouragement.

Finally, I would like to thank my thesis examiners, Professor Gail Bornhorst and Dr Alessio Alexiadis, for their time spent on reviewing my thesis and providing valuable feedback.

Student Declaration

I hereby certify that to the best of my knowledge, the content of this thesis is my own work and has not been submitted to any institution for the award of a degree.

Xinying Liu

February 2023

List of Publications

Journal Articles

1. X. Liu, S.M. Harrison, P.W. Cleary, D.F. Fletcher, "Evaluation of SPH and FVM models of kinematically prescribed peristalsis-like flow in a tube", *Fluids*, vol. 8, p. 6, 2023, doi: 10.3390/fluids8010006.

2. X. Liu, D.F. Fletcher, "Verification of fluid-structure interaction modelling for wave propagation in fluid-filled elastic tubes", *Journal of Algorithms and Computational Technology*, vol. 17, 2023, doi: 10.1177/17483026231159793.

3. X. Liu, C. Zhong, D.F. Fletcher, T.A.G. Langrish, "Simulating tablet dissolution using computational fluid dynamics and experimental modelling", *Processes*, vol. 11, p. 505, 2023, doi: 10.3390/pr11020606.

4. X. Liu, S.M. Harrison, P.W. Cleary, D.F. Fletcher, "Numerical simulation of buoyancy-driven flow in a human stomach geometry: comparison of SPH and FVM models", *Applied Mathematical Modelling*, submitted: 14/02/2023, submission under review.

Conferences

1. X. Liu, S.M. Harrison, M.D. Sinnott, P.W. Cleary, D.F. Fletcher, "*Evaluation of methods for numerical simulation of peristaltic transport and its application in stomach modelling*", Food Structures, Digestion and Health 6th International Conference, 16-19 November 2021.

2. X. Liu, S.M. Harrison, S. Ghosh, M.D. Sinnott, D.F. Fletcher, P.W. Cleary, "*Numerical simulation of buoyancy-driven flow in a human stomach*", 23rd Australasian Fluid Mechanics Conference, 4-8 December 2022.

Authorship Attribution Statement

Significant parts of Chapters 3, 4, 6 and 7 of this thesis are submitted for publication.

1. Evaluation of SPH and FVM models of kinematically prescribed peristalsis-like flow in a tube by Xinying Liu, Simon M. Harrison, Paul W. Cleary and David F. Fletcher is published in ***Fluids.***

2. Verification of fluid-structure interaction modelling for wave propagation in fluid-filled elastic tubes by Xinying Liu and David F. Fletcher is published in ***Journal of Algorithms and Computational Technology.***

3. Simulating tablet dissolution using computational fluid dynamics and experimental modelling by Xinying Liu, Chao Zhong, David F. Fletcher, Timothy A.G. Langrish is published in ***Processes***.

4. Numerical simulation of buoyancy-driven flow in a human stomach geometry: comparison of SPH and FVM models by Xinying Liu, Simon M. Harrison, David F. Fletcher and Paul W. Cleary is submitted to ***Applied Mathematical Modelling***.

I certify that the aforementioned authorship attribution statement is correct and that I have received permission from the other authors to include the published material. In addition to the statements above, in cases where I am not the corresponding author of a published item, permission to include the published material has been granted by the corresponding author.

Xinying Liu

Signature

Date

As the supervisor for the candidature upon which this thesis is based, I can confirm that the authorship attribution statements above are correct.

David F Fletcher

Signature

Date

Table of Contents

List of Figures

List of Tables

Nomenclature

Roman

a	[m]	Tube diameter
A	[m^2]	Surface area
A	[-]	Arbitrary variable (Ch. 3)
b	[m]	Wave amplitude
c	[m/s]	Wave speed
c_s	[m/s]	Sound speed
C	[kg/m^3]	Mass concentration
D	[m^2/s]	Species diffusion coefficient
D_m	[kg/m/s]	Mass-based species diffusion coefficient ($= \rho D$)
$\boldsymbol{e}$	[-]	Strain tensor
E	[Pa]	Young's modulus
$\boldsymbol{f}$	[kg/m^2/s^2]	Body force
F	[-]	Deformation gradient
$\boldsymbol{g}$	[m/s^2]	Acceleration due to gravity
G	[Pa]	Shear modulus
h	[m]	Occlusion amplitude or smoothing distance (Ch. 3)
		or wall thickness (Ch. 4)
H	[m]	Wall displacement
$\boldsymbol{I}$	[-]	Identity tensor
k	[-],	Dimensionless wavenumber (Ch. 3)
	[Pa/s],	or pressure ramp rate (Ch. 4)
	[m^2/s^2],	or turbulence kinetic energy (Ch. 5)
	[m/s]	or mass transfer coefficient (Ch. 6)

K	[Pa]	Bulk modulus of the fluid
L	[m]	Tube length (Ch. 3 and 4)
		or length-scale (Ch. 6)
m	[kg]	Mass of a particle
m_{sol}	[kg]	Mass of solute
n	[-]	Density exponent
N	[rev/s]	Rotation rate
N_p	[-]	Power number
P, p	[Pa]	Pressure
P_k	[kg/m.s^3]	Production rate of turbulence kinetic energy
Q	[m^3/s]	Volumetric flow rate
$\bar{Q}$	[m^3/s]	Time-mean volumetric flow rate
$\boldsymbol{r}$	[m]	Particle position vector
r_{ab}	[m]	Distance between particle a and b
R_i	[m]	Tube inner radius
R_o	[m]	Tube outer radius
Re	[-]	Reynolds number
Sc	[-]	Schmidt number
Sh	[-]	Sherwood number
t	[s]	Time
$\boldsymbol{u}$	[m/s]	Fluid velocity
	[m]	Displacement vector
$\boldsymbol{v}$	[m/s]	Particle velocity
$\dot{V}$	[-]	Dimensionless time-averaged volumetric flow rate (Ch. 3)
V^*	[-]	Dimensionless time-averaged volumetric flow (Ch. 3)

W	[m^{-3}]	Interpolation function
x	[m]	Longitudinal distance
y	[-]	Ratio of wall thickness to tube inner radius
Y	[-]	Mass fraction

Greek

α	[-]	Volume fraction
δ_r	[m]	Radial displacement
δ_{r0}	[m]	Radial displacement at the tube entrance
ΔP	[Pa]	Pressure rise
Δt	[s]	Timestep
Δx	[m]	Initial particle separation
γ	[-]	Ratio of wall thickness to tube outer radius
λ	[m]	Wavelength
μ	[Pa.s]	Dynamic viscosity
ν	[-]	Poisson's ratio
ϕ	[-]	Amplitude ratio ($= b/a$)
ρ	[kg/m^3]	Fluid density
ρ_s	[kg/m^3]	Solid density
$\boldsymbol{\sigma}$	[N/m^2]	Stress tensor
σ_Y	[-]	Turbulent Schmidt number for mass fraction
τ	[N.m]	Torque
θ	[radians]	Angle
Υ	[-]	Isentropic exponent in the particle equation of state
ξ	[-]	Modelling constant in the viscous term in SPH

ω	[1/s]	Turbulence frequency

Subscript

0, 1, .. 5	Denotes sound speed based on different assumptions, i.e., c_i (Ch. 4)
0	Initial
a, b	Representative particles
b	Bulk (Ch. 6)
g	Grid
i	Initialisation (Ch. 3) or impeller (Ch. 6)
k	Wall particle
m	Mixture
off	Offset
s	Sound or surface or stirrer
t	Turbulence or tablet
o	Oil
O	Reference
w	Water

Superscript

T	Transpose of a vector or matrix

Chapter 1. Introduction

Maintaining a healthy digestive system is vital as many health problems are related to the function of the stomach. Excess weight and obesity are high health risks worldwide, as they can lead to many diseases, such as diabetes, heart disease, stroke, and certain types of cancer. The World Health Organization also reported that around 39% of the world's adult population were overweight, while 13% were obese in 2016, and the rates have tripled since 1975 [1]. Therefore, it is essential to understand the digestion process in the human stomach to prevent associated health risks and diseases.

Researchers have investigated gastric digestion mechanisms by *in vivo*, *in vitro*, and *in silico* studies. *In vivo* studies involve living organisms and rely on animal studies and clinical trials. It is often believed that *in vivo* studies provide the most comprehensive insights compared with the other two. However, *in vivo* experiments for gastric function are invasive and very difficult to perform, require strict ethics approval and specific technical skills, and are hard to control for specific variables. *In vitro* studies are experiments performed outside of a living organism but within a controlled environment that mimics the stomach conditions. *In vitro* models have been developed intensively because of their good reproducibility without ethical issues [2-5]. Due to recent improvements in computing speed and algorithm development, the use of *in silico* models to investigate in-body processes has also become viable. Computational models can provide more detailed insights into the flow conditions, food mixing and breakdown mechanisms. Various *in silico* models have been developed to simulate numerically the gastric digestion process in the stomach as discussed later in Chapter 2.

Tablet dissolution is an important topic in gastric digestion and is primarily studied by *in vitro* models. The rate of dissolution is closely related to the flow behaviour of the gastric system. Shear strain rates and shear stresses at the tablet surface are likely to be related to the mass-transfer coefficients and the tablet release kinetics. This concept can also be applied to the surface erosion effect in food disintegration, which can be characterised as a mass-transfer process [6, 7]. Therefore, it is important to also develop *in silico* models that can be used to assist with experimental interpretation and provide inputs into models of the complete digestion process.

1.1. Thesis aims

This thesis is concerned with the modelling of flow inside the stomach and model systems used to study the digestion process using *in silico* models. Particular emphasis is given throughout on the tasks of model verification and validation that have often been overlooked in this application. As a starting point, a comparison between different methodologies is made and suitable models based on the results achieved are applied to both stomach simulators and stomach geometries. Tablet dissolution in a stirrer system is investigated by comparing results between *in vitro* and *in silico* studies to provide correlations between mass-transfer coefficients and flow behaviour. This thesis is divided into nine chapters to achieve the aims mentioned above and its structure is shown in Figure 1.1.
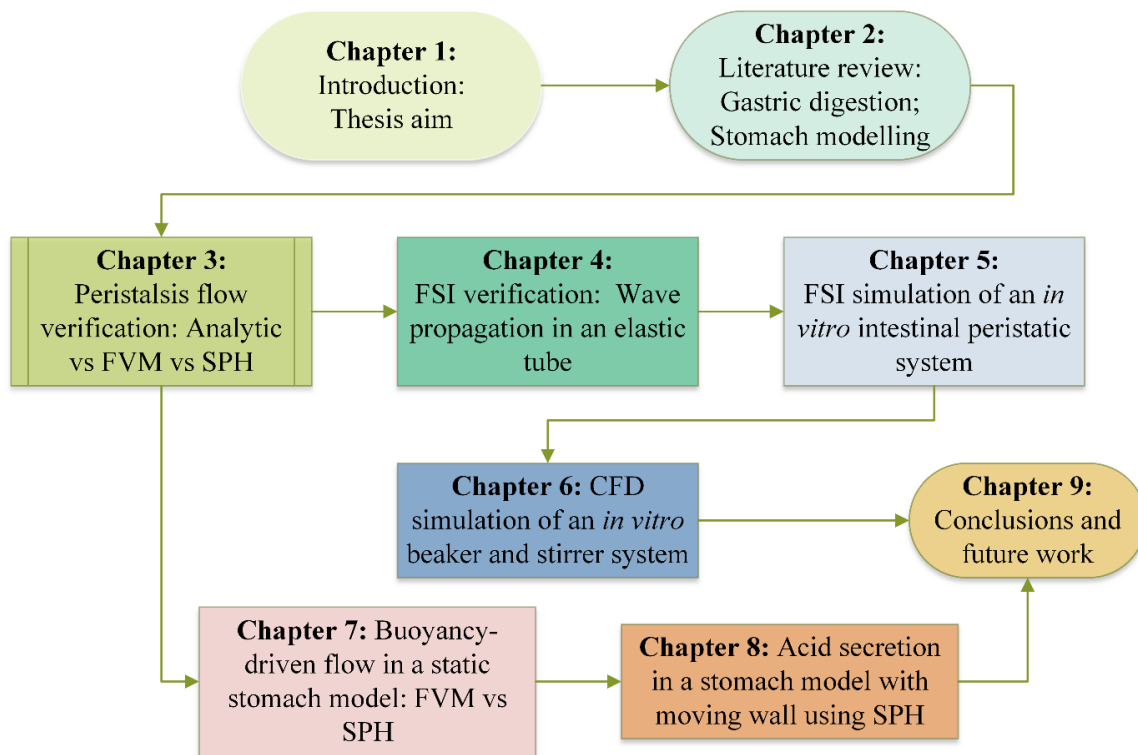
Figure 1.1: Flow diagram of the thesis structure.

Chapter 2 introduces the anatomy of the stomach, its mechanical properties and functions. It then reviews the literature on stomach modelling, including the gastric emptying patterns of different meal compositions, mathematical modelling of the digestion process, numerical methods for solving fluid mechanics problems and the developed computational stomach models. The capabilities and limitations of current stomach modelling are discussed in this chapter.

Chapter 3 evaluates the accuracy of two numerical methods: Smoothed Particle Hydrodynamics (SPH) and the Finite Volume method (FVM) when modelling a kinematically prescribed peristalsis flow, which is a feature found in most components of the gastrointestinal tract. The results achieved from both methods are verified against an analytical solution.

Chapter 4 presents a validation study of wave propagation in a fluid-filled elastic tube using Fluid-Structure Interaction (FSI), which is an extension study of the peristalsis flow that closely related to the digestion process. The speed of the elastic wave calculated from the simulation is compared against the theoretical value. The effect of element type, wall properties and tube constraints are investigated.

Chapter 5 reports on the simulation of an *in vitro* intestinal peristaltic system using FSI. The model is built based on an experimental model made of deforming elastic material. The model shows the fluid flow inside the system and the stresses and displacement on the structure. The time evolution of the concentration of an injected dye in the system is compared between the experiment and the simulation. This work demonstrates how *in vitro* models can be better understood, and potentially improved in function and physiological applicability, by using *in silico* modelling.

Chapter 6 presents a Computational Fluid Dynamics (CFD) simulation of an *in vitro* beaker and stirrer system. The mass transport achieved by different stirrers is analysed in the simulation and compared with experimental results. The relationship between the Reynolds number of the flow and the shear strain rate around the tablet is examined to understand the dissolution process of a tablet with different stirrers. Such simulations demonstrate how *in silico* models can reproduce the mechanical and chemical processes that occur in the stomach to make nutrients and medicines available to the body.

Chapter 7 presents numerical simulations of buoyancy-driven flow in a human stomach geometry using both the FVM and SPH approaches. A static stomach model is filled with fluids with different densities to investigate the buoyancy effect. The separation process is visualized, and the flow behaviour is discussed. The differences in the results achieved by the two numerical methods are discussed in detail.

Chapter 8 extends the model developed in Chapter 7 to include motion of the stomach wall and acid mixing. The impact of fluid viscosity, acid diffusion coefficient and wave speed are investigated. Results in this Chapter have not been fully validated but point the way to future work.

Chapter 9 presents the conclusions arising from this thesis and some recommendations for future work.

Chapter 2. Literature Review

This chapter provides a review of the flow and mass transfer phenomena important in the stomach with the aim of providing sufficient background that the essential components of a mathematical model can be identified. As a starting point, the main features and functions of the stomach are described, followed by a review of gastric emptying as this provides information of the end point to which a stomach model should be capable of predicting. Information on food behaviour, the role of acid and the impact of food type are discussed. It then identifies different mathematical modelling approaches that have been used to date, together with some of the important closure models that are utilised. Finally, this information is used to identify gaps in knowledge and to set the scene for the work to be presented in this thesis.

2.1. Anatomy of the stomach

2.1.1. Stomach structure

In the digestion process, the food content first enters the digestive tract through the mouth. It breaks down inside the mouth and forms a lubricated bolus through mastication and chewing. The lubricated food bolus then enters the stomach from the oesophagus through the cardia.
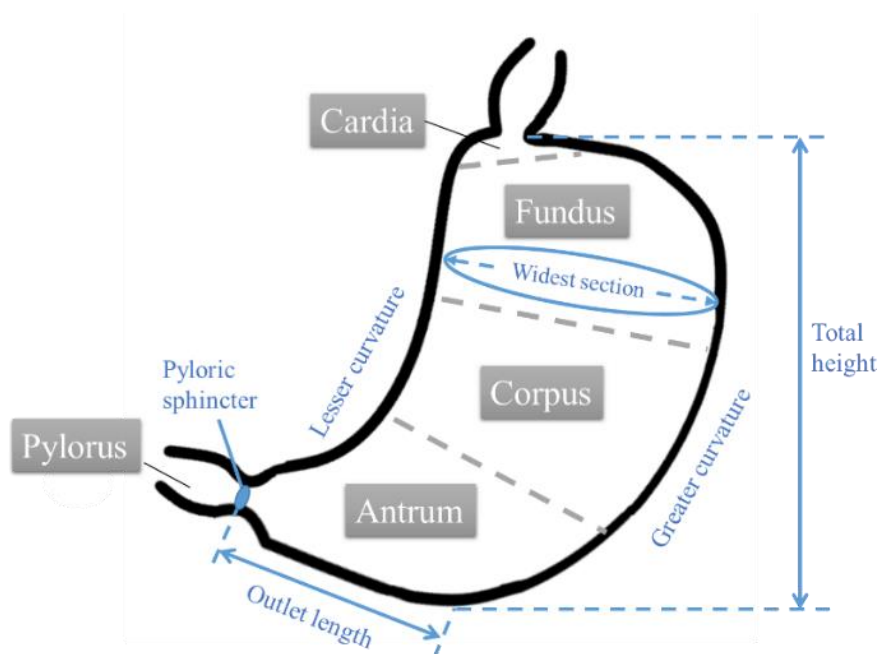
Figure 2.1: Different regions of the stomach.

The human stomach is a J-shaped hollow organ consisting of four anatomic regions: the fundus, corpus (body), antrum, and pylorus (Figure 2.1). These four regions can be divided into two

functional areas, called the proximal stomach and the distal stomach. The proximal stomach (fundus and corpus) serves as a reservoir where undigested food is stored [8]. The distal stomach (antrum and pylorus) serves as a grinder to break down large food particles. It also acts as a pump, by generating peristaltic waves and promoting gastric motility [9, 10]. Partially-digested food, called chyme, is formed after gastric digestion. The pylorus connects the stomach to the duodenum, where the partially digested food exits and flows into the small intestine [11].

The stomach shape and volume varies among individuals depending on many factors, such as age, gender, body position, gastric content, and the surrounding organs. Csendes et al. [12] measured the volume of adult stomachs and found values in the range of 0.7-1.6 L. The long convex lateral border of the stomach has a higher curvature, while the shorter concave medial surface of the stomach has a lower curvature. The widest section of the stomach is at the fundus and it gradually becomes narrower towards the pyloric sphincter, which is the outlet. The total height of the stomach (from the uppermost point of the fundus to the bottom point of the antrum) is 20-22 cm. The distance between the bottom point of the antrum and the outlet is around 8 cm [13]. The pyloric sphincter acts as a valve with a diameter of 1 cm or less, and it only allows small particles to pass through during regular emptying. The geometrical characteristics of adult-sized stomachs after digestion are listed in Table 2.1 [13, 14].

Table 2.1: The geometrical characteristics of adult-sized stomachs.

Volume (L)	Greater curvature length (cm)	Lesser curvature length (cm)	Widest section width (cm)	Total height (cm)	Outlet length (cm)	Pyloric sphincter diameter (cm)
0.7 – 1.6	26 - 31	~ 15	~ 10	20 - 22	~ 8	< 1

2.1.2. Stomach wall

The stomach wall consists of four main layers of tissue: mucosa, submucosa, muscularis externa and serosa (Figure 2.2). Each layer contributes differently to the functional anatomy. When the stomach is empty, large folds are generated by the mucosa and the submucosa. These folds, called rugae, allow the stomach to expand [15]. In mechanical characterization analysis, layers are divided into the mucosa-submucosa section (mucosa and submucosa) and the serosa-muscle section (muscularis externa and serosa).
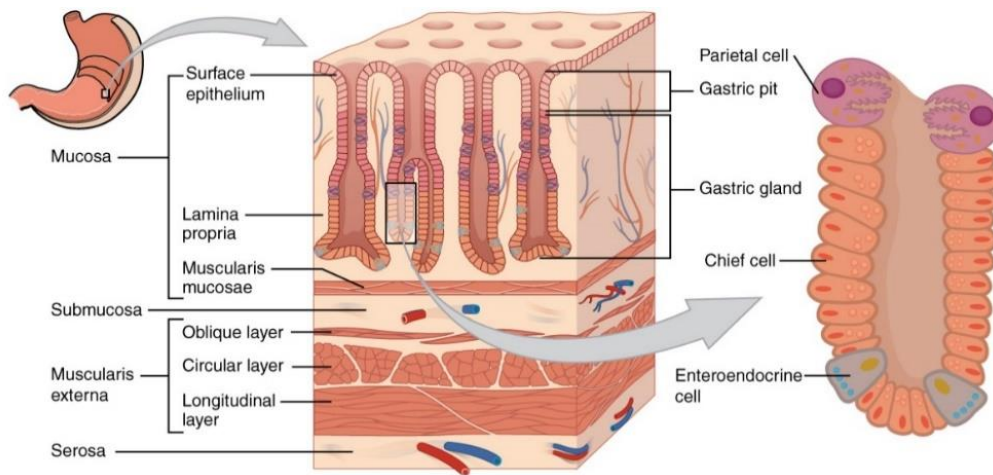
Figure 2.2: The stomach wall anatomy. "Illustration from Anatomy & Physiology [16], Connexions Web Site." by OpenStax College. License: (CC BY-SA 3.0).

Mucosa is the innermost layer of the stomach wall, and it acts as a mucous membrane. It contacts the food directly, and its primary function is gastric secretion [15]. The second layer of the stomach wall is the submucosa, and its primary function is to support the mucosa. The third layer, the muscularis externa, consists of three sub-layers: the oblique layer, the circular layer and the longitudinal layer. The contractions of these smooth muscle layers aid in gastric motility. The serosa is the outmost layer that maintains lubrication between opposing surfaces by secreting serous fluid [15].

Due to individual variations, the overall stomach wall thickness varies from 2.8 to 4.2 mm. As the thickest layer among the four layers, the mucosa thickness alone ranges from 1.0 to 1.6 mm [17]. The depths of the gastric glands and the gastric pits are 1.2 mm and 0.2 mm, respectively [18]. As a soft biological tissue, the stomach wall presents nonlinear viscoelastic properties. Due to the nonlinear relationship between stress and strain, the stiffness of the material changes when undergoing deformation. According to Jia et al. [19] and Zhao et al. [20], the deformation characteristics of the stomach tissue are distinct in different orientations (longitudinal and circumferential), locations (smaller curvature and greater curvature), regions (fundus, corpus and antrum). The stiffness comparisons are listed in Table 2.2 below.

Table 2.2: Stiffness comparison of stomach wall material [19, 20].

Orientation	Longitudinal > circumferential
Region	Corpus > antrum > fundus
Section	In fundus and corpus, mucosa-submucosa > serosa-muscle In antrum, serosa-muscle > mucosa-submucosa
Curvature	Greater > smaller

7

Stress-strain curves constructed by Zhao et al. [20] based on the mechanical properties of the gastric wall are shown in Figure 2.3.
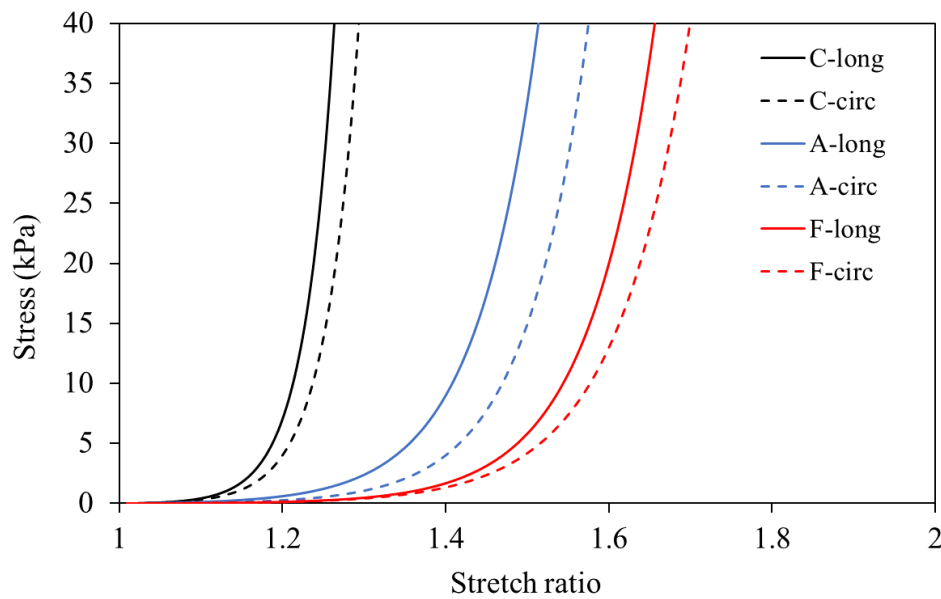
Figure 2.3: Stress-strain relationships of the stomach wall. F, fundus; C, corpus; A, antrum; circ, circumferential direction; long, longitudinal direction. Adapted from Zhao et al. [20].

The biomechanical properties of the wall are crucial in the digestion process because it is closely related to the contraction behaviour of the stomach wall [20]. Diabetic patients have lower material compliance (or higher material stiffness) than those with normal stomachs, and the difference appears in different regions [21].

2.2.   Gastric digestion

Gastric digestion can be categorized into chemical digestion (gastric secretion) and mechanical digestion (gastric motility). Contact between bolus fragments with gastric secretions leads to chemical digestion reactions. Movements of the stomach walls create mechanical breakdown, through which the fragment sizes of the bolus components decrease, and the surface area of the fragments increase. The increased surface area accelerates the chemical reaction between the bolus and the gastric secretions, which lead to enhanced chemical digestion [13].

2.2.1.   Chemical digestion and gastric secretion

Chemical digestion in the stomach is mainly controlled by gastric juice. Gastric juice is secreted at a rate of 2-3 L per day in the cardia, with the secretion rate ranging from 1 mL min^{-1} (when fasting) to 50 ml min^{-1} (during food ingestion). With a pH value varying from 1.5 to 3.5, the main components of gastric juice include hydrochloric acid (HCl), potassium chloride (KCl),

sodium chloride (NaCl), digestive enzymes and water [15]. With a density close to that of water and a viscosity varying from 0.01 to 2 Pa.s, gastric juice is a non-Newtonian fluid with shear-thinning behaviour [22]. Bicarbonate is also produced in the stomach to neutralize gastric acid. Mucus acts as a barrier preventing damage to the stomach wall caused by acidity. The pH in the stomach is around 2 when the stomach is empty and increases up to 6.5 after a meal. It takes 2 – 4 hours for the pH to return to its original value [15]. The primary function of gastric acid is to hydrolyse the carbohydrates and proteins inside the bolus and convert them into chyme [15].

Gastric secretions are produced in the gastric glands, which are in the mucosa of the stomach wall. There are three types of gastric glands: the cardiac glands, the fundic glands, and the pyloric glands (located in the antrum and the pylorus) [15], located in different regions of the stomach wall, as shown in Figure 2.4. Each type of gastric gland contains specific cells as summarised in Table 2.3. All gastric glands contain mucous cells. The secretory products of mucous cells include mucus and pepsinogens. The mucus serves to protect the mucous membrane. Pepsin is transformed from pepsinogen through hydrolysis, and it is the primary enzyme for digesting proteins. The fundic glands occupy more than 75% of the mucosa [18]. The primary cells present in the fundic glands are the parietal and chief cells. Parietal cells produce hydrochloric acid (HCl) and gastric intrinsic factor. HCl is the main component of gastric acid, while gastric intrinsic factor is a glycoprotein vital for vitamin B_{12} absorption. Apart from pepsinogen, chief cells also produce gastric lipase, which is an acidic enzyme that eases the process of fat digestion. G cells exist in the pyloric glands, and gastrin is a hormone produced in G cells that aids in regulating stomach secretions.
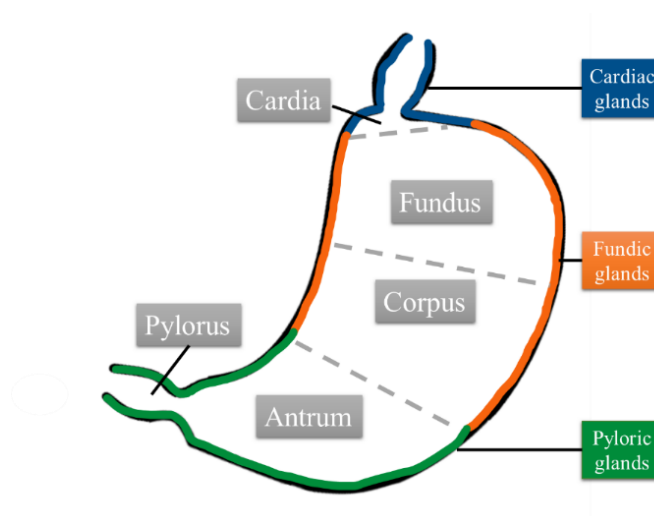
Figure 2.4: Gastric secretion regions.

Table 2.3: Gastric secretions produced inside the stomach [18].

Region	Gastric glands	Cells within the glands	Secretions produced
Cardia	Cardiac (< 5%)	Mucous	Mucus, pepsinogen
Fundus, corpus	Fundic (> 75%)	Parietal	Hydrochloric acid, intrinsic factors
		Chief	Pepsinogen, gastric lipase
		Mucous	Mucus, pepsinogen
Antrum, pylorus	Pyloric (20 - 25%)	Mucous	Mucus, pepsinogen
		G	Gastrin enzyme

There are three phases involved in the regulation of stomach secretions: cephalic, gastric, and intestinal phases. Food sensations (through smell, taste, and even thoughts) can trigger gastric secretions in the cephalic phase. Signals of these sensations are sent from the brain to the stomach via the nerves. Cells in the gastric glands then receive signals and release mucus, hydrochloric acid, intrinsic factor, and gastrin. The gastric phase is triggered when the food enters the stomach. During this period, a large amount of gastric secretion is produced and mixed with the food. When the stomach distends, stretch receptors stimulate the gastric glands to produce hydrochloric acid and pepsinogen. Gastrin is produced as well and leads to additional hydrochloric acid production. The intestinal phase is the final phase when gastric secretions are inhibited, and it is triggered when the chyme exits the stomach and enters the duodenum. The inhibition is primarily controlled by the pH of the chyme. When the pH drops to 2 or below, hormone secretions, including cholecystokinin and gastric inhibitory polypeptide, are produced to inhibit the acid secretion release [23].

2.2.2. Mechanical digestion and gastric motility

Along with chemical digestion, the food bolus breaks down into chyme by mechanical forces inside the stomach. There are two types of mechanical forcing by the stomach walls: tonic contractions and antral contractions [16], as shown in Figure 2.5. The tonic contractions produce slight indentations of the gastric wall, which allow the stomach to adjust itself to the changing volume [24]. During gastric emptying, more muscular tonic contractions happen in the upper part of the stomach.

The antral contractions are a series of peristaltic waves, called antral contraction waves (ACWs). The parameters of the ACWs, such as contraction frequency, propagation velocity, propagation direction, maximum amplitude and life span, are determined by the pacemaker

10

potentials. The origin of the pacemaker activity is the network of interstitial cells of Cajal located at the higher curvature gastric wall [25].
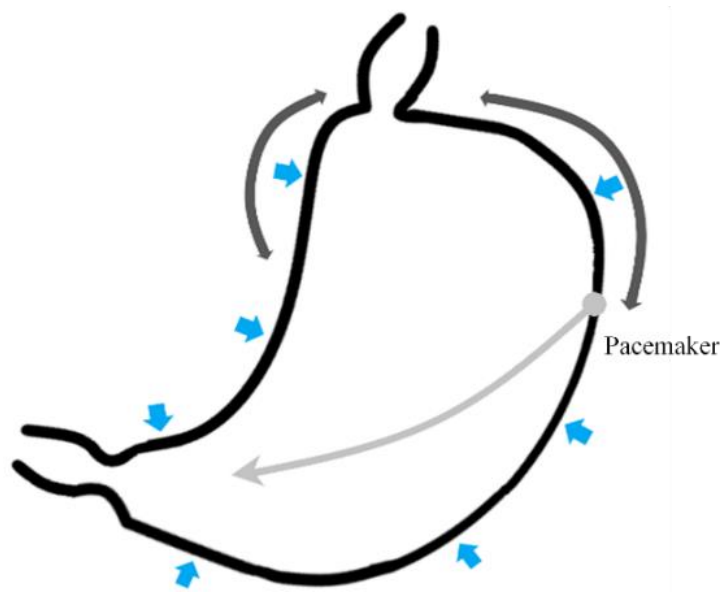
Figure 2.5: Gastric contractions in the stomach.

After 20 to 30 minutes of meal ingestion, ACWs are initiated from the pacemaker [26]. They originate from the upper part of the stomach wall and pass through the antrum, towards the pylorus. The gastric contents are mixed and ground during this process, which can last for hours depending on the food content. ACWs are initiated $2.6 - 3.2$ times per minute from the pacemaker and propagate towards the pylorus with a velocity (c) ranging from 0.22 to 0.33 cm s^{-1}. The wavelength (λ) varies from $1.2 - 1.8$ cm, and the occlusion ($1 - \varepsilon/D$, while ε/D is the occlusion diameter to antral diameter) changes from 60% to 90% throughout the process [26]. The occlusion pattern of ACWs is shown in Figure 2.6.
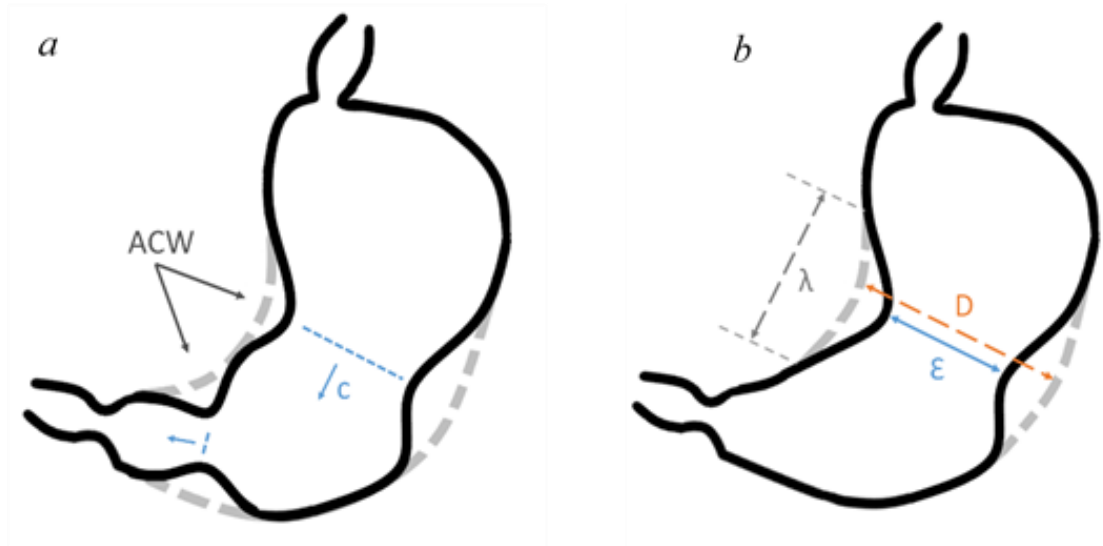
Figure 2.6: Occlusion pattern of ACWs.

There are two main motility patterns during gastric digestion in the developed computational stomach models [14, 26, 27]: propulsive and retropulsive motion, as shown in Figure 2.7. The ACWs travel from the pacemaker toward the pylorus, causing propulsive motion. During the propulsive process, stresses induced in the fluid apply differential stresses to the food particulates, causing the food bolus inside the stomach breaks down into chyme. After gastric mixing, the chyme enters the small intestine through the pyloric ring. The pyloric ring works as a control valve for gastric emptying as it only allows particles with a diameter of less than 2 mm to pass through. If the chyme is not small enough, it is pushed back to the corpus for continued mixing. This push-back behaviour causes retropulsive jet-like motion, which is a backward movement related to the occlusion pattern. However, it needs to noted that the retropulsive behaviour is likely only applicable to a very low viscosity, Newtonian fluid (like water) as this behaviour is not observed in the *in vitro* studies with high viscosity fluids.
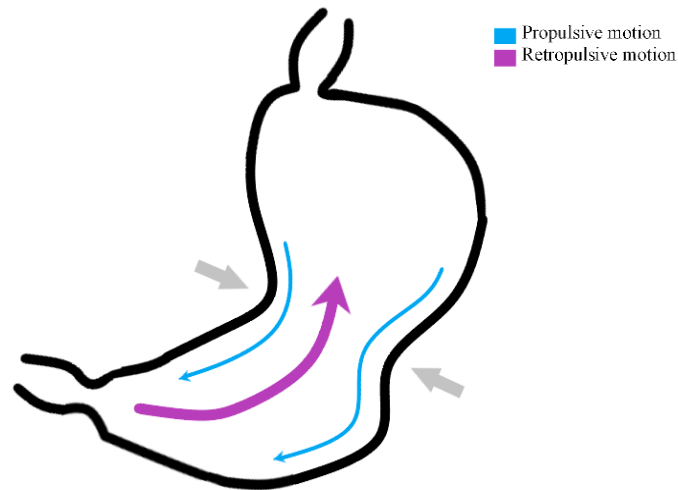
Figure 2.7: Motility patterns inside the stomach.

Another pattern of motion observed is circular motion (also called eddy motion) [14]. It occurs mainly between successive ACWs and is related to the width of the waves. The circular motion is relatively small compared with the other two motions.

2.3. Gastric emptying of liquids and solids

Gastric emptying happens when the chyme exits the stomach and flows into the duodenum along with the ACWs [11, 28] and it is regulated by both the stomach and the duodenum [16]. The gastric emptying rate is primarily affected by individual biological differences and meal compositions. Biological differences mainly include age, gender, body weight, diseases, depression, stress, and blood glucose level [29]. Some studies suggest that females and elders have a slower average emptying rate, probably due to weaker antral contraction waves [29-32]. However, other studies argue that the influence of these biological differences (age, gender, and body weight) was insignificant [33-35]. Therefore, the effect of these factors remains uncertain. Moreover, patients with functional dyspepsia have slower emptying rates than normal participants. After a standard meal (800 calories), the average final emptying time was 248 minutes for the normal subjects and 359 minutes for functional dyspepsia sufferers [36]. Research also showed that depressed patients have slower emptying rates, while emotional stress accelerates the emptying process [37, 38].

While individual biological differences are difficult to compare, most studies focus on the effect of the features of the meal ingested. The gastric emptying profiles of liquids, digestible solids, indigestible solids, and fats are distinctive. Gastric factors also include volume, density,

13

viscosity, caloric content, temperature, acidity, and the texture of the food ingested [39-42]. In general, the gastric emptying time of solids in a meal is much longer than that of liquids in a meal, mainly because extra time is required initially for solid degradation [33, 40, 43].

2.3.1. Liquid emptying

According to Elashoff et al. [40], the gastric emptying profile for liquids follows an exponential curve. It is assumed that liquid emptying largely depends on the pressure gradient in the stomach regulated by the fundic pressure and controlled by the pyloric ring opening [13]. The emptying rate of non-caloric liquids, such as water and isotonic saline, follows a first-order kinetics process and is proportional to the stomach's liquid volume [28]. The mathematical curve for the non-calorie liquids emptying pattern can be represented by a simple exponential equation, as given below [40]:

$$f = 2^{-(t/t_{1/2})} \tag{2.1}$$

where f is the volume fraction of the meal that remains in the stomach at time t, while $t_{1/2}$ is the time when 50% of the meal has emptied.

The estimated $t_{1/2}$ for non-caloric liquids varies from 8 to 18 min due to individual variations among different patients [25]. However, liquid nutritional compositions alter the emptying patterns due to the feedback control regulated by the duodenum [29]. Water, which has no calorie content, has a $t_{1/2}$ of 10 min [44]. The presence of nutrients in the liquids causes processes to be initiated that slow down the emptying rate because they need to be absorbed in the small intestine. Receptors in the duodenum provide a feedback mechanism that ensures the emptying rate is between 2 to 4 kcal min^{-1} caloric content [29]. Therefore, the emptying of low-calorie and high-calorie liquids do not follow the simple exponential equation [40]. Lavin et al. [45] showed that the half-emptying rate of lemon-flavoured drinks with sucrose ($t_{1/2} =$ 86 min) or maltose ($t_{1/2} = $ 115 min) is slower than lemon juice alone with water ($t_{1/2} = $ 39 min). The general emptying patterns of liquids with different calorie contents are shown in Figure 2.8 below.
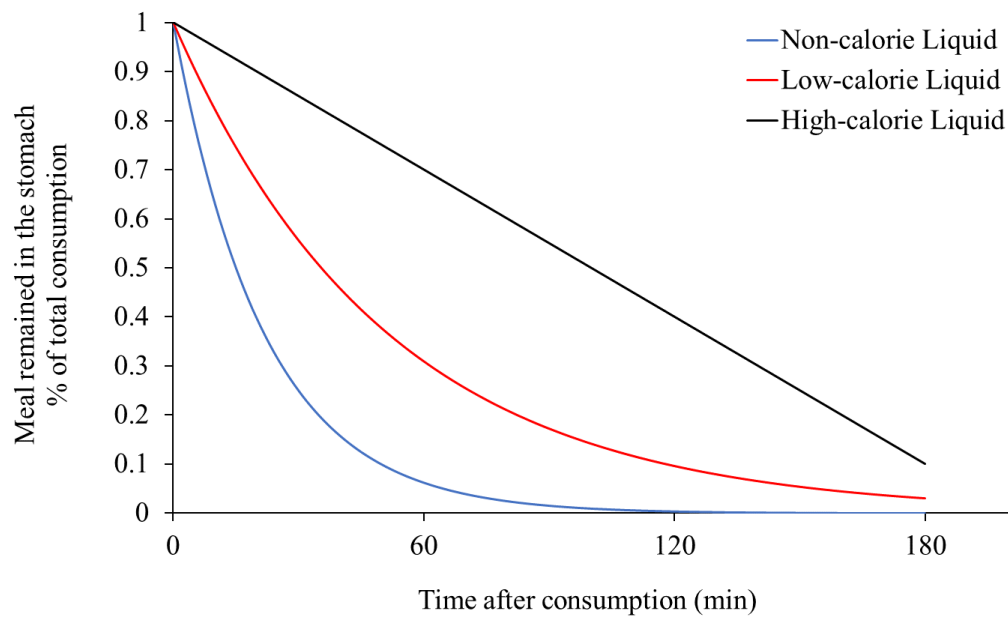
Figure 2.8: Gastric emptying patterns of liquids with different caloric content. Adapted from Elashoff et al. [40].

According to Jin et al. [46], the relationship between viscosity and gastric emptying is controversial. Shimoyama et al. [41] suggested that increased meal viscosity accelerated the gastric emptying process by avoiding the sudden outflow of caloric content and, therefore, led to a smoother emptying process. However, other studies found that increased viscosity delayed the emptying process [47, 48]. Sun et al. [49] found that the liquid temperature has an effect on emptying. Liquid at body temperature (37°C) has a higher initial emptying rate than cold drinks (4°C) and warm drinks (50°C).

A summary of the meal features effect on liquid emptying is shown in Table 2.4 below. The half-emptying time comparison only applies to each feature as the meal compositions vary in different studies.

Table 2.4: Meal features that affect the liquid emptying rate.

Feature	Relationship	Food	$t_{1/2}$ (min)	Model
Calorie content	Negative correlation	Lemon flavoured drinks		*in vivo* – human [45]
		Without sugars	39	
		With sugars	86 (sucrose) 115 (maltose)	
		Dairy-based shakes		*in vivo* – human [47]
		100 kcal	27	
		500 kcal	70	
Viscosity	Positive correlation	Enteral nutrition solution		*in vivo* – human [41]
		Without pectin	258	
		With pectin	195	
	Negative correlation	Locust bean gum (non-nutrient)		*in vivo* – human [48]
		0.02 Pa.s	17	
		1.1 Pa.s	19	
		Dairy-based shakes		*in vivo* – human [47]
		Thin	27	
		Thick	41	
Temperature	Related	Orange juice		*in vivo* – human [38] [49]
		4°C	19	
		37°C	14	
		50°C	18	

2.3.2. Digestible solid emptying

Solid emptying is much slower than liquid emptying due to the extra time required for particle disintegration, called the lag phase. As the pyloric ring only allows particles with a diameter of less than 2 mm to pass through, large particles contained in the solid meal need to break down before exiting the stomach. A widely used mathematical curve shown below is used to represent the rate of digestible solid emptying [40].

$$f = 2^{-\left(\frac{t}{t_{1/2}}\right)^{\beta}} \tag{2.2}$$

As mentioned, f is the volume fraction of the meal remaining in the stomach at time t, while $t_{1/2}$ is the time when 50% of the meal has emptied from the stomach. β is a parameter that affects the duration of the lag phase, which depends primarily on the physical properties of the

meal. Large particles in the meal prolong the lag phase, while small particles of less than 2 mm in diameter can exit the stomach directly.

For a mixed solid-liquid meal, the solid volume fraction of the meal affects the emptying rate. Solid components dominate the lag phase while the liquid content of the meal is emptied promptly compared with the solids [50]. However, once the solid degradation finishes, the presence of the degraded solid components can speed up the emptying process [43]. The nutritional properties of the meal also modify the emptying rate. According to Camps et al. [47], it was evident that increasing the energy density slows the emptying process. Compared with a low-calorie solid meal, the lag phase of a high-calorie solid meal is much longer, as can be seen in Figure 2.9 [28]. Marciani et al. [48] and Camps [47] found that increased viscosity can increase the perceived fullness and may prolong the emptying process [42, 47, 48]. However, the effect of increased viscosity is less significant than the effect of increased calorie content.
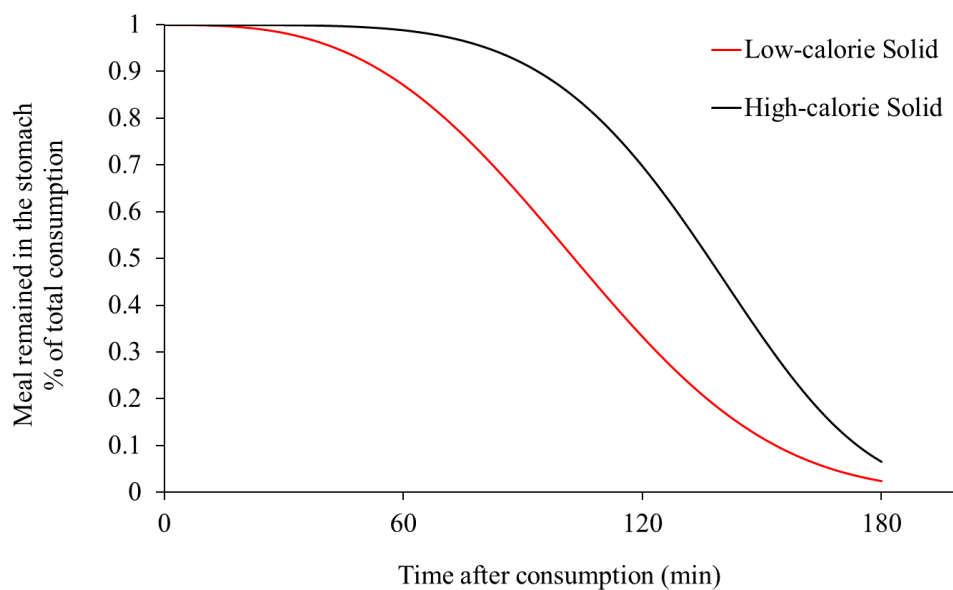
Figure 2.9: Gastric emptying patterns of solids with different caloric content. Adapted from Elashoff et al. [40].

Food structure has a significant impact on emptying time. Bornhorst et al. [51] proposed a food breakdown classification system to predict the breakdown behaviour of solid foods based on their initial hardness and the rate of softening. The initial food hardness was related to the food properties, including structure, physical properties, and chemical compositions. The changes in the hardness were due to the penetration and dissolution of acid and enzymes into the food matrix. The hypothesis was that the initial hardness of the food matrix was closely related to the moisture content and the cooking process. The softening rate correlated with the amount of

17

acid and enzymes that have entered the food matrix. Compared with hard food, soft food can be disintegrated much faster [13].

Different food processing methods change the food structure and thus alter the nutrient release rate. Kong et al. [7] studied the food breakdown kinetics of raw and boiled carrots through an *in vitro* stomach model. The carrot foods matrix became softer and easier for the acid and enzymes to penetrate after boiling. Results showed that the half-emptying time of raw carrots was much longer than 6 min-boiled carrots. The hardness of the carrots decreased from 42 N to 5 N after boiling. The gastric emptying pattern of the raw carrot was like the solid emptying pattern, while the pattern of the 6-min-boiled carrot was closer to the liquid emptying curve. A similar study related to food processing was conducted by Urbain et al. [52] through an *in vivo* study. The half-emptying time of the homogenised egg meal was faster than cubed egg particles. Dried and roasted foods had slower emptying rates, potentially due to loss of moisture content and increased hardness. Fried pasta had a significantly slower emptying rate than non-fried pasta [53]. The overall emptying patterns were not significantly different between raw and roasted almonds [54]. However, the protein content in the roasted almonds emptied slower than for raw almonds. Siegel et al. studied the effect of density by comparing the emptying rate of cooked chicken liver and egg, with similar nutrient content but different densities [50]. Results show that both the lag phase and half-emptying time increased with density.

Table 2.5: Meal features that affect the solid emptying rate.

Meal features	Relationship	Food	$t_{1/2}$ (min)	Model
Hardness	Negative correlation	Carrot		*in vitro* [7]
		6-min boiled	15	
		Raw	62	
		Egg		*in vivo* – human [52]
		Homogenized meal	71	
		5 mm cubed particles	104	
		Pasta		*in vivo* – human [53]
		Non-fried	227	
		Fried	317	
		Almond		*in vivo* – pig [54]
		Raw	Similar, > 10 hr	
		Roasted		
Density	Negative correlation	Egg	78	*in vivo* – human [50]
		Cooked chicken liver	94	

2.3.3. Indigestible solid emptying

The gastric emptying of indigestible solids is mainly related to particle size. If the size of the particles is smaller than 2 mm in diameter, they can directly pass through the pyloric sphincter and enter the small intestine and follow the emptying pattern of digestible solids. Larger particles do not follow the same pattern. Instead, those particles are expelled by the phase III activity, the last phase of the migrating motor pattern [25]. The phase III activity has the most forceful contractions at maximum amplitudes and frequencies, and it serves as a housekeeping function by evacuating any particles that remain in the stomach. Compared with hard particles, soft particles leave the stomach faster. However, when the particles are larger than 2 mm, neither the particle size nor the shape affects the emptying rate [55].

2.4. Composition of a standard meal

According to Australian Dietary Guidelines [56], a healthy man aged 19-50 with average height and weight should consume two servings of grain food, three servings of vegetables, and one serving of meat for dinner. The total weight of a sample meal is 455 g with an estimated energy content of 1869 kJ. The nutritional information of the food is analysed through the Australian Food Composition Database [57]. The food and the corresponding analysed compositions are listed in Table 2.6 below.

Table 2.6: A standard dinner meal for a healthy man aged 19-50 years.

Food	Serve size	Weight (g)	Energy (kJ)	Moisture (g)	Sugar (g)	Starch (g)	Protein (g)	Fibre (g)	Fat (g)
Cooled white rice	2 grain serves	150	988	92.7	0.2	51.9	4.6	1.2	0.3
Baked peeled carrots	3 vegetable serves	225	403	193.5	17.1	1.1	1.6	9.2	-
Grilled chicken breast	1 meat serve	80	478	53	-	-	23.8	-	2

The particle size distributions of the food in the sample meal are listed below in Table 2.7. The bolus size of white rice was measured by Hwang et al. [58] from 20 healthy volunteers, while the carrots and chicken breast measurements were from Jalabert-Malbos et al. [59] collected from 10 subjects. The food samples were collected after mastication.

Table 2.7: Particle size distribution in the bolus after mastication of the sample meal.

Particle size (mm)	< 1.4	1.4 – 2.0	2.0 – 4.0	< 4.0	Median size, d_{50}
Cooked rice	65%	33%	1%	-	0.32
Carrot	32%	22%	36%	10%	1.90
Chicken breast	46%	10%	30%	14%	1.60

2.5. Gastric digestion of carbohydrates in the stomach

Recently, more research has been conducted on the gastric digestion of different food compositions. Food components can be divided into two main categories: energy components and non-energy components. Energy components include carbohydrates (excluding dietary fibre), proteins and fats, all of which provide our bodies with energy sources. Non-energy components are dietary fibres, vitamins, minerals, and water. Although non-energy

components do not contain energy, they are still essential for human health. It should also be noted that although some dietary fibres are carbohydrates, they cannot be absorbed and are not defined as energy sources. Micronutrients, vitamins and minerals are released during the gastric digestion of macronutrients (carbohydrates, proteins, and fats).

Carbohydrates are the primary energy source for human bodies. There are simple and complex carbohydrates. Simple carbohydrates are referred to as sugars, while complex carbohydrates are polysaccharides. Both starch and dietary fibres contain polysaccharides. A key concept in carbohydrate digestion is the glycaemic index (GI). It ranks how quickly carbohydrate-containing foods are transformed into glucose. The glucose contents absorbed by the human body raise blood glucose levels. Apart from the glucose contents, how the foods are cooked or prepared also alters the GI value. Apart from sugars, starch and dietary fibres, glycogen contains glucose. Glycogen serves as the glucose storage source in the human body. When glucose is in excess in our body, it is stored as glycogen.

2.5.1. Gastric digestion of sugars

Simple carbohydrates can be divided into monosaccharides and disaccharides. Monosaccharides include glucose, fructose, and galactose. Disaccharides include maltose (consists of two glucose molecules), sucrose (consists of glucose and fructose) and lactose (consists of glucose and galactose). During gastric digestion, monosaccharides are absorbed directly across the membrane of the small intestine. As for disaccharides, they need to be broken down chemically into monosaccharides first. Common foods that contain sugars are listed in Table 2.8 below.

Table 2.8: Foods that contain sugars.

Sugars	Glucose	Fructose	Galactose	Maltose	Sucrose	Lactose
Foods	Fruit, honey, and some vegetables	Fruits, honey, root vegetables	Milk and dairy foods	Malted grains	Sugar cane	Milk

When swallowed, sugars pass through the stomach quickly. Their digestion and absorption processes happen in the small intestine.

2.5.2. Gastric digestion of starch

Starches are the most consumed type of carbohydrates. They are a mixture of two polymers: amylose and amylopectin, both of which are formed from glucose. The size of most starches

varies from 1 μm to 100 μm [60]. The molecular weight, molecular structure, and amylose to amylopectin ratio of different starches are related to their absorption and energy release rate. Starch digestion begins in the mouth when reacting with salivary amylase produced in the mouth. Starch is hydrolysed into simple carbohydrates (sugars) when it reacts with amylase. The partially digested starch enters the stomach, where solid foods break down into smaller particles through mechanical motion. The remaining starch digestion process happens in the small intestine when reacting with enzymes. Some studies suggested that the digestion of starch-based foods is controlled by the rate of hydrolysis by amylase [61, 62]. Some examples of gastric emptying times of starchy foods are given in Table 2.9.

Table 2.9: Gastric emptying time of starch-based foods.

Meal features	Relationship	Starch-based food	$t_{1/2}$ (min)	Model
Particle size	Longer emptying time as the particle size increases	**Wheat-based**		
		Semolina	88	
Softening rate	Shorter emptying time as the softening rate increases	Couscous	160	
		Pasta	360	*in vivo* – pig [63]
Starch source	Hard to compare	**Rice-based**		
		Couscous	150	
		Noodle	213	
		Grain	233	
Bran layer	Longer emptying time with bran layer	Cooked rice		
		Brown rice	229	*in vivo* – pig [39, 64]
		White rice	227	
Starch content	Longer emptying time as the amount of starch content increases	Starch-contained meal		
		Low starch content	93	*in vivo* – horse [65]
		High starch content	143	

2.5.3. Gastric digestion of dietary fibres

Dietary fibres are a type of carbohydrate that enzymes cannot digest. Although dietary fibres do not provide energy, they can benefit human health in various ways. By increasing the volume occupied in the stomach, dietary fibres can promote satiety and reduce appetite without increasing the caloric content.

There are two main kinds of dietary fibres: insoluble fibres and soluble fibres. Insoluble fibres mainly include lignin, cellulose, and hemicellulose. They are water-insoluble and less fermentable than soluble fibres. Soluble fibres include pectin, gums, and β-glucans. They can bind with water, oil, and oil-in-water emulsion and then turn into viscous gels [66]. Such fibre-bound mixture will be excreted without being absorbed by the body. Moreover, some soluble fibres can delay glucose absorption in the small intestine by decreasing nutrient diffusion rates [66].

Most fibre-rich foods contain both types of fibre. Fibres commonly exist in fruits, vegetables, wholegrain foods, and legumes. In carrot pomace, 96.1% of the dietary fibres are insoluble fibres (51.6% cellulose and 32.2% lignin, 12.3% hemicellulose) while only 3.9% are soluble fibres (3.88% pectin) [67]. Carrot dietary fibre's water-binding and oil-binding capacities are 18.6 g water/g and 5.5 g oil/g, respectively [68].

2.5.4. Gastric digestion of protein

Proteins are constructed from various types of amino acids. When digested, proteins are broken down by the pepsin in the stomach into polypeptides. Polypeptides will then enter the small intestine and decompose into amino acids.

Protein digestion starts from the mouth, where mastication and chewing promote physical breakdown. Partially digested protein then enters the stomach. Pepsinogen is produced by the mucous cells in the stomach wall. Once secreted, it transforms into pepsin through hydrolysis. Pepsin is the main enzyme for protein digestion, breaking proteins into polypeptides in the stomach. Polypeptides then enter the intestine and decompose into amino acids by other enzymes. It is a much more complicated process than starch digestion in the stomach, as chemical and mechanical breakdowns are involved in protein digestion.

The interaction between gastric pH, food structure, and buffering capacity of the meal is essential for protein digestion. The gastric pH significantly impacts protein digestion as it controls the pepsin activity. The presence of acid/base groups in the protein slows down the changes in pH [69]. This resistance is defined as buffering capacity, and it varies between different foods. The lag phase is used to measure the buffering capacity. A longer lag phase in protein digestion represents a higher buffering capacity in foods. Mennah-Govela et al. [70] observed in an *in vitro* study that foods with high protein content and large surface area had higher buffering capacity and thus a longer lag phase.

2.5.5. Gastric digestion of fat

The main type of fats in foods are triglycerides, which consist of glycerol and fatty acids. A small amount of consumed triglycerides are digested in the stomach but most fat digestion occurs in the small intestine [71, 72]. The lingual lipase enzyme is released in the mouth when consuming fat. Gastric lipase is released in the stomach. Lingual lipase and gastric lipase break part of the triglycerides (up to 30%) into diglycerides and fatty acids in the stomach through lipolysis [71]. The remaining triglycerides and diglycerides enter the small intestine for further digestion.

There are two types of fats in foods: saturated fats and unsaturated fats. Fatty meat, fatty poultry, whole-milk dairy products, butter and egg yolks are rich in saturated fats. Saturated fats are harmful to our body because there are strong relationships between high saturated fat consumption and several diseases, such as cardiovascular diseases, cancer, and bone diseases. The saturated fats carried in the blood (cholesterol) can block the arteries if they are in excess.

Unsaturated fats commonly exist in avocados, tofu, olives and olive oils, peanut butter, vegetable oils, fatty fish, nuts, and seeds. They are 'good fats' mainly because of their lower melting points. By replacing saturated fats with unsaturated fats, they can be melted into liquid form more easily and reduce the blockage in arteries in the heart or other parts of the body.

Compared with carbohydrates and protein, fat has the slowest emptying rate from the stomach [73]. Fat digestion and absorption can last for 16-24 hours. As shown in Figure 2.10, the stomach content stratifies into layers based on the material density typically creating a heavier solids layer at the bottom, which is below the pyloric opening (and therefore retained for processing), with a liquid layer above that has direct access to the pylorus for discharge. The fat layer floats at the top and also cannot access the pylorus until the stomach volume is much reduced. Therefore, the liquid layer is the closest to the outlet of the stomach and thus has the fastest emptying rate. In contrast, the emptying rate of fats (floating at the top of the liquid layer) and digestible solids (settled below the liquid layer) are much slower [25]. The operation of the stomach depends on the content structure and is controlled by density stratification. This is a critical aspect of the modelling and remains to be explored.
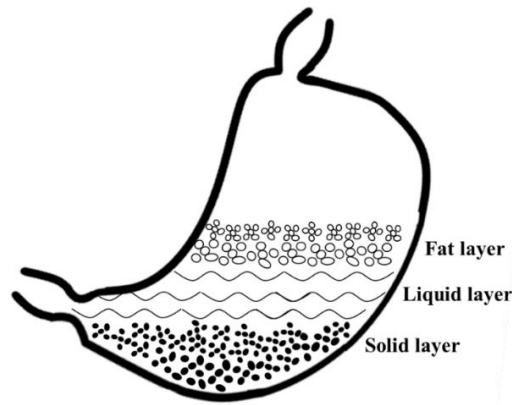
Figure 2.10: Food layering in the stomach.

Armand et al. [74] measured the emulsion droplet size distribution in the human stomach and duodenum after fat ingestion. The test meal was composed of emulsified droplets of various sizes (0.1 μm to 100 μm). Most of the droplets in the test meal (~70%) were between 10 and 100 μm in diameter. After ingestion, the median diameter decreased from 57 μm to 17 μm after 1 hour but then increased to 42 μm after 4 hours. The proportion of the largest particle size (> 100 μm) significantly decreased from 12% to 4% after 4-hour ingestion. Detailed size data are presented in Table 2.10 below.

Table 2.10: Emulsion droplet size distribution in test meal and the stomach after 1, 2, 3 and 4 hours of digestion [74].

Particle diameter	Median	0.1 - 1 μm	1 - 10 μm	10 - 50 μm	50 - 100 μm	> 100 μm
Test meal						
	57 μm	1.6%	21%	35%	35%	12%
Stomach content						
After 1 hour	17 μm	1.6%	44%	35%	14%	3.4%
After 2 hours	38 μm	<1%	12%	52%	35%	3.6%
After 3 hours	52 μm	<1%	8%	35%	53%	0.6%
After 4 hours	42 μm	<1%	12%	45%	40%	1.8%

2.6. Mathematical modelling of the digestion process

Two main steps are involved in the solids digestion process: disintegration and dissolution [29]. Disintegration happens when the food structure is fractured, and large food particles break into smaller particles. Once the food structure is no longer intact, gastric secretion penetrates the food matrix, causing the entrapped nutrient ingredient to dissolve into solution [51].

2.6.1. Disintegration theory of solid foods

Kong and Singh [7] suggested that the disintegration of food particulates is related to surface erosion and tenderization (texture softening). Surface erosion happens when the gastric fluid causes forces (normal, frictional, and shear forces) on the food surface. The erosion rate depends on the food structure strength and the mechanical force applied. The tenderization starts from the food surface and gradually penetrates towards the core of the structure, resulting in liquid uptake and temperature exchange inside the food matrix.
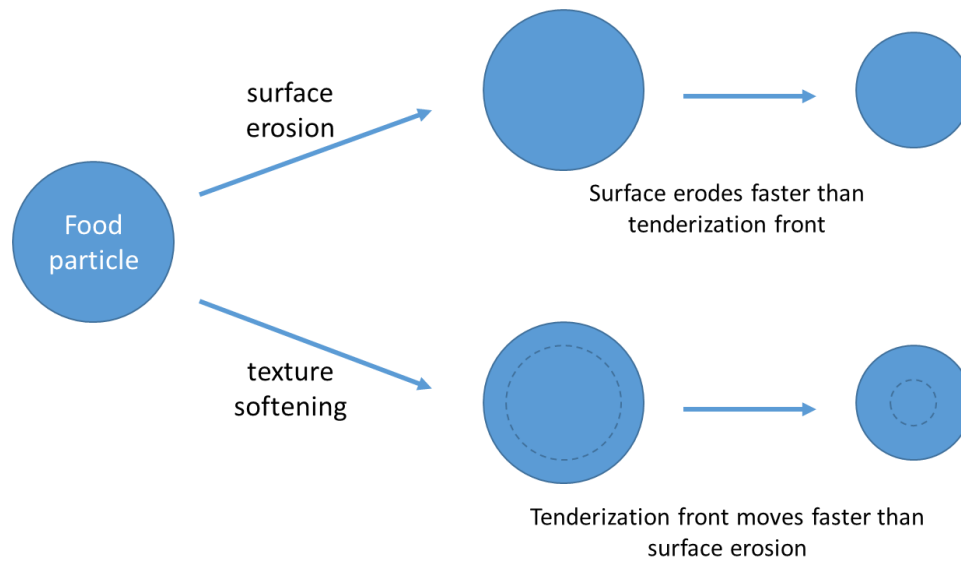
Figure 2.11: Surface erosion and tenderization effect in food disintegration. Adapted from Kong et al. [7]. Copyright (2022), with permission from John Wiley and Sons.

Raw carrots were softened more significantly when digested in 37°C gastric juices compared with in 21°C. Results showed that the softening effect dominated the digestion process of raw carrots when soaking them in gastric juice at 37°C. As shown in Figure 2.11, the tenderization front moves faster than the surface erosion. The internal mass loss potentially leads to increased porosity which increases diffusion and conduction rates.

Food processing strongly affects the strength of the food structure. The disintegration process of cooked carrots was very different from that of raw carrots. The structure of cooked carrots was softened before being digested. Therefore, the erosion rate dominates the disintegration process for cooked carrots. The process was affected significantly by the applied force in the stomach.

2.6.2. Diffusion model

The Noyes-Whitney equation [75] is a fundamental model when calculating the dissolution rate of a substance in a liquid medium.

$$\frac{dM}{dt} = A\frac{D}{d}(C_s - C_t) \tag{2.3}$$

where M is the mass dissolved, t is time, A is the surface area of the solute particle, D is the diffusion coefficient, d is the thickness of the concentration boundary layer at the surface of the dissolving substance, C_s is the saturation concentration of the solute, and C_t is the concentration in the bulk solvent at time t.

The dissolution rate increases when the particle surface area (A) increases. It means that when a large particle breaks down into smaller particles, the dissolution rate can increase dramatically. The diffusion coefficient (D) is associated with the solvent viscosity. Physical movement, such as stirring and agitation, decreases the thickness of the concentration boundary layer at the surface of the dissolving substance (d) and thus, can also accelerate the dissolution process. The saturation concentration of the solute (C_s) is related to temperature and pH. Depending on the solute and solvent relationship, the pH change can either increase or decrease the dissolution rate. If the solute is ionizable, it will dissolve completely in an acidic solution. However, if the solute is a weak electrolyte, the dissolution rate is variable with a peak achieved at a certain pH, depending on the solute and solvent equilibrium.

2.7. Computational analysis

Computational analysis refers to the computer-based calculation that is increasingly used in all fields, especially in engineering and science. It is used to solve complex mathematical problems which cannot be solved analytically. With the growth of computing power, computational simulation has been applied broadly to solve complex real-life problems [76]. For systems where traditional experiments are time-consuming and expensive to conduct, computational simulation becomes a powerful tool to provide insightful results [76].

2.7.1. Computational Fluid Dynamics (CFD)

CFD uses numerical analysis to predict fluid flows by solving the Navier-Stokes equations (NSE) based on mass, momentum, and energy conservation [76]. Four CFD methods have been applied to stomach modelling: Finite Volume Method (FVM) [14, 27, 77-80], Lattice Boltzmann Method (LBM) [26, 81, 82], Smoothed Particle Hydrodynamics (SPH) [83] and

Moving Particle Semi-Implicit Method (MPS) [84]. FVM and LBM are mesh-based methods, while SPH and MPS are particle-based.

Finite Volume Method (FVM)

FVM is a mesh-based CFD method in which the geometry is divided into a finite number of geometrical volumes (mesh elements) as shown in Figure 2.12. The NS equations are solved for each mesh element by applying Gauss's theorem and then converting the partial differential equations to a set of coupled algebraic equations that are solved iteratively [76].
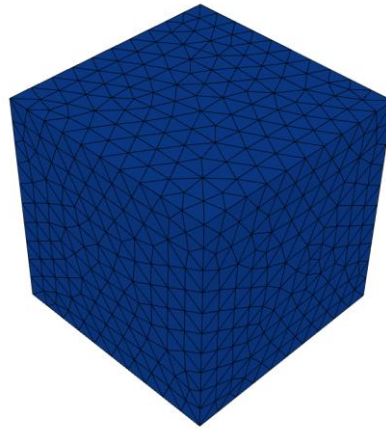
Figure 2.12: Schematic diagram of a FVM volume discretization of a cubic mass of fluid.

This method is dominant in solving CFD problems and is the backbone of commercial CFD software [85]. After solving the algebraic equations, the pressure, temperature, and fluid velocity components are determined within each volume. For problems that involve large deformation, the geometry can be re-divided or re-meshed as time progresses, and the computation can continue based on the new mesh [85]. More extensive computational efforts are required for re-meshing and mesh smoothing when irregular geometries or large deformation are involved [85] and there is numerical diffusion introduced when data are interpolated between meshes.

Lattice Boltzmann Method (LBM)

Most CFD methods solve the conservation equations of the fluid variables at a macroscopic scale (i.e., density, momentum, and energy), while LBM focuses on solving the conservation equations on a microscopic scale [86]. The principle of LBM is to develop kinetic models derived at a microscopic scale but that still obey the macroscopic fluid mechanics processes. There are two fundamental steps in the LBM algorithm: streaming and collision. At each timestep, each particle moves to one of its nearest nodes (streaming) and then particles at the

same node collide with each other (collision). Particle distribution functions are applied in the streaming step to predict the locations of the particles in an equilibrium state. A collision operator is introduced in this method to approximate the macroscopic equilibrium state. LBM is a highly parallel and efficient CFD method for fluid simulation [86]. It is particularly useful for simulating complicated flows and multiphase [86]. However, it has limitations in simulating geometries with complex boundaries and incompressible flow problems [86].

Smoothed Particle Hydrodynamics (SPH)

SPH is a mesh-free Lagrangian particle approach introduced by Gingold and Monaghan [87] for solving partial differential equations (PDEs). It has been applied across a broad range of fields because of its capability to represent complex deformations, the fracturing of continua, and complicated boundary interactions [88-90]. As a mesh-free method based on the discretization of the NS equations, it has been largely applied to solve solid and fluid mechanics problems with complex and time-varying geometries [91]. In this method, a moving set of particles are used to represent the continuum domain and equations of motion of the particles are constructed from the mathematics of the underlying physics. The particle properties are interpolated based on the properties of the neighbouring particles within a defined radius. There are two fundamental components in SPH: an interpolation kernel and particle approximation [92]. The kernel is used to interpolate or smooth the relevant properties of each particle and its nearby neighbours within the defined radius. The particle approximation is used to define the particle properties by reducing the governing PDEs to a set of ordinary differential equations (ODEs).

Problems involving large deformation, moving boundaries, multiphase, and even collision can be simulated relatively easy using SPH [90, 92-94]. The tensile instability in SPH results in a clustering of particles and can lead to negative pressures in the fluid field [95], which is hard to avoid in SPH and artificial stresses are usually needed to improve model stability [96].

Moving Particle Semi-Implicit Method (MPS)

Like SPH, MPS is also a mesh-free particle method that solves the NS equations. This method has two main components: the kernel model and the particle interaction approximation model [97]. SPH applies an equation of state when calculating the pressure, whereas the MPS implicitly estimates the pressure. The two main models in this method are the kernel and particle interaction approximation models, as present in SPH [97]. A semi-implicit algorithm is employed in this method. A Poisson equation is used to calculate the fluid density by

enforcing the incompressibility condition. As a result, MPS has a longer simulation time but potentially could give more accurate results compared with SPH. As particle methods, they both have a higher potential in dealing with large deformation, moving boundaries, multiphase and collision problems compared with traditional grid based CFD methods.

2.7.2. CFD methods comparison

Each CFD method has its strengths and limitations in solving different fluid mechanics problems. A comparison of these methods is given in Table 2.11. FVM is a purely mesh-based method while SPH and MPS are purely particle-based methods. LBM is a hybrid as its solver is mesh-based but its methodology is based on the microscopic particle model. In summary, mesh-based methods are well-established and suitable for simple geometries and two-phase flow simulations. Particle-based methods are more novel approaches and well-suited for complex geometries, large deformation problems, and challenging multiphysics. In terms of stomach modelling, SPH and MPS have advantages in simulating the complex stomach geometry and the deforming wall motion but their solution may not be as accurate as FVM because of the tensile instability.

Table 2.11: Advantages and disadvantages of different CFD methods.

CFD methods	Discretization	Strengths	Limitations
FVM	Mesh-based	Gas flow Turbulent flow	Complex geometries Moving boundaries Large deformation
LBM	Hybrid	Gas flow Moving boundaries	Incompressible flow Complex geometries Large deformation
SPH	Particle-based	Complex geometries Moving boundaries Extreme deformation	Gas flow Turbulent flow Tensile instability
MPS	Particle-based	Complex geometries Moving boundaries Large deformation	Gas flow Compressible fluid flow Turbulent flow Tensile instability

2.7.3. Finite Element Method (FEM)

FEM is the most widely used method for solving computational solid mechanics (CSM) problems [98-101]. The geometries are divided into a finite number of elements. Within each element, the solution is represented using a set of basis functions that represent the variation of the property over the element. The mass of each element remains unchanged. As the geometry deforms, the elements deform accordingly. Approximations are made by connecting all the

elements through a set of linear or nonlinear equations. A large matrix that contains data for the entire geometry is then produced based on interpolation over all the elements. The analysis is carried out by solving the matrix equation system.

This method is commonly used for structural analysis due to its high efficiency in dealing with structural mechanics problems [98]. The primary advantage is that nodes can be placed along the boundaries. Therefore, geometries with complicated shapes, moving boundaries or free surfaces can be simulated efficiently as the elements can be tracked easily. However, the main drawback is that it has difficulty in dealing with geometries with large deformation [98]. Since the grid cells are attached to the geometry, the mesh becomes distorted when the geometry deforms significantly. It may lead to inaccurate or unstable solutions or even force the computation to stop, at which point re-meshing is required.

2.7.4. Discrete Element Method (DEM)

DEM is a numerical method for simulating granular flows at the particle level [102-107]. The main components of DEM include searching to find neighbours and explicit time stepping with force calculation based on the geometric overlap of the particles, and particles with boundaries, using a contact model. The position, velocities, spins and orientations of the particles are assigned during the initialization. During the simulation, the properties of each particle are updated based on conservation equations for linear and rotational momentum. This method can simulate the forces between particles of different shapes and properties and between particles and walls. The number of particles can be easily scaled up because the solution algorithm is ideally suited to GPU computing. DEM has been widely used to solve a range of engineering problems involving granular and discontinuous particle flows, especially in the mining and pharmaceutical industries. It can also be coupled with FVM, SPH and FEM to enable multi-physics simulations, such a food particle motion within the fluid in the stomach.

2.8. Computational stomach models

In the past two decades, various computational techniques have been applied to model the gastric digestion process in the human stomach numerically. The first computational stomach model was developed by Pal et al. in 2004 using an LBM [14, 26]. The model was developed based on physiological data obtained from magnetic resonance imaging (MRI) images. A simplified 2D geometry was presented focusing on the peristaltic contraction waves inside the stomach. The gastric wall motion was simulated by adapting a moving boundary condition that

represented the ACWs [108]. The main finding was that ACWs generate strong movement, which contributes significantly to gastric mixing. Two main fluid flow motions were observed: the retropulsive motion and the circular flow motion between antral contraction waves (ACWs). Pal et al. focused more on gastric emptying in the study conducted later [109], suggesting ACWs also have an essential role in gastric emptying. The gastric mixing rate can be affected significantly by the gastric content. They demonstrated the potential of computational techniques in modelling the stomach system by making a pioneering attempt.

Kozu et al. [77] developed a 2D model for simulating the geometry of the stomach antrum alone. The FVM was applied to develop the model. The properties of gastric fluid, yogurt and starch syrup with various concentrations were measured through experiments and applied in the simulations. Numerical simulations showed that the viscosity of the gastric content affects the flow pattern significantly. The wall movement was defined by the ACWs equations. The effect of the ACWs was reduced markedly with increasing viscosity. Pepsin was considered in the mass transfer simulations. Although the chemical effect of the gastric secretions was not simulated, the concentration change of pepsin during gastric mixing was modelled. The result showed that the gastric secretions could be mixed efficiently during gastric peristalsis. Additionally, this was the first model that involved gravity in the simulation.

Ferrua and Singh [14] developed the first 3D stomach model to understand the gastric flow inside the stomach. With FVM, each node of the computational domain was repositioned as a function of time, based on the ACWs characteristics. The ACWs activities simulated were based on the MRI images observed by Pal et al. [26]. The model simulated a closed system fully filled with incompressible liquid content. Two main flow motions were identified: the retropulsive motion and the circular motion. The retropulsive motion was between the antrum and pyloric regions, while the circular motion was between the top and bottom regions. Two types of Newtonian fluids (water and honey) were simulated to study the effect of viscosity on gastric flow motion. The results showed that with a higher fluid viscosity, the formation of these two motions was diminished significantly, while the pressure was increased appreciably.

Ferrua and Singh [22] used the same model as in [14] to investigate flow behaviour of gastric fluid with different viscosities and their effect on the motion of discrete food particles. The path of the food particles was predicted using an assumed empirical drag law to solve the force balance on the food particles, considering the dilute flow is in an infinite fluid and the particles being very small. The discrete particles were released at the cardia, which connects the

oesophagus and the stomach with a release speed of 0.2 m/s. The particle size varied from 0.4 to 4 mm, with a median size of 1.9 mm. Three types of gastric fluid were simulated: two Newtonian fluids (water and honey) and a non-Newtonian shear-thinning fluid (tomato concentrate-like fluid). The fluid behaviour followed the Power-law model below.

$$\eta = K\dot{\gamma}^{n-1} \qquad (2.4)$$

where η is the dynamic viscosity, $\dot{\gamma}$ is the shear strain rate, and K and n are constants that are material specific. Results showed that particles remained suspended for a longer time within a viscous fluid. However, there was insufficient evidence showing any distinct differences between the Newtonian and non-Newtonian fluids studied.

Based on the model developed by Ferrua and Singh [22], Xue et al. [27] focused on the effect of particle loading in the food mixture using discrete food particles. It was discovered that the flow pattern differed significantly with increasing particle loading. The study also investigated the effect of the density difference between the solid and liquid. The results showed that with a higher density difference, a more robust retropulsive motion was observed. The effect of ACWs were reduced when the particle loading was increased.

Imai et al. [84] used the MPS method to study the effect of antral recirculation in the stomach. The effects of posture and content volume were investigated by including gravity and a free surface. It is the first model that involves a free surface representation. Five body positions (upright, prone, right lateral, supine and left lateral) were modelled. The antral recirculation was found to be the largest when both the antrum and corpus regions were filled with liquid. Moreover, the retropulsive motion was only generated when there was gastric content in the antrum.

Miyagawa et al. [81] used the same 3D geometry as Imai et al. [84]. A multiple-relaxation-time LBM was used in this model to simulate a single-phase liquid flow with a free surface and moving boundary [81]. This model focused on investigating the relationship between the Reynolds number and Strouhal number of the fluid flow and the liquid mixing efficiency in the stomach. The Reynolds number (Re) and the Strouhal number (St) were defined below.

$$\text{Re} = \frac{\rho V D}{\mu} \qquad (2.5)$$

$$\text{St} = \frac{D}{VT} \qquad (2.6)$$

where ρ and μ are the density and dynamic viscosity of the fluid, D is the average diameter of the stomach geometry, V and $1/T$ are the propagation speed and frequency of the contractions. The extent of flow separation and the gastric mixing efficiency increased as Re increased and St decreased.

A multi-component mixture model was developed by Kamaltdinov et al. [78]. Instead of treating the fluid as a single-component liquid, different chemical components (hydrochloric acid, carbonic acid, and sodium hydrogen carbonate) were introduced into the model to study the acidity change. The mass concentrations of the mixture components were determined in the model. The study defined secretion zones for acid and sodium bicarbonate. The absorption rate of the chemicals through the stomach wall was also defined. By solving the concentration equations, the pH value at different regions of the stomach was estimated. In a later study, Kamaltdinov et al. [110] included food particles of different sizes in the model assuming the food and liquid could be treated as a homogeneous Newtonian fluid and the food particles were able to dissolve in the acid. The solid phases were tracked using the volume fraction of each particle size to represent different particle sizes. The chemical absorption rates of different food compositions were analysed for different food sizes, viscosity, and density. This study involved extensive chemical inputs, and secretion and absorption rates were implemented into the model. Instead of using a closed system, the pyloric sphincter remained open to the duodenum in this model. However, antral contractions were not considered in these two studies.

A coupled biomechanical-smoothed particle hydrodynamics (B-SPH) model was built by Harrison et al. [83]. With the SPH method, a free surface was simulated with gravity implemented. By colouring the particles which represent the fluid, the gastric mixing pattern was visualized. The study focused on the effect of the stomach wall contraction behaviour and gastric content viscosity on gastric mixing. The gastric emptying rate was investigated by comparing the mass flow through the pyloric ring and the mass flow in the stomach. This model is the first model that simulated gastric emptying by using an open pyloric sphincter along with antral contraction waves. The rate of change of volume content of gastric discharge was found to be affected by the contraction behaviours and the gastric content viscosity.

Alokaily et al. [79] developed a 2D model using the FVM and dynamic meshing technique. With the simplified geometry and the dynamic meshing technique, the authors were able to conduct a parametric study by varying multiple factors, including the density and dynamic viscosity of the fluid, the speed, width, and maximum relative occlusion of the fluid peristaltic

contraction waves. Compared with low-viscosity fluids, high-viscosity fluids experienced higher strain rates in the retropulsive jet and less mixing in the recirculation flow. In the model, the intensity of the retropulsive motion could be evaluated by its maximum velocity and jet length along the centreline. The maximum velocity and the jet length increased as the Reynolds number increased when the Reynolds numbers are larger than one. They were independent of Reynolds numbers when the Reynolds number was less than one.

Ishida et al. [82] used the LBM to develop a gastric mixing and emptying system. The model's focus was to simulate the pyloric opening and closure to understand the importance of the pyloric function. Gravity and free surface tracking were implemented in this system. The results showed that when the pylorus was unable to close, negative emptying occurred due to the retrograde flow from the duodenum back to the stomach. When there was a slight time delay of the pyloric closure from the antral contraction, the emptying rate increased. However, as the time delay increased, negative emptying (backflow) occurred as well. This study provided some insights into the consequences of the malfunction of the pyloric ring.

Skamniotis et al. [111] built a FEM model to simulate the breakdown of the solid foods inside the stomach model. The stomach geometry was simplified to an axisymmetric configuration without curvature. The breakdown model followed a viscoplastic-damage constitutive law. The mechanical properties of the solid foods were measured through experiments and applied in the model. The gastric wall was composed of a hyperelastic material that followed the van der Waals strain energy potential. It is the first model that simulated the properties of the gastric wall. Prescribed displacements were implemented at the wall. There was no fluid in the model. Instead, a large particle was used to represent the bolus. As the ACWs moved along the gastric wall, the bolus broke down. Based on the results, the authors emphasized the importance of including mechanical breakdown in digestion models. The contact between the gastric wall and the bolus also has a large impact on the breakdown behaviour.

Li and Jin [80] developed a FVM stomach model focused on muscular movements and gastric secretion. The stomach wall movement was simulated using the technique of dynamics mesh. The upper part of the stomach wall was used as the gastric juice secretion region, which was treated as a porous medium to represent the wrinkled structure. Hydrogen ions were constantly produced from this region and released into the gastric content. Apart from simulating the ACWs, the terminal antral contraction (TAC) was considered in this model. The addition of TAC created strong retropulsive motion. By varying the pH, diffusion rate, dynamic viscosity

and emptying rate of the gastric content, different mixing patterns were observed in this study. In a later study, Li et al. [112] included food particles in the same model by assuming they are different fluid phases. The gastric content was assumed to be a mixture filled with different food species.

Acharya et al. [113] proposed a multiphysics model that includes the muscle fibre properties of the stomach wall and the multiphasic components. The construction of the 3D geometry used circular and longitudinal muscle fibre orientations for each layer. A description of the multiphase flow solver is provided but the solution of the flow is not presented in detail in the study. The stomach wall was made of an elastic material. An immersed boundary finite element (IBFE) method was used to model fluid-structure interaction (FSI). A bolus entered the stomach due to gravity and mixed with the fluid content. The bolus was cylindrical in shape and was defined as a second fluid phase. The fluid motion and the movement of the bolus were observed.

Lee et al. [114] studied the effect of body posture and stomach motility on drug bioavailability. A non-disintegrating and non-deformable pill was placed in the homogeneous fluid medium. The pill was assumed to be made of salicylic acid and had a higher density than that of the fluid. It settled at the bottom of the fluid due to gravity and gradually dissolved. The dissolved mass was assumed to be active pharmaceutical ingredient (API) and it was transported to the duodenum along with the fluid medium driven by the antral contractions. The overall liquid and dissolved API emptying rates were estimated by recording the fluid mass that passed through the pylorus. By varying the gravity direction, the effect of the body posture was examined. Results showed that body posture has a crucial effect on the dissolved API emptying rate but not on the overall liquid emptying rate.
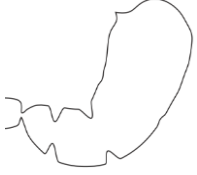
Kuhar et al. [115] used the same model as Lee et al. [114] to study the effect of stomach motility on food hydrolysis and gastric emptying. A sharp-interface immersed boundary method (IBM) solver was used to represent the deforming wall. Protein hydrolysis was simulated in this model by considering first-order catalytic reaction kinetics between protein and pepsin, which was secreted from the proximal stomach. The pH value was assumed to be constant. A long duration of simulation was performed in this study to capture the gastric hydrolysis process.
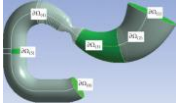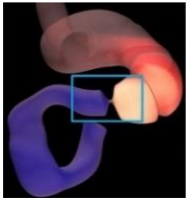
A detailed comparison of all the discussed models is given in Table 2.12, which contains the fluid properties used, the Reynolds numbers estimated based on the parameters, the components simulated (including particles, species, secretion, ACWs, gastric emptying,
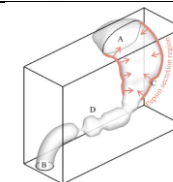
gravity), and the simulated real-time. The pioneering stomach model was developed by Pal et al. [14]. Kozu et al. [77] presented the first model that included gastric species (pepsin for mass transfer). 3D geometries were used instead of 2D geometries starting from Ferrua and Singh [14]. Discrete particles were later introduced to the model by Ferrua and Singh [22].

Free surface is easier to implement in the particle-based CFD methods (SPH and MPS), as seen in Imat et al. [84], Miyagawa et al. [81], Harrison et al. [83], and Ishida et al. [82]. The development started with single-phase fluid simulation with various densities and viscosities. Later, Kamaltdinov et al. [78] developed a multi-component mixture model that involves comprehensive gastric secretion mixing but without ACWs. Li and Jin [80] implemented gastric secretion from the upper part of the stomach wall and tracked the pH changes in the gastric content. Lee et al. [114] simulated the dissolution of API from a pill in the gastric system. Kuhar et al. [115] implemented protein hydrolysis in the model. Most models did not implement the food breakdown or stomach wall characteristics, except for Skamniotis et al. [111] and Acharya et al. [113]. However, the structure of the bolus was relatively simple compared with real solid food particles which have different cell structures and compositions. Besides, no fluid flow was simulated or presented in these two models. Due to the long computational times, the simulated real-time of all developed models was no more than 16 minutes, which is relatively short compared with the actual gastric emptying time, which requires at least 30 minutes. None of the developed models has been used to perform validation studies against any *in vivo* or *in vitro* data. The current state of computational stomach modelling is still in exploring the capabilities of different computational methods and has not reached the point of providing a comprehensive model yet.

Table 2.12: Investigations of the developed stomach computational models.

Method	Geometry	Fluid density (kg/m^3)	Fluid viscosity (Pa.s)	Estimated Reynolds number	Particle diameter (mm)	Gastric species included	Secretion	ACWs	Gastric emptying	Gravity	Simulated real-time	Published year	Ref
LBM		1000	1	0.1 – 0.4	-	-	-	Yes	-	-	2 min	2004	[26, 109]
FVM	(antrum only)	989 - 1379	0.73 - 4760	100 – 700 (from paper)	-	Pepsin, NaCl, HCl	-	Yes	-	Yes	3 min	2010	[77]
FVM		1000	0.001/ 1/ 2.33	0.1 - 140	0.4 – 4	-	-	Yes	-	-	1 min	2010, 2011	[14, 22]
FVM		1000	1	0.1 - 3	2	-	-	Yes	-	-	1 min	2012	[27]
MPS		1000	1	0.1 - 10	-	-	-	Yes	-	Yes	10 min	2013	[84]

Method	Geometry	Fluid density (kg/m³)	Fluid viscosity (Pa.s)	Estimated Reynolds number	Particle diameter (mm)	Gastric species included	Secretion	ACWs	Gastric emptying	Gravity	Simulated real-time	Published year	Ref
LBM		-	-	0.1 – 30 (from paper)	-	-	-	Yes	-	Yes	6 min	2016	[81]
FVM		1000	0.001	30 – 200	0.2 – 3.6	HCl, NaHCO$_3$	HCl, NaHCO$_3$	-	Yes	-	14 min	2017, 2018	[78, 110]
SPH		1000	0.01/ 0.1/ 1	0.1 - 50	-	-	-	Yes	Yes	Yes	3 min	2018	[83]
FVM		1000/ 1360	0.001 - 10	0.01 – 100 (from paper)	-	-	-	Yes	-	-	10 min	2019	[79]
LBM		1000	0.001 - 10	0.1 – 30 (from paper)	-	-	-	Yes	Yes	Yes	10 min	2019	[82]

Method	Geometry	Fluid density (kg/m³)	Fluid viscosity (Pa.s)	Estimated Reynolds number	Particle diameter (mm)	Gastric species included	Secretion	ACWs	Gastric emptying	Gravity	Simulated real-time	Published year	Ref
FEM		-	-	-	25.6	-	-	Yes	Yes	-	32 s	2020	[111]
FVM		1000	0.001	50 - 1500	-	H^+	H^+	Yes	Yes	Yes	10 min	2021	[80, 112]
FEM		900/ 1000	0.01/ 1	-	-	-	-	-	Yes	Yes	-	2022	[113]
FVM		1000	0.001	-	10	Salicylic acid	-	Yes	Yes	Yes	3 min	2022	[114]
FVM		1000	0.001	100 - 700	-	Pepsin, protein	Pepsin	Yes	Yes	Yes	16 min	2022	[115]

2.9.   Conclusions and gaps in knowledge to be addressed

It is evident from the review presented above that although much has been achieved, there remains much left to be done on stomach modelling, including integration of comprehensive models of food breakdown and chyme chemistry, and most importantly verification and validation of the computational models. The following key points have emerged from this review and an attempt will be made to address them in this thesis.

Firstly, Harrison et al. [83, 116] and Sinnott et al. [117-119] have presented the capability of the SPH model in simulating the digestive system. The strengths of SPH are its ability to represent flexible geometry and the free surface, to combine with DEM particles and to handle chemistry. This novel approach provides huge potential in modelling complicated stomach behaviour. However, this method has not been used widely in the digestive area, and its solution stability and accuracy need to be explored, verified, and validated.

Secondly, the elastic properties of the stomach wall are very important to the digestive function as the stomach is a hollow organ. Additionally, many *in vitro* models involve complicated mechanical means to generate motion. However, FSI studies in this field are very limited and require further investigation. The selected method also needs to be validated before being implemented into *in silico* stomach modelling. It is at present unclear whether this is best done in a FVM or SPH framework, the answer to which will most likely depend on the application.

Thirdly, *in vitro* studies are widely used in gastric mixing studies, but the flow patterns are usually difficult to quantify in an experimental setup. In this case, computational simulation can be used to facilitate the study by predicting and visualizing these patterns. Furthermore, when particles are involved, shear stresses on the food particles can easily be determined through simulations. It is therefore a goal of this thesis to investigate suitable numerical methods for this process and to validate them.

Finally, many components of the digestion process in the stomach remain to be developed. These essential components include gastric emptying, gastric secretion, integration of the material properties of the gastric wall, food particle mixing, calculation of the stresses on the particles, and food breakdown behaviour. *In silico* models can be very time-consuming and computationally demanding, especially when complicated components are involved. However, with the rapid development in computational power nowadays, *in silico* models have become more reliable and efficient. Therefore, there is a huge potential in the future for computational stomach models to provide a better and more comprehensive understanding of the complicated

human gastric digestion process. It is a key aim of this thesis to provide guidance on the pro and cons of the FVM and SPH approaches as a basis for this task moving forward.

In the next chapter, the process of model verification is started by comparing simulation results from SPH and FVM models with an analytical solution for peristaltic flow in a tube.

Chapter 3. Evaluation of SPH and FVM Models of Kinematically Prescribed Peristalsis-like Flow in A Tube

An early version of work in this chapter was presented as a poster at the Food Structure Digestion & Health International Conference held virtually on November 16th to 19th, 2021. The bulk of this chapter is published as X. Liu, S.M. Harrison, P.W. Cleary, D.F. Fletcher, "Evaluation of SPH and FVM models of kinematically prescribed peristalsis-like flow in a tube", Fluids, vol. 8, p. 6, 2023, doi: 10.3390/fluids8010006.

3.1. Introduction

Peristaltic flow arises when a series of contraction and expansion movements propagate along elastic tube-shaped structures. The fluid and/or solid content inside moves along with the wave as it propagates. In physiology, peristaltic waves are generated by the longitudinal and circular muscular fibres along the wall [120]. This motion is essential in the digestive system for its role in transporting and mixing food/nutrients in the gastrointestinal tract (GIT) [83, 118, 121]. The peristaltic motor patterns in the human gut are very complex and governed by multiple mechanisms and factors, including muscle activity, the thickness of the muscularis, and muscle tissue characteristics (elasticity, contractility, extensibility) [122].

In vivo studies provide the most relevant insights into the digestion process due to the complexity and inter-person variabilities of the digestion system. Researchers usually use animal models to study digestion because human subjects are not easy to recruit, experiments are hard to perform and get measurements from and complex ethical approval is required [5]. Even though animal models are often used as an alternative to humans [39, 54, 63, 64], they do not necessarily accurately reflect the human situation and still require strict ethics approval and specific technical skills. Therefore, *in vitro* models (e.g., test tube-based or similar) are designed to replicate the digestion process. These experimental studies are constructed with an aim to replicate the fluid flow conditions, shear stresses and complex chemistry in the GIT. Detailed reviews of *in vitro* digestion models are provided by Bornhorst and Singh [5], Dupont et al. [2] and Hur et al. [123]. *In vitro* models allow control of many factors that cannot be controlled in the *in vivo* system [5], which affords a better systematic understanding of individual factors.

However, these experimental systems can be hard to design to replicate local flow and concentration fields that occur in the body and can be very hard to customise to represent *in*

vivo scenarios. With the massive improvements in numerical methods and computing power over the last few decades, *in silico* methods have the huge advantage that local data can be obtained for all variables, such as velocity, pressure, and species concentration [80, 83, 117-119, 124, 125]. Therefore, if a suitably accurate computational model of an *in vivo* system can be constructed, the *in silico* results can provide insights into the *in vivo* system behaviour. Although the primary aim is to understand *in vivo* behaviour, *in silico* models can guide *in vitro* experimental design after being validated by data from the *in vitro* model. This synergistic approach is important in later chapters that utilise *in silico* models that benefit from the verification work performed here. Ultimately, the *in silico* and *in vitro* work will lead to *in silico* model that can model the full digestion process happening in the human stomach.

In the past two decades, many numerical models of this process based on Computational Fluid Dynamics (CFD) methods have been developed. Models have been built for different parts of the GI tract, including the oesophagus [126], stomach [26, 83, 127] and intestine [117-119, 124, 125, 128, 129]. These models provide valuable insights into the flow pattern of the digestion content, which is not easily quantified in both *in vivo* and *in vitro* studies. In the early developed models, single-phase fluid was simulated with various densities and viscosities. Recently, multiphase flow simulations (including with free surfaces and particles) have been implemented and improved by Sinnott et al. [118] and Harrison et al. [83]. Some models also include gastric secretion [80] and electrophysiology [128]. The developed models have demonstrated their capability and high potential in simulating this complex system but, to date, lack systematic validation for replicating physical outcomes. It is therefore important to verify and validate the components of established models to demonstrate their accuracy and stability.

An analytical solution [130], described later, can be used to calculate the detailed peristaltic-induced fluid motion for an idealised tube geometry. However, numerical analysis is needed to understand complicated systems, such as the intestine and the stomach, which involve the combination of fluid flow, free surfaces, complex boundary conditions, and solids content. The capability of SPH in simulating the digestion model has been demonstrated in the intestine models developed by Sinnott et al. [117-119, 124, 125, 129] and the stomach model developed by Harrison et al. [83]. However, the developed models have not yet been validated or verified against any experimental data or analytical solution. Peristaltic flow is a fundamental component of all these models, and it is therefore useful to validate computational models for this process and then to perform additional validation as more physics is added, knowing that the underlying flow model is well validated.

The main aim of this chapter is to validate the accuracy of the Smooth Particle Hydrodynamics (SPH) method when applied to the peristaltic motion of a single-phase Newtonian fluid. Although it is not a validation study for the stomach, once the model is validated for the simple peristaltic system, it will provide a high level of confidence for stomach modelling, where peristalsis is involved. The Finite Volume method (FVM) is also employed in the study and acts as a comparison approach. Compared with the novel mesh-free SPH method, FVM is a traditional mesh-based method that has been well-established for decades [85]. By comparing the performance of both numerical methods, their accuracy and efficiency can be explored.

3.2. Analytical solution

Several studies have investigated flow in a tube during simplified peristalsis driven by a moving wall [120, 130-132]. Under constrained flow conditions the flow field and pressure distribution can be calculated from the amplitudes of the wall deformations only. In this study, the analytical solution of Shapiro et al. [130] is used to validate the numerical models of peristalsis. A continuous sinusoidal wave train moving in one direction along the tube axis with a constant speed is used to determine the instantaneous shape of a moving boundary wall on a tube of uniform initial diameter. The applied motion generates a volumetric flow which can be compared with analytic results. An illustration of the fluid-filled tube with the deforming wall is shown in Figure 3.1.
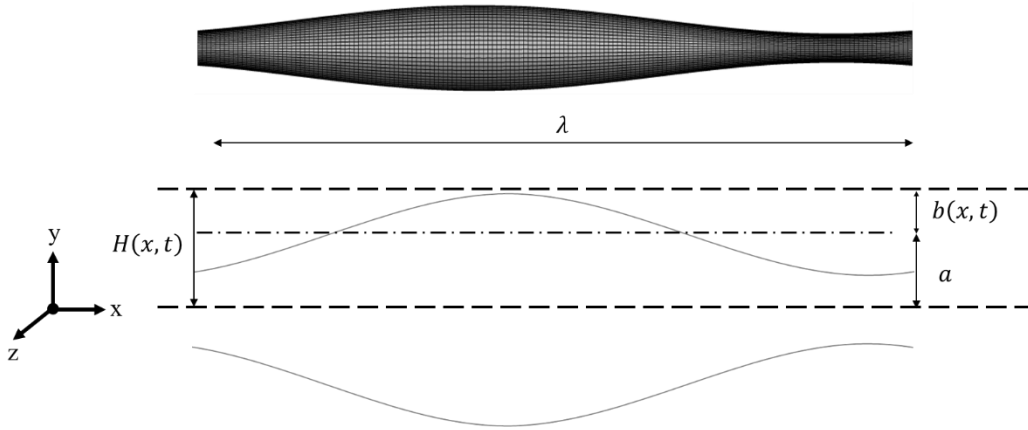
Figure 3.1: Illustrations of tube geometry used in the peristalsis verification model.

In the simulations, the wavelength λ of the imposed wave is specified, which is related to the wavenumber by:

$$k = \frac{a}{\lambda}$$

(3.1)

where a is the radius of the tube. Using these definitions, a Reynolds number can be formed as

$$Re = \frac{\rho a c}{\mu} \times \frac{a}{\lambda} \qquad (3.2)$$

where c is the speed of the imposed wave, μ is the dynamic viscosity and ρ is the fluid density.

The analytical model assumes a continuous train of waves and inertia-free fluid flow, which requires two criteria to be met. Firstly, the wavenumber (k), which is the ratio of the radius to the wavelength, should be close to zero, as it is assumed to be zero in that analytical solution. Under this condition, the transverse velocities and pressure gradients are negligible compared with their longitudinal counterparts. Secondly, the Reynolds number (Re), which gives the ratio of inertial to viscous forces must be close to zero, as it is again assumed to be zero in the analytical solution.

From Fung and Yih [120], the equation for the imposed peristaltic waves is:

$$b(x,t) = a\phi \sin 2\pi \left(\frac{x - ct}{\lambda}\right) \qquad (3.3)$$

where $b(x,t)$ denotes the wall deformation in the radial direction, x is the longitudinal location, t is time and $\phi = b/a$ is the amplitude ratio, which is set to a range of 0.1 to 0.6, corresponding to occlusions of 10% to 60%, deemed to be sufficient given the purpose of this study.

The effect of changing the amplitude ratio, ϕ, on the fluid flow is investigated. In the analytical solution, the fluid is assumed to be incompressible. The fluid flows through the tube with constant static pressure at the tube boundaries. The dimensionless time-average volumetric flow rate $(\dot{V})$ is a good measure of the flow behaviour and is dependent on the amplitude ratio (ϕ) [130]:

$$\dot{V} = \frac{\phi(4 + \phi)}{2 + 3\phi^2} \qquad (3.4)$$

3.3. Numerical models setup

3.3.1. Physiological parameters

The physiological data for the human ureter [120] are used in the peristalsis model developed in this work. As shown in Table 3.1, the input parameters include the tube dimensions, the characteristics of the imposed motion and the properties of the fluid inside the tube. The amplitude ratios are set to be 0.1 to 0.6 for the comparison test case because 0.7 and 0.8 were

not achievable in the SPH model (see later). Both the wavenumber and Reynolds number need to be close to zero as required for the analytical solution and therefore the dimensions from the gastrointestinal tract are not used in this study.

Table 3.1: Parameters used in the numerical models.

Geometrical dimensions		
Radius	a	0.001 m
Length	L	0.05 m
Peristaltic waves characteristics		
Wave speed	c	0.03 m/s
Wavelength	λ	0.05 m
Amplitude ratio	ϕ	0.1 – 0.6
Fluid properties		
Dynamic viscosity	μ	0.01 Pa.s
Density	ρ	1000 kg/m^3
Conditions		
The ratio of tube radius to wavelength	k	0.02 (close to 0)
Reynolds number	Re	0.06 (close to 0)

3.3.2. Peristaltic motion

The nodes on the boundary are displaced radially according to the profile given by equation 3.3 in both the SPH and FVM simulations. The wall location used in the simulation, $H(x,t)$, is determined from the imposed wave motion given by $b(x,t)$ (equation 3.3) with a linear ramping equation applied to start the simulation gradually to prevent mesh distortion:

$$H(x,t) = a\left(1 + \min\left(\frac{t}{t_i}, 1\right) \times \phi \sin 2\pi \left(\frac{x - ct}{\lambda}\right)\right) \qquad (3.5)$$

where t_i is the ramp time, set to λ/c. Results before time t_i are not included when calculating the averaged flow rate.

The following equations are applied to convert the equations into Cartesian coordinates.

$$\theta = \tan^{-1}\left(\frac{z}{y}\right) \qquad (3.6)$$

$$y = H(x,t)\cos(\theta) \tag{3.7}$$

$$z = H(x,t)\sin(\theta) \tag{3.8}$$

where y and z are the transformed coordinates in a Cartesian coordinate system.

The problem described above is next set up and solved using both SPH and FVM so that the results can be compared for the same geometry, boundary conditions and fluid properties.

3.3.3. SPH model

In the SPH approach, the NSE are used to solve fluid dynamics problems, with particles representing discrete "lumps" of fluid, that are tracked in a Lagrangian framework. The formulation of the model results in a set of ordinary differential equations describing the motion of fluid particles [90]. More details of the method can be found in Monaghan [88, 133] and Cleary et al. [90, 124]. The CSIRO SPH code [134] is used in this study.

To obtain values of quantities such as density and velocity at a given point, data must be obtained from the surrounding region. The interpolated value of a function A at a point $\boldsymbol{r}$, is the sum over all particles within a radius of distance related to h from point $\boldsymbol{r}$ [88]:

$$A(\boldsymbol{r}) = \sum_b m_b \frac{A_b}{\rho_b} W(\boldsymbol{r} - \boldsymbol{r}_b, h) \tag{3.9}$$

where A_b is the value of A at $\boldsymbol{r}_b$, m_b is the mass of fluid particle b, and W is an interpolation kernel function with a smoothing length of h evaluated at a distance $|\boldsymbol{r} - \boldsymbol{r}_b|$ from the position of interest. In this work, h is set to be 1.2 times the initial particle separation distance, Δx. The concept of a smoothing kernel is shown in Figure 3.2 below.
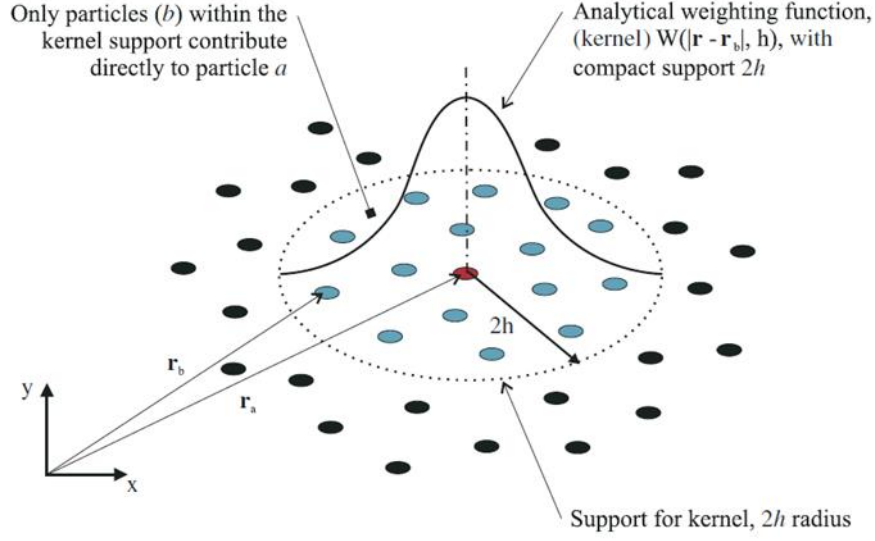
Figure 3.2: Schematic representation of a typical kernel. Reprinted with permission from Cummins et al. [135]. Copyright 2022 John Wiley and Sons.

The kernel is essential to the entire method as it is used for the calculation of both interpolated values and gradients. The effect of three different kernels is examined in this work for the same smoothing length.

The dimensionless distance used in the kernel is defined as

$$\Delta = \frac{r_{ab}}{h} \tag{3.10}$$

where $\boldsymbol{r}_{ab} = \boldsymbol{r}_a - \boldsymbol{r}_b$, is the position vector between particles b and a, and $r_{ab} = \|\boldsymbol{r}_a - \boldsymbol{r}_b\|$.

The quartic spline kernel [135] is used for the base case in this study

$$W(\boldsymbol{r}_{ab}, h) = \frac{1}{20\pi h^3} \begin{cases} (2.5 - \Delta)^4 - 5(1.5 - \Delta)^4 + 10(0.5 - \Delta)^4, & \Delta \leq 0.5 \\ (2.5 - \Delta)^4 - 5(1.5 - \Delta)^4, & 0.5 \leq \Delta \leq 1.5 \\ (2.5 - \Delta)^4, & 1.5 \leq \Delta \leq 2.5 \\ 0, & \Delta \geq 2.5 \end{cases} \tag{3.11}$$

The fifth-order Wendland kernel [135, 136] is also studied:

$$W(\boldsymbol{r}_{ab}, h) = \frac{7}{85.336\pi h^3} \begin{cases} (2 - \Delta)^4(1 + 2\Delta), & 0 \leq \Delta \leq 2 \\ 0, & \Delta \geq 2 \end{cases} \tag{3.12}$$

as well as the cubic spline kernel [133, 137]:

$$W(\boldsymbol{r}_{ab}, h) = \frac{1}{\pi h^3} \begin{cases} 1 - \frac{3}{2}(\Delta)^2 + \frac{3}{4}(\Delta)^3, & \Delta \leq 1 \\ \frac{1}{4}(2 - \Delta)^3, & 1 \leq \Delta \leq 2 \\ 0, & \Delta \geq 2 \end{cases} \tag{3.13}$$

49

A comparison of the kernel shapes is shown in Figure 3.3. To display them the dimensionless kernel $W(\boldsymbol{r}_{ab}, h)h^3$ was plotted as a function of the normalized distance.
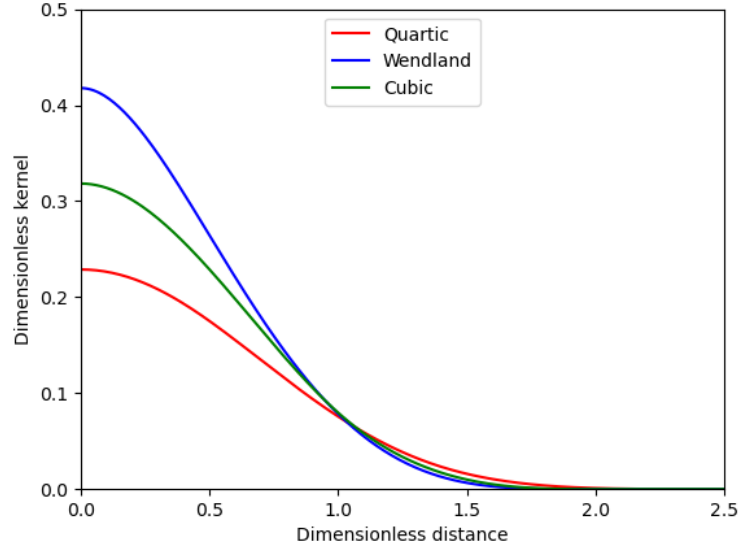
Figure 3.3: Comparison of the kernels used in this work.

From Figure 3.3 several important observations can be made:

1. The value of any variable at a given point depends on all particle values inside a sphere of radius nh centred on that point. In SPH this is usually referred to as a kernel having compact support with radius nh. For the cubic and Wendland kernels $n = 2$, and for the quartic kernel $n = 2.5$. Therefore, for any given particle configuration the quartic kernel involves the summation of more particles over a greater spatial extent than the other two.

2. The kernels give different relative weighting to particles closer to the point of interest. This impacts not only the value but also the gradients of variables.

The gradient of the function A is obtained by differentiating equation 3.9:

$$\nabla A(\boldsymbol{r}) = \sum_b m_b \frac{A_b}{\rho_b} \nabla W(\boldsymbol{r} - \boldsymbol{r}_b, h) \tag{3.14}$$

The conservation equation for mass can then be formulated as [88, 138]:

$$\frac{d\rho_a}{dt} = \sum_b m_b \, \boldsymbol{v}_{ab} \cdot \nabla_a W_{ab} \tag{3.15}$$

where ρ_a is the density of fluid particle a, t is time, $\boldsymbol{v}_{ab} = \boldsymbol{v}_a - \boldsymbol{v}_b$, is the relative velocity between particles a and b.

The fluid pressure can then be calculated based on the particle density. Although the analytic solution is derived for an incompressible fluid, a weakly compressible approach is adopted here and is configured to have low compressibility. This approach is applied by introducing an equation of state of the form:

$$P = P_0 \left[\left(\frac{\rho}{\rho_0} \right)^{\Upsilon} - 1 \right] + P_{\text{off}} \tag{3.16}$$

where P is the fluid pressure; P_0 is the pressure scale factor; ρ is the particle density; ρ_0 is the reference density, set to 1000 kg/m^3 for water in this work; $\Upsilon = 7$, which is a material constant defined for water [139]; P_{off} is a background pressure that is added to avoid negative pressure values.

Weakly compressible SPH is designed for free surface flow prediction [88] with an essential component being the ability of diverging fluid (which has a negative pressure when calculated by equation 3.16 when $P_{\text{off}} = 0$ Pa) to create new free surface. In a fully enclosed expanding flow this will allow unphysical internal void formation. However, the analytical model assumes that the tube content is a single-phase fluid without internal free surfaces. The equation of state therefore needs to be adapted to ensure that $P > 0$ throughout the tube and for the entirety of the simulation. This is achieved by including a pressure offset P_{off} which is sufficiently large to guarantee that the pressure remains positive. Since the fluid dynamical force only depends on the pressure gradient, the addition of such a constant has no other effect aside from ensuring the positivity of the pressure.

The effect of this offset pressure in the current work is very important, as shown in Figure 3.4. Without the offset pressure voids are created, which is not present in the single-phase flow being modelled here. A background pressure of 100 Pa is found to be sufficient to ensure $P > 0$ and therefore inhibit this internal free surface generation and is used for all cases.

$P_{\text{off}} = 0$ Pa

$P_{\text{off}} = 100$ Pa
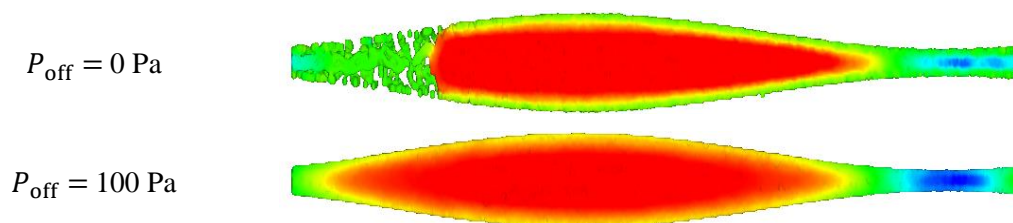
Figure 3.4: Addition of a background pressure is used to prevent void formation. The contours show velocity, but the key point is the breakup of the fluid in the top picture is avoided when the offset pressure is present.

The pressure scale factor P_0 in equation 3.16 is given by

$$\frac{\Upsilon P_0}{\rho_0} = c_s{}^2 = (10V)^2 \tag{3.17}$$

where c_s is the local speed of sound, which needs to be large enough to make sure the density variations are small and the fluid is close to incompressible, but it also needs to be low enough to avoid the need for very small timesteps [139] (see later); c_s needs to be at least 10 times larger than the characteristic fluid velocity in the flow field (V), which corresponds to a Mach number of 0.1 or smaller and gives a density variation of less than 1% [88].

The conservation equation for momentum becomes:

$$\frac{d\boldsymbol{v_a}}{dt} = -\sum_b m_b \left[\left(\frac{P_b}{\rho_b^2} + \frac{P_a}{\rho_a^2} \right) - \frac{\xi}{\rho_a \rho_b} \frac{4\mu_a \mu_b}{(\mu_a + \mu_b)} \frac{\boldsymbol{v_{ab}} \cdot \boldsymbol{r_{ab}}}{(r_{ab}^2 + \eta^2)} \right] \cdot \nabla_a W_{ab} + \sum_k \boldsymbol{f_{ak}} \tag{3.18}$$

where P_a and P_b are the pressure of particles a and b, μ_a is the viscosity of particle a, ξ is a calibration factor associated with the viscous term, which is calculated during the simulation. The calculation of this factor is described in Cleary [140]; η is a small parameter used to regularise the singularity when $\boldsymbol{r_{ab}} = \boldsymbol{0}$. The term $\boldsymbol{f_{ak}}$ represents the particle-wall force between particle a and wall particle k and is present only near boundary walls (see [124, 135] for details).

An explicit integration scheme [88] is used in the simulations. The timestep is governed by the Courant condition modified to account for the viscous term to ensure simulation stability. The details of the modification can be found in Cleary [134] and gives

$$\Delta t = \min_a \left(\frac{0.5h}{c_s + 2\xi\mu_a / h\rho_a} \right) \tag{3.19}$$

For this application, a constant spatial resolution h and a constant particle size are used. Adaptive resolution can be used to improve accuracy in regions of high wall deformation, but the simpler uniform resolution SPH is sufficient for the deformations of interest (ϕ up to 0.6). For the base case simulation, a particle size of 0.10 mm is used to construct the domain in the SPH model. The tube is filled with 158,000 particles, representing the fluid content, with an initial spacing of 0.10 mm.

The tube wall is represented by 66,000 SPH boundary particles with a particle size of 0.10 mm. The boundary particles are arranged with an equidistant spacing around the circumference and length of the tube. At each timestep, their position, velocity and normal vector are updated

using equation 3.5, which are functions of time. Interaction between boundary and fluid particles is calculated using a Lennard Jones penalty force in the direction of the wall normal vector and a no-slip boundary condition in the plane perpendicular to this [88]. The inlet and outlet of the tube are set to be periodic boundaries. The average volumetric flow rate is calculated based on the average velocities of the particles at the mid-plane of the tube.

Once the velocity of the particles is known (from equation 3.18) their position can be updated using equation 3.20.

$$\frac{d\boldsymbol{r}_a}{dt} = \boldsymbol{v}_a + 0.5 \sum_b \frac{2m_b}{\rho_a + \rho_b}(\boldsymbol{v}_b - \boldsymbol{v}_a)W_{ab} \qquad (3.20)$$

The first term represents the usual dynamical behaviour, whilst the second is the XSPH smoothing term which is advantageous for solution stability [141]. Details of the solution process used by the CSIRO SPH code are given elsewhere [134].

3.3.4. FVM model

In FVM, the mass and momentum conservation equations employed for incompressible flow with a moving mesh are [142]:

$$\nabla \cdot \left(\boldsymbol{u} - \boldsymbol{u}_g \right) = 0 \qquad (3.21)$$

$$\frac{\partial(\rho\boldsymbol{u})}{\partial t} + \nabla \cdot \left(\rho\left(\boldsymbol{u} - \boldsymbol{u}_g \right) \otimes \boldsymbol{u} \right) = -\nabla P + \nabla \cdot \mu(\nabla\boldsymbol{u} + \nabla\boldsymbol{u}^T) \qquad (3.22)$$

where $\boldsymbol{u}$ is the fluid velocity, $\boldsymbol{u}_g$ is the velocity of the moving mesh, ρ is the fluid density, t is time, μ is the dynamic viscosity, and P is the pressure.

The FVM model is developed using Ansys Fluent, version 2022R2. Using the Ansys SpaceClaim Meshing tools, the geometry is split into 68,000 hexahedral elements. Figure 3.5 shows the computational mesh generated on the tube in the longitudinal and transverse directions. The mesh is swept between the inlet and outlet faces. Two inflation layers are placed on the boundary. The minimum orthogonal quality of the generated mesh is 0.64, and the maximum skewness is 0.69. The undeformed cell volume varies from 1.2×10^{-12} to 3.9×10^{-12} m^3, which is equivalent to cell sizes of 0.11- 0.16 mm.
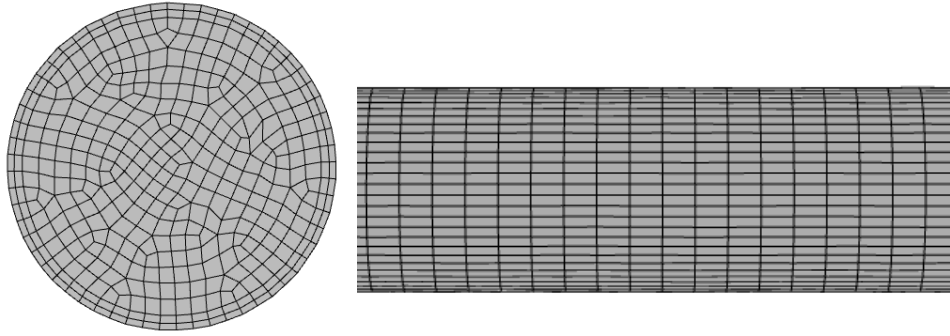
Figure 3.5: Computational mesh for the undeformed tube in the transverse and the longitudinal directions. (Only a short section of the longitudinal mesh is displayed.)

Figure 3.6 shows the computational mesh in the transverse direction for the deformed tube when $\phi = 0.6$. The original element aspect ratio is 3:1 (Figure 3.5). The volume of the cell is maintained when deformed and therefore the aspect ratio of the cells changes. When deformed, the aspect ratio is roughly 2:1 at the widest section (Figure 3.6b) and 6:1 at the narrowest section (Figure 3.6c), which is well inside the acceptable range for the Ansys Fluent solver.

(a) entire length
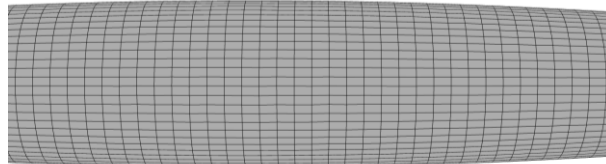
(b) expansion section

(c) compression section

Figure 3.6: Computational mesh for the deformed tube in the transverse direction.

The tube wall is prescribed to have a no-slip boundary condition. A diffusion-based method is used to distribute the boundary motion uniformly throughout the interior mesh with the number and connectivity of the mesh cells remaining constant. The inlet and outlet of the tube are set to be periodic boundaries. The initial values for the gauge pressure, x, y and z velocities are set to zero.

The transient, pressure-based solver is used with the laminar flow assumption. The SIMPLE [143] algorithm is used for pressure-velocity coupling, with the first-order implicit transient scheme. Gradients are determined using the least-squares cell-based method, the pressure is determined using a second-order method, and the bounded second-order upwind scheme is used for the momentum equation. A time step of 0.01 s is chosen after assessing the timestep effect upon results. The simulation is run for 8,000 steps for each amplitude ratio. The maximum iteration number for each time step is set to 20, with 5 iterations typically being needed for convergence. Convergence is deemed to have occurred when the locally-scaled root-mean-square (RMS) residual values for continuity and the three velocity components are below 10^{-5}.

The mass flow rate passing through the mid-plane of the tube is recorded during the simulations. The mass flow rate is then converted to a volumetric flow rate and integrated over time to retrieve the time-mean volumetric flow rate (Q). The integration process is conducted using Matlab R2020a.

3.4.   Simulation results

Figure 3.7 shows the axial velocity contours on the mid-longitudinal plane for a single wavelength and different amplitude ratios for both models. In the FVM, nodal values are interpolated onto a longitudinal cross-sectional plane and in the SPH model data from adjacent particles (which are disordered) are interpolated onto the plane. As the amplitude of the wave increases, larger deformation results in faster flow through the tube. The data show a larger region of positive flow in the expanded region and a smaller region of negative flow in the contracted region. The positive flow region becomes much larger than the negative region as the occlusion ratio is increased. The flow patterns achieved by both methods show good agreement. Visually the regions of high positive and negative velocity are slightly larger for the FVM results, principally because the gradients are higher so there is a smaller region of the duct occupied by transition values.

The volumetric flow rate at the mid-plane from both models is recorded over time and is shown in Figure 3.8 for the six levels of contraction. The quartic spline kernel is used for the base case in the SPH model (see later). The overall patterns from both models are very similar. The periodic behaviour is established in both models after the ramp time has elapsed and the flow pattern is smooth for all amplitude ratios.

After the initial ramp-up period, there is a strong forward flow with a shorter period of reverse flow that becomes relatively less important as the amplitude ratio is increased. The reverse flow magnitude is sensitive to the applied wave amplitude ratio. At low amplitudes, the difference between the forward and backward flow is small making the net flow sensitive to this balance. However, as the wave amplitude is increased there is a significant increase in the forward flow which completely overwhelms the reverse flow. Both methods show very similar behaviour.
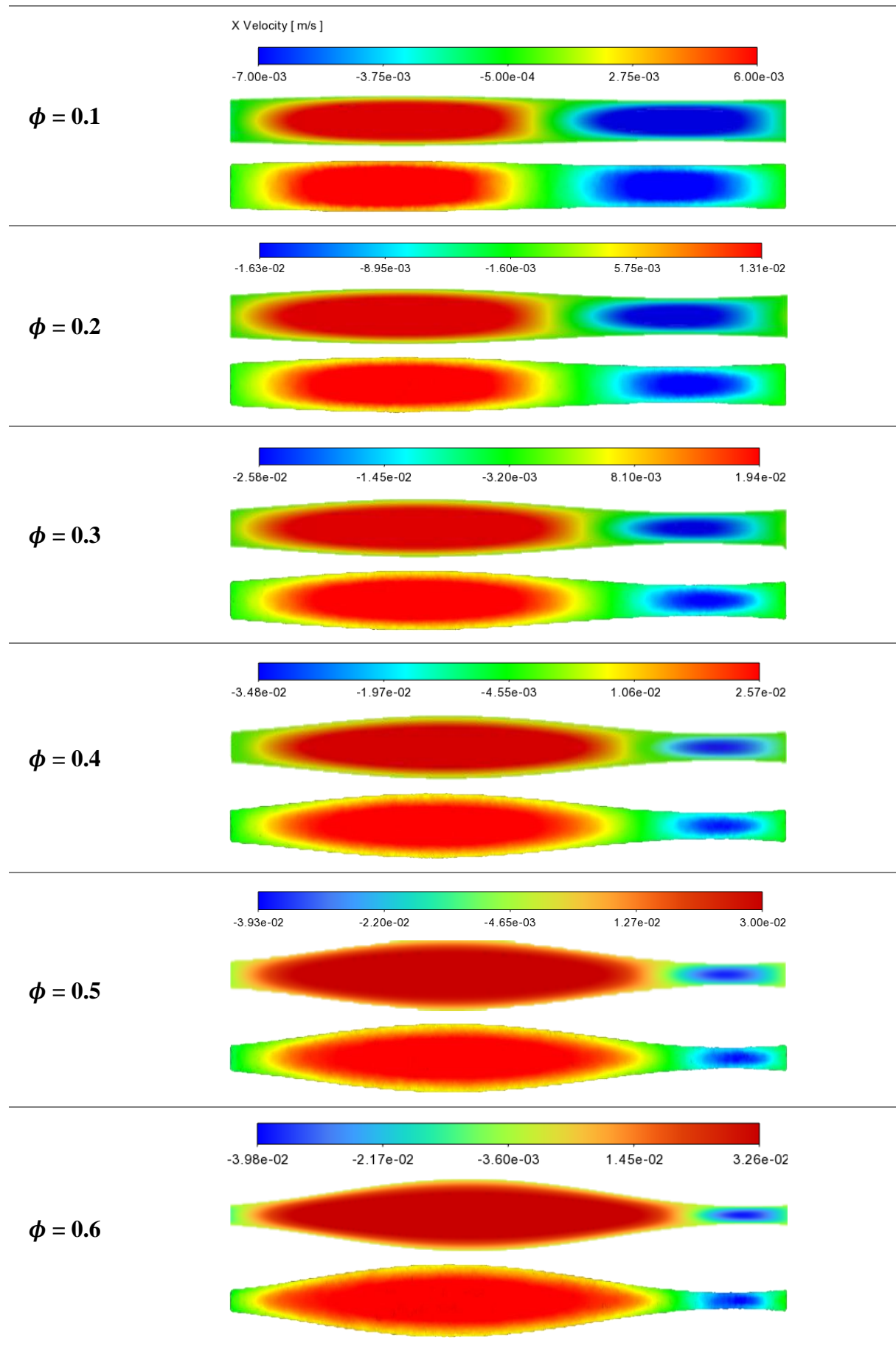
Figure 3.7: Axial velocity contours at 5 s from the FVM model (top) and the SPH model (bottom), where ϕ is the amplitude ratio.
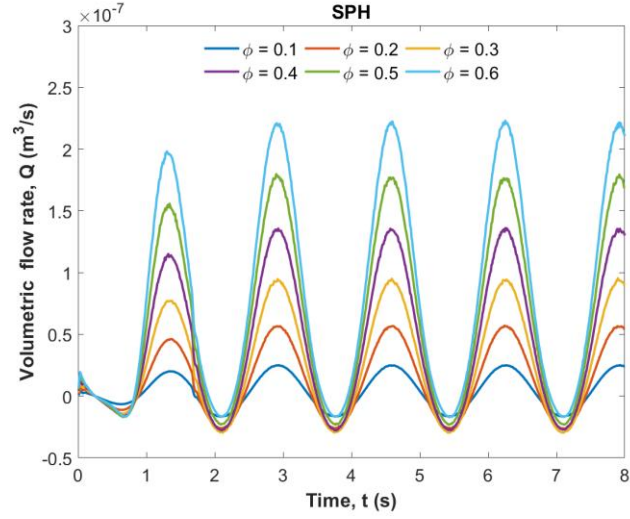
(a)
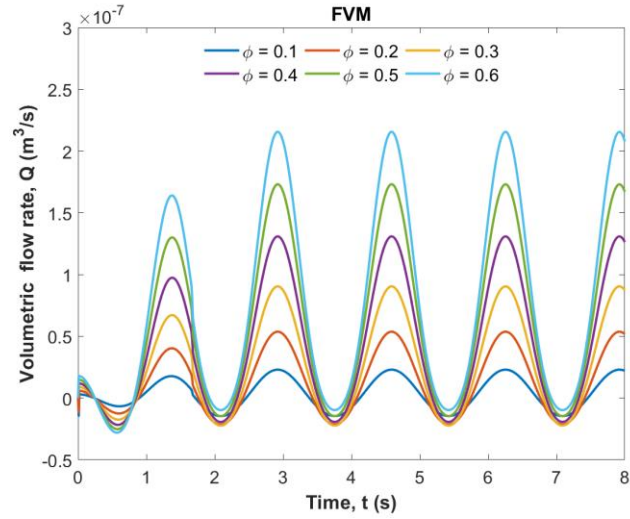
(b)

Figure 3.8: Volumetric flow rate at the mid cross-section over time: (a) SPH, (b) FVM.

Figure 3.9 compares FV and SPH results for volumetric flow rates at different amplitude ratios over time. There is good agreement between the two methods for all the amplitude ratios studied. The volumetric flow rates at the two extremes are slightly different with the SPH model giving slightly higher extreme values compared with the FVM model for all amplitude ratios. However, as the amplitude ratio increases, this difference becomes proportionally smaller bringing the results closer together.
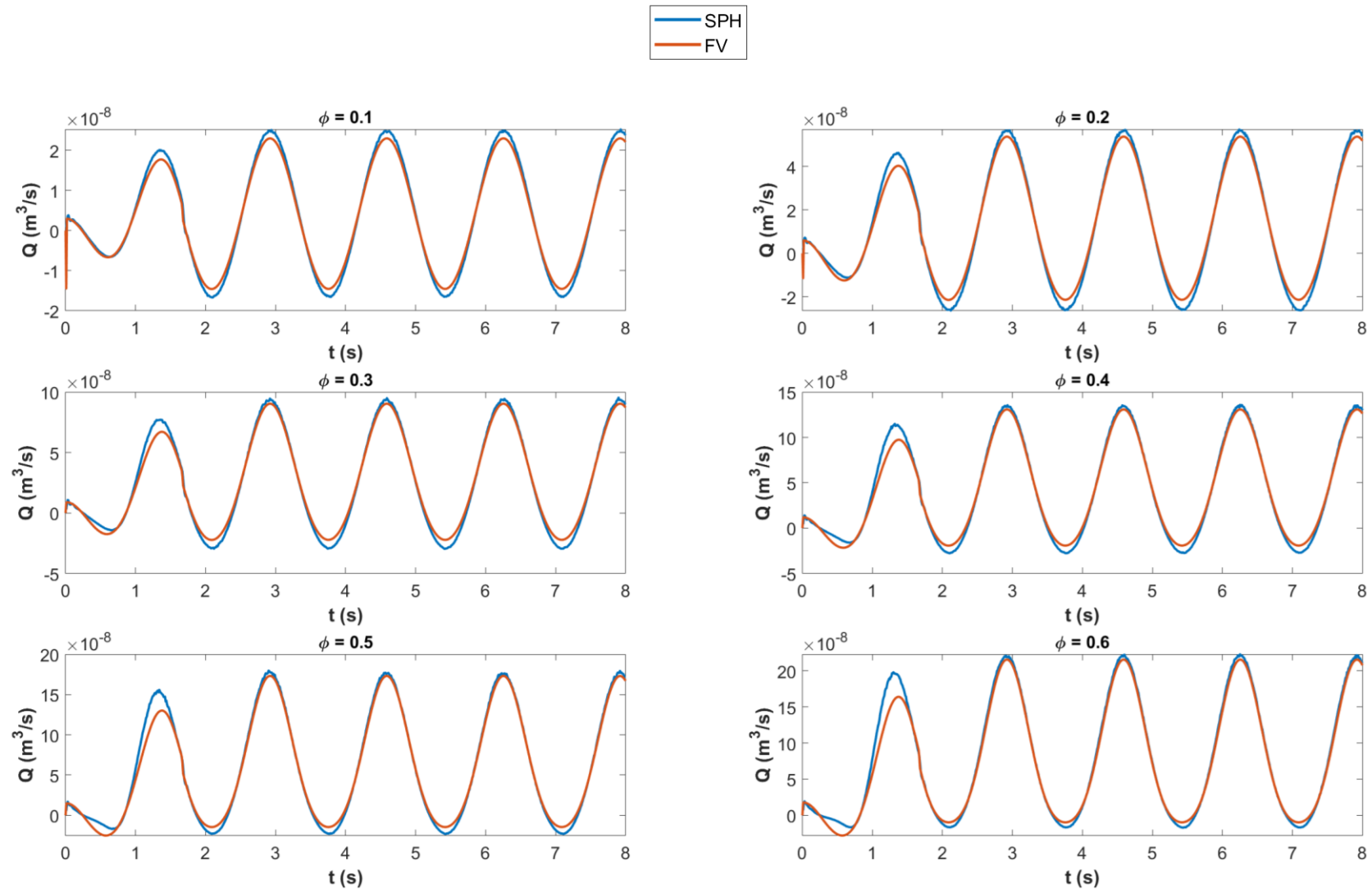
Figure 3.9: Volumetric flow rate at the mid cross-section over time from both models.

The dimensionless time-averaged volumetric flow (V^*) recorded from both models is then calculated based on the time-mean volumetric flow rate ($\bar{Q}$).

$$V^* = \frac{\bar{Q}}{\pi a^2 c \left(2\phi - \frac{1}{2}\phi^2\right)} \tag{3.23}$$

The dimensionless results are compared with the analytical solution in Figure 3.10. The volumetric flows from both models match the analytical solution very well for all occlusion ratios. Both methods are very suited to this problem and give high and comparable accuracy.
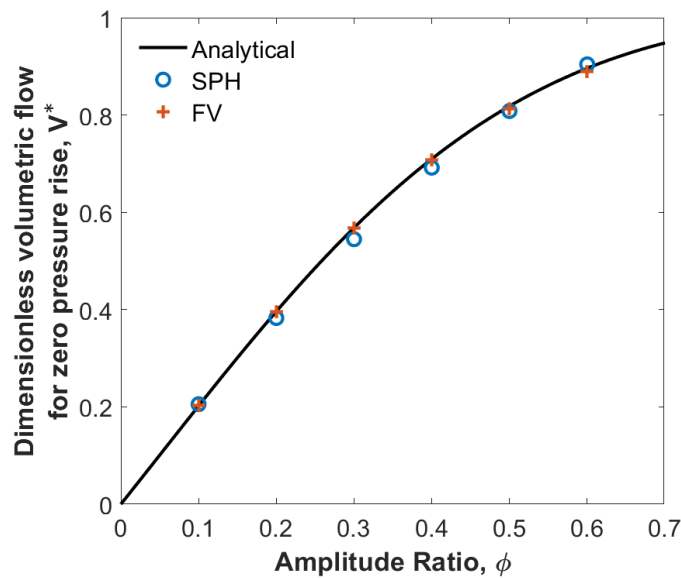
Figure 3.10: Comparison of computed dimensionless volumetric flow for the two numerical methods with the analytical solution.

3.5. Sensitivity studies

The influence of numerical parameters is tested here to examine the sensitivity of both methods. In the FVM method, the resolution of a simulation is checked by investigating the sensitivity of the results to both the computational mesh size and the timestep. In the FVM, if the solution is independent of these, the accuracy of the results is then determined by the order of the discretization scheme (typically for the convective term in the equation) and level of convergence (i.e., how well matrix equations are solved) [144]. Typically bounded second-order differencing is used for the temporal and spatial derivatives (albeit that in some regions these must be modified to first order to preserve solution boundedness). This is a highly

researched topic and although a huge number of different schemes exist, most software uses a set that has been tried and tested [144].

The situation is much less well-developed in the case of SPH. This arises partly because there has been much less development of this method compared with the FVM but mainly from the difficulty of performing detailed mathematical analysis when the data are stored at the centre of disordered particles that can be arranged in an arbitrarily complex manner in space that evolves with the solution. Just as the results from the FVM depend on the computational mesh and choice of the differencing scheme, the SPH results depend on the particle size, choice of the kernel and initial particle separation as discussed earlier.

3.5.1. SPH model

Effect of initial particle arrangement

It is non-trivial to populate an arbitrarily shaped region of matter evenly with SPH particles, which is the equivalent of generating a high-quality mesh in the FVM. Certain arrangements are thought to contribute to lower solution quality, for example when a line of particles is compressed perfectly along that line, they can exhibit an artificial resistance to compression followed by a buckling failure. In this work, the aim is to fill a cylinder evenly with a precise volume of SPH particles. Despite the tube geometry (Figure 3.1) being simple in shape, it has not been established which type of particle packing will lead to optimal results. Thus, three different particle-filling approaches are examined: a cubic arrangement, a cylindrical arrangement, and a hybrid of the two above. Here we describe the properties of each filling approach:

(a) A cubic arrangement of particles with the centre of each adjacent particle located on a cubic grid that is spaced by the particle size in each of the Cartesian directions.

(b) A cylindrical arrangement of particles with the particle centres one particle diameter apart in the longitudinal direction and arranged in concentric rings around the longitudinal axis of the cylinder that are spaced by one particle diameter and particles in each ring approximately one particle diameter apart on the circumference of the ring.

(c) A hybrid of the above two approaches: a cylindrical arrangement of one ring of particles near the boundary surface and a cubic arrangement of particles within.

The initial particle arrangements at a cross-section for the three cases described above are shown in Figure 3.11. The hybrid discretisation approach was used in the base case presented above.

61

<div align="center">(a) cubic   (b) cylindrical   (c) hybrid</div>
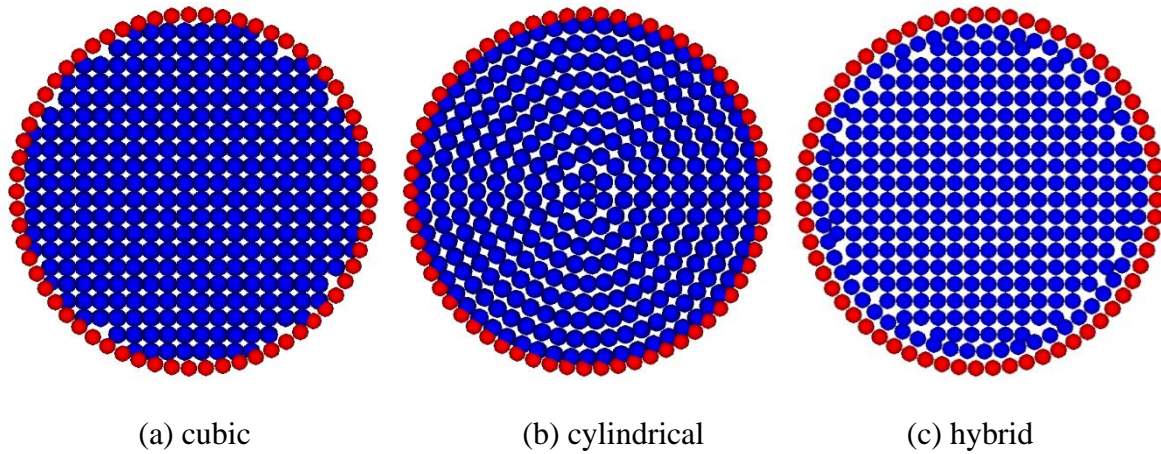
Figure 3.11: Initial particle arrangement for different assumptions.

A cylindrical packing approach is the most obvious choice for fitting particles evenly but is likely to lead to circumferentially adjacent particles having artificial resistance to radial compression, rather than smoothly naturally re-arranging as randomly located particles would. A cubic packing is easy to implement for any arbitrary geometry but a poor initial alignment of fluid particles with boundary particles typically occurs and often leads to non-representative early results as boundary layers of particles are established. A hybrid of both methods where the external surface of the fluid closely matches the boundary surface, but the internal particle distribution minimises any risk of artificial resistance to compression may prove optimal and is used in the base case here for this reason.

The volumetric flow rate history over time shows very similar results for the different initial particle arrangements. The only differences observed are during the ramp time, as shown in Figure 3.12. The flow pattern for the cylindrical arrangement is less smooth compared with the other two. For the 0.3 amplitude ratio case the cylindrical case also shows greater reverse flow than the other two. The ease of rearrangement of the particles as the tube contracts and expands causes these differences – with the cylindrical packing being harder to rearrange with the cylindrical shells of particles at each radius being able to resist deformation, as expected. The averaged flow rates resulting from the three approaches are compared with the analytical solution in Figure 3.13. Only small differences are observed, with all three approaches yielding high accuracy, as shown in Table 3.2.
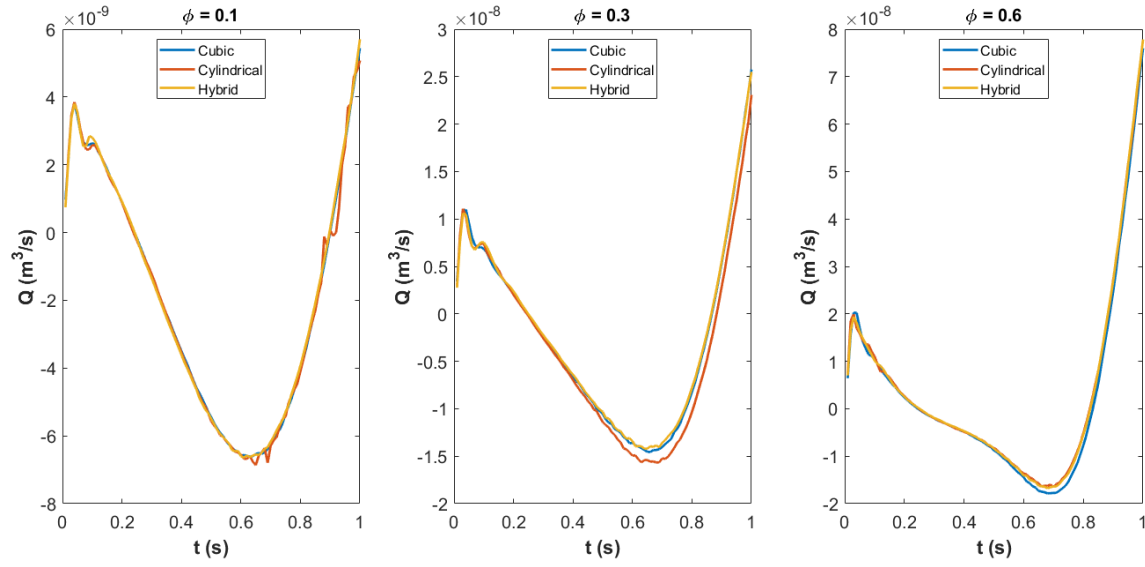
Figure 3.12: Volumetric flow rate history during the ramp time for different initial particle arrangements.

Table 3.2: Effect of particle arrangement in the SPH simulations.

Arrangement	Normalised flow rate	Variation from analytic result	Normalised flow rate	Variation from analytic result	Normalised flow rate	Variation from analytic result
	$\phi = 0.1$		$\phi = 0.3$		$\phi = 0.6$	
Cubic	0.207	3%	0.540	5%	0.901	0.5%
Cylindrical	0.197	3%	0.529	7%	0.903	0.8%
Hybrid	0.207	2%	0.546	4%	0.904	0.8%
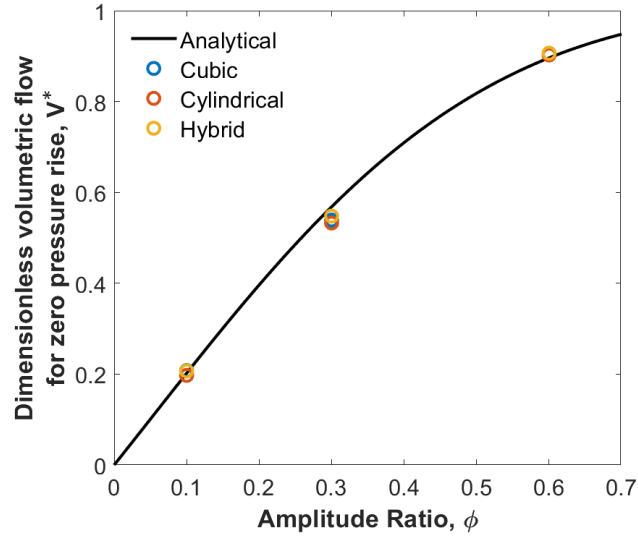
Figure 3.13: Effect of initial particle arrangement in the SPH model on the dimensionless volumetric flow.

Effect of kernel choice

The choice of the kernel is important in this study. A comparison between results obtained with different kernels is given in Figure 3.14. It shows that the results obtained using the quartic kernel give the best match to the analytic solution. The Wendland kernel shows slightly worse agreement, while the cubic kernel performs the worst of these three commonly used SPH kernels. Figure 3.15 shows the axial velocity contour at 5 s from the SPH models with different kernels. The quartic kernel provides the smoothest and least diffused pattern compared with the Wendland and cubic kernel, with this effect being most obvious in the $\phi = 0.1$ case, where external forcing is the smallest. Therefore, the quartic option is the best kernel for this problem as it shows the smoothest result and the best agreement with the analytical solution. This can potentially be explained by the shape of the kernels, shown in Figure 3.3. Firstly, the quartic kernel has larger compact support ($2.5h$ instead of $2h$ for the other two) so can resolve steep gradients better. Secondly, it appears that the greater emphasis placed on the nearest particles of the Wendland kernel compared with the cubic kernel is advantageous in this case. The quartic kernel and to some extent the Wendland kernel capture the boundary layer near the wall better (See Figure 3.15), which is important in resolving the overall flow field, which in turn determines the net peristaltic flux.
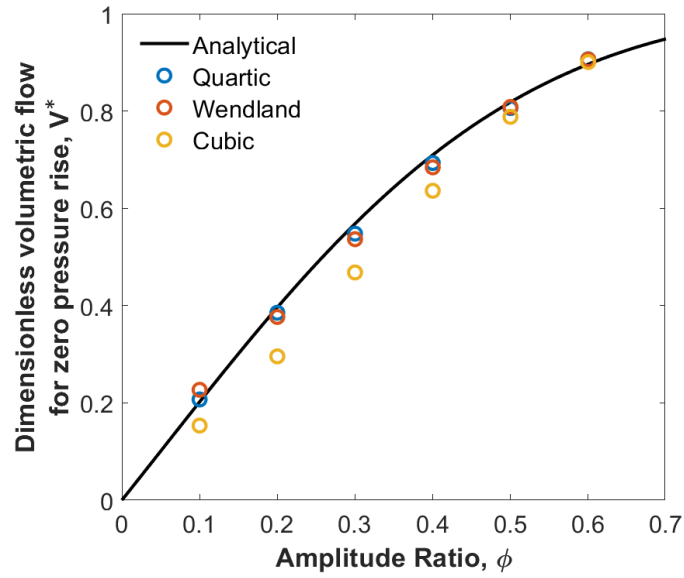
Figure 3.14: Comparison of dimensionless volumetric flow for the SPH models with different kernels.
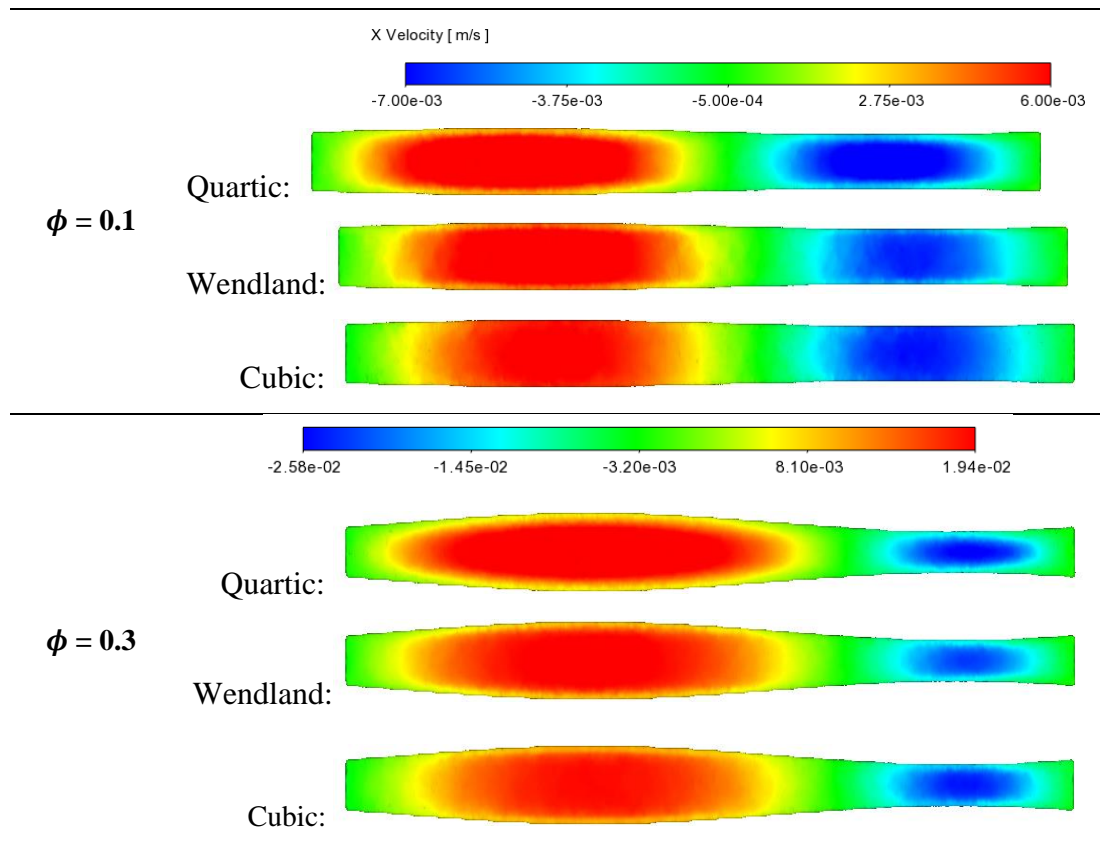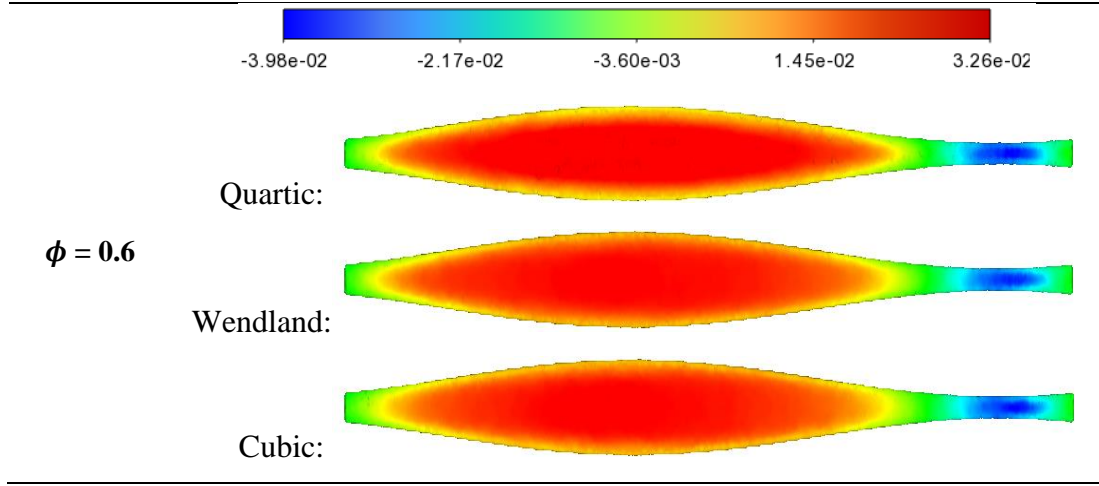
Figure 3.15: Axial velocity contour at 5 s from the SPH models with different kernels.

Effect of fluid sound speed

As shown in equations 3.17 and 3.19, the local sound of speed (c_s) controls the pressure scale for the fluid flow and the timestep used in the model. In this work, a characteristic velocity, V, is estimated based on the wall wave speed (0.03 m/s). c_s for $\phi = 0.1$ is set to be 20 times the wave speed, making sure the density variation is less than 1%. A numerical convergence study is conducted on the fluid sound speed for the different amplitude ratios listed in Table 3.3. The results are shown in Figure 3.13. The chosen base fluid sound speed is acceptable as neither decreasing nor increasing this speed has an impact on the simulation results.

Table 3.3: Tested sound speed for different amplitude ratios.

c_s (m/s)	$\phi = 0.1$	$\phi = 0.3$	$\phi = 0.6$
Base	0.60	0.68	0.79
Lower (5% lower than base)	0.57	0.64	0.75
Higher (5% higher than base)	0.63	0.71	0.83
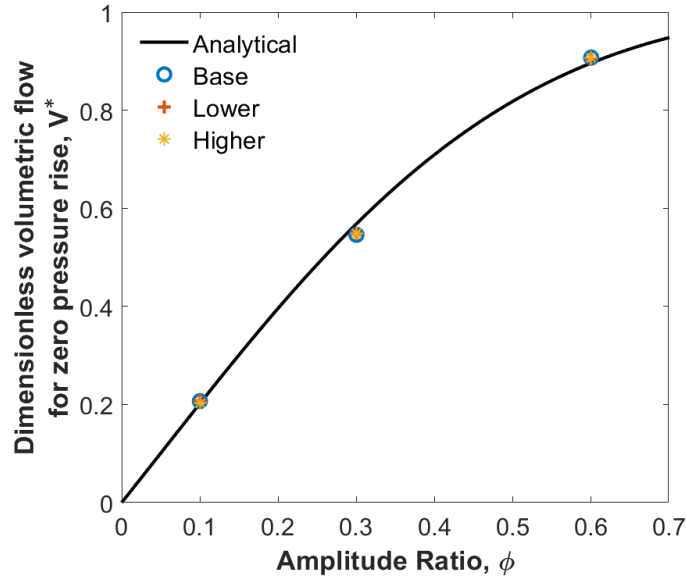
Figure 3.16: Effect of the fluid sound speed on the net volumetric flow rate for changes in the sound speed.

Effect of spatial resolution

A test of convergence is performed on the spatial resolution used in the SPH model. The effect of four different particle sizes (0.15, 0.125, 0.1, and 0.0875 mm) is tested and the results are shown in Table 3.4. As the particle size decreases, the variation of the normalised flow rate from the analytic results decreases for the different amplitude ratio cases. As shown in Figure 3.17, the results for particle sizes of 0.1 mm and 0.0875 mm are very close, demonstrating that the solution is well converged and that 0.1 mm particle size is sufficient for accurate prediction, with its results being very close to the analytical solution.

Table 3.4: Effect of particle size in the SPH simulations.

Particle size (mm)	Number of particles	Normalised flow rate	Variation from analytic result	Normalised flow rate	Variation from analytic result	Normalised flow rate	Variation from analytic result
		$\phi = 0.1$		$\phi = 0.3$		$\phi = 0.6$	
0.15	77,000	0.077	62%	0.333	42%	0.583	35%
0.125	124,000	0.185	9%	0.444	22%	0.767	14%
0.1	224,000	0.207	2%	0.546	4%	0.907	1%
0.0875	320,000	0.197	2%	0.550	3%	0.903	1%
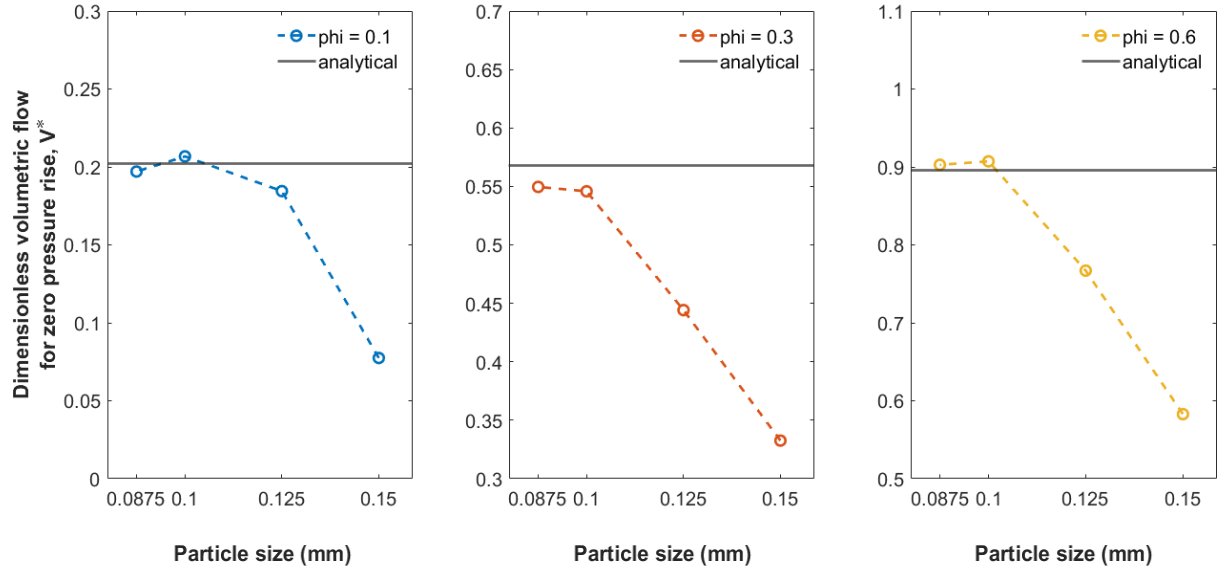
Figure 3.17: Dimensionless volumetric flow for different particle sizes.

3.5.2. FVM model

Mesh and timestep independent studies

A simulation with a refined mesh is made to establish mesh independence. The number of mesh elements was increased from 68,000 to 240,000. The average element size decreased from 0.15 mm to 0.1 mm. A smaller timestep, by a factor of 10, is used to examine the effect of timestep on the numerical results. The results of these analyses are shown in Figure 3.18. It is evident that the simulations are properly resolved using the original solution parameters.
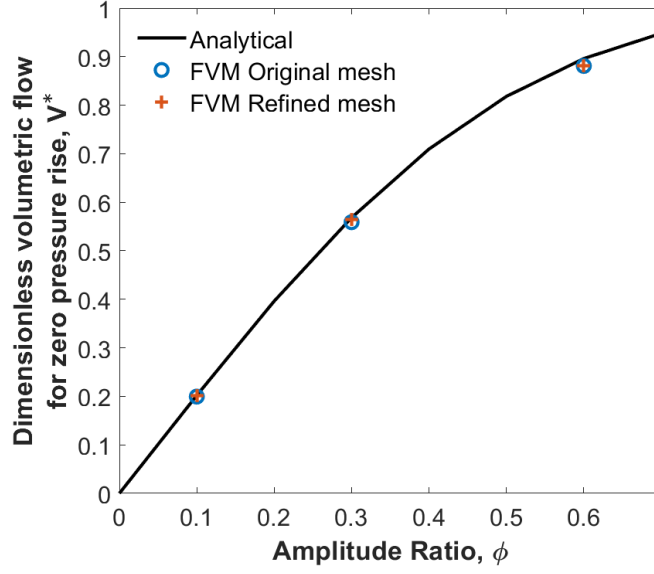
(a) Mesh independence
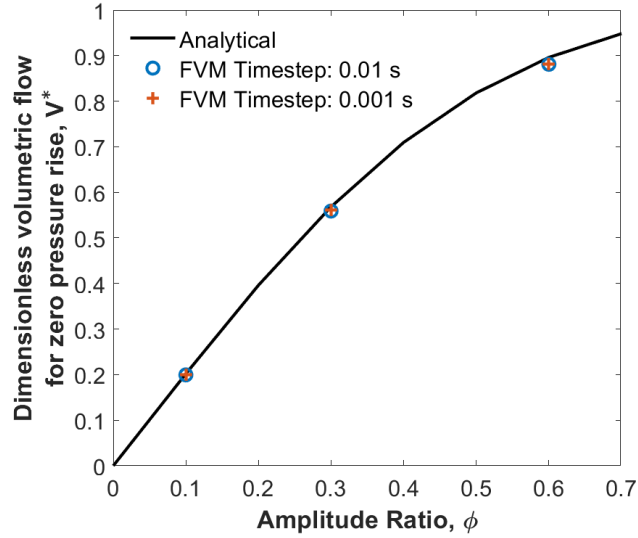
(b) Timestep independence

Figure 3.18: Mesh and timestep independence studies on the FVM model.

3.6. Extended simulations in FVM

3.6.1. Extreme amplitude ratios

In the comparison test case, the highest amplitude ratio is 0.6. Two extreme amplitude ratios, $\phi = 0.7$ and $\phi = 0.8$ are also tested in the FVM model and show excellent agreement with the analytical solution. The volumetric flow rate for all cases is shown in Figure 3.19 and the integrated flow rate in Figure 3.20. These two extreme cases are not tested in the SPH model used for two reasons. Firstly, the use of uniform resolution formulation of SPH would

necessitate the use of a very small particle size to resolve the fluid in the regions of constriction that drive the flow for extremely high amplitude ratios. This type of model would be computationally prohibitive. An alternative approach for very high amplitudes would be to use an adaptive SPH method (where the resolution varies spatially in the same way as was done for the FVM). Secondly, the objective of this work is to verify the accuracy of a uniform resolution formulation of SPH in modelling peristaltic motion and therefore the main interest is to test typical occlusions that occur in peristalsis, which range from 0.1 to 0.6.
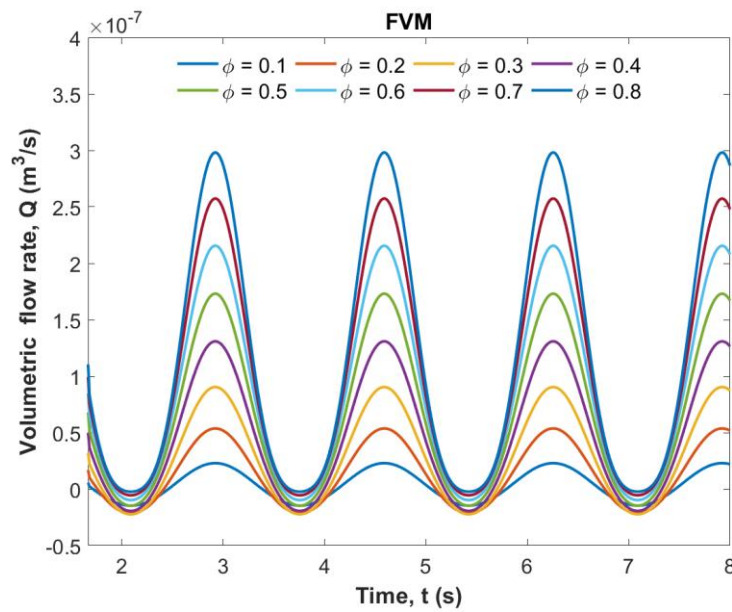
Figure 3.19: Volumetric flow rate at the mid cross-section over time for ϕ = 0.1 to 0.8 for the FVM model.
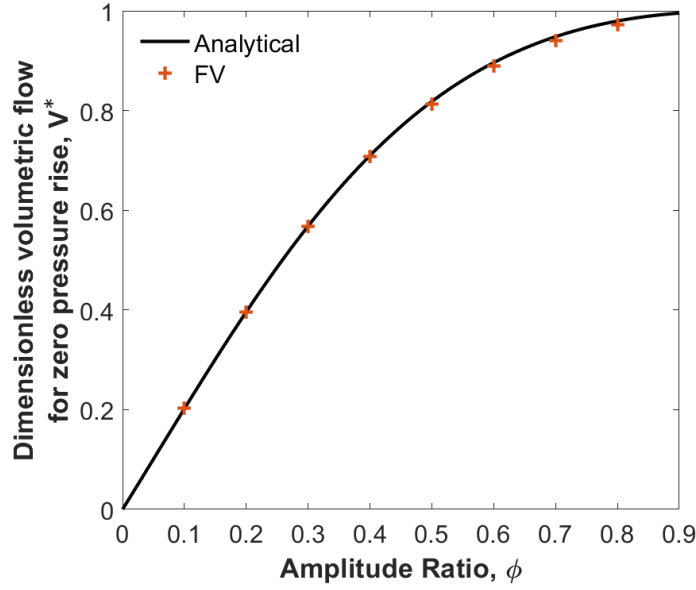
Figure 3.20: Dimensionless volumetric flow for ϕ = 0.1 to 0.8 for the FVM model.

3.6.2. Pressure rise for zero time-mean flow

There is also an analytical solution for a case where the ends of the tube are closed, and the peristaltic waves generate a pressure rise [130]. This situation may arise in some *in vitro* experiments and this work was done for an experiment at the time. The simulation was designed for an experiment in which support was provided (see Chapter 5) and therefore this case was simulated in a closed system. In this case, the dimensionless pressure rise over a wavelength (ΔP) can be calculated as a function of the amplitude ratio (ϕ) [130]:

$$\Delta P = 8\phi^2 \frac{1 - \frac{1}{16}\phi^2}{(1 - \phi^2)^{\frac{3}{2}}} \qquad (3.24)$$

Given the ease with which this could be set up in the FVM, it was used to simulate this system. The inlet and outlet of the tube are treated as no-slip walls. All the other aspects of the setup are the same as in the periodic comparison case. The area-averaged static pressures at both the inlet and outlet are recorded at each time step, and their difference is calculated. The pressure difference over time is shown in Figure 3.21 and the dimensionless value calculated using equation 3.24 is compared with the analytical solution in Figure 3.22. The latter shows excellent agreement between the FVM results and the analytical values across all amplitude ratios. There is a very strong effect of amplitude ratio on the pressure rise with the value for a ratio of 0.8 becoming slightly noisy.

71
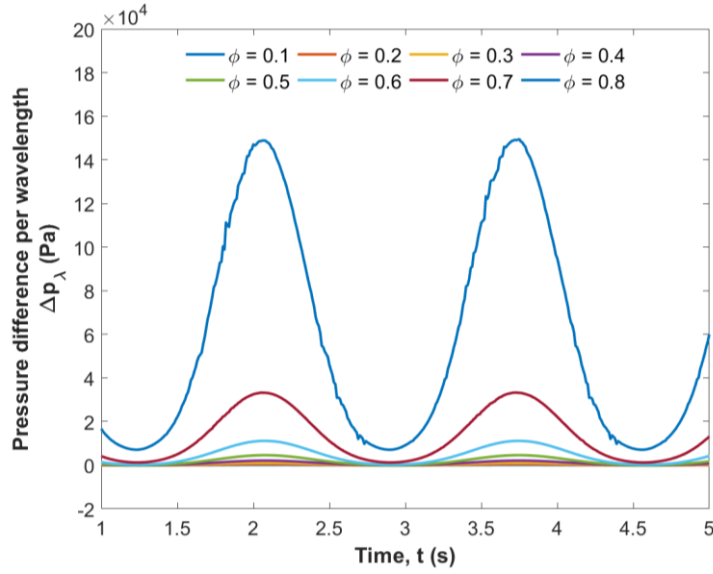
Figure 3.21: Pressure difference at the mid cross-section over time in FVM for a closed system.
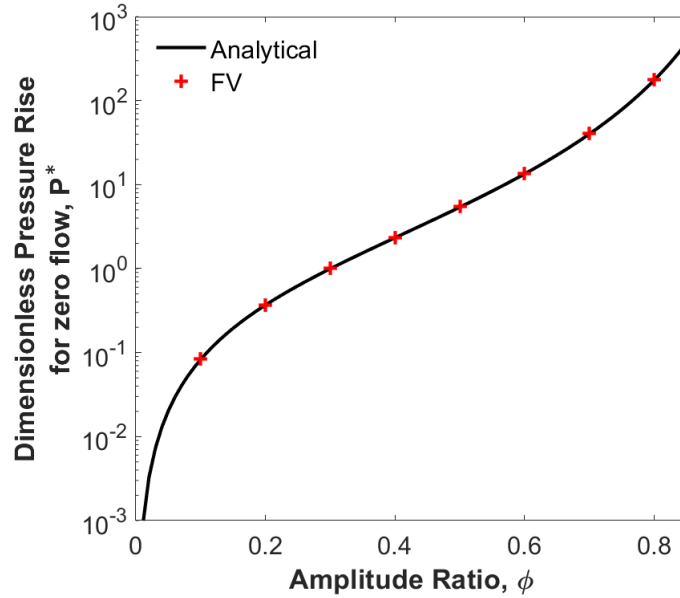
Figure 3.22: Dimensionless pressure difference from the FVM compared with analytic values for a closed system.

This case was not simulated using the SPH model as at this stage it was evident that it is not needed for future stomach modelling.

3.7. Conclusions

Two numerical methods, FVM and SPH, are used to solve a peristaltic flow problem and results from these are compared with the analytical solution. Simulation results show that both methods yield very good agreement with the analytical model results across the large range of occlusion amplitudes that are found in peristalsis. The moving wall boundary condition results

in flows in the forward and reverse directions. As the occlusion ratio increases the forward flow component increases much faster than the negative component resulting in a significant increase in the net flow rate.

The results of both approaches depend on the resolution of the simulation and the numerical schemes used but with sufficient resolution, the methods tend to have an asymptotic result that matches the analytic model. The spatial resolution in the FVM model depends on the mesh size and in the SPH model it depends on the chosen particle size. Both methods gave resolution independent results. In the FVM model, the mesh was refined near the wall but in the SPH model a constant particle size was used, as this was deemed to be the best choice for future work, meaning the number of particles needed would become prohibitive to resolve higher occlusion ratios.

The underlying methodology of the two solvers meant that different assumptions were made in the two approaches. The FVM model assumed incompressible flow, used implicit time-stepping and solved a Poisson's equation to determine the pressure field. The SPH method assumed a weakly compressible flow, and an explicit time integration method, which required a characteristic numerical sound speed to be set based on the expected flow velocities to obtain the pressure field. Despite these differences, both methods gave the same well-resolved solution for the cases presented. This work also highlights the very different experience that is needed for use of these complementary solution methods.

The effect of different parameters used in the SPH model was discussed in detail, which provides a comprehensive basis for further development of the stomach model using SPH. This work also validated the FVM for deforming mesh simulations. In the next Chapter, the coupling of this FVM with an FEA model is validated for later use in modelling an *in vitro* digestion experiment.

Chapter 4. Verification of Fluid-Structure Interaction Modelling for Wave Propagation in Fluid-filled Elastic Tubes

The bulk of this chapter is published as X. Liu and D.F. Fletcher, "Verification of fluid-structure interaction modelling for wave propagation in fluid-filled elastic tubes", Journal of Algorithms and Computational Technology, vol. 17, 2023, doi: 10.1177/17483026231159793.

4.1. Introduction

The pulse wave velocity (PWV) is the pressure wave propagation speed in a fluid-filled elastic tube. Experimentally the PWV can be determined by using pressure sensors placed at a known distance along a tube. In blood flow, PWV is considered clinically as a measure of the performance of the arteries' stiffness, which explains the large amount of work performed in this area. The equations relating to PWV have been developed for over a century. The most famous is the Moens-Korteweg equation [145, 146], developed in 1878. They found that PWV depends on not only the elastic modulus of the structure but also the geometrical dimensions of the tube and the fluid density. This equation is derived based on many assumptions and only accounts for the most important factors. A critical review of the equation is given by Lambossy [147]. Studies were carried out later by other researchers to provide more precise information on wave propagation characteristics [148-153]. Most studies focused on estimating the elastic properties of the arterial wall and calculating the velocity of the blood flow through the measured PWV. Bergel [154-156] modified the Moens-Korteweg equation by including two more parameters into the calculation, which are the Poisson's ratio and the ratio of thickness to outer radius of the tube. This modification compensates for the inaccuracies introduced from the thin wall assumption of the Moens-Korteweg equation.

In the calculation of PWV, the arteries are assumed to be constrained axially, meaning that tube elongation is not considered. Therefore, the effect of tube constraints is not considered when estimating PWV in the circulatory system. However, it has been shown that the wave propagation velocity is also related to the longitudinal support of the tube [157-161]. Different tube constraints can cause different fluid behaviours in an elastic tube. This finding is very important, particularly for the water hammer phenomenon in pipeline systems.

In this study, an investigation of wave propagation in a fluid-filled elastic tube is carried out through numerical simulation. The modelling of fluid structure interaction (FSI) has been of interest for decades. It describes the coupling of fluid dynamics and structural mechanics.

When a fluid leads to deformation, this can be quite large or very small, depending on the fluid properties and the structural properties. If the structural deformation is large enough, the fluid's behaviour will change to accommodate the deformation and coupling must be performed iteratively.

The aim of this study is to verify the FSI coupling method before it is used in the FSI study presented later in Chapter 5. Also, it provides valuable insights when stomach wall coupled motion is implemented in any future study. In this study, the accuracy of an FSI model is verified by comparing the simulation results with theoretical values. Firstly, different structural elements are used to build the elastic structure, and their behaviour for various wall thicknesses is discussed. Secondly, the effect of the material properties, which include the wall stiffness and Poisson's ratio, are analysed. Thirdly, some additional parameters that are not present in the PWV equations are tested in the numerical model. These parameters include the density of the wall material, the fluid viscosity, and the ramp rate of the pressure pulse. The effect of all parameters is studied for two different longitudinal restraint conditions.

4.2. Analytical solutions

4.2.1. Pulse wave velocity

The transient propagation of fluid in a thin-walled elastic tube has been studied by many researchers. The most well-known equation is the Moens-Korteweg equation [145, 146] is

$$c_0 = \sqrt{\frac{Eh}{2\rho R_i}} \tag{4.1}$$

where c_0 is the wave speed, ρ is the fluid density, R_i is the inner radius of the tube, h is the tube wall thickness, and E is the Young's modulus of the wall material.

The assumptions made in the derivation of the equation are listed below:

    i.   The tube is filled with incompressible and inviscid fluid.

    ii.   The wall thickness is very small compared with the radius.

    iii.   The wall material is elastic and isotropic.

    iv.   The effect of the Poisson's ratio of the wall material is not considered.

    v.   The wall only deforms radially.

Bergel [155] modified the Moens-Korteweg equation by including the effect of Poisson's ratio through the wall thickness. This correction compensates for the inaccuracies resulting from the

thin-wall assumption in the original equation. Although this correction accounts for the effect of the Poisson's ratio, it is still assumed that the length of the tube does not alter.

The modified wave speed becomes

$$c_1 = c_0 \times \sqrt{\frac{(2 - \gamma)}{(2 - 2\gamma(1 - v - 2v^2) + \gamma^2(1 - v - 2v^2) - 2v^2)}} \qquad (4.2)$$

where v is the Poisson's ratio, and $\gamma = h/R_o$, which is the ratio of the wall thickness to the outer radius.

The effect of v and γ is visualised in Figure 4.1. The wave speed increases as v and γ increase. When $v = 0$ and $\gamma = 0$, $c_1 = c_0$. When $v = 0.5$ and $\gamma = 0.2$, c_1 is 15% faster than c_0. This correction is significant, especially for blood flow in the arteries. For arteries, v is close to 0.5 and γ ranges from 0.1 to 0.13, corresponding to a 12% increase in wave speed when considering the correction.
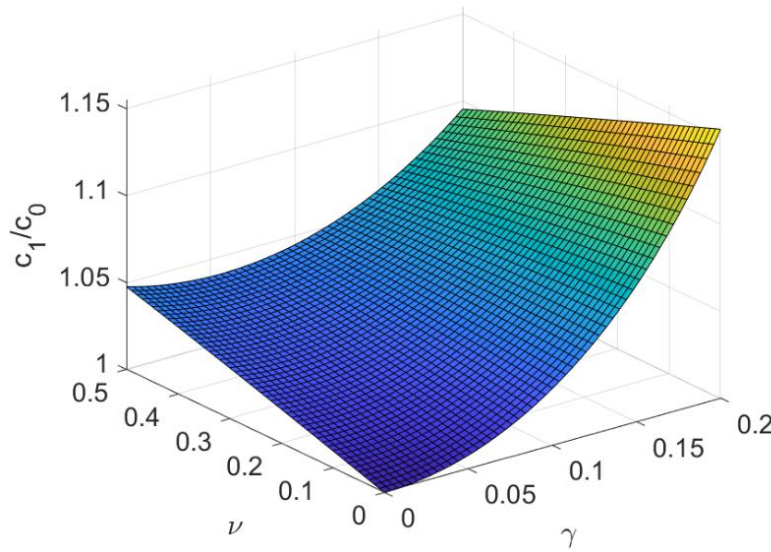
Figure 4.1: The effect of Poisson's ratio and the ratio of wall thickness to the tube radius on Bergel's correction.

4.2.2. Effect of tube constraints

In the derivation of both the Moens-Korteweg equation and Bergel's correction, the elastic tube is not allowed to elongate. The effect of different longitudinal tube constraints was investigated by Wylie et al. [157] theoretically. The wave speed formulas are modified based on whether longitudinal motion is allowed. Different coefficients are used based on the ratio of the wall

thickness to the inner radius. When the ratio $y = h/R_i$ is smaller than 0.08, the tube is considered to have a thin wall. Otherwise, the wall is treated as being thick.

Case (a) - When the tube is anchored against axial movement throughout, the tube is not allowed to elongate. The axial unit strain, $\xi_{axial} = 0$. This scenario is the same as that used to derive equation 4.2. A different approximation is made to that of Bergel, and the following equations are derived.

For a thin-walled tube, the wave speed is

$$c_2 = \frac{c_0}{\sqrt{1 - \nu^2}} \tag{4.3}$$

For a thick-walled tube, the wave speed is

$$c_3 = \frac{c_0}{\sqrt{y(1 + \nu) + \frac{2(1 - \nu^2)}{2 + y}}} \tag{4.4}$$

Case (b) - When axial movement is allowed along the tube, the axial stress, $\sigma_{axial} = 0$ Pa. The wave speed equations are written below.

For a thin-walled tube, the wave speed is

$$c_4 = c_0 \tag{4.5}$$

For a thick-walled tube, the wave speed is

$$c_5 = \frac{c_0}{\sqrt{y(1 + \nu) + \left(\frac{2}{2 + y}\right)}} \tag{4.6}$$

A comparison between Cases (a) and (b) can be seen in Figure 4.2. When $\nu = 0$, the wave speed of Case (a) equals that of Case (b). When $\nu = 0.5$, the wave speed of Case (b) is around 11% slower than that of Case (a). This means that the wave speed becomes slower when axial motion is allowed. The difference increases as the Poisson's ratio increases.
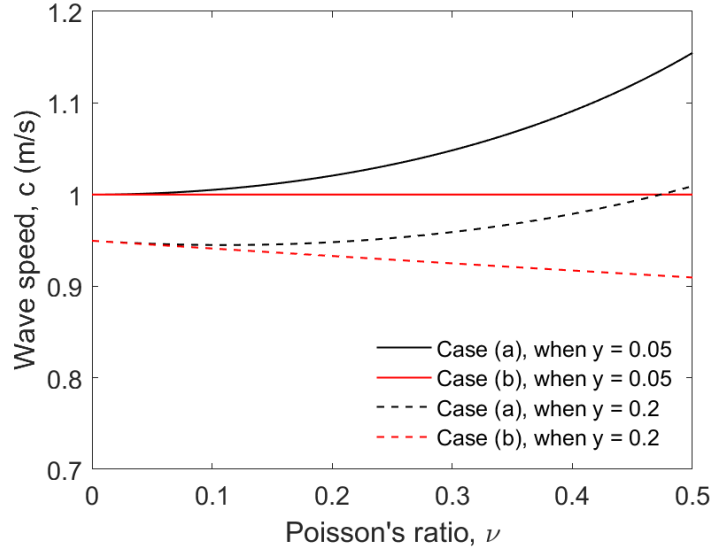
Figure 4.2: The effect of tube constraints on elastic wave speed as a function of Poisson's ratio.

4.2.3. Radial displacement

In an elastic tube, when a pressure pulse is applied, the radial displacement along the tube can be calculated based on the simple equation below derived from the analytical solution of Womersley [150, 152]. However, this equation only applies when the tube is constrained axially.

$$\delta_r = \frac{p(z,t)R^2(1-v^2)}{Eh} \tag{4.7}$$

where $p(z,t)$ is the pressure distribution at axial distance z, at time t.

In the simulation, a linearly increasing pressure is applied at the inlet of the fluid domain. The pressure at the inlet follows the following equation:

$$p(0,t) = kt \tag{4.8}$$

where k is a constant.

Therefore, when the tube is constrained axially the radial displacement at the inlet can be calculated from the equation below:

$$\delta_{r0}(t) = \frac{ktR^2(1-v^2)}{Eh} \tag{4.9}$$

4.2.4. Effect of fluid compressibility

The fluid is assumed to be incompressible in the Moens-Korteweg equation. By taking the fluid compressibility into account, the wave speed can be calculated using [147]:

$$c_6 = \sqrt{\frac{1}{\rho\left(\frac{1}{K} + \frac{2R}{Eh}\right)}} \tag{4.10}$$

The relationship between c_6 and c_0 is:

$$c_6 = \sqrt{\frac{1}{\left(\frac{\rho}{K} + \frac{1}{c_0}\right)}} \tag{4.11}$$

where K is the bulk modulus of fluid.

The density of common fluids is of the order of 10^3 kg/m^3, and the bulk modulus is of the order of 10^9 kPa. Therefore, ρ/K is very small compared with the inverse propagation speed, and it is reasonable to assume the fluid to be incompressible when calculating the wave speed. However, it should be noted that if gas is present in the fluid, the effect of the mixture compressibility becomes significant, and the wave speed can be reduced dramatically. Detailed calculations can be found in Kobori et al. [162] and Pearsall [158].

4.3. Numerical model

Ansys System Coupling 2021R1 is used to set up the fluid-structure interaction in this study. Ansys Fluent is used to perform the fluid flow analysis, while Ansys Mechanical is used to conduct the structural analysis. The geometry constructed is shown in Figure 4.3.
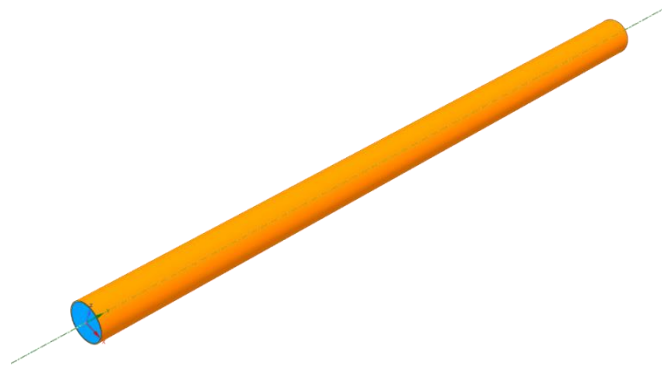
Figure 4.3: Geometry of the numerical model: showing the fluid region (coloured in blue) and solid region (coloured in orange).

The parameters listed in Table 4.1 are used to construct the numerical model. The parameters include the tube geometry, the properties of the fluid inside the tube, and the mechanical properties of the wall material.

Table 4.1: Parameters used in the baseline numerical model.

Geometrical dimensions		
Radius	R	0.002 m
Thickness	h	0.0001 m
Length	L	0.08 m
Ratio of wall thickness to outer radius	γ	0.048
Ratio of wall thickness to inner radius	y	0.05
Wall properties		
Density	ρ_s	1000 kg/m^3
Young's modulus	E	1×10^6 Pa
Poisson's ratio	ν	0.4999
Fluid properties		
Dynamic viscosity	μ	0.001 Pa.s
Density	ρ	1000 kg/m^3
Pressure ramp rate	k	35,250 Pa/s

4.3.1. Fluid model

Computational Mesh

The fluid model is developed using ANSYS Fluent, version 2020R1. A size control of 0.5 mm is used to generate the mesh in the fluid domain, shown in Figure 4.4. It has 14,720 nodes and 18,796 cells with 3 inflation layers. The minimum orthogonal quality of the mesh is 0.72, and the maximum skewness is 0.28. Mesh refinement tests showed this level of mesh refinement to be sufficient.
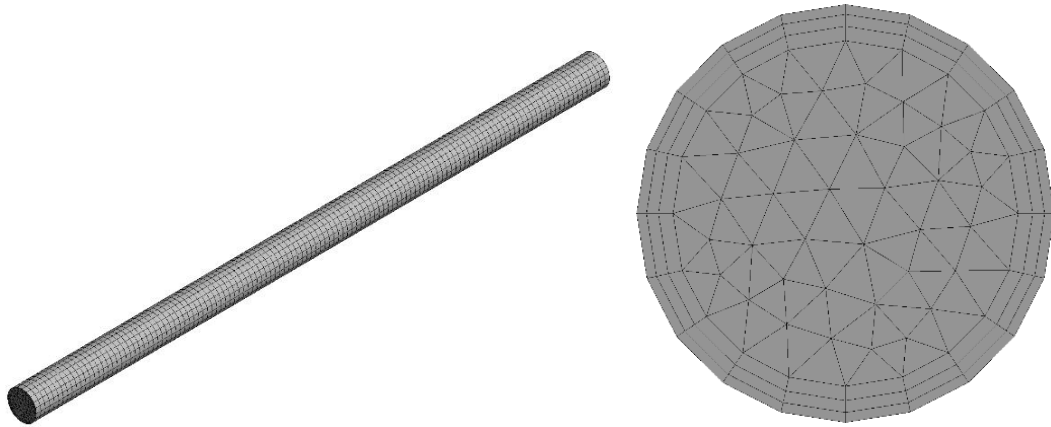
Figure 4.4: Computational mesh on the fluid domain.

Conservation equations

The mass and momentum conservation equations for incompressible flow with a moving mesh are given by equations (3.21) and (3.22) presented previously in Chapter 3.

Setup

The entrance of the tube is set as a pressure inlet with a linearly increasing pressure applied (equation 4.8). The exit is set as a pressure outlet (static pressure of 0 Pa). The no-slip condition is applied at the tube wall. A dynamic mesh model is enabled, which allows the shape of the domain to change with time. The diffusion-based smoothing method is chosen to diffuse the boundary motion throughout the interior mesh. The inlet and outlet of the tube are allowed to deform in the planes normal to the axial direction. The tube wall is set as a system coupling zone, which transfers data to and from the structural model. The simulated fluid properties are listed in Table 4.1.

The second-order implicit transient, pressure-based solver is used to conduct the analysis. The coupled scheme is used, which means the momentum and pressure correction equations are solved in a fully coupled manner. Gradients are determined using the least-squares cell-based option, the pressure is determined using the second-order method, and the second-order upwind scheme is used for the momentum equation. Converged solutions are achieved when the residual values for continuity, x, y and z velocities are below 10^{-5}. The residual values are calculated based on the locally scaled Root Mean Square (RMS) errors.

4.3.2. Mechanical model

Element type and mesh

Three types of elements can be used in Ansys Mechanical to construct the tube: shell, solid, and solid shell. Details are given in Table 4.2. Figure 4.5 shows the recommended selection criterion, which depends on the aspect ratio, γ.
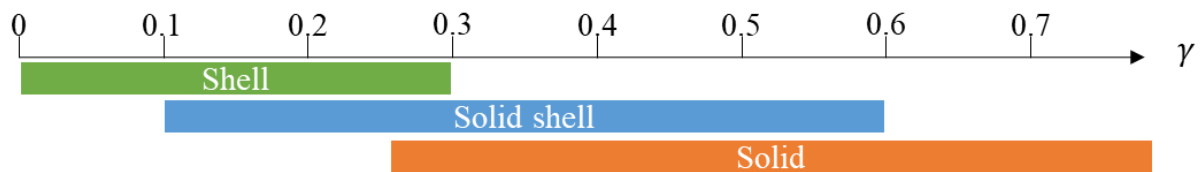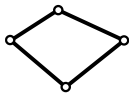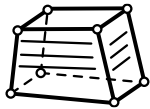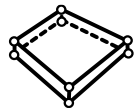
Figure 4.5: Element type selection criteria. Based on Akin [163].

Shell elements are two-dimensional (2D) and are only suitable for modelling thin structures. In a shell model, the structure is represented by a single plate at the mid-surface. Without the thickness dimension, shell elements cannot achieve precise stress and strain profiles through the wall thickness. Each node of the shell element has six degrees of freedom to compensate for the geometric limitation. In addition to the degrees of freedom in translation, the shell element has degrees of freedom in rotations. Therefore, shell elements can capture the bending behaviour at each node explicitly.

Solid elements are well suited for modelling three-dimensional (3D) thick structures because they can simulate the stress and strain profile through the thickness. However, solid elements cannot capture bending behaviour due to the lack of degrees of freedom in rotations. Shear locking occurs when solid elements are used for thin walls. It means that the structure becomes artificially stiffer than its actual stiffness.

Solid shell elements are designed for simulating thin structures. The solid shell model represents the solid structure using a single-layered solid element. The single-layered solid element allows the model to obtain the stress and strain profile through the thickness. Solid shell elements can overcome shear locking when their thickness is small enough due to their unique kinematic formulations [164].

Table 4.2: Structural element comparison based on the Ansys manual [165].

	Shell	Solid	Solid shell
Element code in Ansys	SHELL181	SOLID185	SOLSH190
Geometry			
Element	4-node structural shell	8-node structural solid	8-node structural solid shell
Degrees of freedom	Six: translations and rotations in the nodal x, y, and z directions	Three: translations in the nodal x, y, and z directions	Three: translations in the nodal x, y, and z directions

Different element types are used to build the same model to test their effect. An element size of 0.5 mm is used in all three models. The shell model is represented by a single plate. The solid model has three layers, while the solid shell model only has one. The cross-sectional mesh constructed with different element types are shown in Figure 4.6. The mesh statistics for the different structural models are summarised in Table 4.3.

(a) (b) (c)
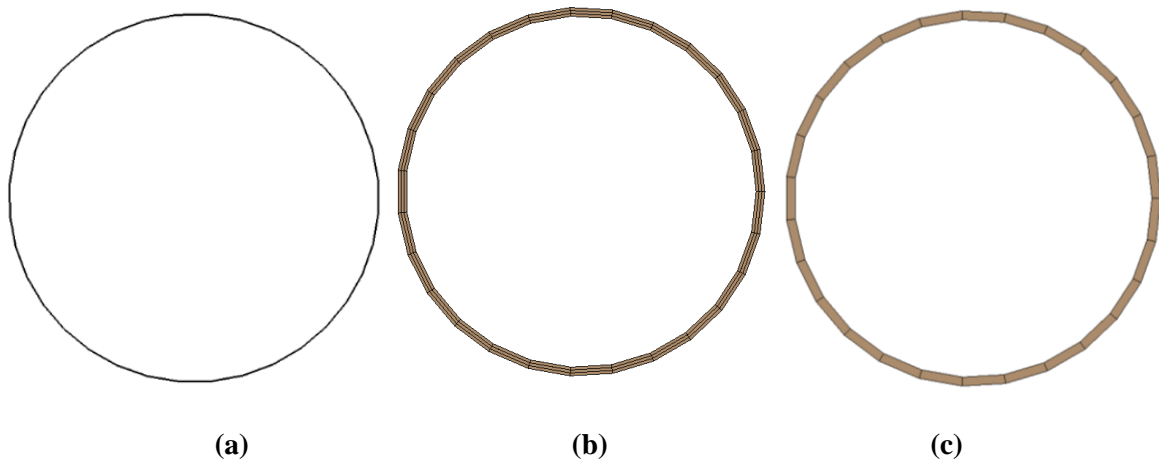
Figure 4.6: Cross-sectional mesh on the structural domain for thickness of 0.1 mm (a) shell; (b) solid; (c) solid shell.

Table 4.3: Mesh statistics for the different structural models.

	Shell	Solid	Solid shell
Number of nodes in the model	4,502	18,032	9,016
Number of elements in the model	4,480	13,440	4,480

Equation of motion

The equation of motion for a linear elastic, homogeneous, isotropic medium is given by [166]:

$$\rho_s \frac{\partial^2 \boldsymbol{u}}{\partial t^2} = \boldsymbol{f} + \nabla \boldsymbol{\sigma} \tag{4.12}$$

where ρ_s is the instantaneous solid density, $\boldsymbol{u}$ is the displacement vector, $\boldsymbol{f}$ is the body force (henceforth ignored), and $\boldsymbol{\sigma}$ is the stress tensor.

Using conservation of mass, the instantaneous density, ρ_s, can be related to the initial material density, ρ_0, via

$$\rho_s = \rho_0 \det(F) \tag{4.13}$$

where det denotes the determinant and F is the deformation gradient, which is defined by

$$F = \frac{\partial \boldsymbol{u}}{\partial \boldsymbol{X}} \tag{4.14}$$

where $\boldsymbol{X}$ is the location of the undeformed model.

In addition, it is readily shown that the strain tensor, $\boldsymbol{e}$, can be calculated from the displacement via

$$\boldsymbol{e} = \frac{1}{2}(\nabla \mathbf{u} + (\nabla \mathbf{u})^T) \tag{4.15}$$

For an isotropic media, the stress tensor is given by

$$\boldsymbol{\sigma} = \lambda \mathrm{tr}(\boldsymbol{e})\boldsymbol{I} + 2G\boldsymbol{e} \tag{4.16}$$

where $\boldsymbol{I}$ is the identity tensor, tr denotes the trace of a tensor and λ and G are the Lamé constants. However, it is usual to work with the Young's modulus, E, and the Poisson's ratio, ν, which are related to the Lamé constants as follows

$$\lambda = \frac{E\nu}{(1+\nu)(1-2\nu)} \tag{4.17}$$

$$G = \frac{E}{2(1 + \nu)} \tag{4.18}$$

where G is the shear modulus (usually written as μ, but μ is used for the fluid viscosity in this study).

Using equations 4.14, 4.19 and 4.20, the equation of motion can be rewritten as

$$\rho_s \frac{\partial^2 \boldsymbol{u}}{\partial t^2} = (\lambda + 2G)\nabla(\nabla.\boldsymbol{u}) - G\nabla \times \nabla \times \boldsymbol{u} \tag{4.19}$$

Setup

The inner surface of the wall is set as a fluid-solid interface, which transfers information between the solid and fluid. Axial displacement is constrained in the structure. The material properties of the wall material are listed in Table 4.1. Large deflections are enabled to allow accurate calculation of the material deformation. The sparse matrix direct solver is used.

4.3.3. Coupling model

Setup

Ansys System Coupling, version 2021R1, is used to couple the fluid and structural analyses. A two-way data transfer is performed at the interface. The pressure impulse at the inlet causes the fluid to flow along the tube. The force at the fluid interface is then transferred across the structural interface, causing the structural model to deform. The structural displacement information is then transferred back to the fluid domain. This is continued until convergence is obtained.

The analysis setup for the FSI model is controlled in the System Coupling setup. The duration of the analysis was set as 0.006 s. A timestep of 0.0005 s was selected after assessing the timestep effect upon results. The maximum number of coupling iterations was set to 20, while 13 were usually needed for convergence. Quasi-Newton stabilisation was activated to achieve convergence. This method is derived from an interface quasi-Newton coupling algorithm with an approximation for the inverse of the Jacobian (IQN-ILS) [167]. The initial relaxation factor applied during the start-up iteration was set to 0.01. The maximum number of time steps to be retained in the Quasi-Newton history was set to one. Data transfers at the interface were deemed to have converged when the globally scaled RMS of the residual values are below 0.01. Ten cores of *Intel(R) Xeon Bronze 3204, @1.90 GHz* processor with 64 GB RAM were

used to run the model. Two cores were used for the Mechanical solver and eight cores were used for the Fluent solver during the simulation.

4.4. Model verification

4.4.1. Effect of structural element type and wall thickness

The effect of the structural element type is examined by building the same model using different element types. Figure 4.7 shows the radial mesh displacement along the tube when using shell elements. The pressure impulse at the inlet increases over time, causing mesh displacement to gradually increase. The simulation ends before the wave reaches the end of the tube as it would cause reflections and disturb the profiles. All models show a very similar pattern.
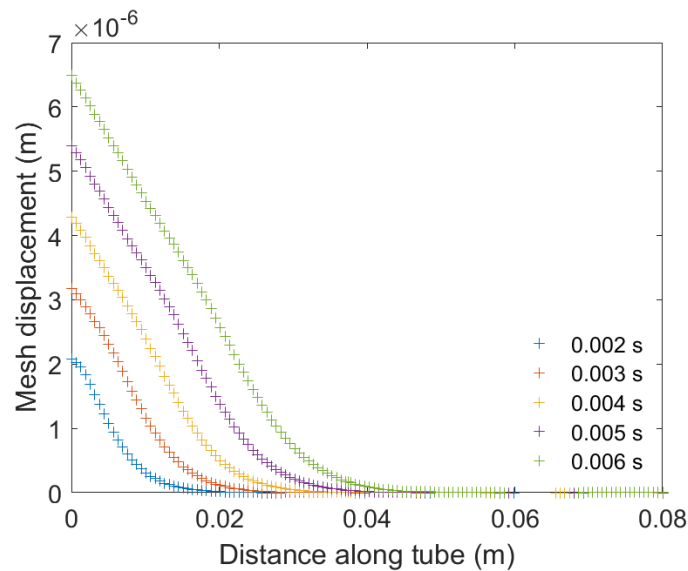
Figure 4.7: Radial mesh displacements along the tube with shell elements.

The radial displacement at the inlet over time is recorded and compared with the theoretical results following equation 4.9. Results show a high level of accuracy for different wall thicknesses.
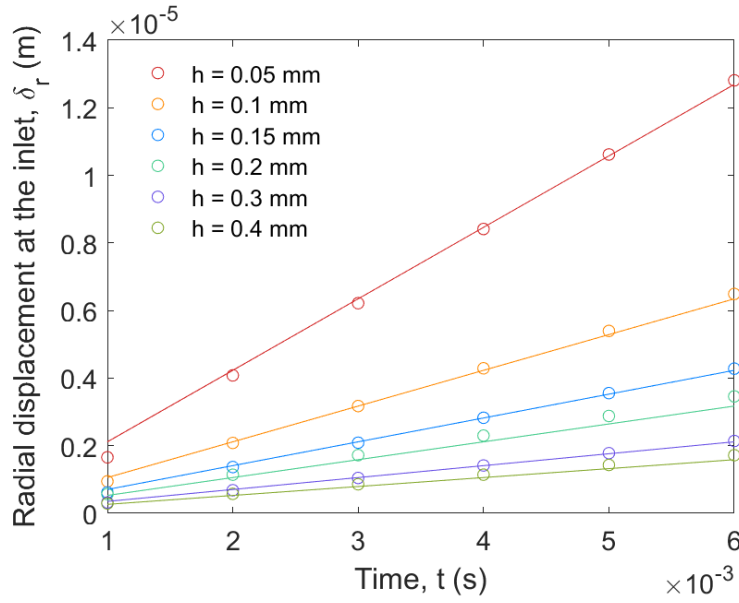
Figure 4.8: Radial displacements at the inlet compared with the analytical solution for various wall thicknesses with shell elements.

The wave speeds are estimated by calculating the distance travelled by the wave over time. The calculated wave speeds for different structural models are shown in Figure 4.9. The simulation results from all models are very similar when y is smaller than 0.1. The trends begin to deviate as the wall gets thicker. When $y > 0.1$, c_3 provides a better alignment with the solid and solid shell models compared with the shell model. These results are consistent with the structural element selection criteria shown in Figure 4.5. Solid shell and solid elements provide more accurate results when the wall is relatively thick. Moreover, the solid shell model and solid model produce very similar results. Therefore, the solid shell model is used to represent a solid model in the subsequent studies because it is much less computationally expensive.
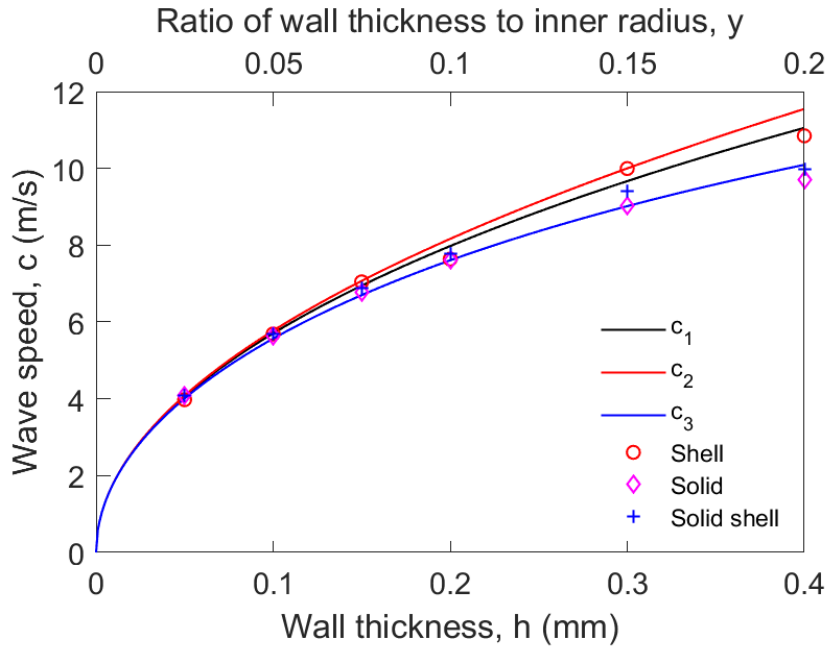
Figure 4.9: The effect of wall thickness on wave speed for different element types.

4.4.2. Mesh independence studies

A mesh-resolution study was performed by reducing the element size from 0.5 mm to 0.25 mm. Simulation results are compared against the analytical propagation speed c_1 as it provides a better result when y is smaller than 0.1. Figure 4.10 shows that both models give the same solution, demonstrating mesh independence in both models.
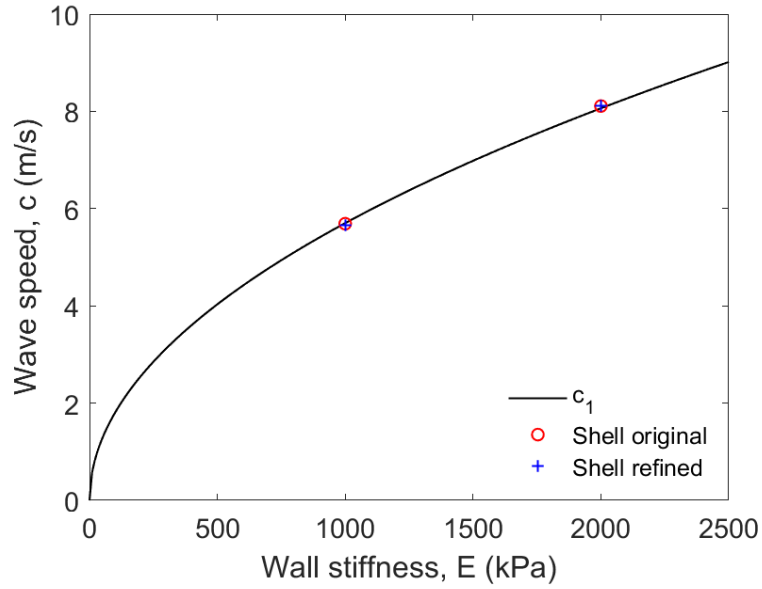
(a)
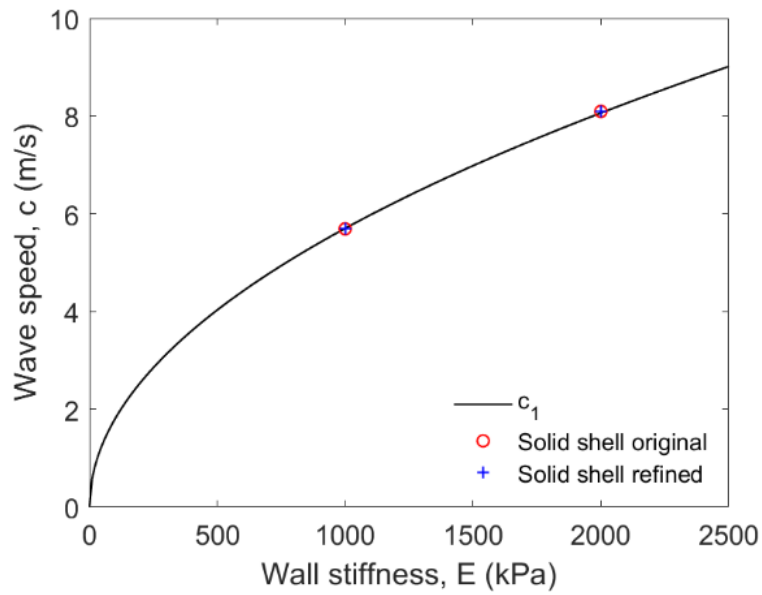
(b)

Figure 4.10: Mesh resolution studies (a) shell model; (b) solid shell model.

4.4.3. Timestep independence study

A timestep independence study is presented in this section. A reduced timestep of 0.2 ms instead of 0.5 ms was tested. Figure 4.11 shows that the results are timestep independent in both models.
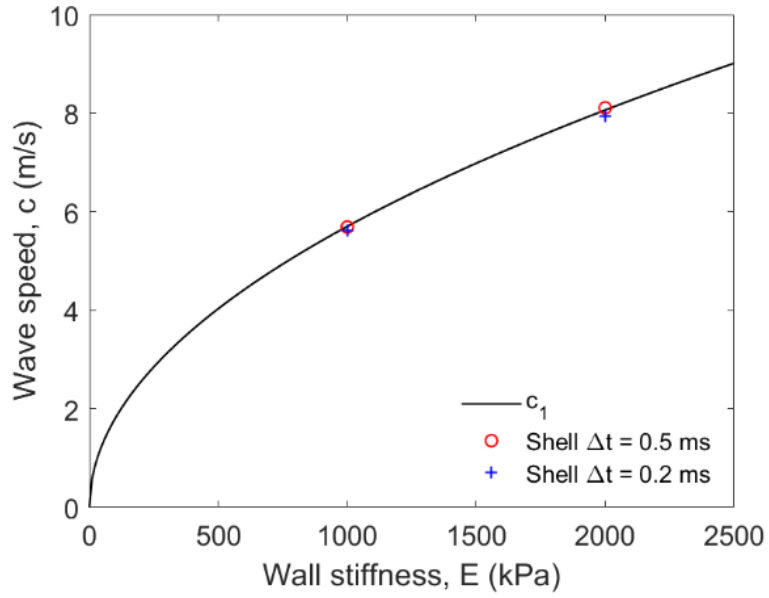
(a)
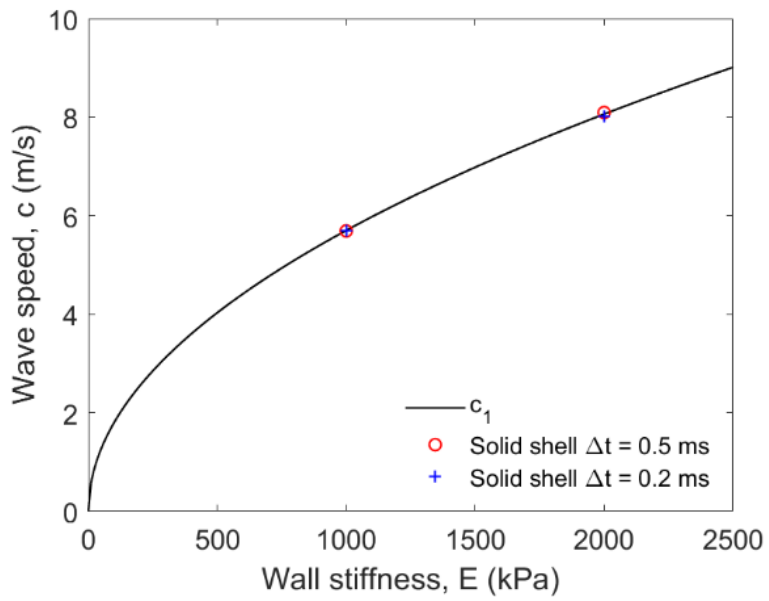
(b)

Figure 4.11: Timestep independence studies (a) shell model; (b) solid shell model.

4.5. Discussion

4.5.1. Effect of wall stiffness

The tube is constrained axially

The effect of wall stiffness is examined in the simulations and the results for the propagation speed are compared with the analytical value c_1. As shown in Figure 4.12, both models show

good agreement. The wave speed increases as the wall stiffness increases and the data fit perfectly with equation 4.2. The radial displacement at the inlet for different wall stiffnesses fits very closely with equation 4.9.
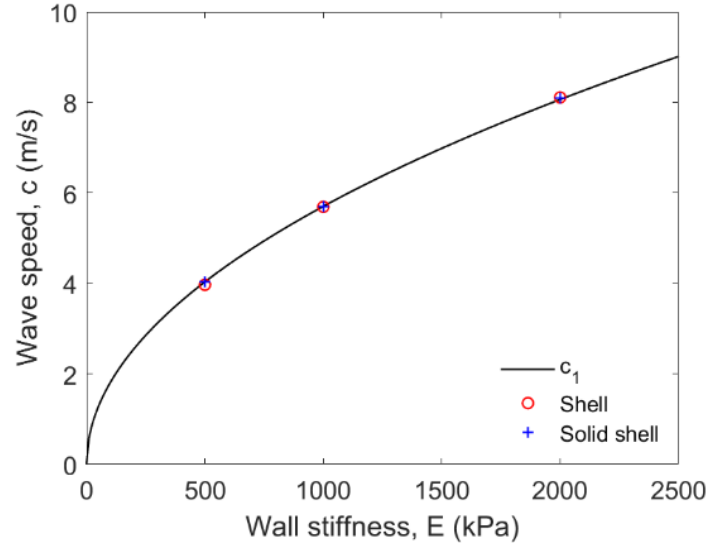
(a)
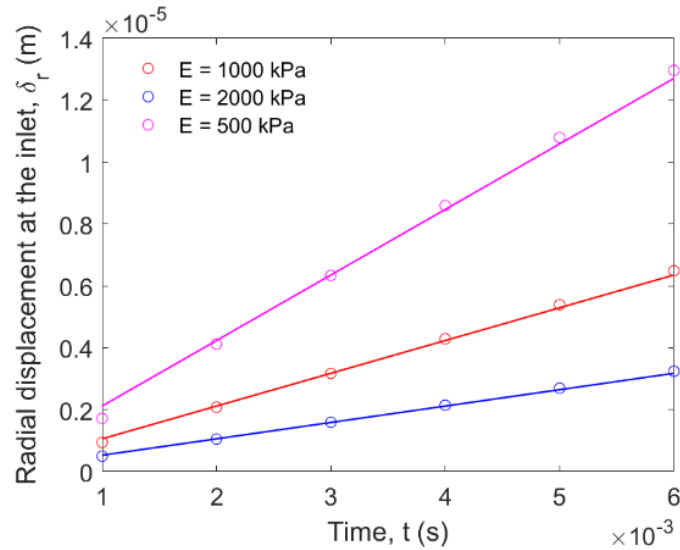
(b)

Figure 4.12: The effect of wall stiffness when the tube is constrained axially on:
(a) wave speed; (b) radial displacement.

The axial stress and strain profiles are shown in Figures 4.13 and 4.14, respectively. When the tube is constrained axially, axial strain along the tube is zero while the axial stress varies along the tube. These profiles match very well with the assumption of Case (a) from Wylie et al. [157].

Unit: Pa
Global Coordinate System
Time: 6.e-003

2248 Max
1998
1748
1498
1248
998.4
748.4
498.4
248.4
-1.562 Min
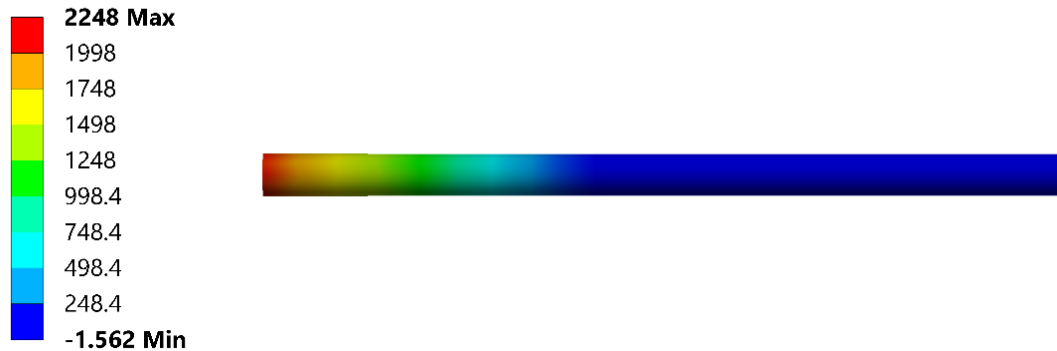
Figure 4.13: Axial stress profile when the tube is constrained axially, E = 1000 kPa.

Unit: m/m
Global Coordinate System
Time: 6.e-003

5.56e-5 Max
4.33e-5
3.09e-5
1.86e-5
6.18e-6
-6.18e-6
-1.85e-5
-3.09e-5
-4.33e-5
-5.56e-5 Min
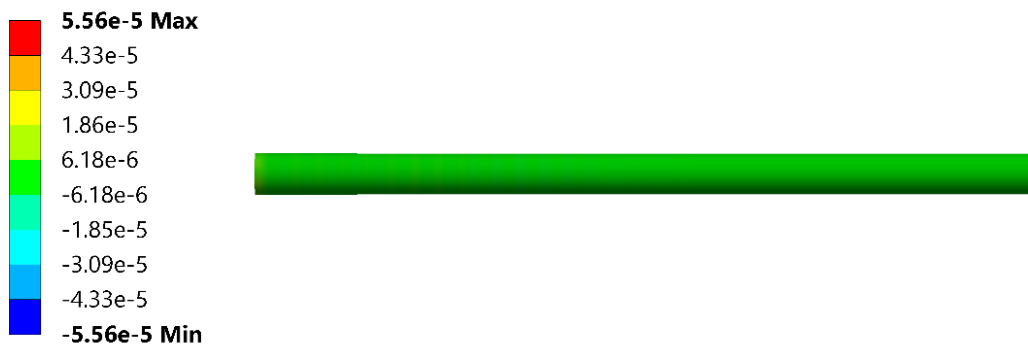
Figure 4.14: Axial strain profile when the tube is constrained axially, E = 1000 kPa.

The tube is free to elongate

When the tube is free to elongate, the simulated wave speeds are compared with the values for wave speed c_4. Without the axial constraint, the wave speeds become slower, while the radial displacement becomes larger. The axial stress and strain profiles are shown in Figures 4.16 and 4.17, respectively. The axial stress along the tube is zero, while the axial strain varies along the tube. These profiles also match well with the assumption of Case (b) from Wylie et al. [157].
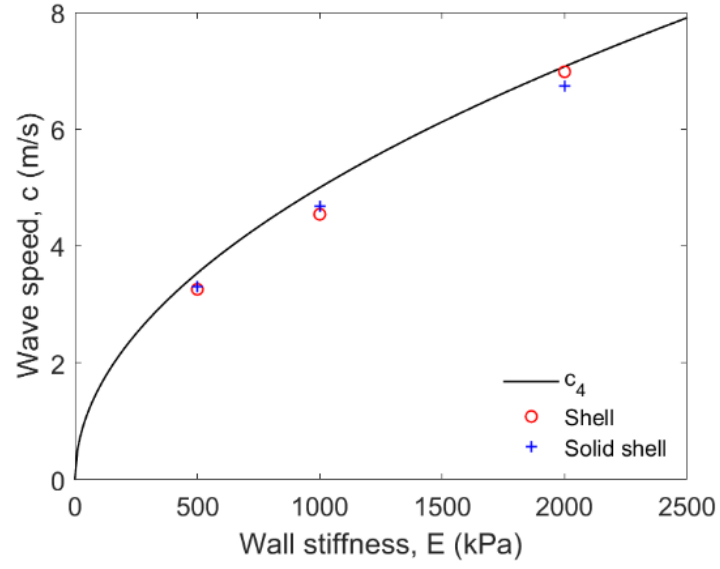
(a)
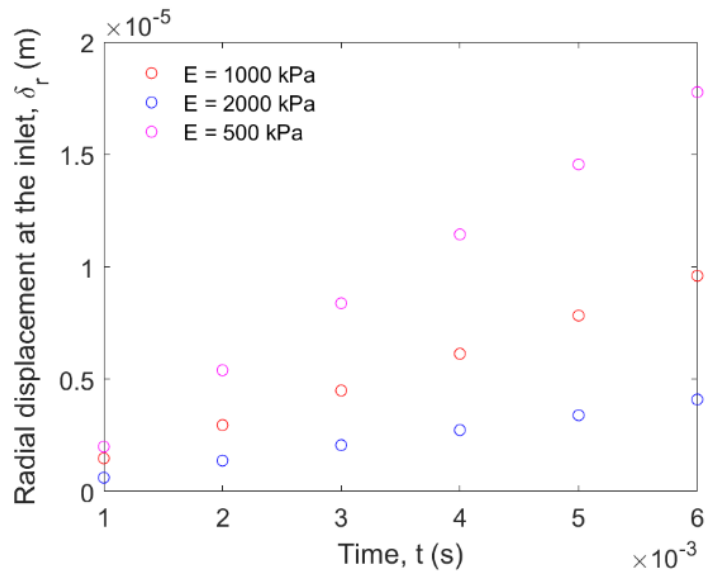
(b)

Figure 4.15: The effect of wall stiffness on wave speed when the tube is free to elongate: (a) wave speed; (b) radial displacement.

Unit: Pa
Global Coordinate System
Time: 6.e-003

210 Max
164
119
73.4
27.9
-17.5
-63
-108
-154
-199 Min

Figure 4.16: Axial stress profile when the tube is free to elongate, E = 1000 kPa.

Unit: m/m
Global Coordinate System
Time: 6.e-003

-3.52e-7 Max
-2.45e-4
-4.90e-4
-7.34e-4
-9.79e-4
-1.22e-3
-1.47e-3
-1.71e-3
-1.96e-3
-2.20e-3 Min
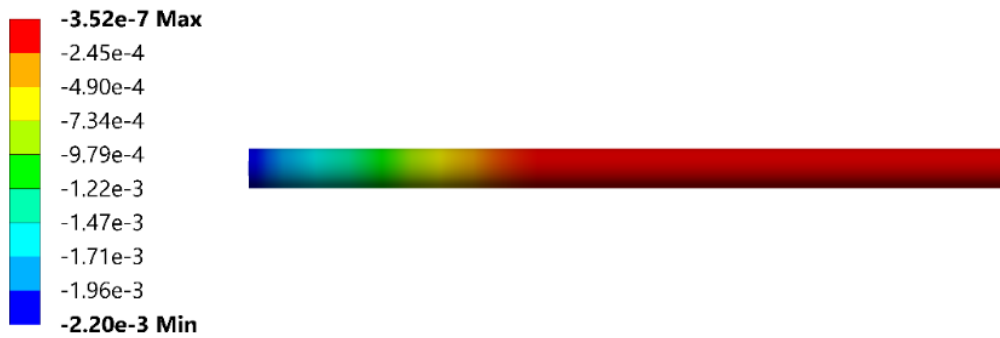
Figure 4.17: Axial strain profile when the tube is free to elongate, E = 1000 kPa.

4.5.2. Effect of Poisson's ratio

The tube is constrained axially

The effect of Poisson's ratio is examined when the tube is constrained axially. Figure 4.18 shows that as the Poisson's ratio increases, wave speeds from both models increase, following the trend of the analytic solution yielding the wave speed c_1. When the Poisson's ratio increases from 0 to 0.5, the wave speed increases by 15% in the shell model and 6% in the solid shell model. The radial displacement at the inlet with different wall stiffness matches well with equation 4.9.
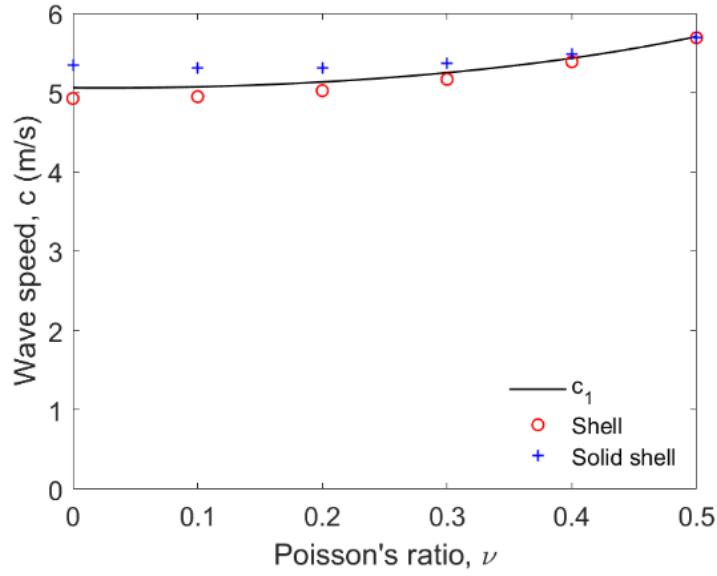
(a)
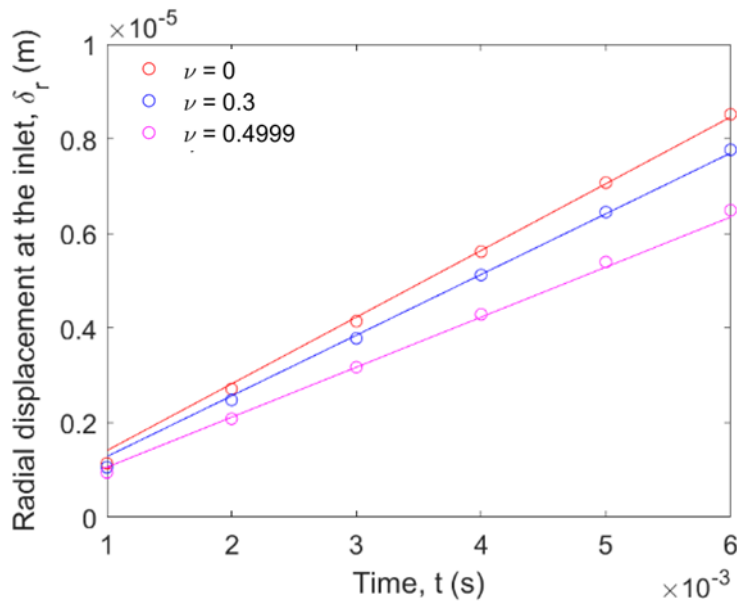
(b)

Figure 4.18: The effect of Poisson's ratio when the tube is constrained axially: (a) wave speed; (b) radial displacement.

The tube is free to elongate

When the tube is free to elongate, the Poisson's ratio does not have a significant impact on either the wave speed or the radial displacement. When the Poisson's ratio is increased from 0 to 0.5, the wave speed for both models decreased by only 2%.
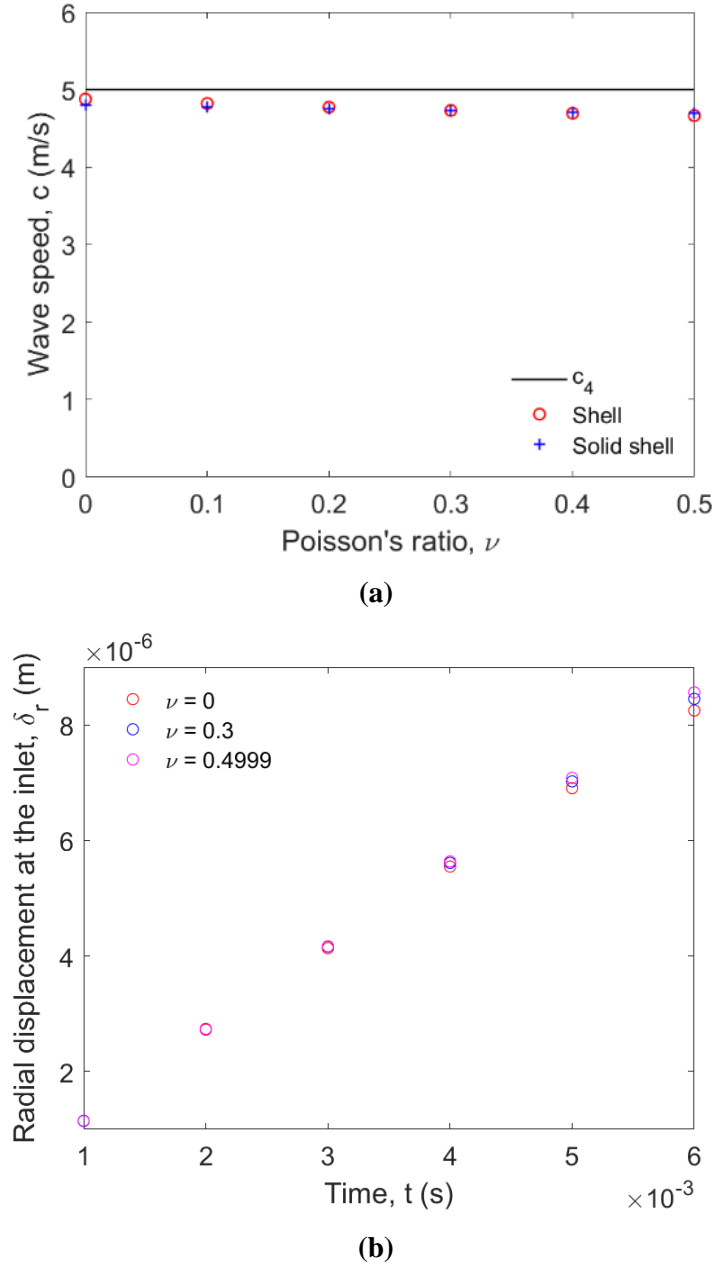
Figure 4.19: The effect of Poisson's ratio when the tube is free to elongate
(a) wave speed; (b) radial displacement.

4.5.3. Effect of wall material density

In the theoretical PWV calculation, the effect of the added mass, which is the wall mass and the fluid that moves with it, is not considered. In the study of Morgan and Ferrante [149], the effect of solid density was discussed. The study was then extended by Womersley [152], examining the effect of mass-loading of the solid. He stated that the wall material density only

affects the wave speed if the tube constraint allows longitudinal motion. Womersley [152] defined the term K_{ml} to include the effect of mass-loading and longitudinal constraint:

$$K_{ml} = \left(1 + \frac{h_s}{h} \cdot \frac{\rho_s R_s}{\rho R_i}\right)\left(1 - \frac{m^2}{n^2}\right) \qquad (4.20)$$

where K_{ml} is related to the wave speed, h_s, ρ_s, and R_s are the thickness, density, and mean radius of a tube that provides the added mass of the solid, m is the natural frequency of the longitudinal constraint, and n is the frequency of the pressure pulse.

If $m = n$, $K_{ml} = 0$, the tube behaves as if there is no mass loading. If the longitudinal constraint is stiff enough to prevent any longitudinal motion of the wall, $m \gg n$ and $K_{ml} \to -\infty$. In this case, the value of ρ_s does not have any effect. However, if the constraint is not very stiff and leads to longitudinal motion, K_{ml} is related to the ratio of ρ_s/ρ. In this section, the effect of the wall material density is estimated through numerical simulations.

The tube is constrained axially

When the tube is constrained axially, results for the effect of the wall material density are shown in Figure 4.20. The largest difference between the results is only 3%. Therefore, the wall material density does not have a significant impact on either the wave speed or radial displacement when the tube is constrained axially.
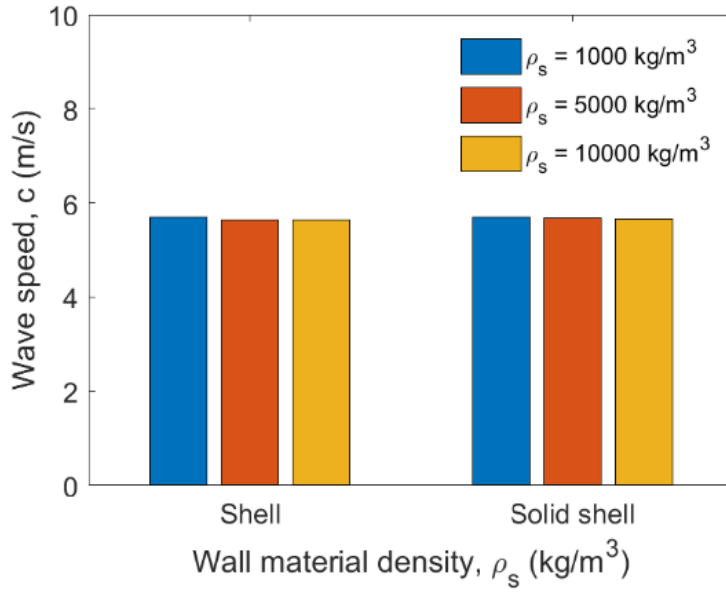
(a)
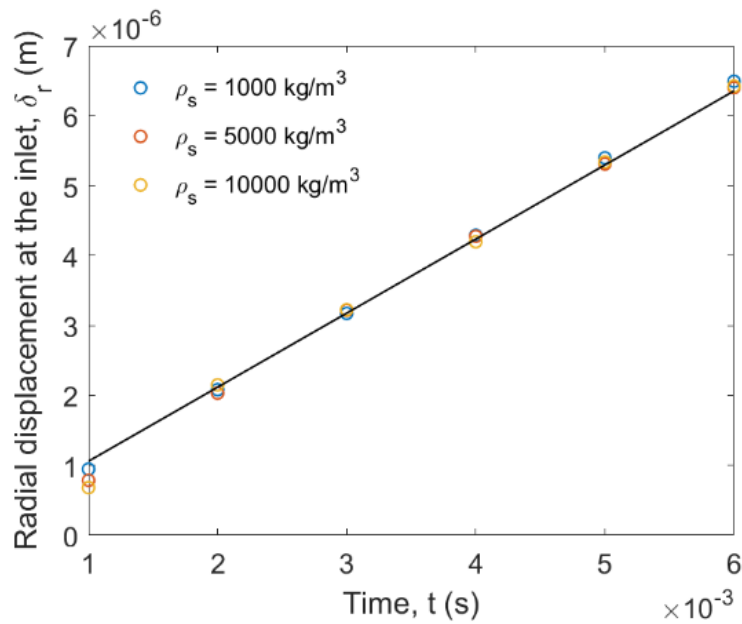
(b)

Figure 4.20: The effect of wall material density when the tube is constrained axially (a) wave speed; (b) radial displacement.

The tube is free to elongate

When the tube is free to elongate, the wall material density shows an effect on both wave speed and radial displacement, as shown in Figure 4.21. When the density increases from $1,000\,\mathrm{kg/m^3}$

to 10,000 kg/m^3, the wave speed decreases by around 16%. It also has an impact on radial displacement. However, the radial displacement at the inlet is almost the same when the density increases from 5,000 kg/m^3 to 10,000 kg/m^3.

(a)

(b)
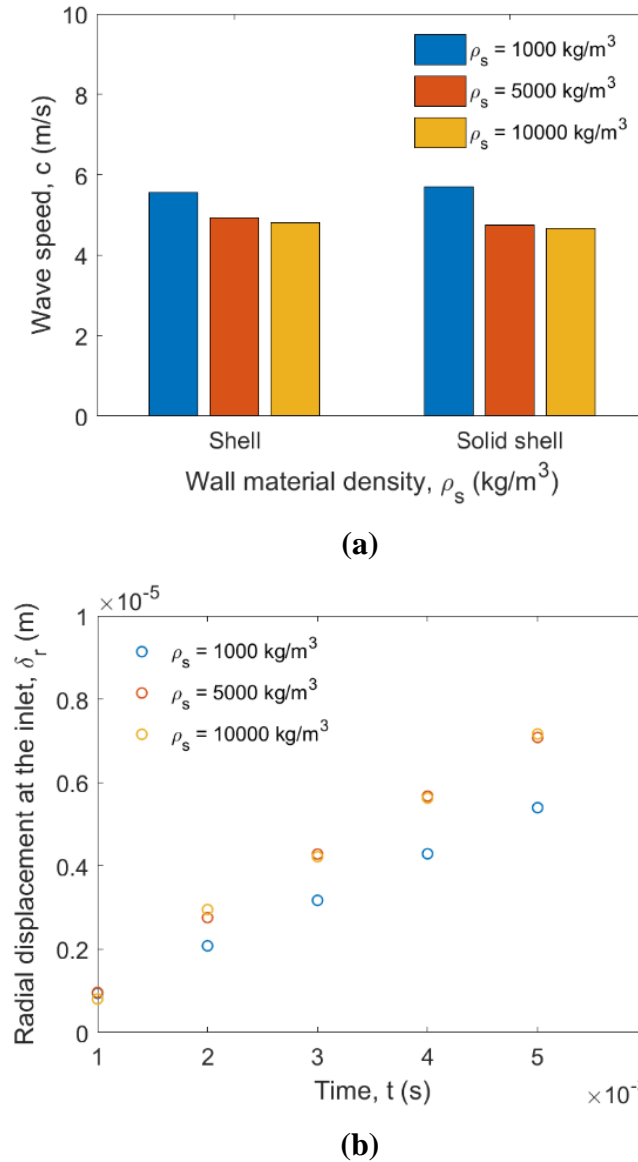
Figure 4.21: The effect of wall material density when the tube is free to elongate
(a) wave speed; (b) radial displacement.

4.5.4. Effect of fluid viscosity

The fluid is assumed to be inviscid in the PWV calculation to simplify the equations. However, the fluid viscosity affects the wave velocity significantly according to Womersley [150] and Bergel [154]. In this section, the effect of the fluid viscosity is examined through numerical simulation.

The tube is constrained axially

Fluid viscosity has a significant impact on wave speed when the tube is constrained axially. There is a 10% difference when the viscosity is changed from 0.001 Pa.s to 0.1 Pa.s, as can be seen in Figure 4.22(a). However, the radial displacement remains the same when the fluid viscosity is changed (see Figure 4.22b).
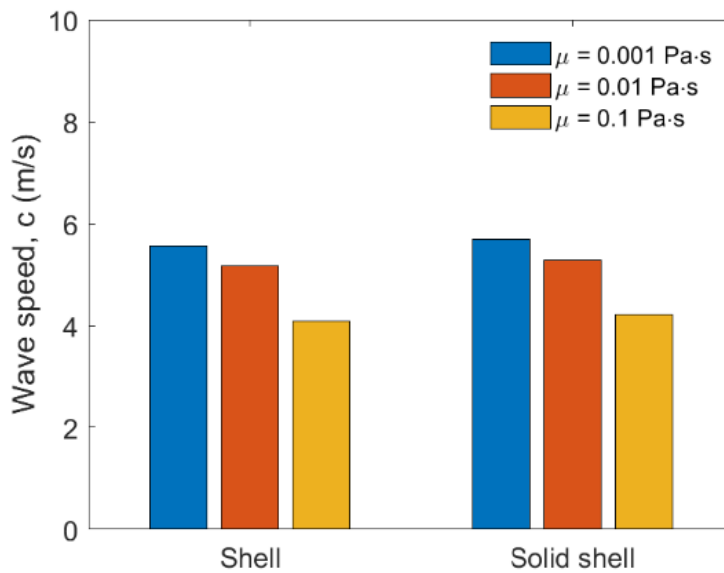
(a)
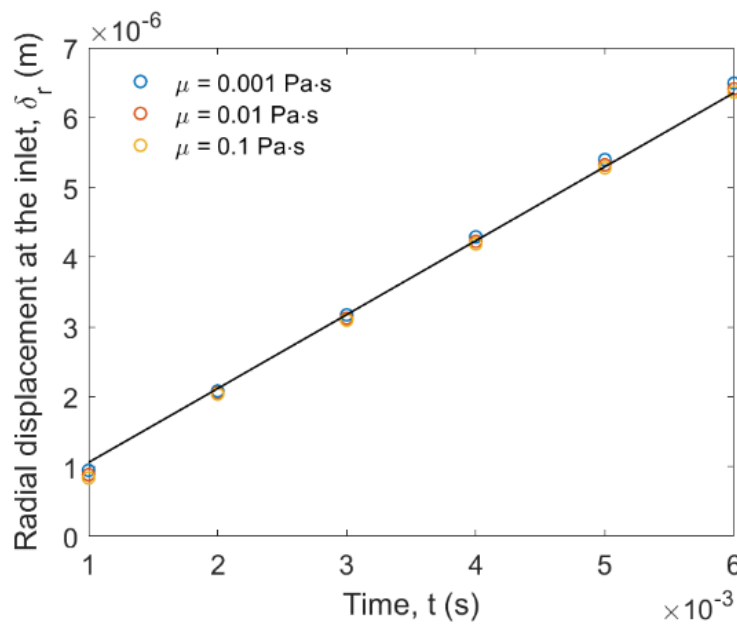
(b)

Figure 4.22: The effect of fluid viscosity when the tube is constrained axially

(a) wave speed; (b) radial displacement.

The tube is free to elongate

The wave speed is also affected by fluid viscosity when the tube is free to elongate, as seen in Figure 4.23(a). When the fluid viscosity is increased from 0.001 Pa.s to 0.1 Pa.s, the wave speed decreases by around 16%. The radial displacement decreases when the fluid viscosity increases up to 0.01 Pa.s, and then the effect is small (see Figure 4.23b).
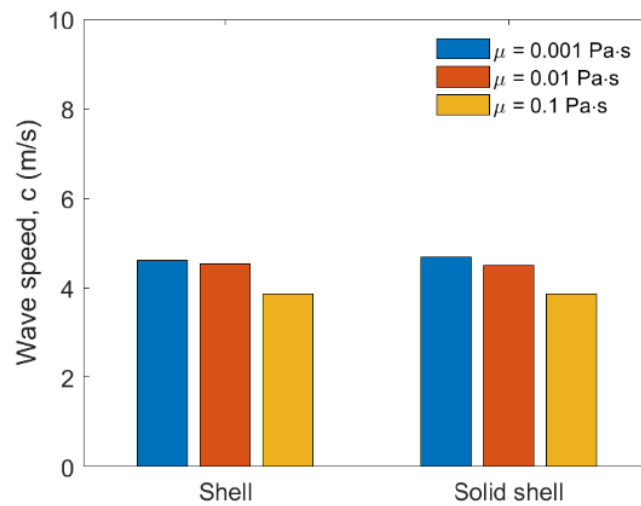
(a)
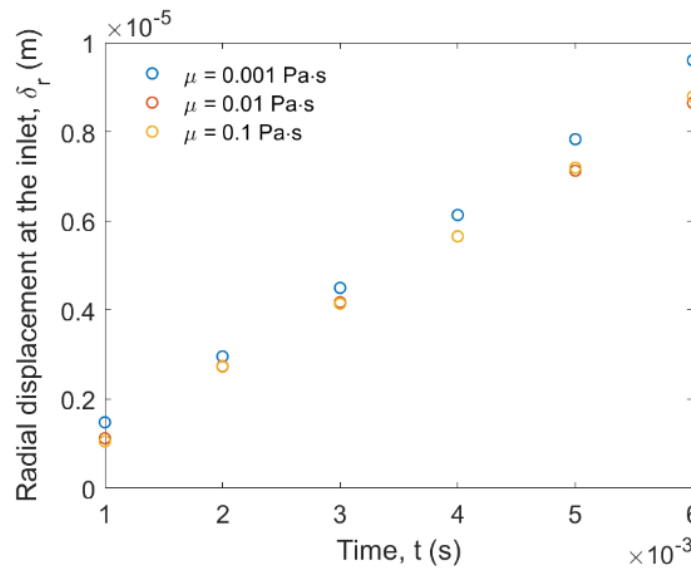
(b)

Figure 4.23: The effect of fluid viscosity when the tube is free to elongate
(a) wave speed; (b) radial displacement.

4.5.5. Effect of pressure ramp rate

The tube is constrained axially

The effect of the pressure ramp rate is examined when the tube is constrained axially. As shown in Figure 4.24, the wave speeds remain the same in both models when the pressure ramp rate changes. The radial displacement results fit almost perfectly with the results from equation 4.9.
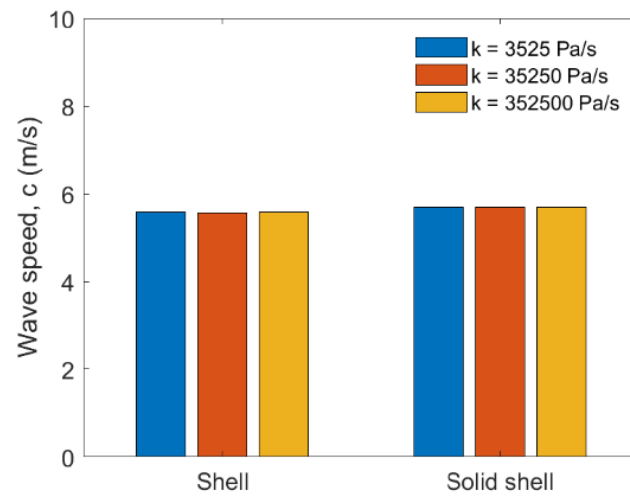
(a)
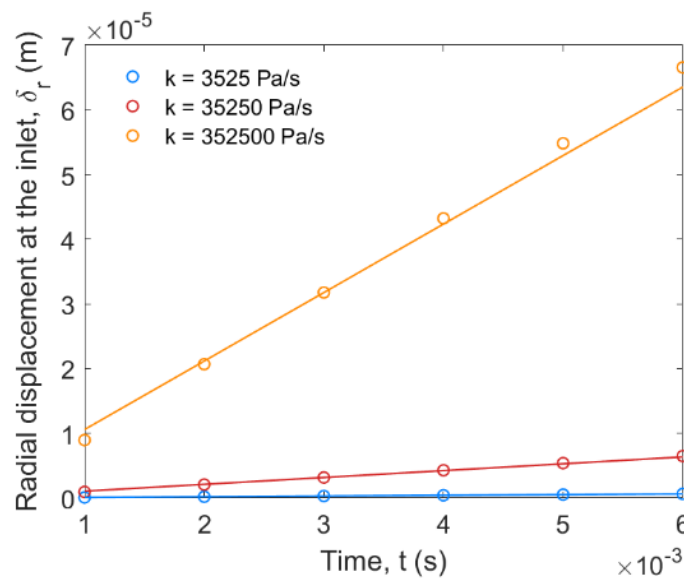
(b)

Figure 4.24: The effect of pressure ramp rate when the tube is constrained axially (a) wave speed; (b) radial displacement.

The tube is free to elongate

When the tube is free to elongate, the wave speed also remains unchanged when the pressure ramp rate is changed, as shown in Figure 4.25(a). The radial displacement at the inlet also increases in this case, as shown in Figure 4.25(b).
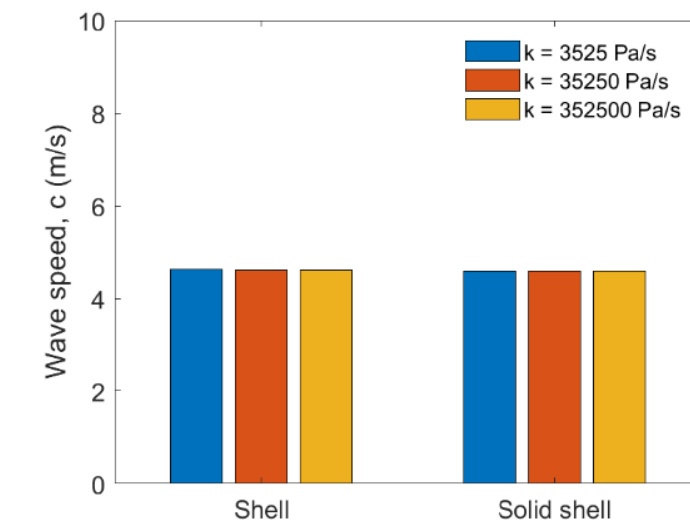
(a)
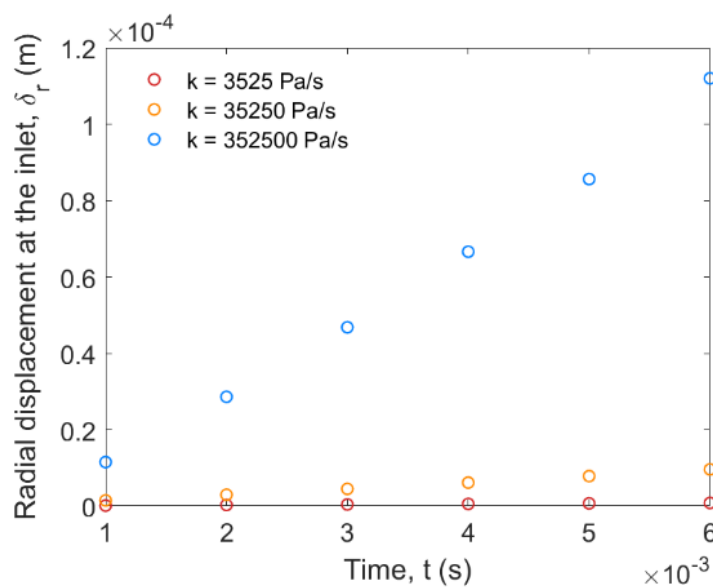
(b)

Figure 4.25: The effect of pressure ramp rate when the tube is free to elongate

(a) wave speed; (b) radial displacement.

4.6.   Conclusions

Model verification is crucial for simulation development. In this study, the accuracy of the Ansys System Coupling approach to model FSI of wave propagation in a fluid-filled tube is verified. The choice of structural element type is shown to be important when modelling different wall thicknesses and for moderately thick walls solid shells gave the best results. Specifically, if the ratio of the wall thickness to the tube inner radius is less than 0.1 ($y < 0.1$), shell elements perform best and above this ratio solid shell or solid elements are required. This corresponds closely with the limit set by Wylie et al. [157] of $y < 0.08$ for a tube to have thin walls. Where applicable, solid shells are preferred over solids due to their lower computational cost.

The tube constraint has an impact on the axial stress and strain profiles of the elastic tube material, as presented and discussed in this study. The simulation results also show the effect of the tube materials, tube constraints and fluid properties, which are not readily available from theoretical studies.

Importantly, it can be concluded that the solution methodology presented here is suitable for the simulation of a peristaltic mixing experiment that forms the subject of the next chapter.

Chapter 5. FSI Simulation of An In Vitro Gastric Digestion Model

The modelling in this Chapter uses the unpublished experimental data of Chao Zhong, a PhD student working under the supervision of Prof. Tim Langrish at The University of Sydney. The experiments were developed and refined during the course of this thesis, as data were regularly shared and discussed between the experimental and modelling teams.

5.1. Introduction

The flow motion inside our digestion system is very complicated due to the complex geometry and gastric motility. Researchers have been using human or animal models to conduct *in vivo* studies, which are invasive and require difficult ethical approval [168, 169]. Apart from *in vivo* studies, many *in vitro* stomach models have also been developed to understand the complex digestion process [170-175]. Compared with *in vivo* models, *in vitro* experiments are easier to perform, more controllable, and more factors can be taken into consideration. However, the limitations of *in vitro* experiments lie in visualizing the flow pattern and understanding the mechanisms. In the past two decades, computational techniques have been introduced to model the gastric digestion process. Several *in silico* models have been developed to study the fluid mechanisms in the stomach as mentioned in Chapter 2. With the use of *in silico* models, the fluid flow can be visualized easily. They can also be used to optimize the experimental design based on the simulation results.

In this study, a new approach is proposed using Fluid-Structure Interaction (FSI) to study the interaction between the fluid flow and the structural change in a digestion mixing system. The computational model is built based on a real *in vitro* intestinal peristalsis model made of a deforming transparent elastic material. Dye is injected into the experiment to explore the mixing behaviour. During the peristaltic motion, the location of the dye is tracked and compared in both models.

5.2. In vitro model setup

The *in vitro* model consists of an elastic, semi-transparent and deformable chamber that is made of thermoplastic polyurethane (TPU). Four pistons are used to compress the chamber, mimicking the peristaltic motion. The experimental setup is shown in Figure 5.1. Fluorescein dye is injected into the chamber from a long vertical tube at the left.
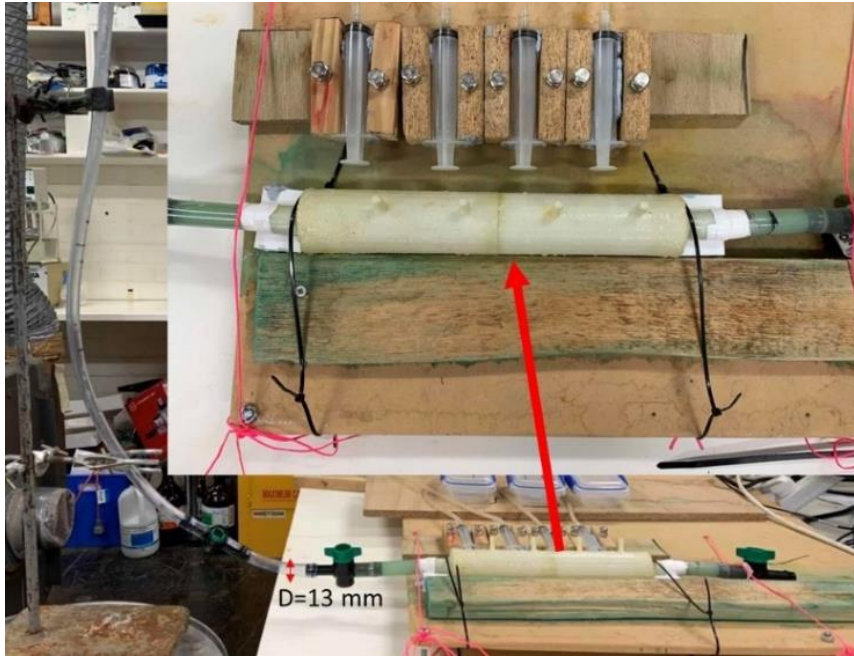
Figure 5.1: Experimental setup for the intestinal peristalsis system (courtesy of Chao Zhong).

After the dye is injected, it moved along the elastic tube as the pistons compressed the chamber. In the experiment, the transportation of the dye is recorded via the fluorescein concentration and image colour analysis. The location of the dye is captured by the camera for the visualisation setup shown in Figure 5.2. The colour at five points along the centreline of the tube are recorded and converted to dye concentration by image analysis and colour calibration.
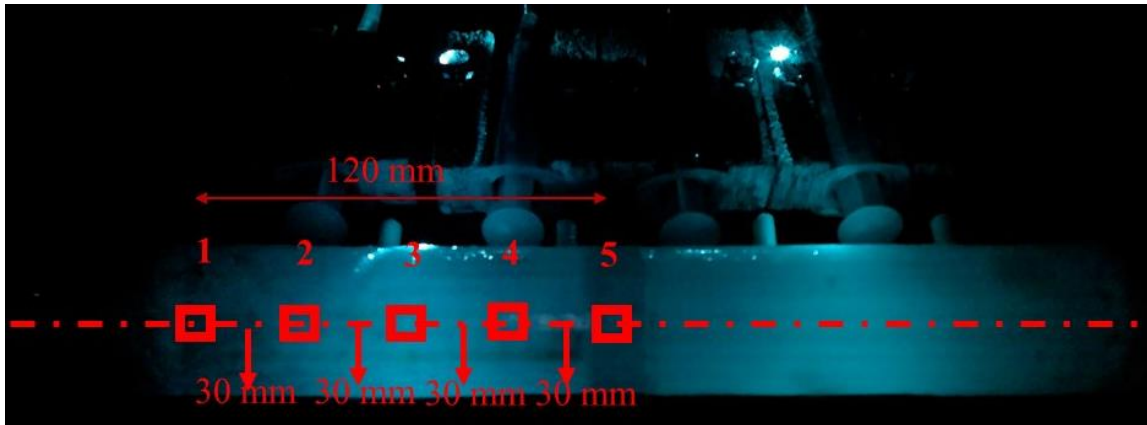
Figure 5.2: Dye visualization setup in the experiment (courtesy of Chao Zhong).

5.3. Numerical model setup

The FSI analysis in this study is performed using Ansys System Coupling 2022R1. The fluid dynamics analysis is conducted using Ansys Fluent, version 2022R1, using the finite volume

method (FVM). The transient structural analysis is developed using Ansys Mechanical, version 2022R1, using the finite element method (FEM). During the simulation, the Fluent and Mechanical solvers run simultaneously while data at the interface are transferred between them via System Coupling 2022R1. A flowchart of the FSI analysis is shown in Figure 5.3 below.
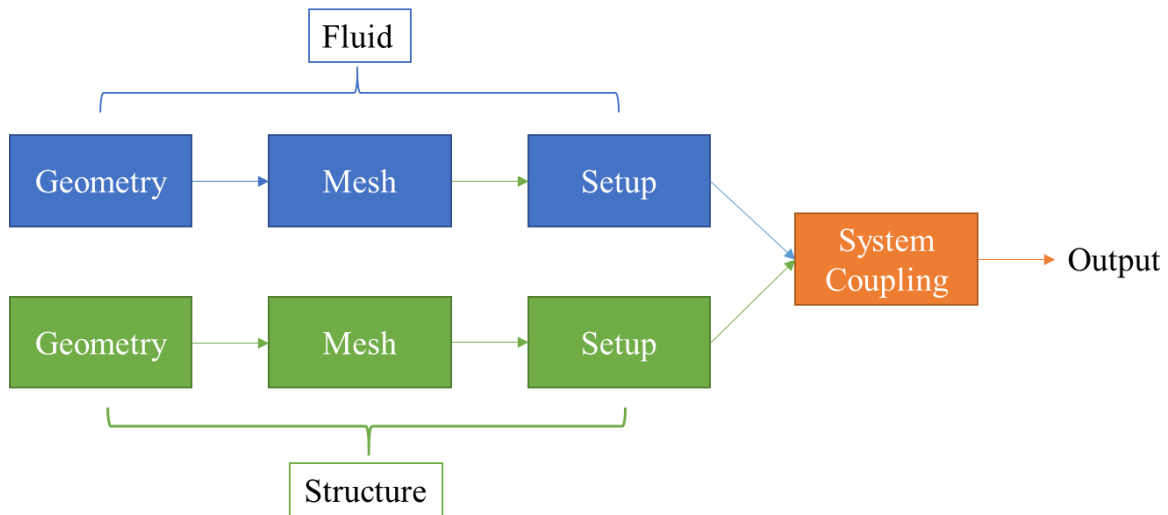
Figure 5.3: Flowchart of the FSI analysis.

5.3.1. Fluid model

The fluid model is set up via the following steps: constructing the fluid geometry, generating the mesh, defining the boundary conditions and initial dye region, setting up the system coupling region, and choosing the solver.

Geometry

Ansys SpaceClaim is used to construct the fluid domain, containing the main mixing chamber and a riser tube. The riser tube contains a vertical part and a 90° bend connected to the chamber. In the experiment, a smaller tube inside the riser tube is used to inject the dye into the system. The location of the small inner tube is fixed using 3D-printed supports. The fluid flow domain and the 3D-printed support geometries are shown in Figure 5.4.

(a) front view

(b) cross-sectional view
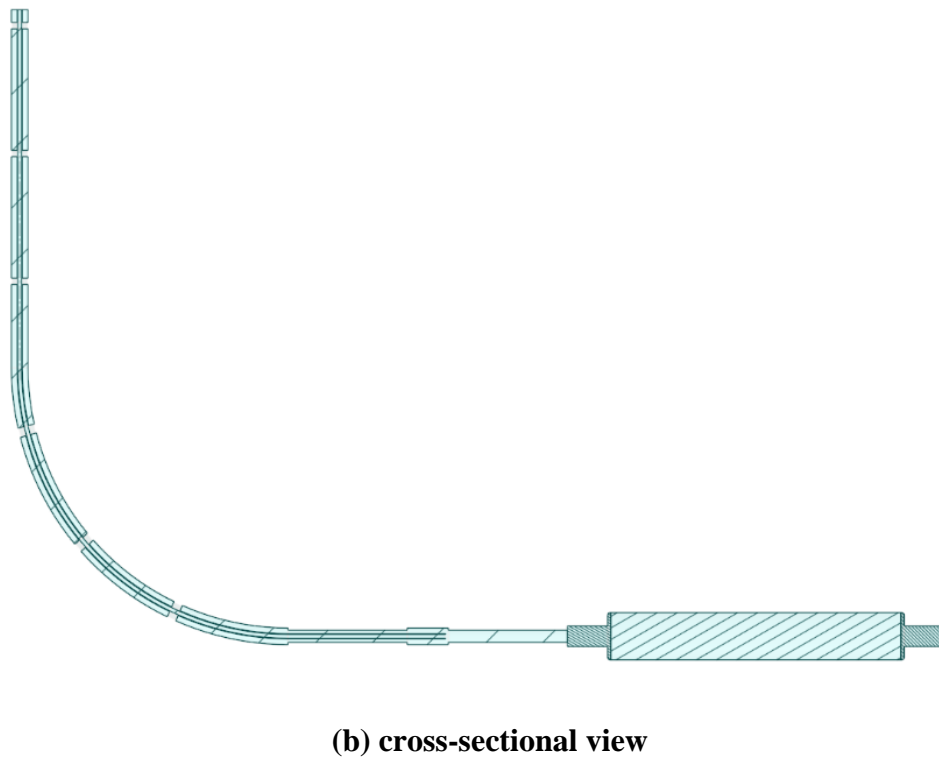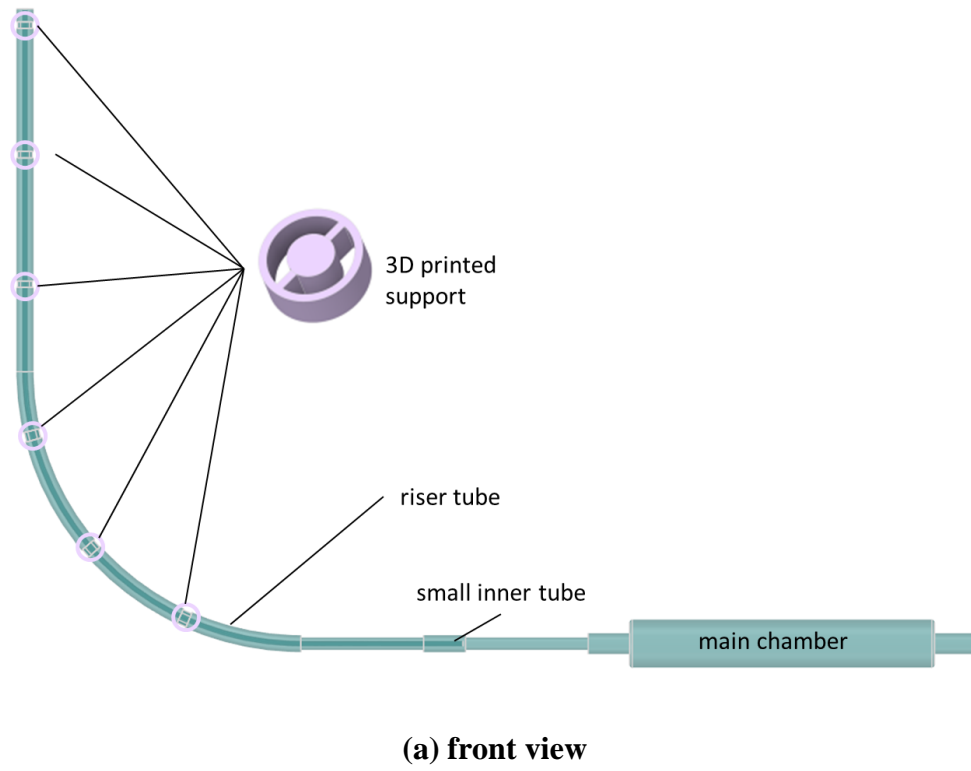
Figure 5.4: Fluid flow geometry.

Computational Mesh

Ansys Fluent Watertight Geometry meshing template is used to generate the mesh in the fluid region. It has 930,000 cells with a minimum orthogonal quality of 0.25. It comprised tetrahedral elements with inflation at the wall. The mesh sizing is chosen based on test cases conducted previously.
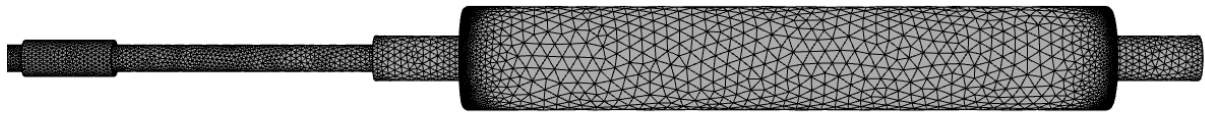
Figure 5.5: Computational mesh on the fluid domain.

Model description

The transient, pressure-based solver is used to solve for turbulent flow. The Reynolds number is around 3,000 (see later), which means it is a turbulent flow, but the Reynolds number is low, lying within the laminar-turbulent transition regime. The SST k-ω model [176] is used to simulate the turbulent flow as it behaves well even at lower Reynolds numbers because of its ability to integrate to the wall.

Conservation and closure equations

The conservation equations for mass, momentum and species transport are listed below. Compressible flow equations are solved so that artificial compressibility can be used to make the solution more stable, as observed by La Spina [177], and was found to be especially important here when high pressures develop during convergence (see later).

Conservation of mass for a compressible fluid flow gives:

$$\frac{\partial \rho}{\partial t} + \nabla \cdot \rho(\boldsymbol{u} - \boldsymbol{u}_g) = \boldsymbol{0} \tag{5.1}$$

where ρ is the fluid density, t is time, $\boldsymbol{u}$ is the fluid velocity, and $\boldsymbol{u}_g$ is the velocity of the moving mesh.

The Tait equation of state is used to represent compressible liquids in Ansys Fluent. A nonlinear relationship between liquid density and pressure under isothermal conditions is applied:

$$\left(\frac{\rho}{\rho_0}\right)^n = \frac{K}{K_0} \tag{5.2}$$

where ρ_0 is the reference liquid density, n is the density exponent, K_0 is the reference bulk modulus, K is the bulk modulus at pressure, P, and is equal to

$$K = K_0 + n\Delta P \tag{5.3}$$

where

$$\Delta P = P - P_0 \tag{5.4}$$

The density ratio is limited to a range:

$$\rho_{r,\min} < \frac{\rho}{\rho_0} < \rho_{r,\max} \tag{5.5}$$

where $\rho_{r,\min}$ is the minimum density ratio limit, and $\rho_{r,\max}$ is the maximum density ratio limit.

Conservation of momentum gives:

$$\frac{\partial(\rho \boldsymbol{u})}{\partial t} + \nabla \cdot \left(\rho\big(\boldsymbol{u} - \boldsymbol{u}_g\big) \otimes \boldsymbol{u}\right) = -\nabla P + \nabla \cdot \mu_{\text{eff}}(\nabla \boldsymbol{u} + \nabla \boldsymbol{u}^T) \tag{5.6}$$

where μ_{eff} is the sum of the laminar and turbulent dynamic viscosities.

The transport equations for the turbulence kinetic energy (k) and the turbulence eddy frequency (ω) are [176]:

$$\frac{\partial}{\partial t}(\rho k) + \nabla.\big(\rho(\boldsymbol{u} - \boldsymbol{u}_g)k\big) = \nabla.\left[\left(\mu + \frac{\mu_t}{\sigma_{k1}}\right)\nabla k\right] + P_k - \beta^* \rho k \omega \tag{5.7}$$

$$\frac{\partial}{\partial t}(\rho\omega) + \nabla.\big(\rho\left(\boldsymbol{u} - \boldsymbol{u}_g\right)\omega\big) =$$
$$\nabla.\left[\left(\mu + \frac{\mu_t}{\sigma_{\omega 1}}\right)\nabla\omega\right] + (1 - F_1)2\rho\frac{1}{\sigma_{\omega 2}\omega}\nabla k.\nabla\omega + \alpha_1\frac{\omega}{k}P_k - \beta_i \rho\omega^2 \tag{5.8}$$

where $\sigma_{k1} = 1.176$, $\beta^* = 0.09$, $\sigma_{\omega 1} = 2.0$, $\sigma_{\omega 2} = 1.168$, $\alpha_1 = 0.52$ and $\beta_i = 0.075$.

The turbulence production rate (P_k) is given by:

$$P_k = \mu_t \nabla \boldsymbol{u}.(\nabla \boldsymbol{u} + \nabla \boldsymbol{u}^T) \tag{5.9}$$

The blending function, F_1, is a function of both the near-wall distance and the local values of k and ω;

$$F_1 = \tanh(\Phi_1^4) \tag{5.10}$$

where

110

$$\Phi_1 = \min\left(\max\left(\frac{\sqrt{k}}{\beta'\omega y}, \frac{500\nu}{y^2\omega}\right), \frac{4\rho k}{CD_{k\omega}\sigma_{\omega2}y^2}\right) \quad (5.11)$$

y is the near-wall distance, ν the kinematic viscosity, and

$$CD_{k\omega} = \max\left(2\rho\frac{1}{\sigma_{\omega2}\omega}\frac{\partial k}{\partial x_j}\frac{\partial \omega}{\partial x_j}, 1.0 \times 10^{-10}\right) \quad (5.12)$$

F_1 is expected to be 1.0 inside the boundary layer and zero outside. A second blending function, F_2, is used to explicitly limit the eddy viscosity inside the boundary layer (μ_t) [176]

$$\mu_t = \frac{\alpha_1\rho k}{\max(\alpha_1\omega, SF_2)} \quad (5.13)$$

where α_1 is a constant, set to be 0.31. S is the magnitude of the shear strain rate.

The second blending function is given by;

$$F_2 = \tanh(\Phi_2^2) \quad (5.14)$$

where

$$\Phi_2 = \max\left(\frac{2\sqrt{k}}{\beta'\omega y}, \frac{500\nu}{y^2\omega}\right) \quad (5.15)$$

Conservation of species mass gives:

$$\frac{\partial(\rho Y_{\text{dye}})}{\partial t} + \nabla \cdot \left(\rho(\boldsymbol{u} - \boldsymbol{u}_g)Y_{\text{dye}}\right) = \nabla \cdot \left(\rho D_{\text{eff}}\nabla Y_{\text{dye}}\right) \quad (5.16)$$

where Y_{dye} is the mass fraction for the dye species, and D_{eff} is the effective diffusion coefficient, given by:

$$D_{\text{eff}} = D + \frac{\mu_t}{\rho\sigma_Y} \quad (5.17)$$

where the turbulent Schmidt number is set to the default value of 0.7.

Model setup

The compressible liquid has a reference density (ρ_0) of 1000 kg/m³, a reference bulk modulus (K) of 100 kPa, a density exponent (n) of 1, and a density ratio limit of 0.9 ($\rho_{r,min}$) to 1.1 ($\rho_{r,max}$). It means that the density of the liquid (ρ) can vary from 990 to 1100 kg/m³. The

species transport model is selected to simulate the mixing between the water and fluorescein solution (dye). Water and dye are assumed to have the same properties. The species diffusion coefficient (D) is set to 4.2×10^{-10} m^2/s. All walls are set to have no slip and no flux of dye. The boundary that is open to the atmosphere is set as a pressure opening (static pressure of 0 Pa).

A dynamic mesh model is activated to specify the system coupling zone. The diffusion-based smoothing method is chosen so that the boundary motion can diffuse uniformly throughout the interior mesh, which are deformed smoothly to maintain a high quality [142]. The deforming boundary cells are remeshed when the cell skewness is higher than 0.9. The region coloured in red in Figure 5.6 is set as a system coupling zone, which transfers data to and from the structural model.
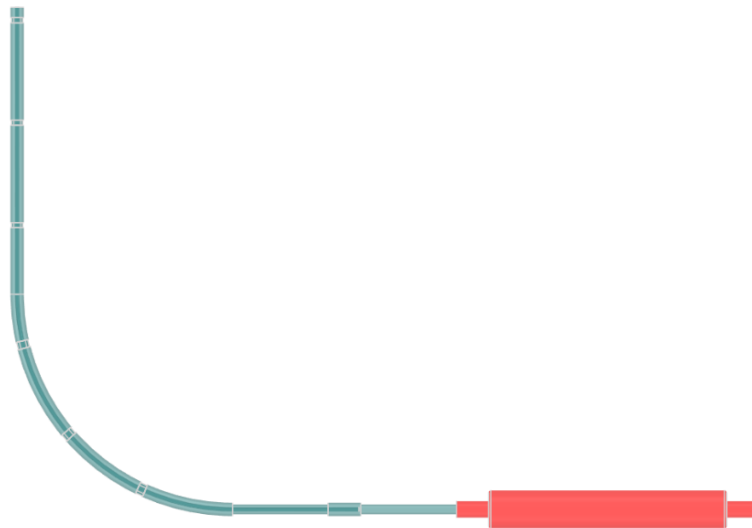
Figure 5.6: Coupling wall region for the fluid domain, shown in red.

To set up the initial condition, the fluid domain is filled with water. Then a small region is patched with the dye, as shown in Figure 5.7. The regions in blue colour represent water, while the region in red colour represents dye. The initial dye concentration is 0.3 g/L with a total mass of 1.9 mg.
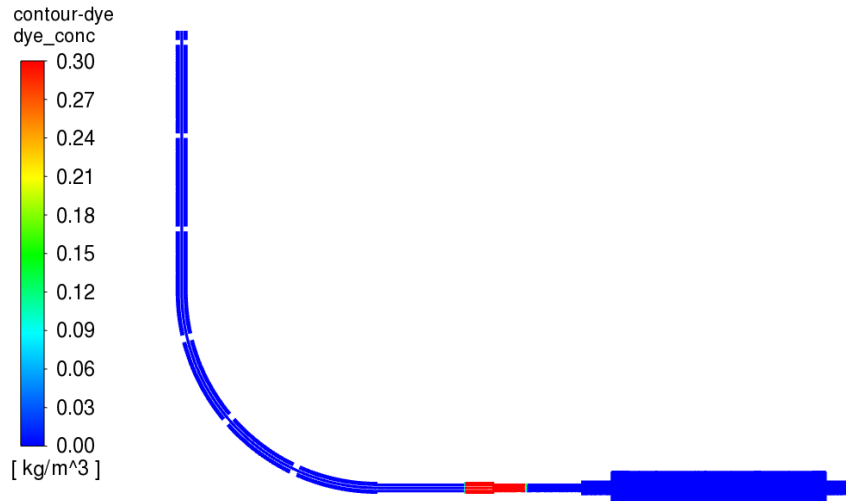
Figure 5.7: Initial dye region, with the dye shown in red.

To record the dye concentration, five locations along the centreline of the tube are selected. In the experiment, the dye concentration at each location is measured through colour calibration. The TPU material used is not fully transparent and the clear colour observation range is tested to be 10 mm from the surface. Therefore, in the simulation, a line is drawn into the flow from each visualisation point. The average dye concentration along the entire line and 10 mm from the surface, as shown in Figure 5.8, are recorded every 0.1 s to accommodate the uncertainty in the experimental observation window.

(a)

(b)
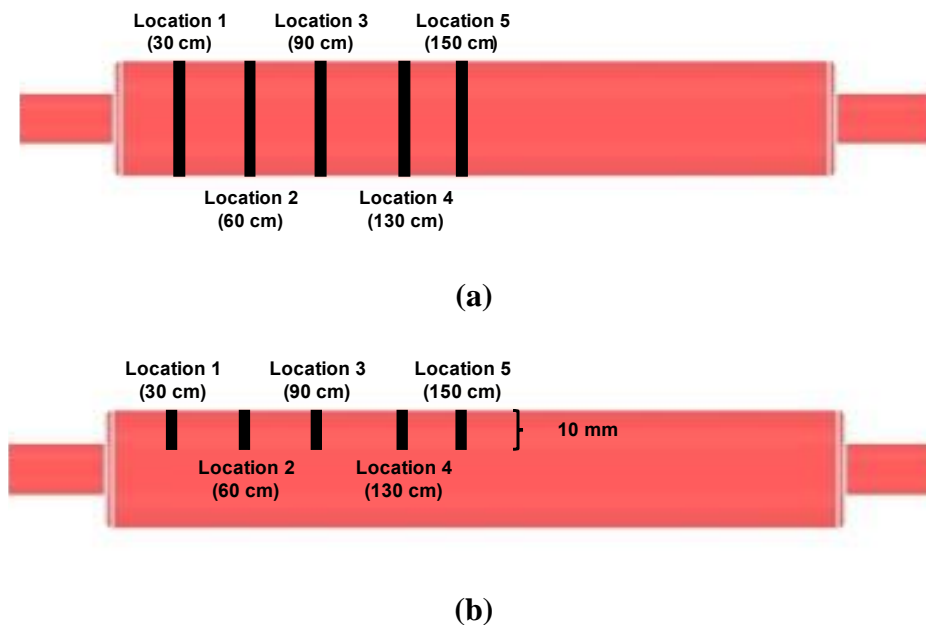
Figure 5.8: Monitors used to record dye concentrations

(a) average over the entire line; (b) average over 10 mm from the surface.

Solution method

The PISO pressure-velocity coupled scheme is used to solve the equations and the first-order implicit transient formulation. Gradients are determined using the least-squares cell-based option, the pressure is determined using the second-order method. The first-order upwind scheme is used for the density and turbulence variables. The second-order upwind scheme is used for the momentum equations and the dye concentration.

Converged solutions are achieved when residual values for the continuity, x, y, z velocities, turbulence quantities and dye mass fraction are below 10^{-3}. The residual values are calculated based on the globally scaled Root Mean Square (RMS) value of the error vector. The maximum iteration number for each coupling step was set to 50, while usually 20 were needed for convergence.

5.3.2. Structural model

The first step of setting up the mechanical model is to define the material properties of the bodies. Connections are defined between the deformable body, supporting body, and pistons. The deformable body is then divided into a finite number of elements through meshing. After setting up loads and support, the analysis is made using the FEA solver.

Geometry

Ansys SpaceClaim is used to construct the structural domain. It is composed of three parts: the main body where the peristaltic motion occurred, four pistons that are used to compress the main body, and the supporting structure. The structural geometry is shown in Figure 5.9. The main body (coloured in green) is deformable. Both the pistons (coloured in purple) and the supporting body (coloured in pink) are treated as rigid bodies.

(a)

(b)
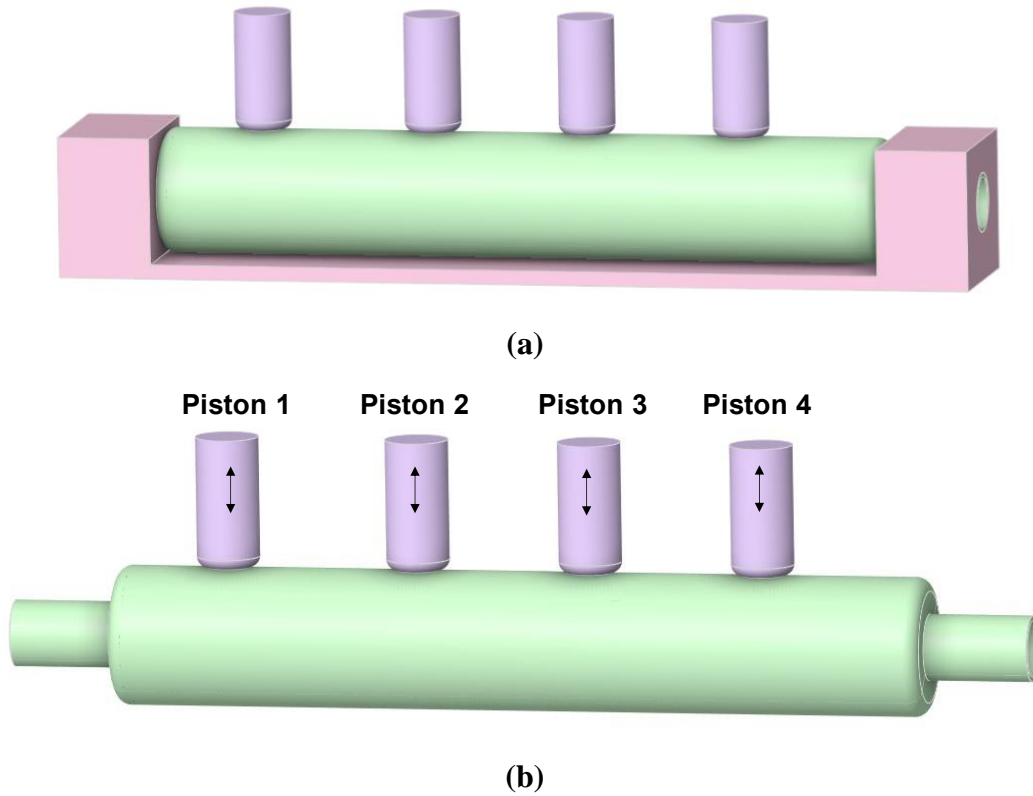
Figure 5.9: Geometry of the structure

(a) with the supporting body (b) without the supporting body.

Material

Thermoplastic Polyurethane (TPU) is used to construct the deforming body of the model. Based on the results from mechanical testing by the experimentalists, the Young's modulus and Poisson's ratio of the material are set to 15.5 MPa and 0.45, respectively.

Connections

The main body of the system can be easily deformed by the pistons due to the elasticity of the TPU material. To hold the main body in place, it is crucial to define the connections between the main body and its nearby bodies properly. The connections between the main body and the pistons are defined as frictional with a frictional coefficient of 0, meaning that the contact surfaces can slide and separate without resistance. To hold the main body in place, the connections between the main body and the supporting bodies are set to be frictional with a frictional coefficient of 0.05. Both ends of the deforming geometry are constrained to avoid movement outside of the supporting body. These connections are summarized in Figure 5.10.
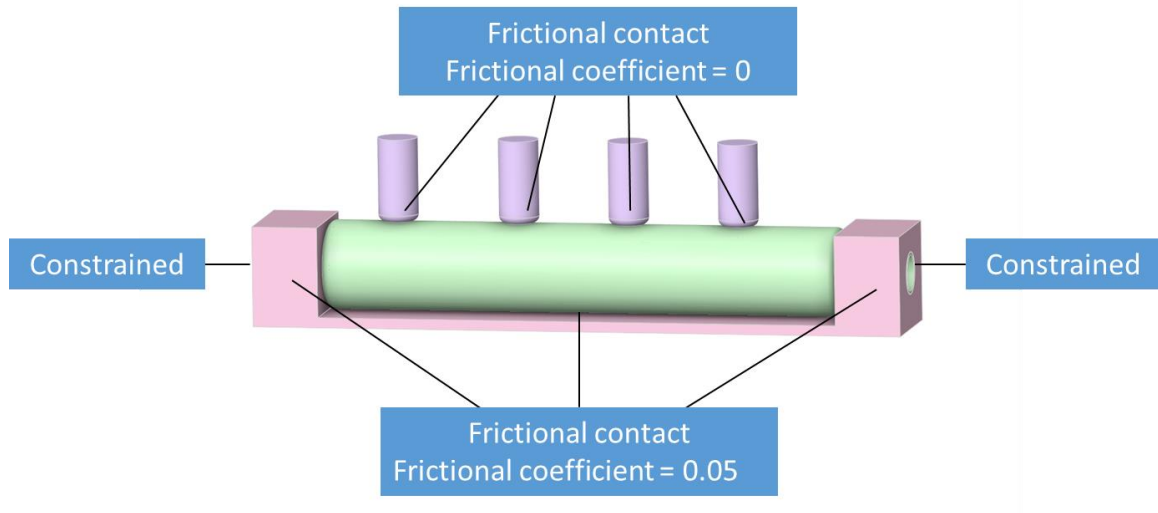
Figure 5.10: Connections between the main body and its nearby bodies.

Augmented Lagrange and nodal detection methods are used for all contacts. Augmented Lagrange is a penalty-based formulation that follows the equation below

$$F_{normal} = k_{normal}x_{penetration} + \lambda \qquad (5.18)$$

where F_{normal} is the finite contact force, k_{normal} is the contact stiffness, $x_{penetration}$ is the penetration distance, and λ is an additional term that makes the force less sensitive to the contact stiffness. The normal stiffness factor is chosen to be 0.01 N/m in this model to ease the convergence difficulties.

Mesh

Virtual topology and body splitting are utilized before mesh generation, as shown in Figure 5.11. This approach allows for better mesh control so that the solid can be split into hexahedral elements which are preferred over tetrahedral elements in FEA.
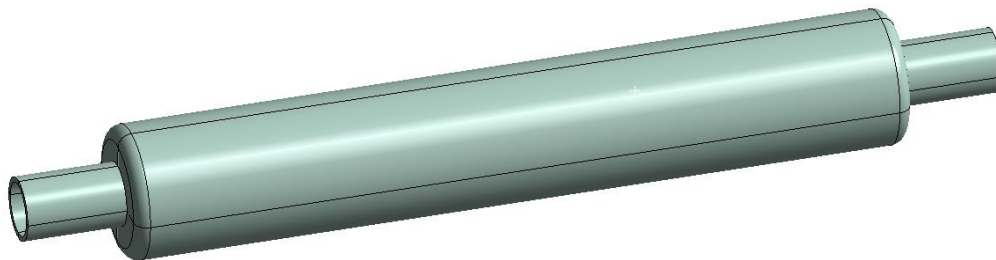
Figure 5.11: Virtual topology and body splitting applied to form the faces.

Ansys Mechanical meshing is used to generate the mesh of the structure. Eight multizone mesh regions are defined following the virtual faces. The whole body is mapped with 4,100

hexahedral elements, with a maximum skewness of 0.87. It is evident in Figure 5.12 that a high-quality mesh has been produced.
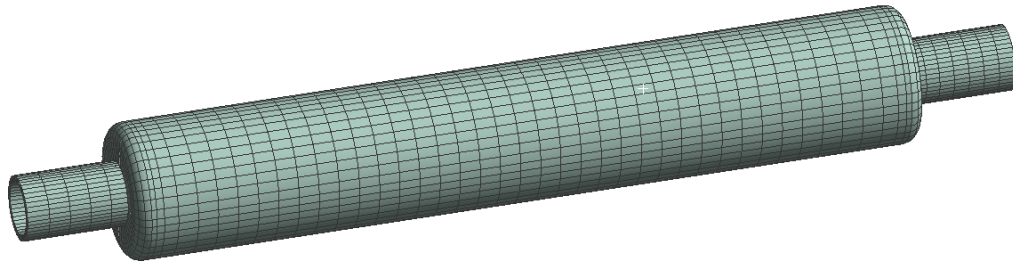
Figure 5.12: Mesh of the structural model.

Equation of motion

The behaviour of a linear elastic solid is given by the equation of motion (equation 4.21) presented previously in Chapter 4.

Setup

Remote displacements are placed on the pistons to simulate their movement. The compression distance of each piston is extracted from the experimental data, shown in Figure 5.13.
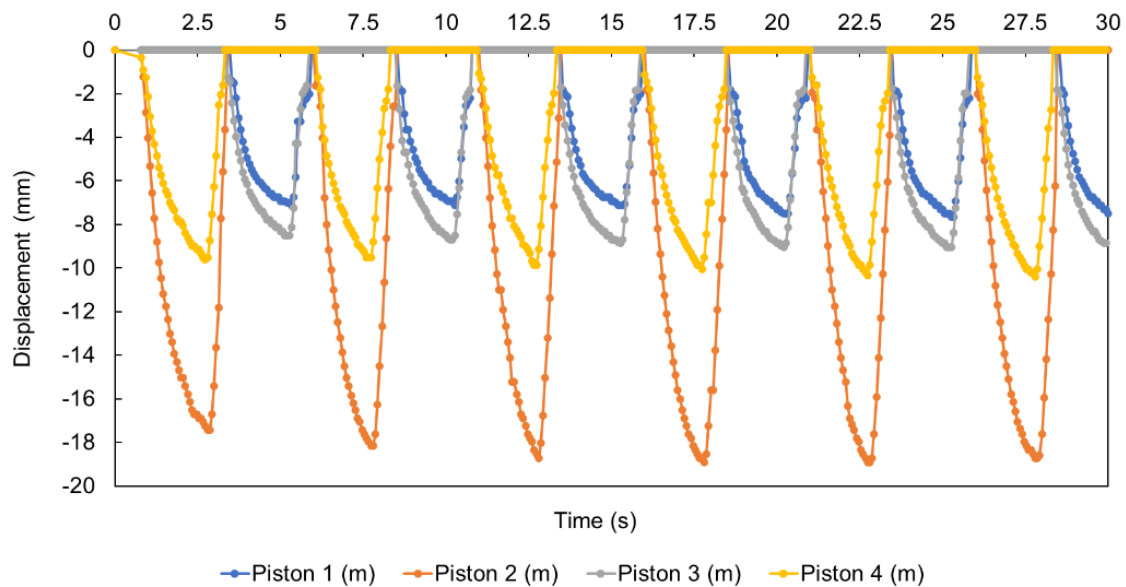
Figure 5.13: Displacement distance of the pistons from the experiment.

The displacement data are modified before being used in the simulation. After trial and error, it was found that the coupling simulation became unstable and required a much smaller timestep when no piston was contacting the main body. For the first 0.8 s, no piston is contacting with the main body in the experiment and is therefore not simulated, assuming no

dye is diffused without piston movement. The number of time points used is also reduced in the simulation to make the data smoother. The solver is able to interpolate the displacement according to the timestep. However, the critical time points are retained to capture the movement of the pistons. The modified temporal displacement of the pistons is shown in Figure 5.14.
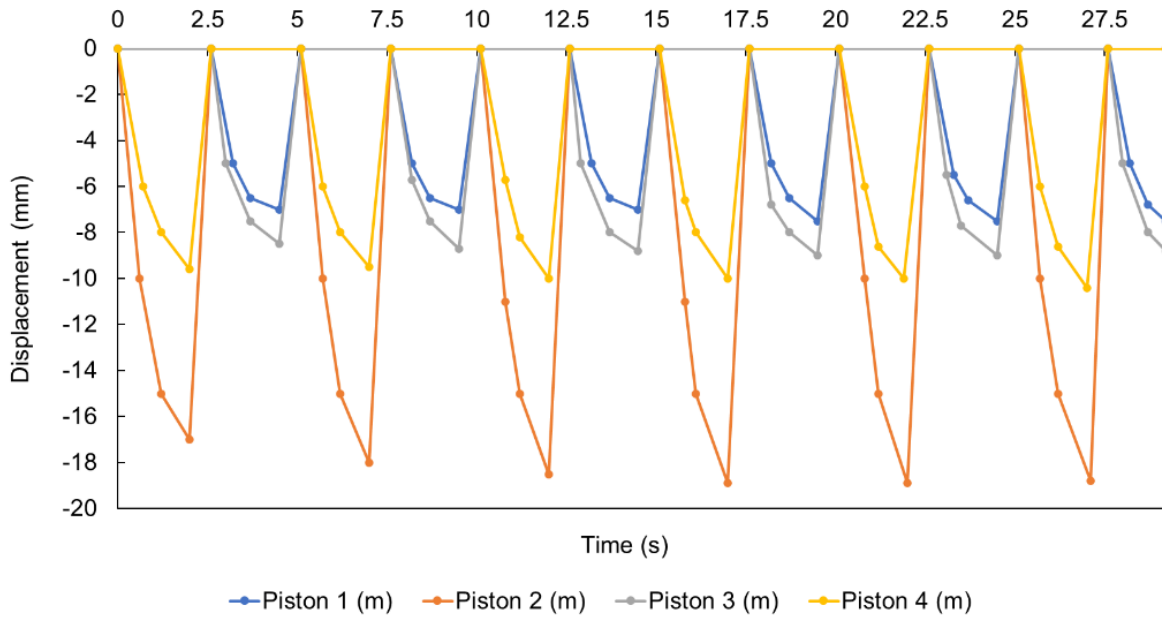
Figure 5.14: Displacement distance of the pistons used in the simulation.

After modification, the total simulation time is 29.2 s. There are six cycles of data, around 5 s for each cycle. In the first cycle (0 – 5.1 s), pistons 2 and 4 started to compress the tube at 0 s, reaching the maximum displacement at 2 s, 9.6 mm for piston 2 and 17.0 mm for piston 4. Both pistons then gradually returned to their original positions. At 2.6 s, pistons 2 and 4 stopped contacting the deformable body while pistons 1 and 3 started to compress the body. At 4.5 s, both pistons reached their maximum distances of 7.0 mm and 8.5 mm, respectively. The first cycle finished at 5.1 s when all the pistons returned to their original state. In the next five cycles, the duration and maximum displacement are slightly different but followed the same trend as the first cycle. The maximum displacement of the pistons during the entire run is 18.8 mm, around half of the tube diameter.

A system coupling zone is defined in the structural model. The region coloured yellow in Figure 5.15 is defined as the fluid-solid interface which exchanges data with the fluid model via System Coupling.

118
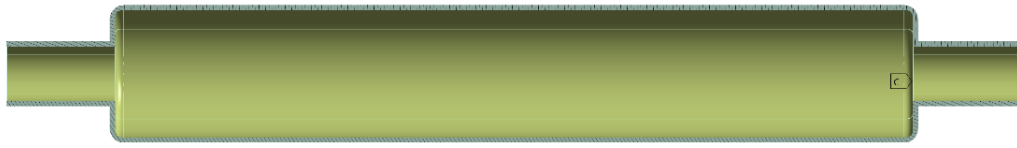
Figure 5.15: System coupling region of the structure.

The direct solver is used to determine the structural deformation, with large deflection activated to accommodate the expected bending behaviour of the deformable body.

5.3.3. System Coupling

System Coupling, version 2022R1 is used to couple the fluid and structure interfaces. The simulation starts with the motion of the pistons on the deformable body.
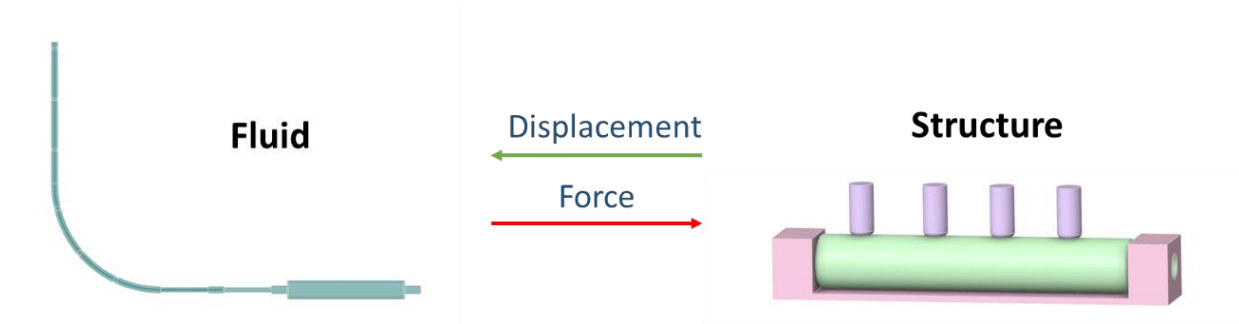
Figure 5.16: System coupling analysis data transfer between fluid and structural models.

Setup

The timestep setup for the FSI model is controlled in the System Coupling setting. With a timestep size of 0.1 s, the simulation ran for 292 steps, giving a total simulation time of 29.2 s. The maximum iteration number for each time step was set to 10, while usually 6 were needed for convergence. Quasi-Newton stabilization is activated for data transfer, with an initial relaxation factor of 0.05 and one retained timestep in the Quasi-Newton history. Data transfers at the interface converged when the globally scaled RMS of the residual values are below 0.01. Twelve cores of a computer having an *Intel(R) Xeon Bronze 3204, @1.90 GHz* processor and 64 GB RAM are used to run the model. Fluent and Mechanical are allocated five and seven cores, respectively. An NVIDIA Quadro RTX 6000 graphic card (GPU) is utilized to accelerate the structural simulation process. The total simulation time for the FSI analysis is 88 hrs running on the above machine, with Fluent using 38 hrs and Mechanical using 50 hrs.

5.3.4. Convergence study

The residual plots from the simulation model are presented to demonstrate the convergence of the coupled solution. The values over the first second are representative of the entire simulation. Figure 5.17 shows the residual history from the FSI model from 0 s to 1 s. Convergence is achieved when the residual value of the data transfer at each interface (six in total) are all below 0.01. It is shown in Figure 5.17(a) that a total of 65 iterations are needed for 10 coupling steps and therefore an average of six iterations is needed for each step. Figures 5.17(b) and 5.17(c) show that the coupled solution is converged after each coupling step as the residual values are below 0.01.
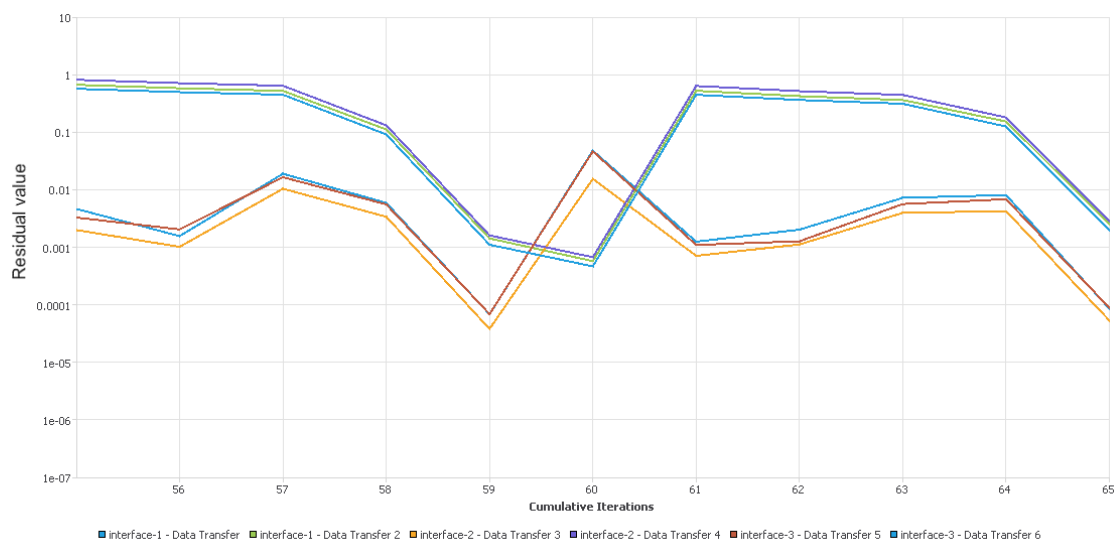
(a) iteration view (for simulation time from 0.8 s to 1 s)
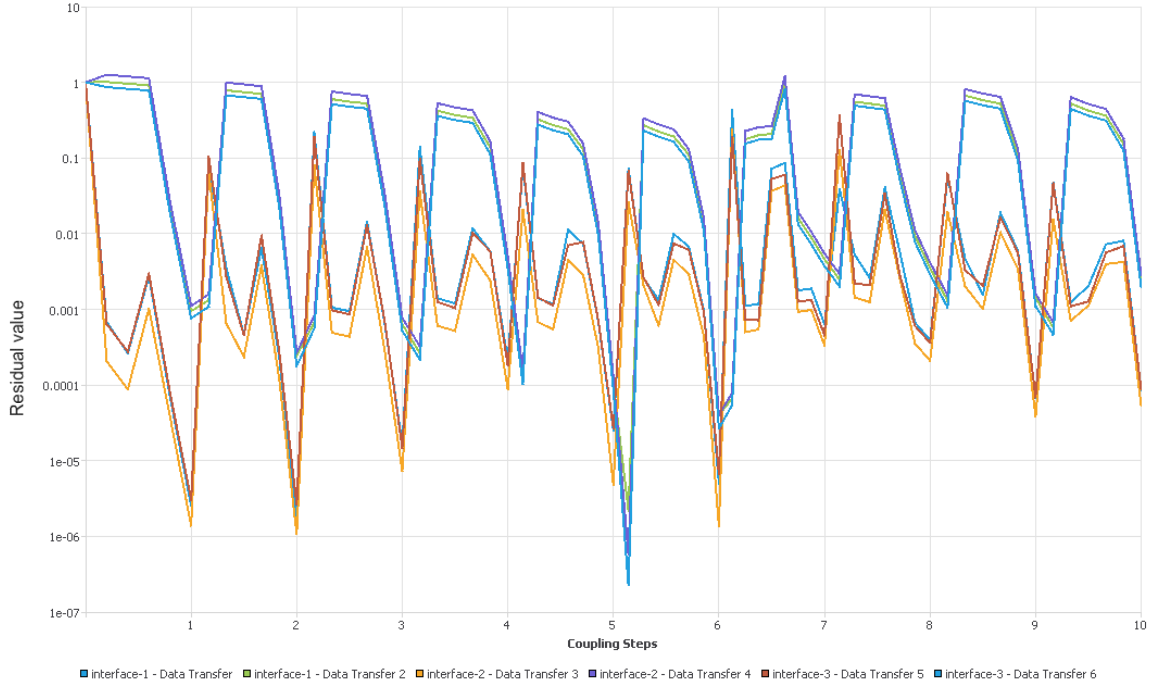
(b) coupling step count view (for simulation time from 0 s to 1 s)
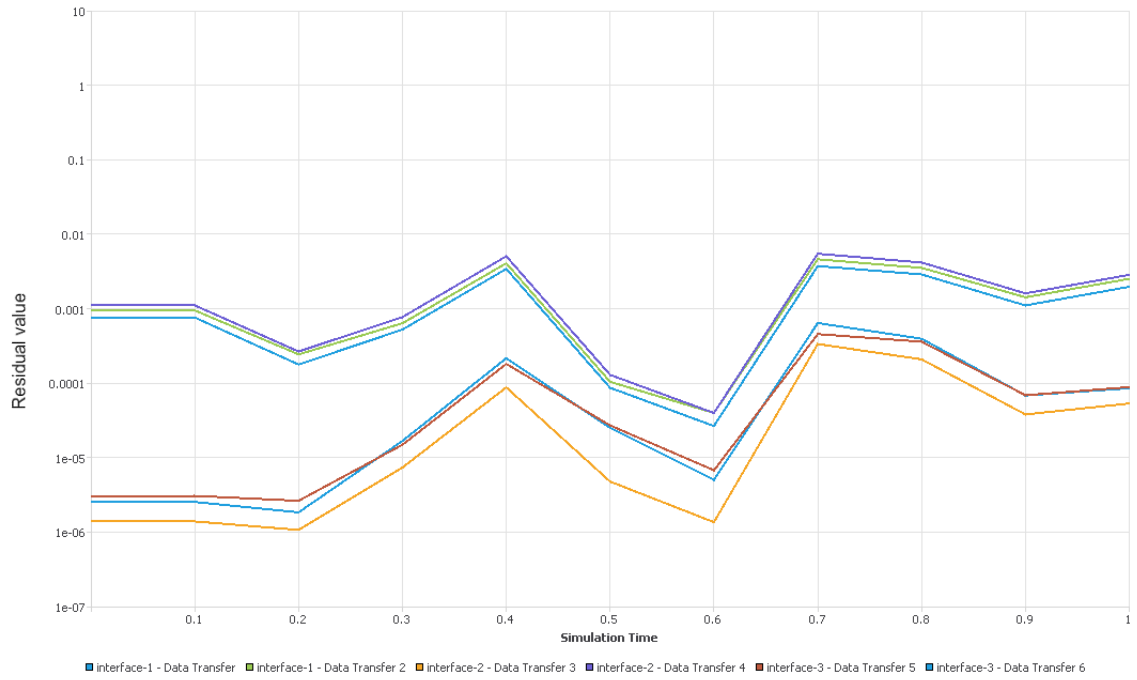
(c) simulation time view (for simulation time from 0 s to 1 s)

Figure 5.17: Residual history from the FSI model.

Figure 5.18 shows the residual history from the fluid model. 200 iterations were needed in total for a simulation time of 1 s, which means that 20 iterations were used on average for each coupling step (0.1 s). At the end of each iteration, residual values for the continuity, x, y, z velocities, turbulence quantities and dye mass fraction are below 10^{-3}.
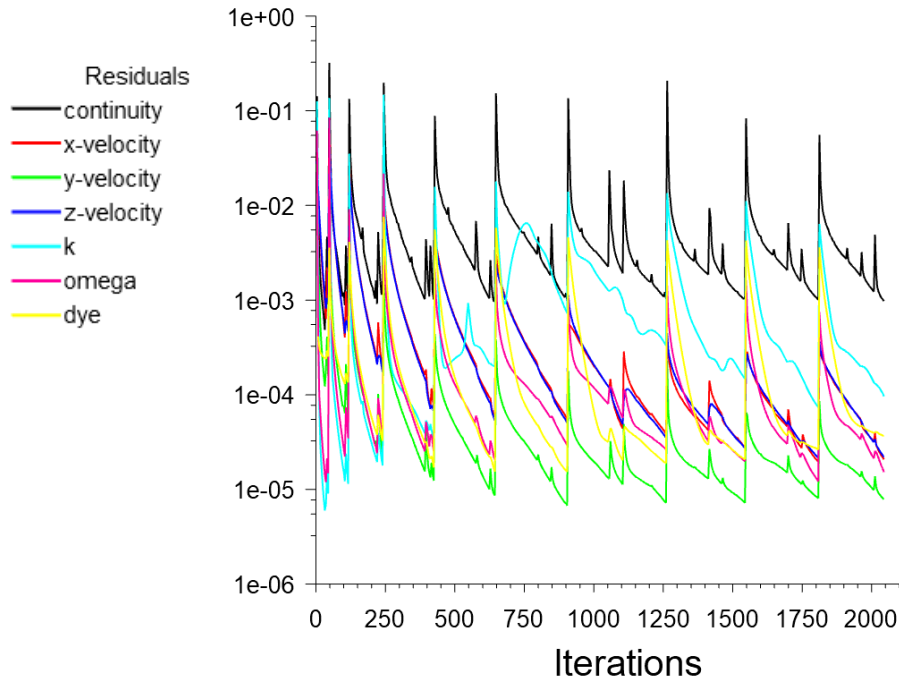
Figure 5.18: Residual history from the fluid model for simulation time from 0 s to 1 s.

The transient force acting on the coupling region is shown in Figure 5.19 with values lying in the range −0.05 - 0.01 N. It is evident that at each step the force is converging monotonically to a stable value at the end of each step.
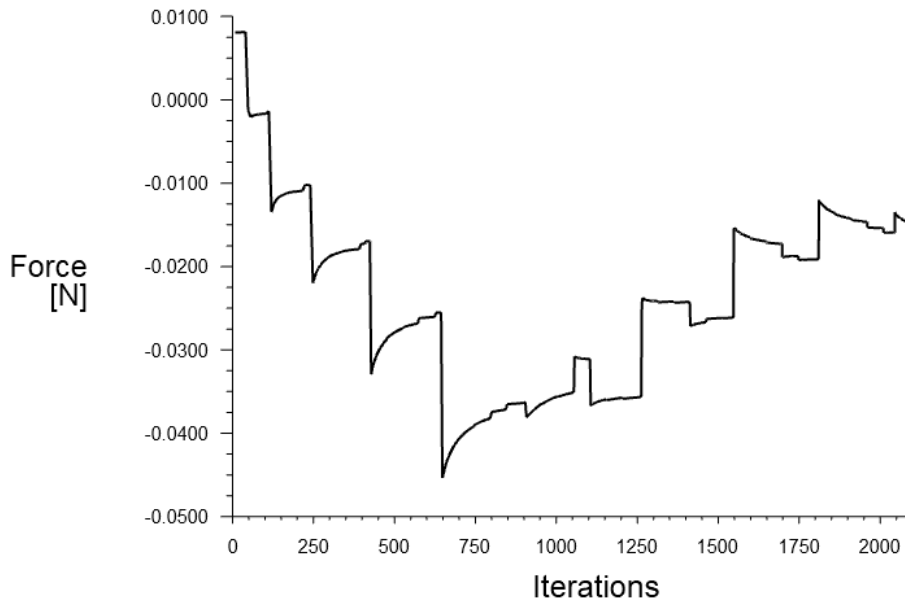
Figure 5.19: Force history from the fluid model for simulation time from 0 s to 1 s.

The above analysis shows that the coupling scheme is working as expected with both individual solvers converging, as well as the coupling process.

5.4. Simulation results

Data were extracted from the output files and plotted using Ansys EnSight 2022R1.

Dye concentration and chamber displacement

The dye flow in the fluid domain and the deformation of the main chamber in the first cycle (0 – 5.1 s) are shown every 1 s in Figure 5.20. The top images present the dye flow, and the bottom images show the deformation of the deformable body. From 0 to 2 s, pistons 2 and 4 are compressing the tube and the dye started to spread out along the riser tube. From 2 to 2.6 s, pistons 2 and 4 began to lift, causing fluid to flow back into the main chamber. After the movement of pistons 1 and 3 from 2.6 to 5.1 s, more dye spreads out in the chamber.

(0 s)

(1 s)

(2 s)

(3 s)

(4 s)

(5 s)
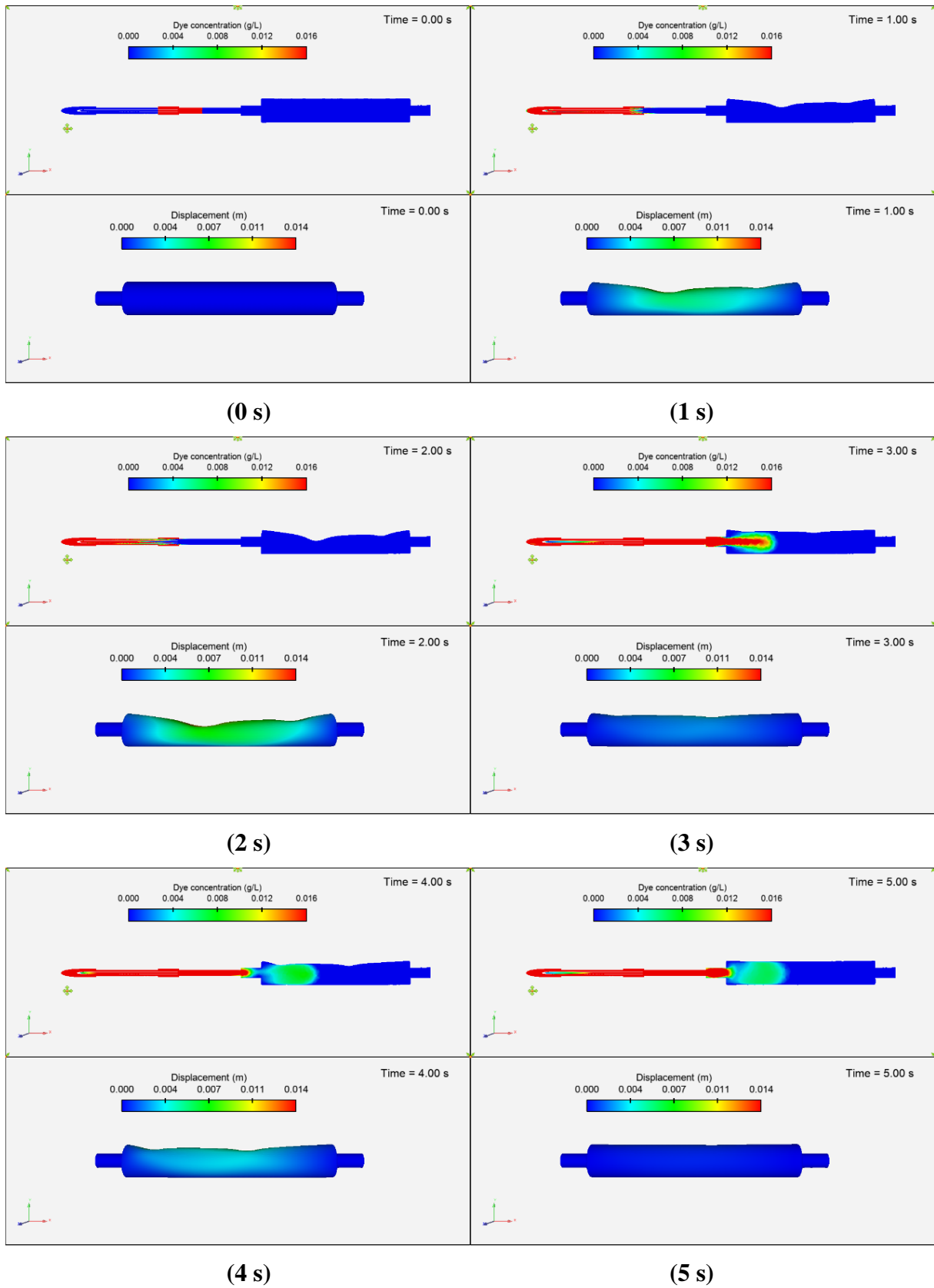
Figure 5.20: FVM predictions of dye concentration (top) and displacement on the chamber (bottom) in the first cycle.

After each cycle, more dye is pulled into the main chamber due to suction caused by decompression. Figure 5.21 shows the dye concentration at the end of each cycle. At the end of the simulation (29 s), the dye has spread to the middle of the main chamber.

(5 s)   **(10 s)**

(15 s)   **(20 s)**

(25 s)   **(29 s)**
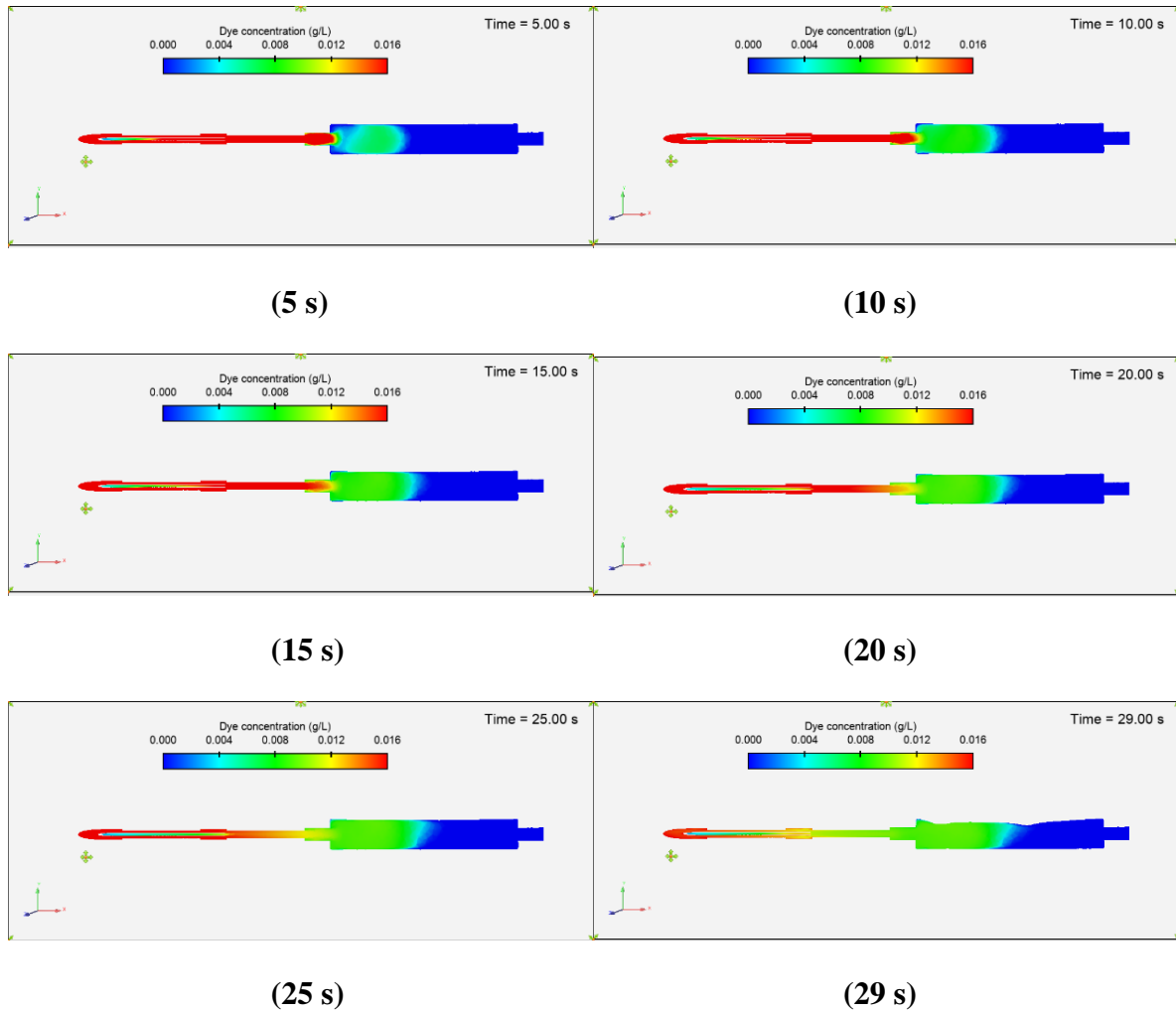
Figure 5.21: FVM predictions of dye concentration at the end of each cycle.

Fluid velocity field

Figure 5.22 shows the fluid velocity magnitude field in the first cycle. The top images show velocity contour plots, and the bottom images present the velocity vectors. The highest speed inside the chamber is around 0.1 m/s at 3 s when the pistons lifted, and flow is returning into the chamber. Most of the fluid motion occurs in the first half of the chamber and does not reach the other end.

(0 s)	**(1 s)**
(2 s)	**(3 s)**
(4 s)	**(5 s)**
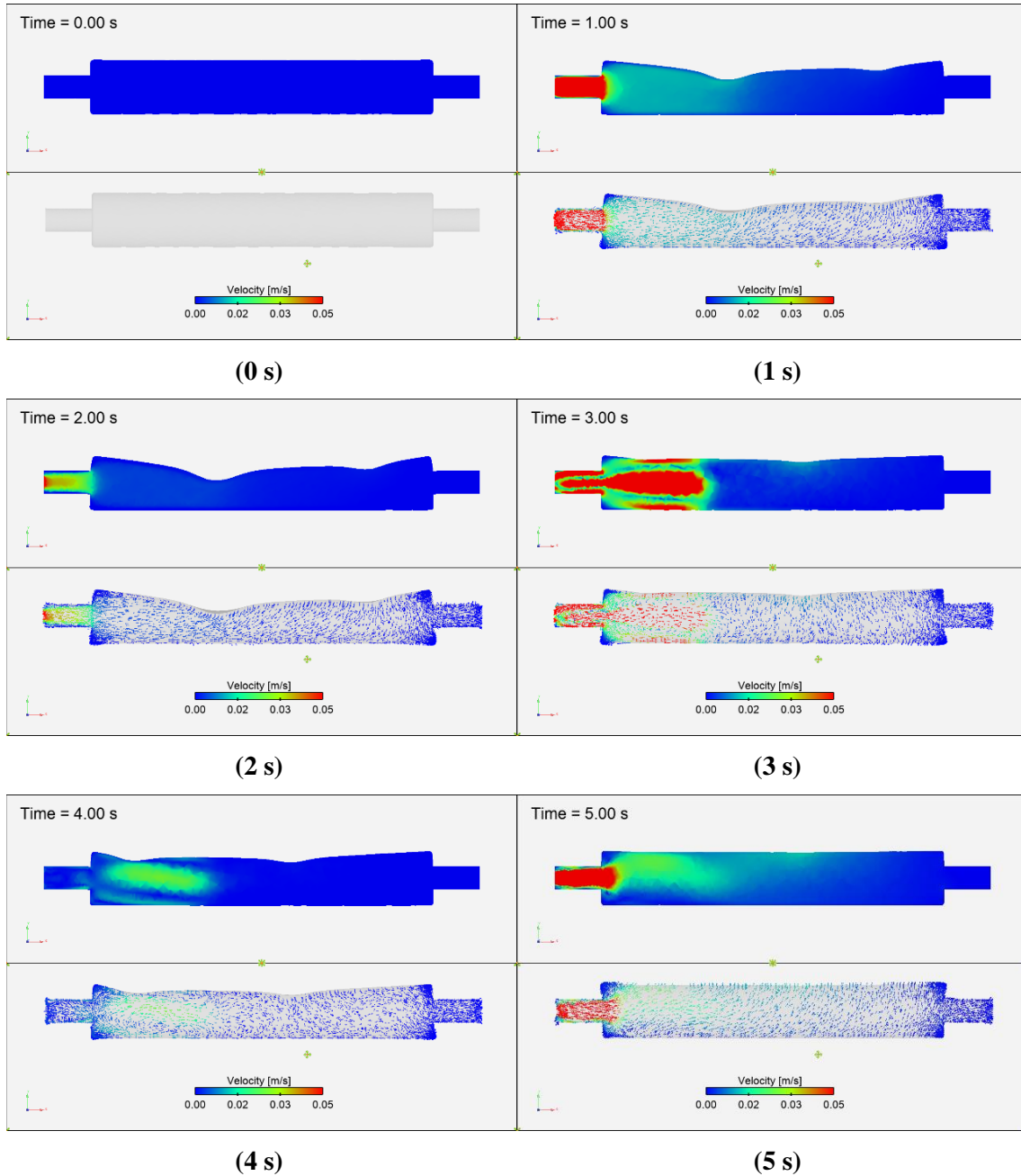
Figure 5.22: FVM predictions of the fluid velocity field in the first cycle (Top: contour; Bottom: vector).

Fluid strain rate changes

Strain rate is closely related to food disintegration and dissolution in the digestion process. It describes the velocity gradients in the fluid flow. The fluid strain rate contour plots for the first cycle are presented in Figure 5.23. The top images show the side view, and the bottom images show the contact surfaces where the pistons are compressing. The strain rate inside the flow ranges from 0 to 60 s^{-1}, which matches the strain rates in different digestion systems [4]. The

126

red colour in the figure represents values that are 60 s^{-1} or above. The values near the wall at the entry are much higher and reach up to 380 s^{-1}.
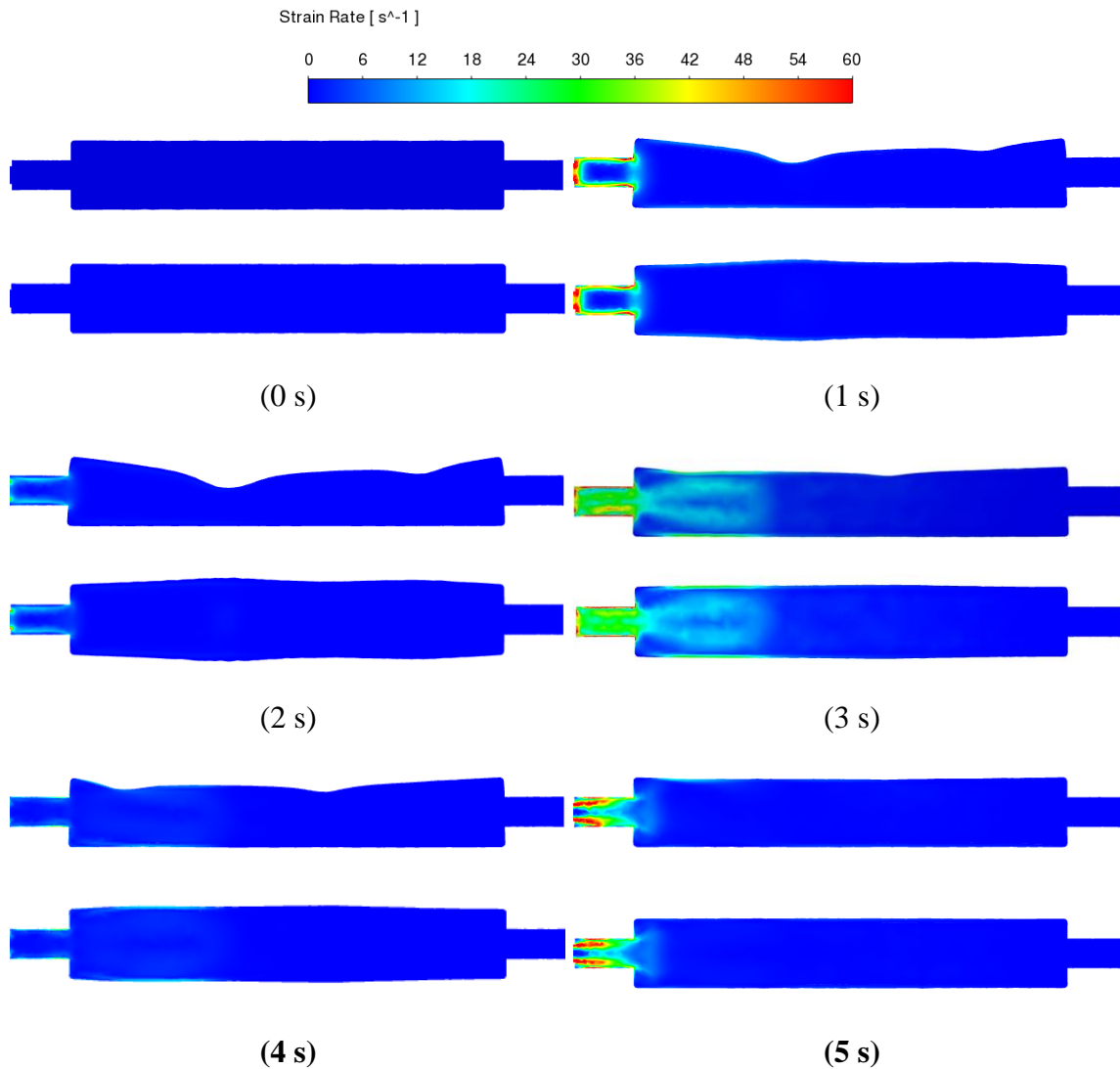
Figure 5.23: FVM predictions of strain rate changes in the fluid in the first cycle (Top: side view; Bottom: contact surface view).

Fluid density changes

A weakly compressible liquid is used to solve the fluid flow to help with convergence. The changes in fluid density at 3 s and 5 s when compression and decompression happen can be seen in Figure 5.24. The density variation is less than 1% and therefore the fluid flow is very close to incompressible.
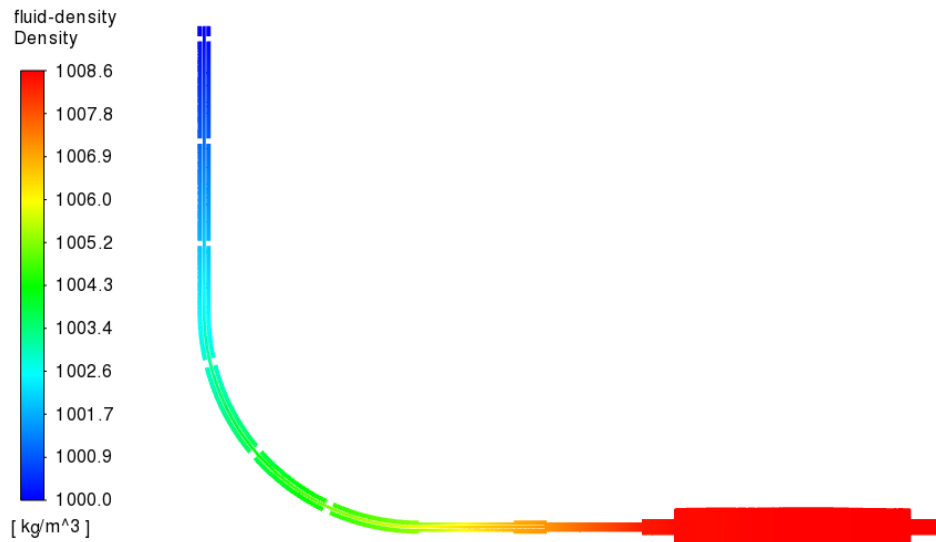
(3 s)
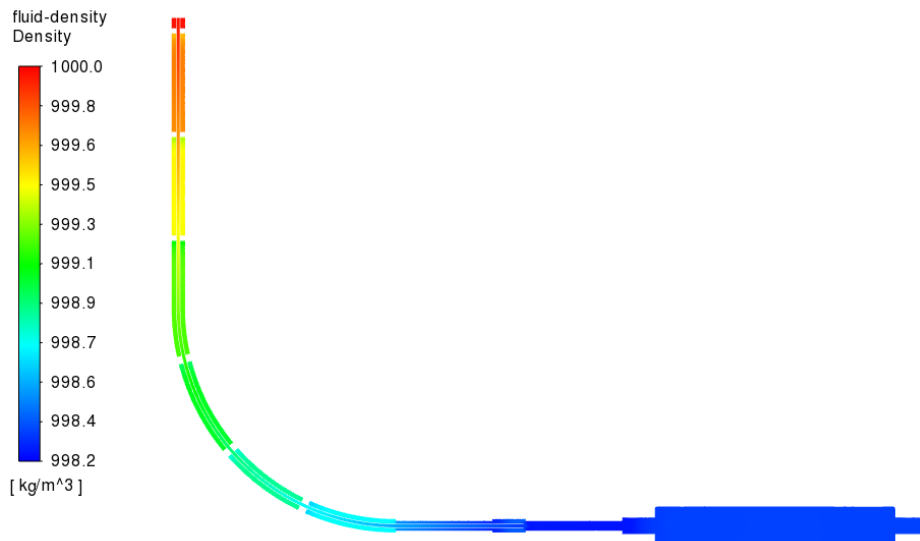
(5 s)

Figure 5.24: FVM predictions of fluid density in the system at 3 s and 5 s.

Reynolds number and turbulence behaviour in the flow regime

The Reynolds numbers are different in the riser tube and the main chamber and the maximum speed at each part are observed at different time. The peak flow speed in the riser tube is around 0.25 m/s at 1 s, when the compression distances of the pistons are the largest, as shown in Figure 5.25. With a riser tube diameter of 13 mm, the Reynolds number is estimated to be 3,250 for the riser tube at 1 s. Only a small effect of turbulence is observed at this time point as the turbulent viscosity ratio in the fluid is less than 3, as shown in Figure 5.26.
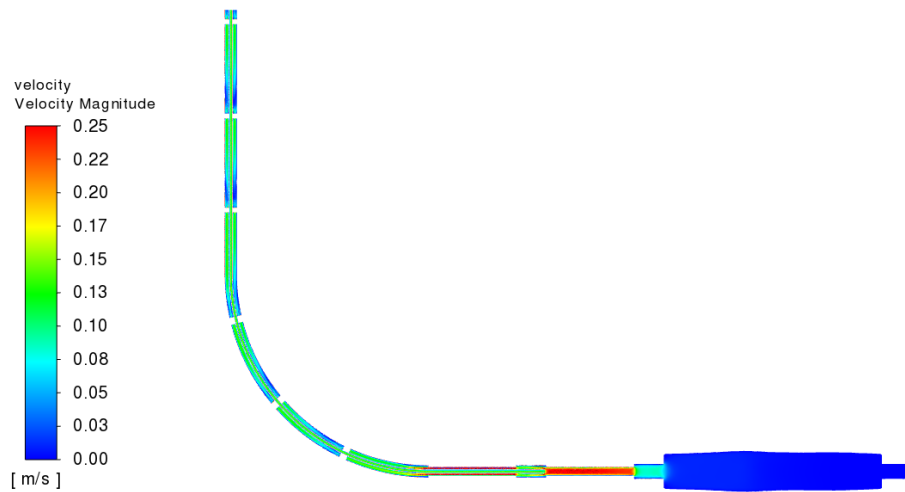
Figure 5.25: FVM predictions of velocity in the system at 1 s.
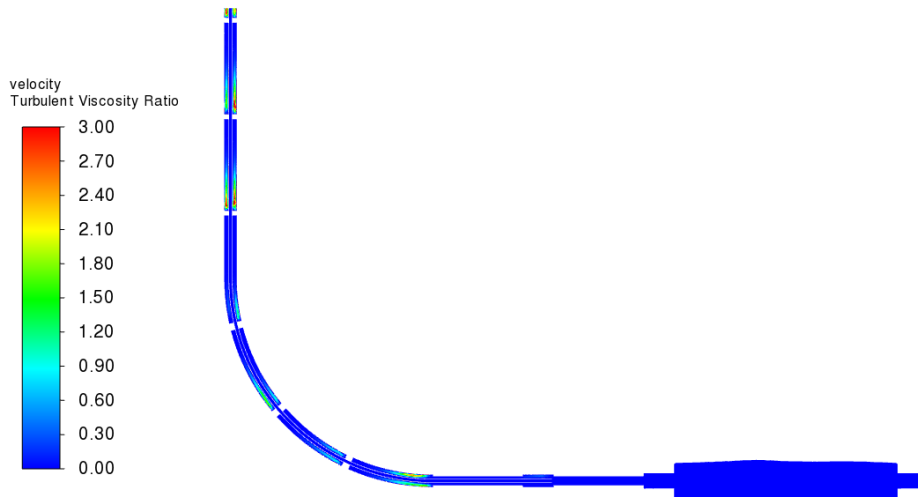
Figure 5.26: FVM predictions of turbulent viscosity ratio in the system at 1 s.

The peak flow speed in the main chamber is around 0.1 m/s at 3 s when the pistons are lifted, and flow is returning into the chamber, as shown in Figure 5.27. With a chamber diameter of 37 mm, the Reynolds number is 2,960 at the main chamber at 3 s. The turbulent viscosity ratio in the system is much higher at this time point, as shown in Figure 5.28. Therefore, the fluid flow is turbulent which explains why the SST k-ω model, which is physically consistent at lower Reynolds numbers, is used to solve the flow.
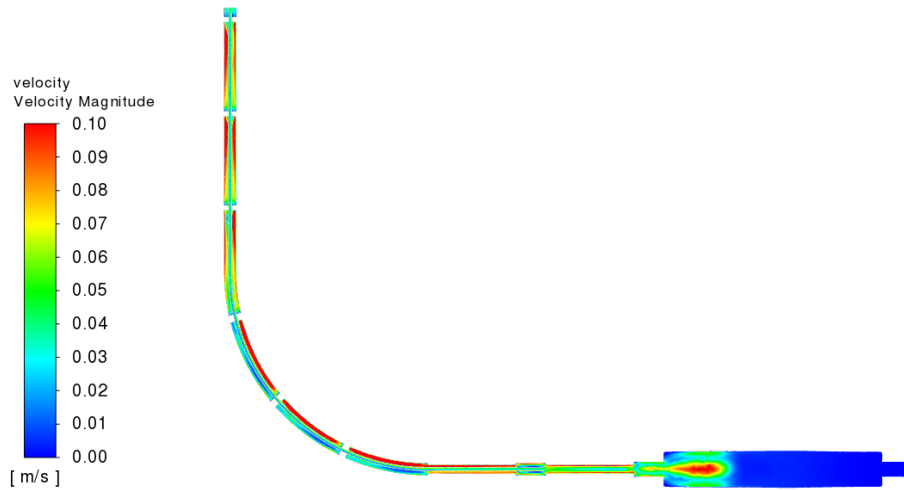
Figure 5.27: FVM predictions of velocity in the system at 3 s.
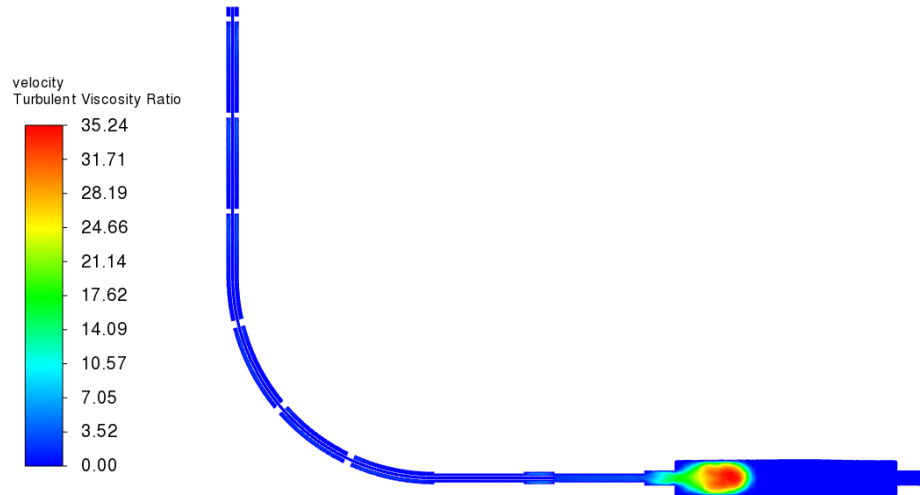
Figure 5.28: FVM predictions of turbulent viscosity ratio in the system at 3 s.

von Mises stress

The von Mises stress in the deforming structure is shown in Figure 5.29 at every second for the first cycle. The top images show the side view, and the bottom images show the view of the contact surfaces. The maximum von Mises stress in the deforming structure is 1.17 MPa at 2.1 s.
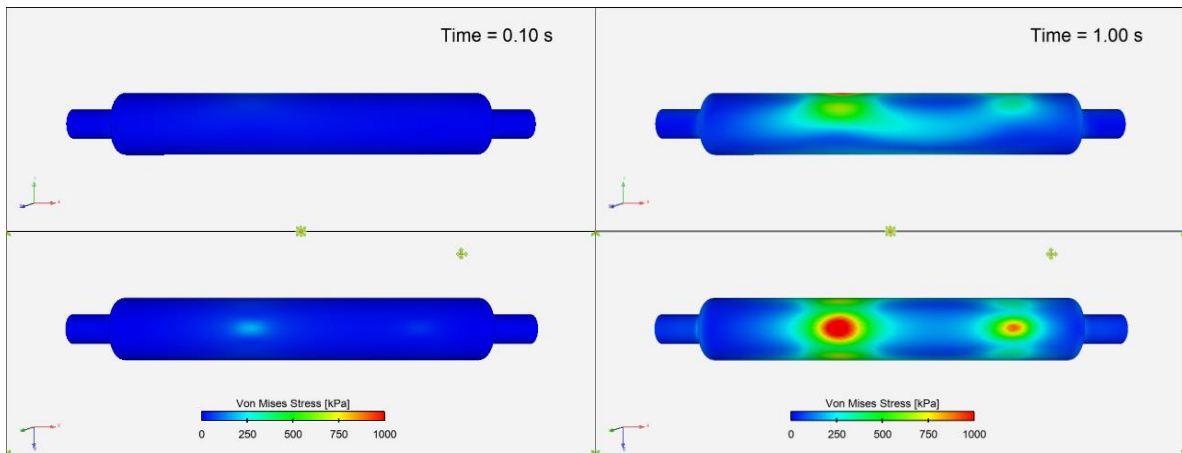
(0.1 s)   **(1 s)**
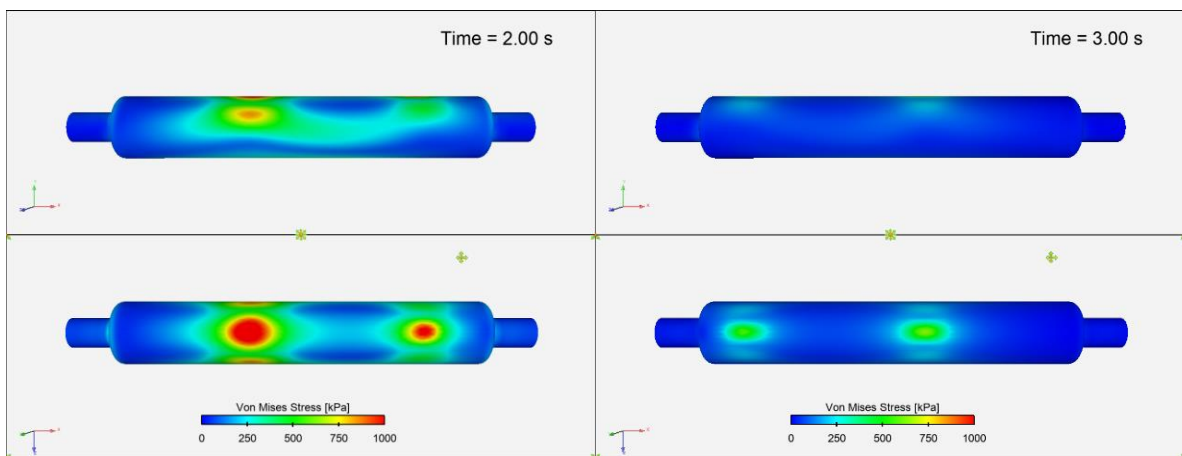
(2 s)   **(3 s)**
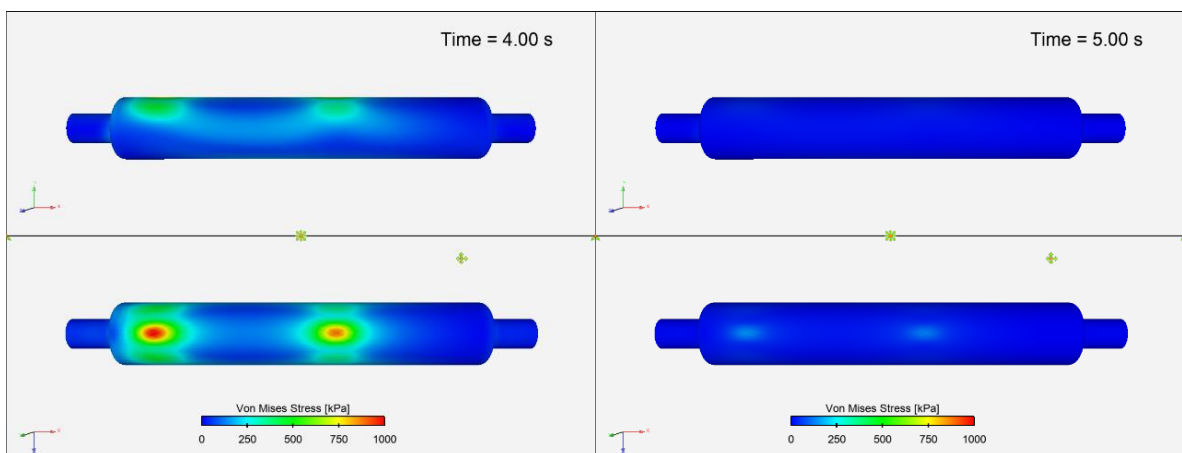
(4 s)   **(5 s)**

Figure 5.29: FEM predictions of von Mises stress in the structural model in the first cycle (Top: side view; Bottom: contact surface view).

5.5. Comparison between simulation and experiment for the base case

The dye concentration at each location is compared between the experiment and simulation in Figure 5.30. At 2.3 s, the dye entered the main chamber, and its concentration is observed to rise rapidly in both the experiment and simulation, this being especially obvious at points 1, 2 and 3. From 2.4 to 2.8 s, pistons 2 and 4 are lifting and causing expansion in the chamber. The dye flowed into the chamber and reached the first peaks at around 2.7 s. When pistons 1 and 3 compressed the chamber from 2.7 to 4.8 s, fluid is pushed out of the chamber, and part of the dye exited the chamber and causing a concentration drop after the first peak. The experimental results and simulation results of the entire line matched very well for this pattern. The simulation results from 10 mm from the surface did not show these peak values as they are not capturing the data at the centreline of the tube, where the dye is injected. The simulation results showed a very smooth trend towards the end, representing continuous mixing in the chamber. The results from the experiment are still fluctuating, potentially due to the uncertainty of light capturing during image visualisation. Over the entire run, the magnitude of the dye concentration matches very well between the experiment and both simulation results.
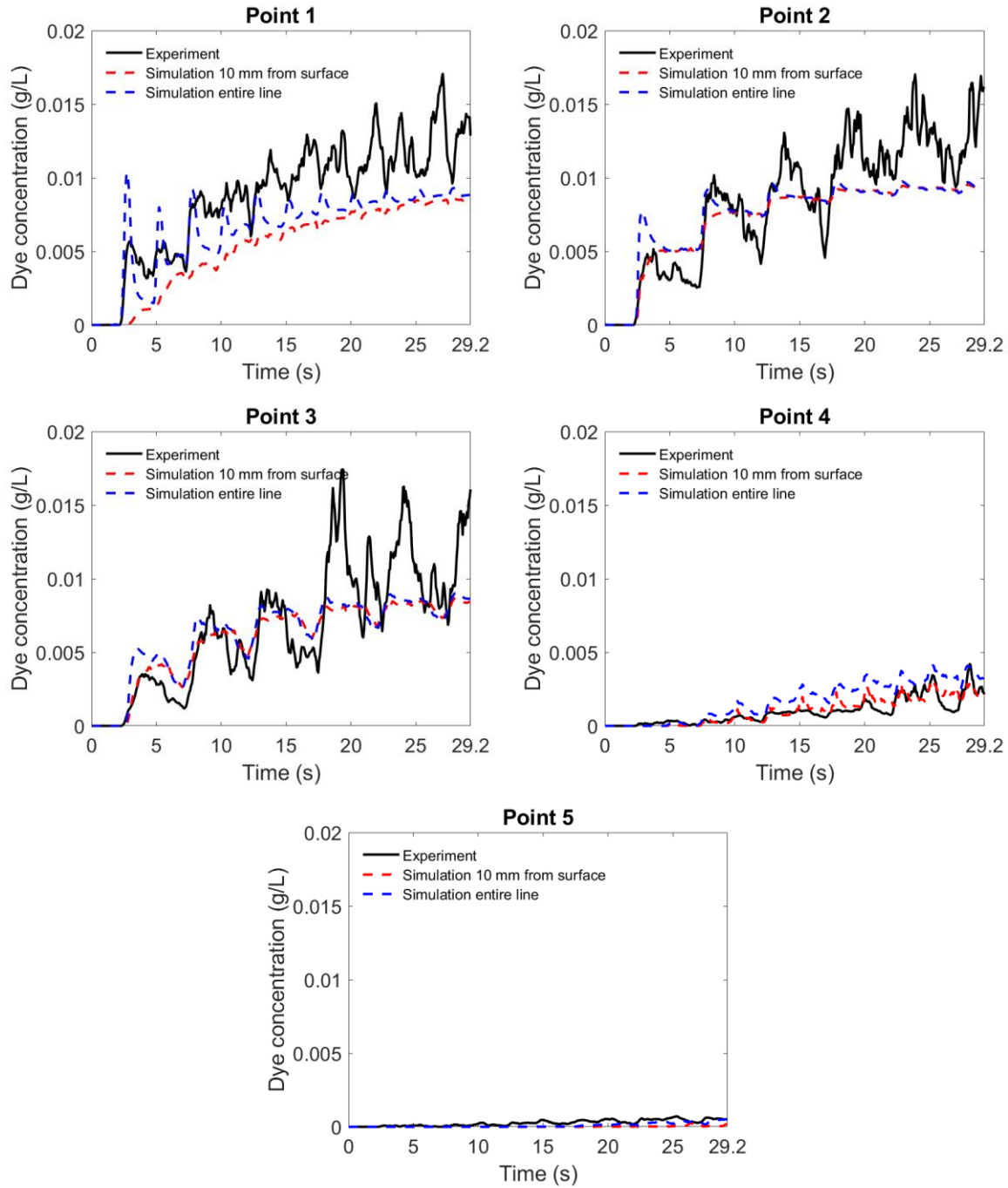
Figure 5.30: Comparison of transient evolution of the dye concentration at the five measuring points between experimental and simulation results.

5.6.   Changed pistons operating conditions

The operating conditions of the pistons were changed in some experiments and corresponding simulations are developed to compare the results. Two sets of changes are made to the piston motion: one with reduced frequency of the piston motion and one with reduced force acting on the pistons.

5.6.1. Effect of reduced frequency

The frequency of the piston motion was reduced by removing the piston motion between 5 s to 22.5 s in this test case. The displacement distance of the pistons from the experiment is shown in Figure 5.31, and the modified displacement used in the simulation is shown in Figure 5.32.
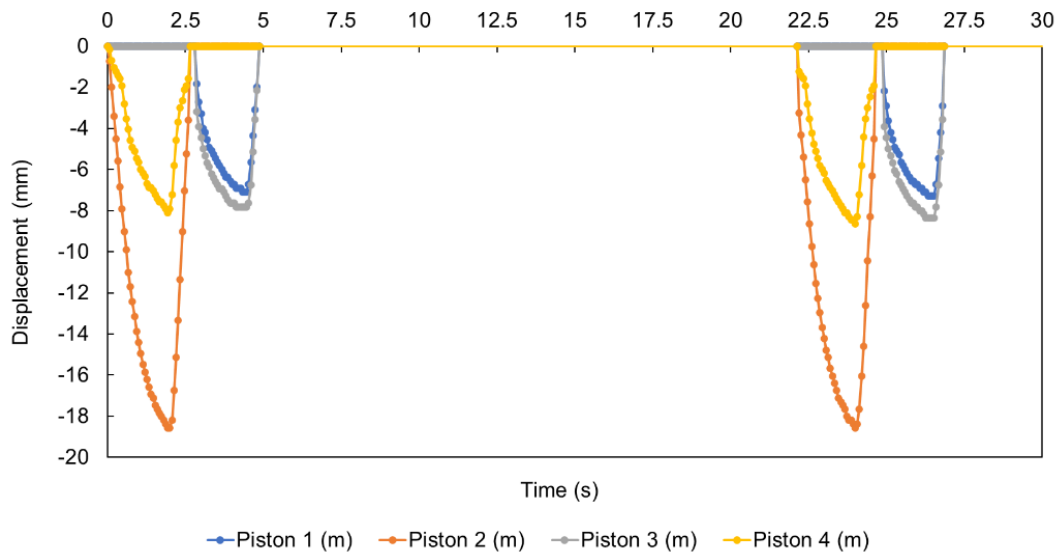
Figure 5.31: Displacement distance of the pistons from the experiment for the reduced frequency case.
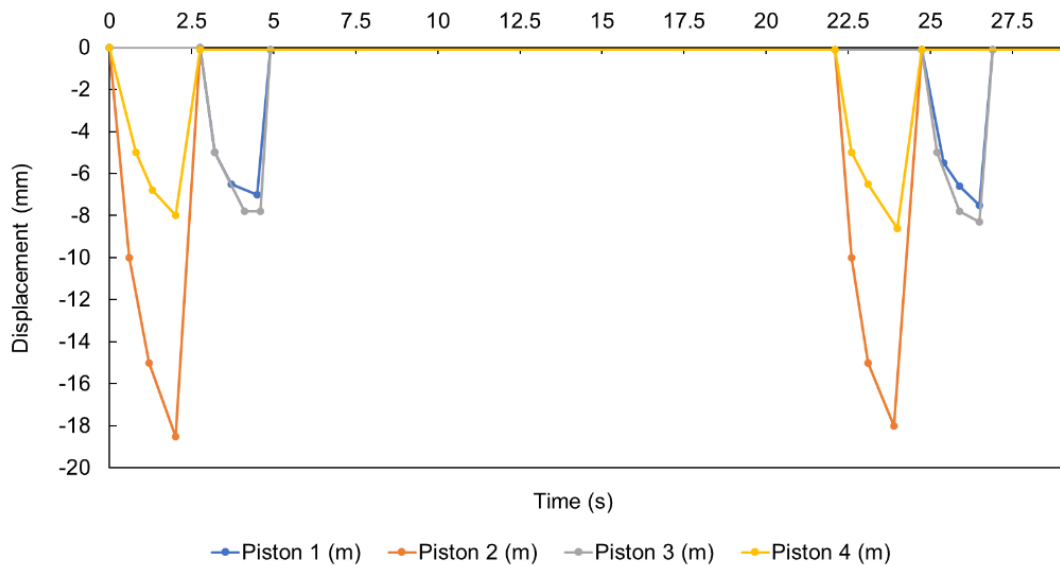
Figure 5.32: Displacement distance of the pistons used in the simulation for the reduced frequency case.

The comparison between the simulation results from the base model and the reduced frequency case is shown in Figure 5.33. The magnitudes of the initial peaks of the dye concentration in

each measuring point are similar. When there is no piston motion (5 s to 22.5 s), the dye concentration remains relatively constant. When the pistons start to compress the elastic tube again at 22.5 s, the magnitudes of the concentrations at points 1, 2, and 3 match with the second peak value in the base model.
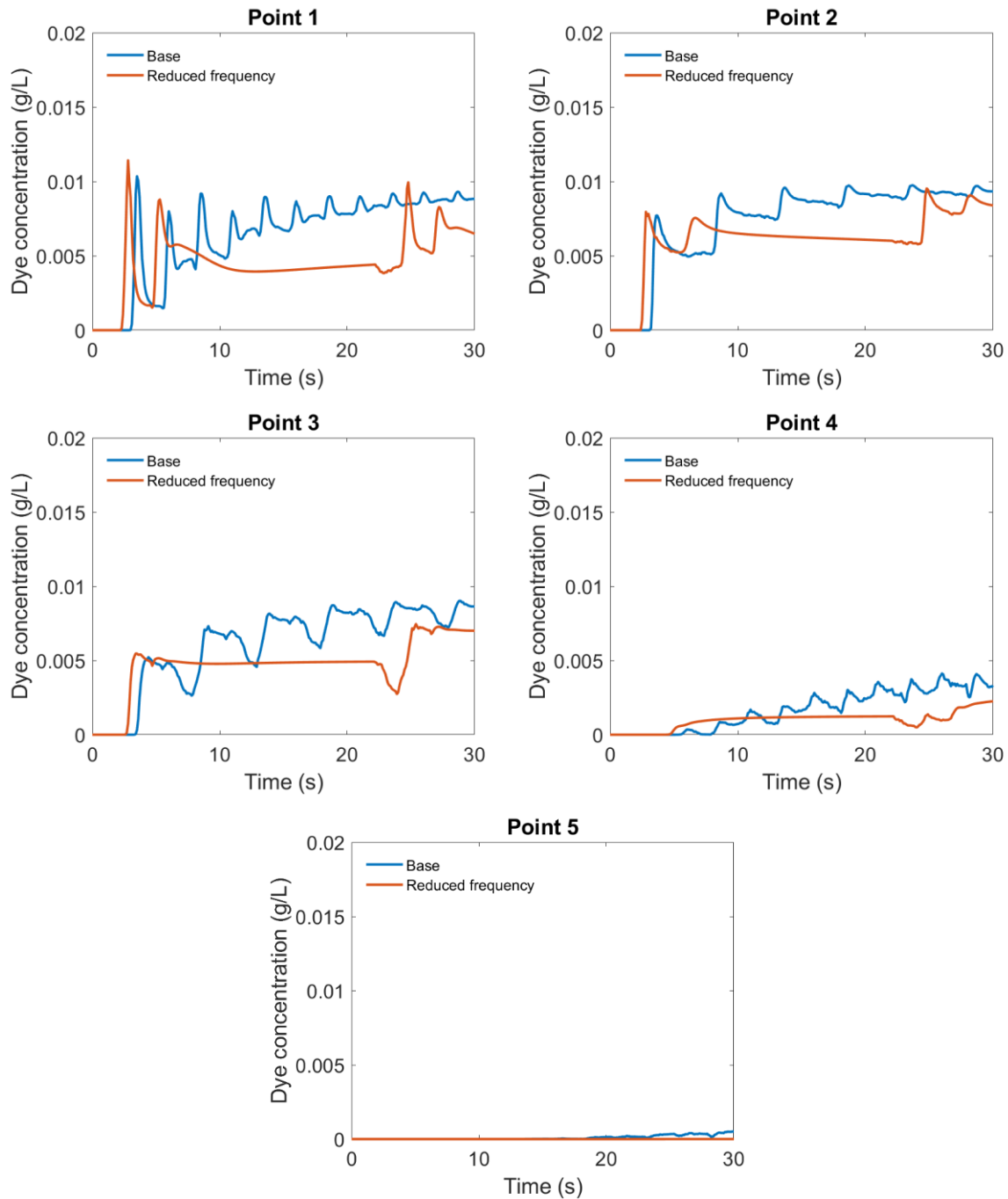
Figure 5.33: The comparison of transient evolution of the dye concentration at the five measuring points between the base case and reduced frequency case.

Comparison between simulation and experiment

The simulation results are compared with the experiment results in Figure 5.34. Two sets of experimental data are plotted corresponding to two repeats with the same conditions. The values at measuring point 1 match well, with the experimental results lying within the range of the simulation results tracked from two monitoring methods. However, the simulation results at points 2 and 3 are higher than the values from the experiment. The differences are potentially caused by uncertainties in the experiment as the results from the two simulation cases are comparable. The elastic tube is not completely transparent and the lighting around the system is not distributed evenly, which could cause difficulty in the colour calibration test. The material of the elastic tube has degraded and changed colour over time, which would affect the calibration curves. This is an ongoing study, and these aspects still require further investigation.
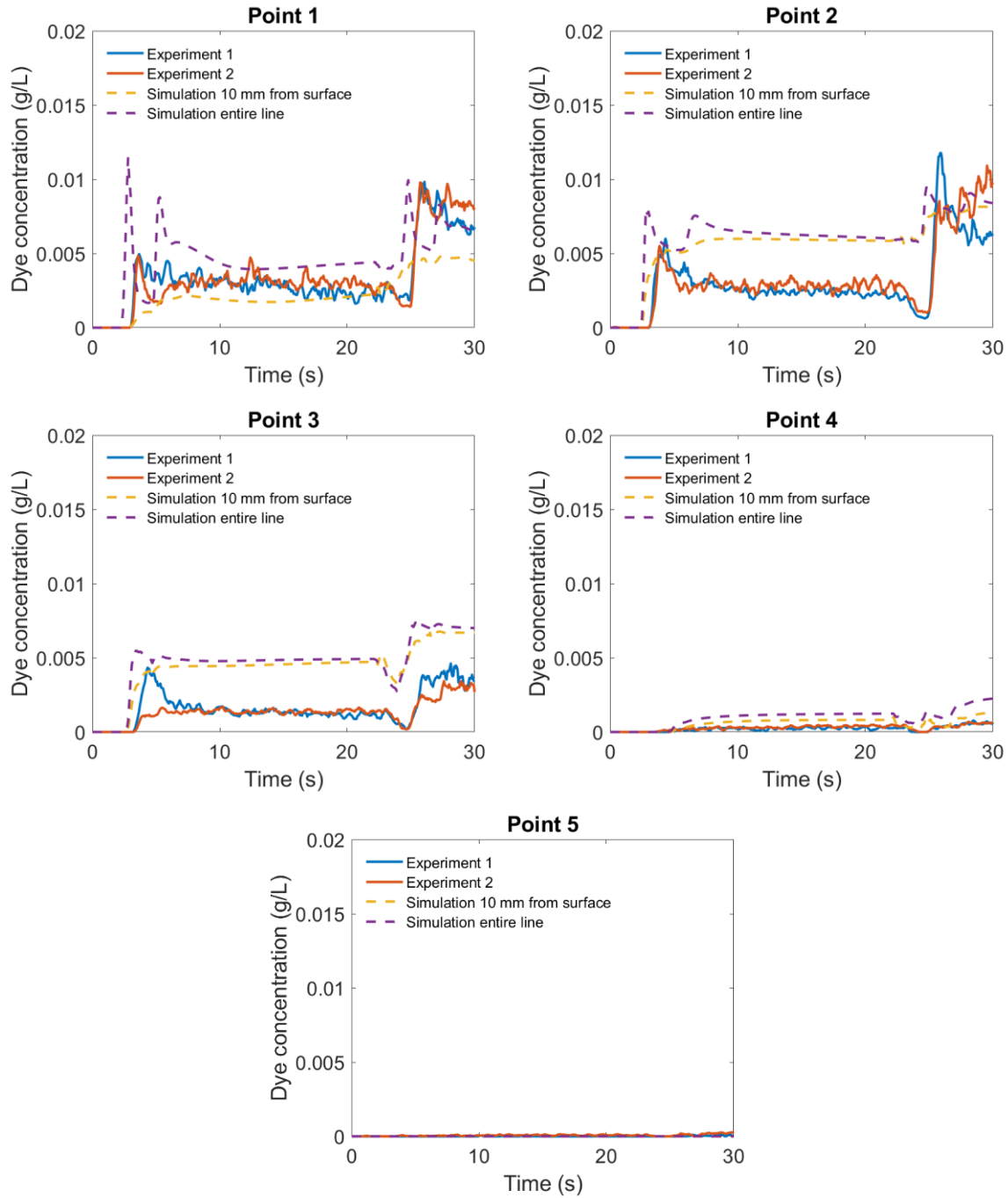
Figure 5.34: Comparison of transient evolution of the dye concentration at the five measuring points between experimental and simulation results for the reduced frequency case.

5.6.2. Effect of reduced force

The force acting on the pistons was reduced in this test case. The resulting displacement is reduced to half of its original values. The displacement distance of the pistons from the experiment for this test case is shown in Figure 5.35, and the modified displacement used in the simulation is shown in Figure 5.36.
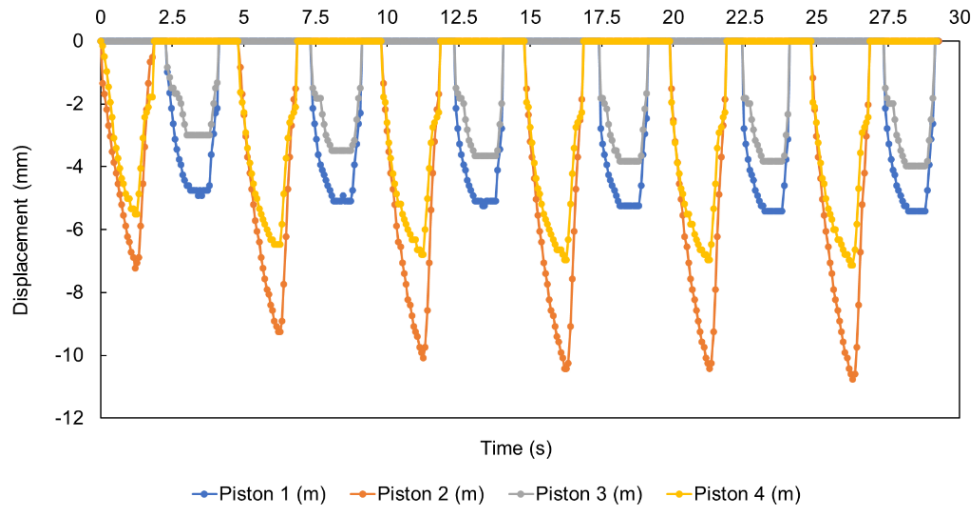
Figure 5.35: Displacement distance of the pistons from the experiment for the reduced force case.
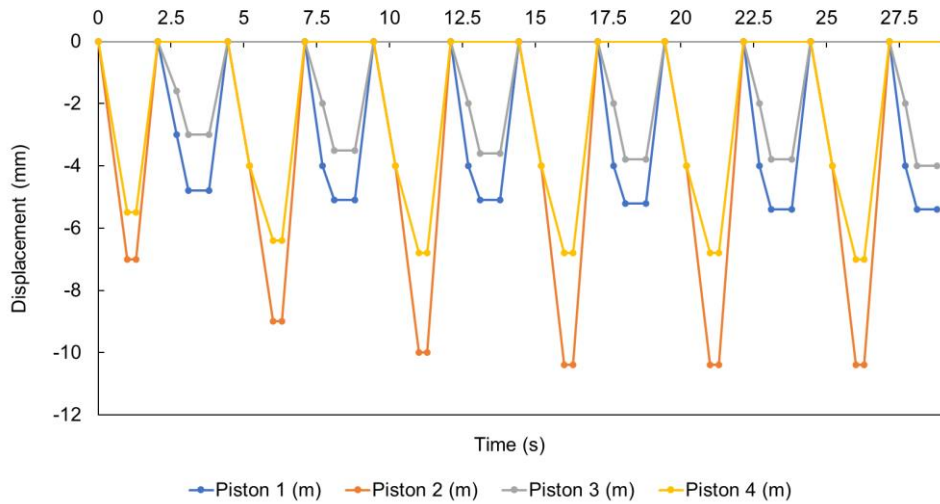
Figure 5.36: Displacement distance of the pistons used in the simulation for the reduced force case.

The comparison between the simulation results from the base model and the reduced frequency case is shown in Figure 5.37. The dye concentration at each measuring point is approximately half of its original value. The entry of the dye into the chamber is delayed in this test case compared with the base model, due to the reduction in tube deformation.
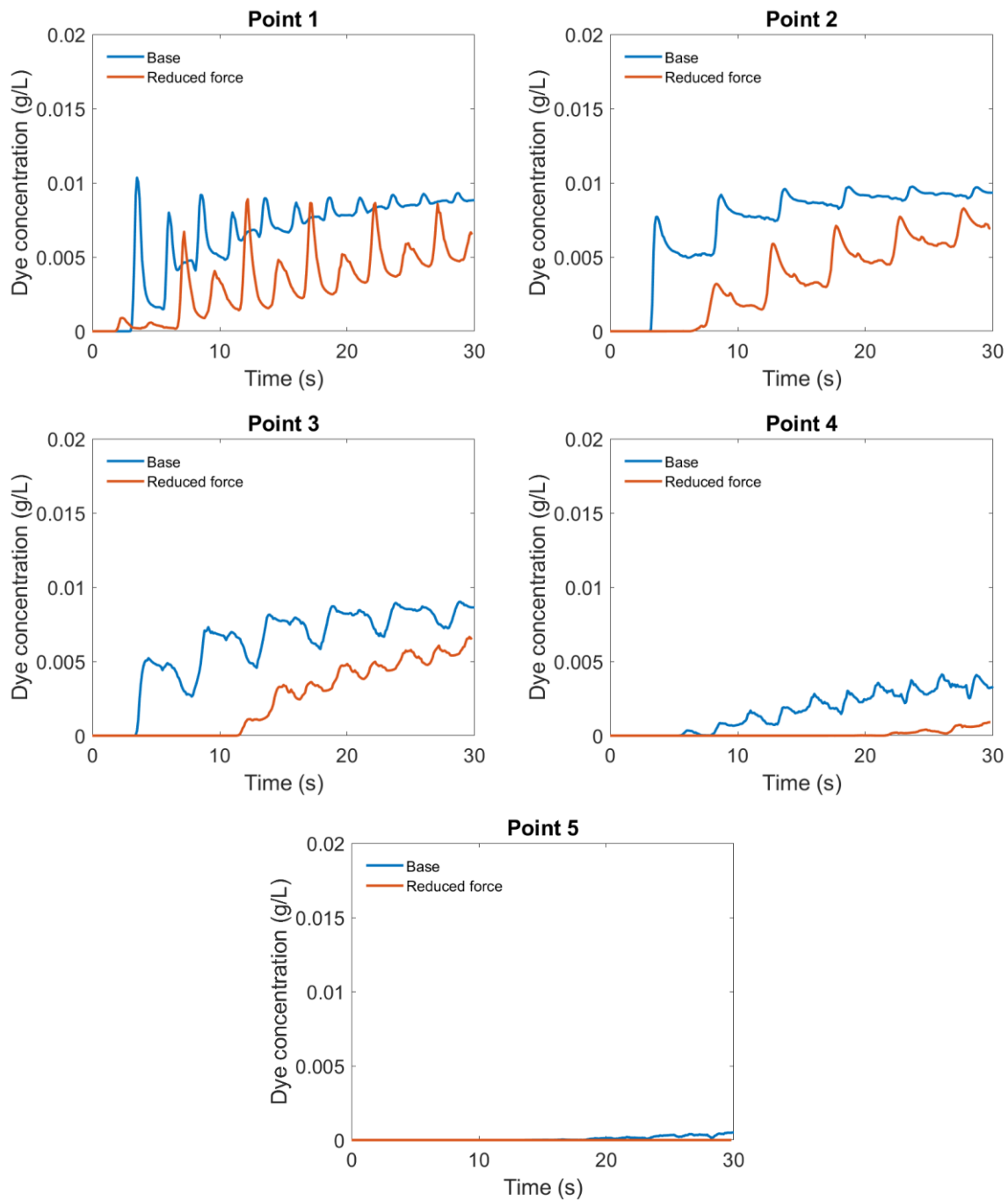
Figure 5.37: The comparison of transient evolution of the dye concentration at the five measuring points between the base case and reduced force case.

Comparison between simulation and experiment

Similar to the reduced frequency case, the values at measuring point 1 match well between the simulation and experimental results. However, the experimental values at points 2 and 3 are much lower than the simulation results, which requires further investigation.
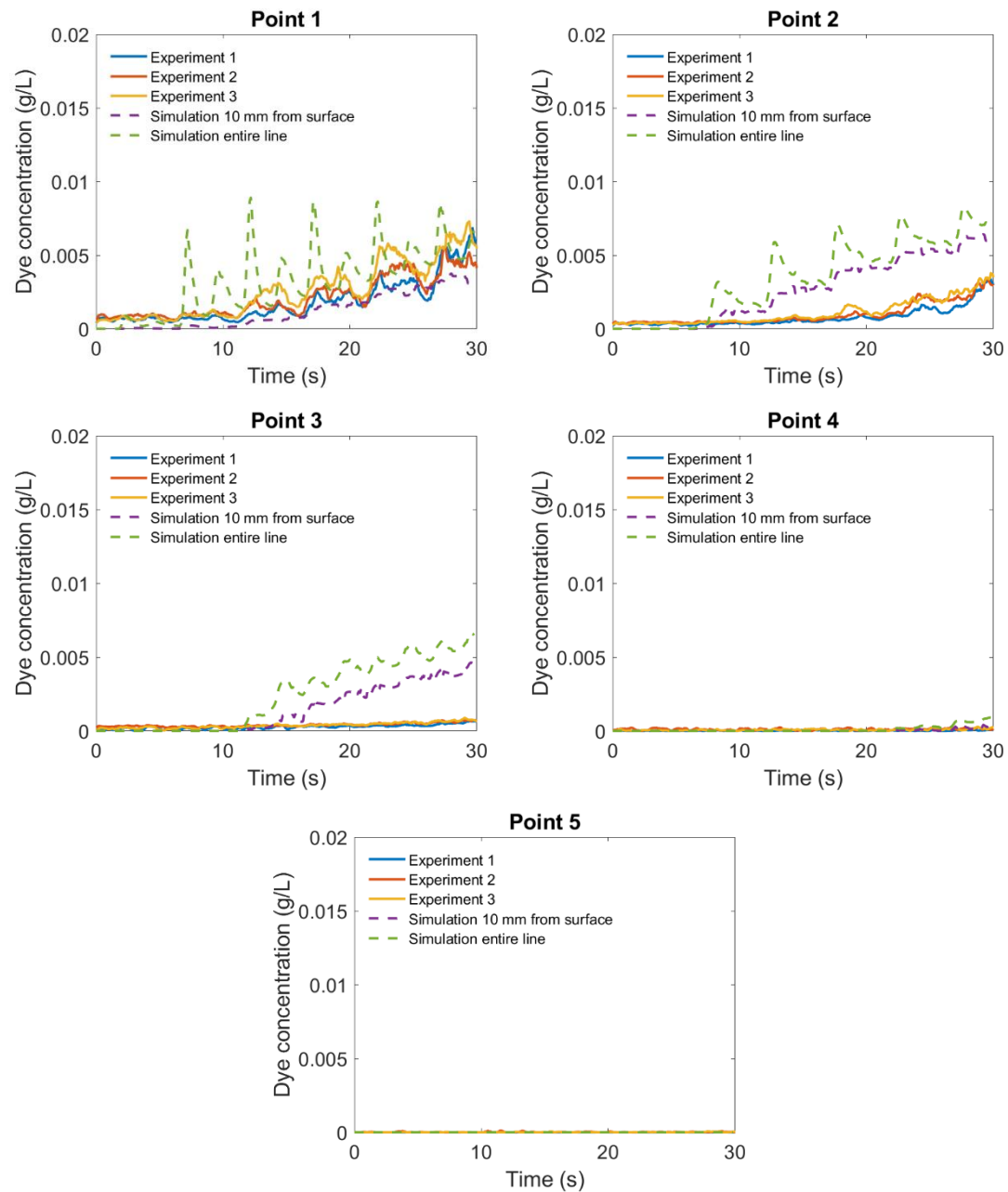
Figure 5.38: Comparison of transient evolution of the dye concentration at the five measuring points between experimental and simulation results for the reduced force case.

5.7. Timestep independence study

A timestep independence study was conducted on the reduced frequency case to examine the timestep effect. A timestep of 0.01 s is used to conduct the analysis and the results are shown in Figure 5.39. The values at each measuring point are similar and therefore the simulation results show that the timestep choice does not explain the differences between the experimental and simulation results.
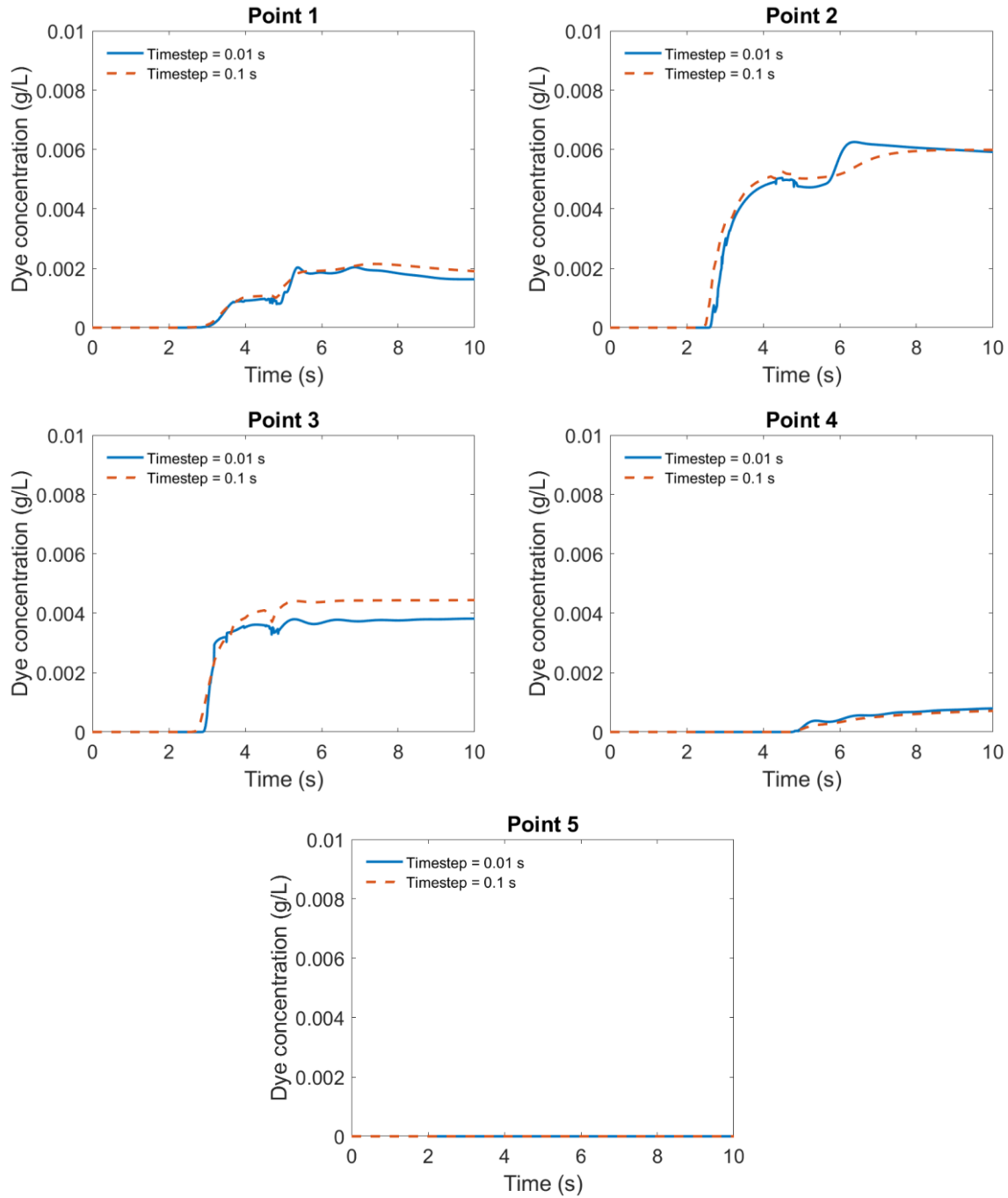
Figure 5.39: Timestep independence studies on the FSI model.

5.8.   Conclusions

A robust FSI model that can be used to simulate an *in vitro* intestinal peristaltic system has been developed. Simulation results, including the velocity and strain rate in the fluid domain and the stresses in the structure provide useful insights that helped improve the experimental design. The predicted strain rate from the fluid is within the typical range of that observed in

digestion models, which has demonstrated the utility of this system in the modelling digestion process. The simulated dye concentration shows good agreement with the experimental data in the base model, suggesting the model is a good representation of the physical system. The simulation model also shows consistent results when the piston operating conditions are changed. Further investigation is required to understand why the agreement between the experimental and simulation data is poor in the final two cases.

In the next chapter simulation of a beaker and stirrer system is performed based on an *in vitro* study, investigating tablet dissolution in the fluid.

Chapter 6. Numerical Simulation of an In Vitro Beaker and Stirrer System

The modelling in this Chapter uses the published experimental data from Langrish et al. [178]. Prof. Tim Langrish kindly provided the raw data and details of the experimental setup and operation, as well as helpful discussions on the analysis. The bulk of this chapter is published as X. Liu, C. Zhong, D.F. Fletcher, and T.A.G. Langrish, "Simulating tablet dissolution using computational fluid dynamics and experimental modelling", Processes, vol. 11, p. 505, 2023, doi: 10.3390/pr11020606.

6.1. Introduction

From the mathematical modelling point of view, the solid digestion process can be characterized as following two steps, which are disintegration and dissolution [29]. In the first step, food particles break into small fragments and the entrapped nutrient ingredients are exposed to the gastric juice. In the second step, the nutrient ingredients dissolve in the gastric system. Currently, there is no published standard measurement for food digestion. However, the United States Pharmacopeia (USP) has introduced standard apparatus to perform dissolution tests for tablets and this is widely used in the pharmaceutical industry [179]. The USP principal can potentially be applied to the evaluation of the food digestion process. Therefore the study of dissolution is fundamental in both the food industry [3, 4] and the pharmaceutical industry [180, 181].

Mass transfer is closely related to dissolution and is essential in the human digestion process and is closely related to the characteristics of the fluid flow and the composition of the food [6]. Langrish et al. [178] conducted an *in vitro* study to investigate the mass-transfer coefficients in a beaker and stirrer digestion system, that is similar to the USP apparatus, using benzoic acid tablets.

There has been significant work in the past on the investigation of the dissolution of tablets in stirring apparatuses as various authors have modelled systems used to determine mass transfer rates. However, these were performed around 10 years ago, since which time there have been significant advances in CFD modelling.

In 2003, McCarthy et al. [182] used CFD to model the US Pharmacopeia dissolution apparatus using an early version of the Fluent software to model steady, laminar flow in a hemispherically-bottomed vessel with a suspended paddle stirrer. The authors modelled the

entire system in a single frame of reference rotating at the speed of the impeller with counter-rotating walls. This method has the unwanted effect of introducing artificial swirl and the low-order schemes available at that time would have resulted in significant numerical diffusion. However, the results were in reasonable agreement with PIV data. No tablet was modelled initially so there are no shear stress data on the tablet surface. They added a tablet in some later runs and showed its effect on the flow. Later work [183] displayed streamlines that highlighted the predicted solid body rotation of the flow, which is expected in the absence of baffles, and gave more details of the wall shear stress on the tablet.

In 2009, D'Arcy et al. [184] modelled laminar flow in a cylinder with a stirrer suspended from the top. The tablet was not modelled, but instead data were recorded on a 5 mm radius plane located 2 mm above the base of the vessel located on the centreline. They again used the single reference frame approach.

Bai and Armenante [185] modelled a similar apparatus to McCarthy et al. using the same software and a similar approach. They extended the work to investigate off centre tablets using a multiple reference frame approach, in which the lower part of the vessel was modelled in a stationary frame with a horizontal interface between the frames.

In this study, a CFD model is built based on the *in vitro* study conducted by Langrish et al. [178] to simulate the dissolution process. Compared with the experiment, simulation results provide more insight into the details of the fluid flow, including velocity field, turbulence characteristics, and strain rate in the fluid. Although detailed studies of the predicted flow field in the USP apparatus system have been conducted experimentally and numerically using CFD [185-191], the shear stress on the surface of the tablet was not always estimated or predicted in previous work. In addition, mass transfer was not modelled, so mass-transfer rates had to be inferred from calculated wall shear stresses. The dissolution behaviour between the experiment and simulation is analysed and compared, including the estimation of the mass-transfer coefficient, and the correlation between the Reynolds number and the Sherwood number. Three different stirrers are used with different rotation speeds, and their effects are investigated.

6.2. In vitro model setup

In the experiment, a 150 mL beaker was used and filled with 80 mL of water. Three different types of stirrers were used and placed at the centre of the beaker, rotating at different stirring speeds: 100 revolutions per minute (rpm) and 200 rpm. A supporting platform was 3D printed,

and a tablet was placed upon it. A sketch of the experimental setup is shown in Figure 6.1, and the dimensions of the different stirrers are shown in Figure 6.2.
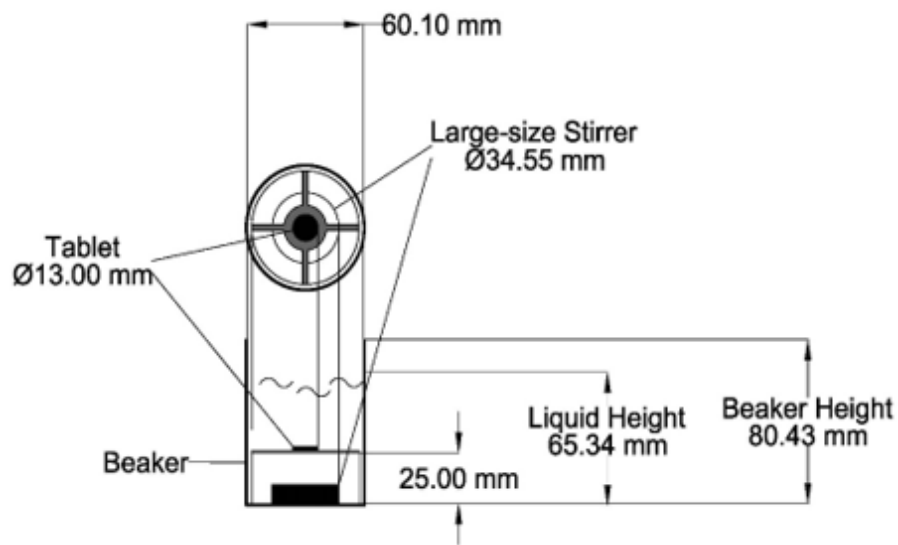
Figure 6.1: A sketch of the experimental setup of the beaker and stirrer system. Reprinted from Langrish et al. [178].

(a)

(b)

(c)
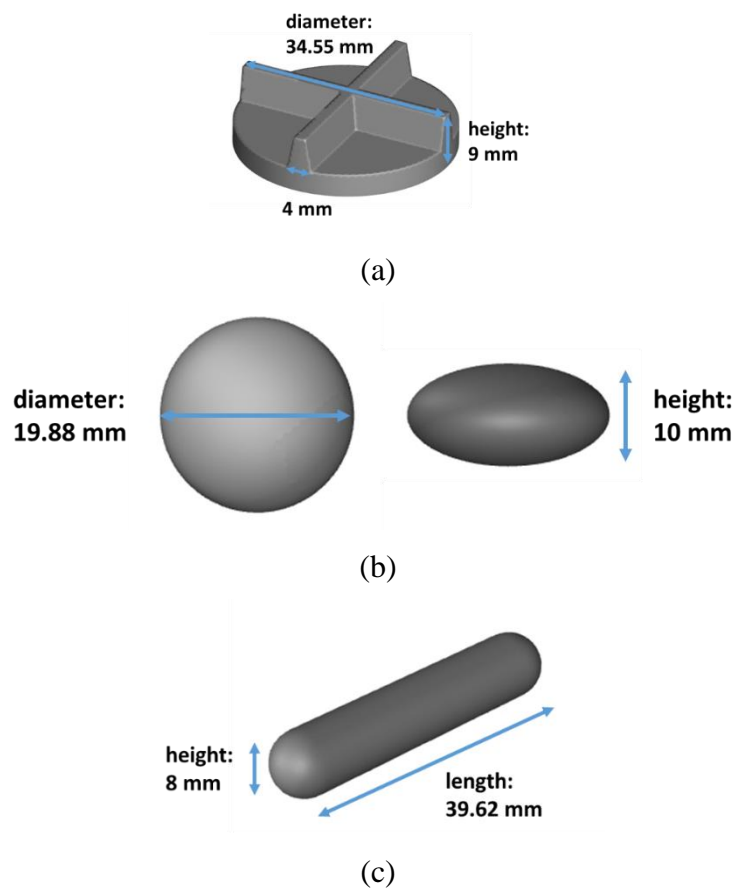
Figure 6.2: Illustration of three different stirrers (a) stirrer 1; (b) stirrer 2; (c) stirrer 3.

6.3.   Numerical model setup

Geometry

Ansys SpaceClaim was used to construct the geometry for the simulation. Figure 6.3(a) shows the solid bodies in the beaker: the supported platform (light blue), the stirrer blade (green), and the tablet (pink). Figure 6.3(b) shows the fluid domain, the bottom fluid domain (brown) was set to be a moving zone to allow the rotating motion to be simulated in the local reference frame. This is a significant advance over previous modelling, as large-scale transient structures, as well as flow interaction with the tablet support structure, can be captured correctly.

(a)   **(b)**
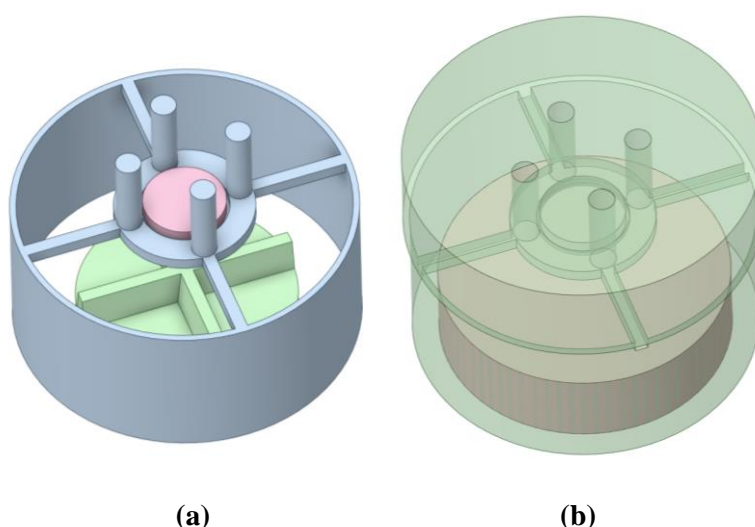
Figure 6.3: Geometry of the beaker and stirrer system and the fluid domain with stirrer 1 (a) the stirrer colored in green, the supporting frame colored in blue and the tablet colored in pink (sitting on a solid surface); (b) the stationary fluid domain colored in green and the rotating fluid domain colored in brown.

Computational mesh

The Ansys Fluent Watertight geometry meshing tool was used to generate the mesh in the fluid region. The generated mesh has 264,000 cells and comprises poly-hexcore elements with inflation at the walls. Ten layers of fine inflation were used on the tablet to capture the thin concentration boundary layer. The minimum orthogonal quality of the mesh is 0.38. A sensitivity study showed that this mesh gave sufficient resolution.

(a)

(b)
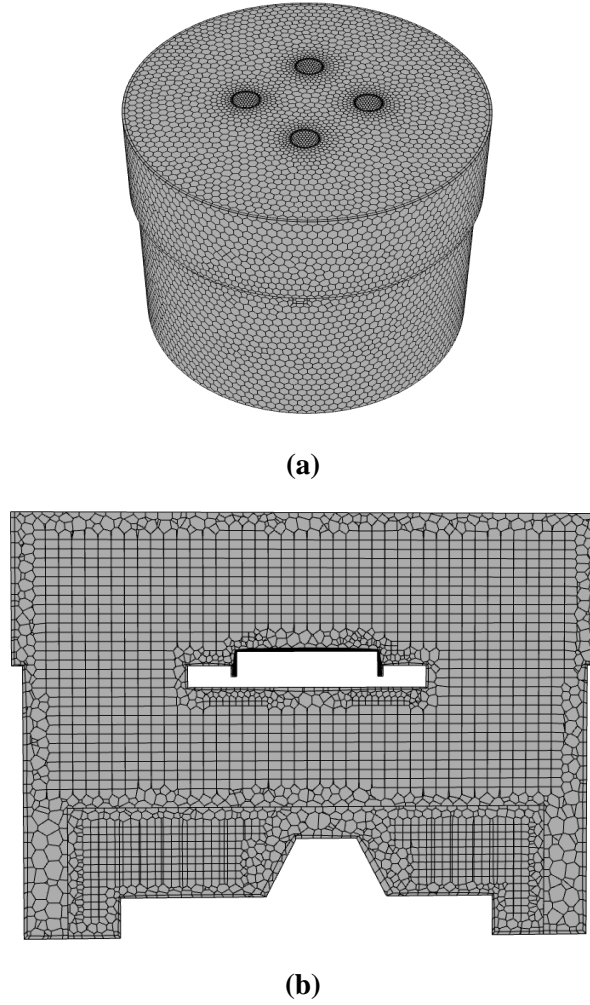
Figure 6.4: Computational mesh on the fluid domain with stirrer 1.

(a) surface mesh; (b) cross-section of the mesh.

Model description

The transient, pressure-based solver was used to solve for turbulent flow. The SST k-ω model [176] was chosen as the turbulence model. The bottom fluid zone was set as a rotating zone with a vertical rotation axis, and the mesh motion was determined from the rotation rate.

Conservation equations

The conservation equations for mass and momentum with the sliding mesh model are given by equations 5.1 and 5.6 presented previously in Chapter 5. The conservation of species mass is given by equation 5.17. The transport equations for the turbulence kinetic energy and turbulence eddy frequency are given by equations 5.7 and 5.8.

Again, this represents a significant improvement over the cited works in that mass transfer rates can now be calculated based on a realistic species distribution and turbulence effects are captured in regions where they are important.

Model setup

The mixing vessel was filled with water, with a constant density of 998.2 kg m^{-3} and a constant viscosity of 0.001 Pa.s. The benzoic acid diffusion coefficient in water was taken from [192]. The tablet wall is assumed to have a constant benzoic acid mass fraction of 0.0328 [192]. The rotating speed of the moving fluid is 100 rpm or 200 rpm corresponding to the stirrer speeds used in the experiment. Each case was run for 20 s, which was sufficient enough to reach a steady solution. A timestep was selected to give 5° of rotation in a single step, which for 200 rpm was 0.66 ms. An additional case was run with no rotation.

Solution method

The coupled pressure-velocity scheme was used to solve the equations with the bounded second-order implicit transient formulation. Gradients were determined using the least-squares cell-based option, the pressure was determined using the second-order method. The second-order upwind scheme was used for all the transport equations, except those for turbulence that used the first-order upwind scheme. Converged solutions were achieved when residual values for the continuity, x, y, z velocities and dye were below 10^{-5}. The residual values were calculated based on the locally scaled Root Mean Square (RMS).

6.4. Results and discussion

6.4.1. Flow results from the simulation

Mass fraction of benzoic acid

The mass fraction contours of benzoic acid at 20 s with different stirrers and rotation speeds are shown in Figure 6.5. The benzoic acid is more distributed at a higher rotation speed with all stirrers. Stirrer 1 provides the most diffused mixing pattern, followed by stirrer 3, while stirrer 2 seems to be the least effective.

(i) stirrer 1, 100 rpm   **(ii) stirrer 1, 200 rpm**

benzoic-acid
Mass fraction of ben

3.30e-03
1.37e-03
5.68e-04
2.36e-04
9.79e-05
4.06e-05
1.69e-05
7.00e-06
2.90e-06
1.20e-06
5.00e-07

(iii) stirrer 2, 100 rpm   **(iv) stirrer 2, 200 rpm**

(v) stirrer 3, 100 rpm   **(vi) stirrer 3, 200 rpm**
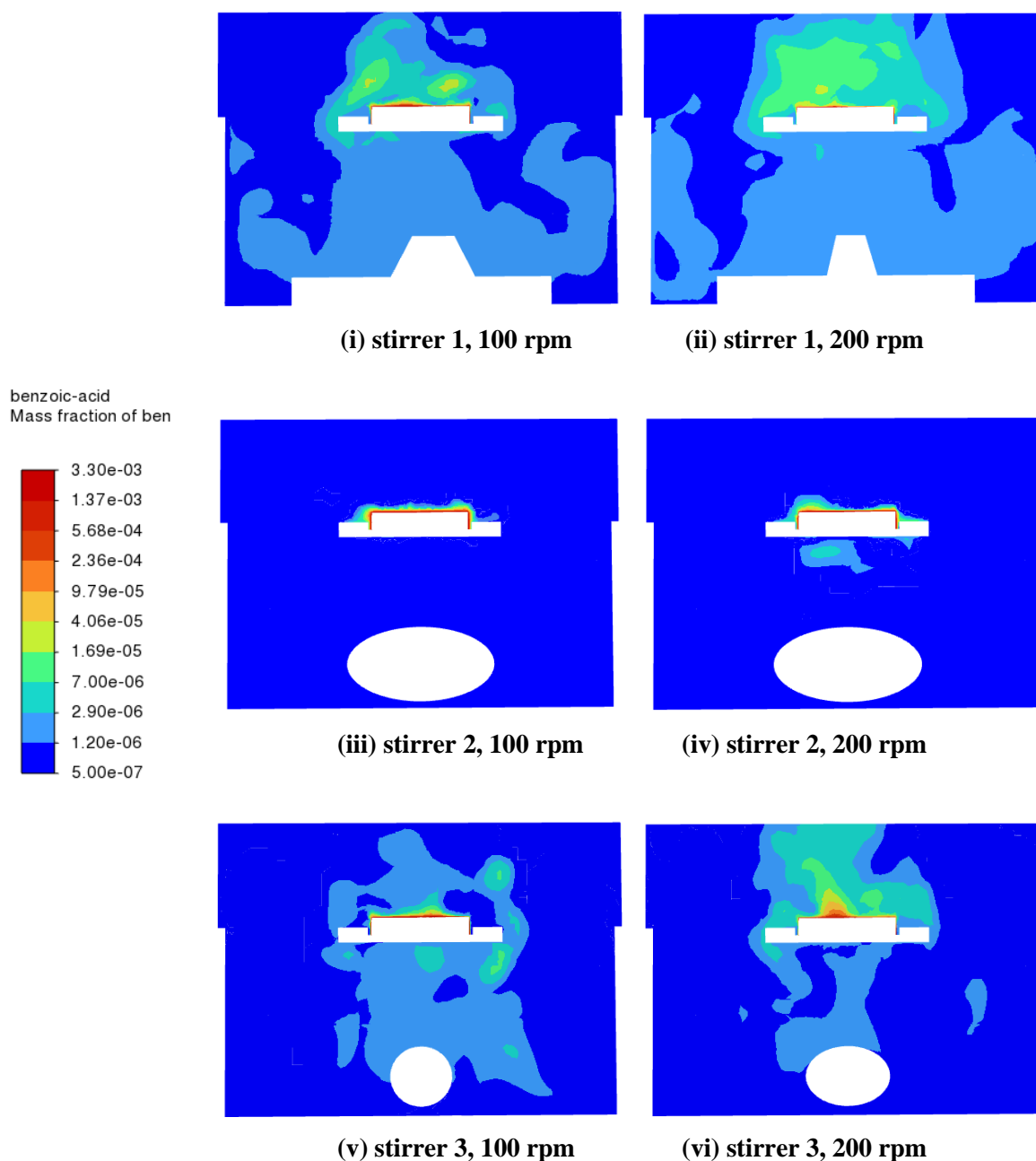
Figure 6.5: CFD predictions of the benzoic acid mass fraction on the vertical middle cross-section for different stirrers at different rotation speeds (100 rpm and 200 rpm) at 20 s.

Velocity in the stirrer system

Figures 6.6 and 6.7 show the fluid velocity for different stirrers at different rotation speeds. The velocity magnitude is much higher with stirrers 1 and 3 than with stirrer 2. The velocity magnitude ranges from 0 m/s to 0.4 m/s, which is of the same order of magnitude as in the previous studies conducted by D'Arcy et al. [184], Bai and Armenante [185, 188, 189], and

McCarthy et al. [183]. The complex eddy patterns generated by the stirrers are evident in Figure 6.7.

<table>
<tr><td>v-rel
Relative Velocity Mag</td></tr>
<tr><td>0.40</td></tr>
<tr><td>0.36</td></tr>
<tr><td>0.32</td></tr>
<tr><td>0.28</td></tr>
<tr><td>0.24</td></tr>
<tr><td>0.20</td></tr>
<tr><td>0.16</td></tr>
<tr><td>0.12</td></tr>
<tr><td>0.08</td></tr>
<tr><td>0.04</td></tr>
<tr><td>0.00</td></tr>
<tr><td>[m/s]</td></tr>
</table>

(i) stirrer 1, 100 rpm   **(ii) stirrer 1, 200 rpm**

(iii) stirrer 2, 100 rpm   **(iv) stirrer 2, 200 rpm**

(v) stirrer 3, 100 rpm   **(vi) stirrer 3, 200 rpm**
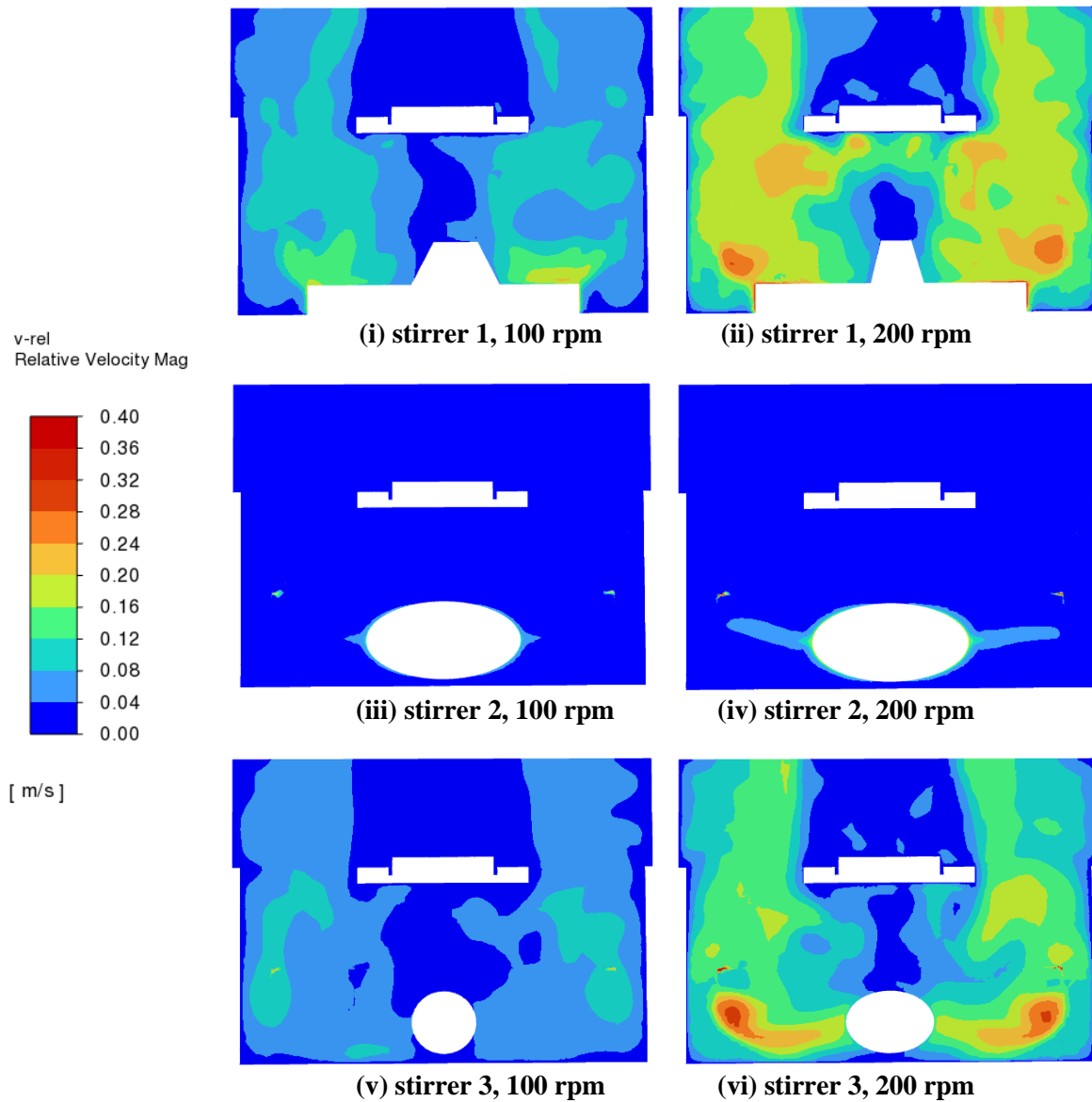
Figure 6.6: CFD predictions of velocity magnitude contour on the vertical middle cross-section for different stirrers at different rotation speeds (100 rpm and 200 rpm) at 20 s.

(i) stirrer 1, 100 rpm　　　　**(ii) stirrer 1, 200 rpm**

v-rel
Relative Velocity Mag

	0.40
	0.36
	0.32
	0.28
	0.24
	0.20
	0.16
	0.12
	0.08
	0.04
	0.00

[m/s]

(iii) stirrer 2, 100 rpm　　　　**(iv) stirrer 2, 200 rpm**

(v) stirrer 3, 100 rpm　　　　**(vi) stirrer 3, 200 rpm**
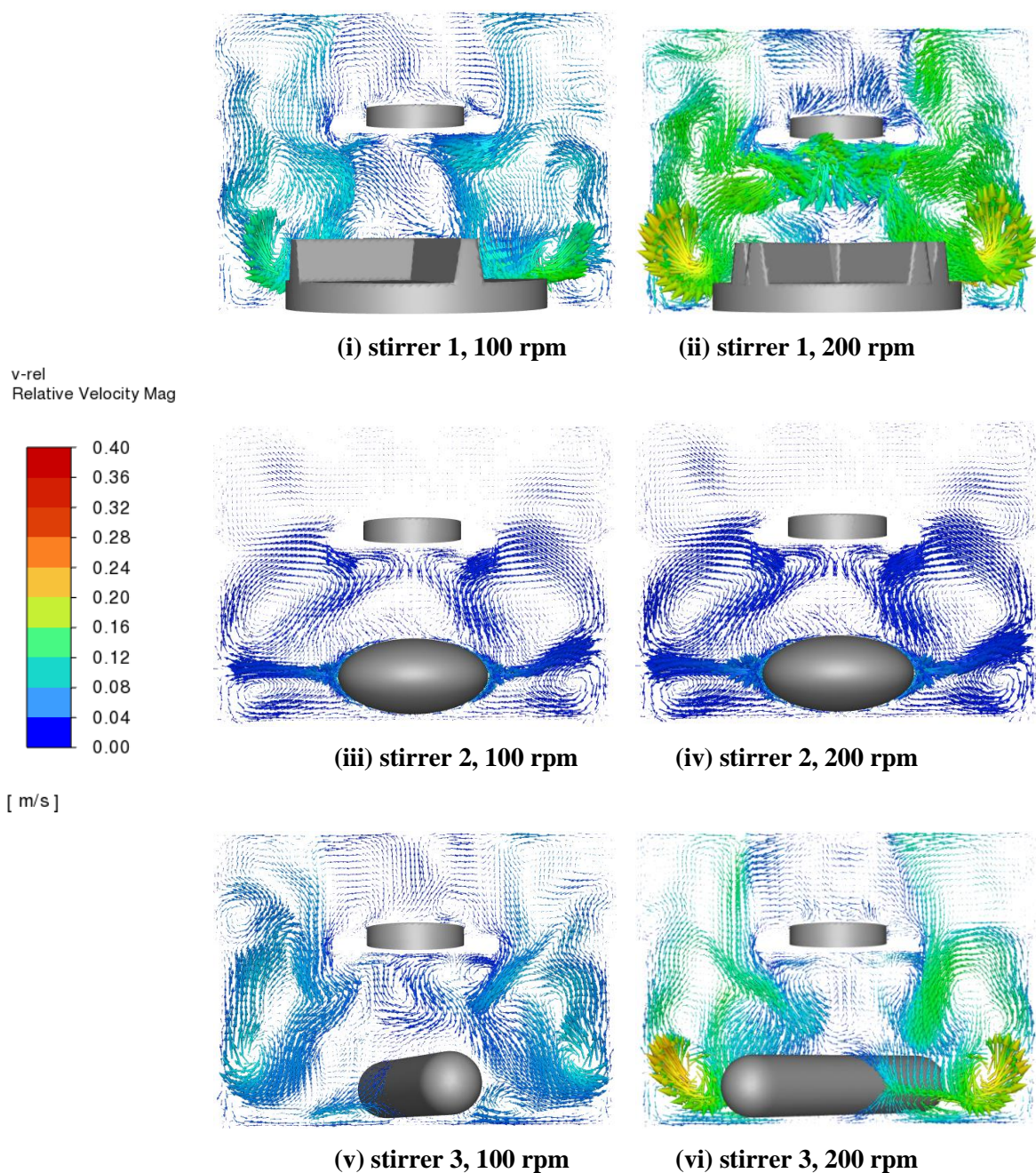
Figure 6.7: CFD predictions of velocity vectors on the vertical middle cross-section for different stirrers at different rotation speeds (100 rpm and 200 rpm) at 20 s.

Velocity above the tablet

The velocity vectors in a horizontal plane located above the tablet are shown in Figure 6.8. Although the velocity in the system is higher with stirrer 1, the velocity above the tablet for stirrer 1 is similar to that of stirrer 3. The velocity above the tablet with stirrer 2 is very small compared with the other two.
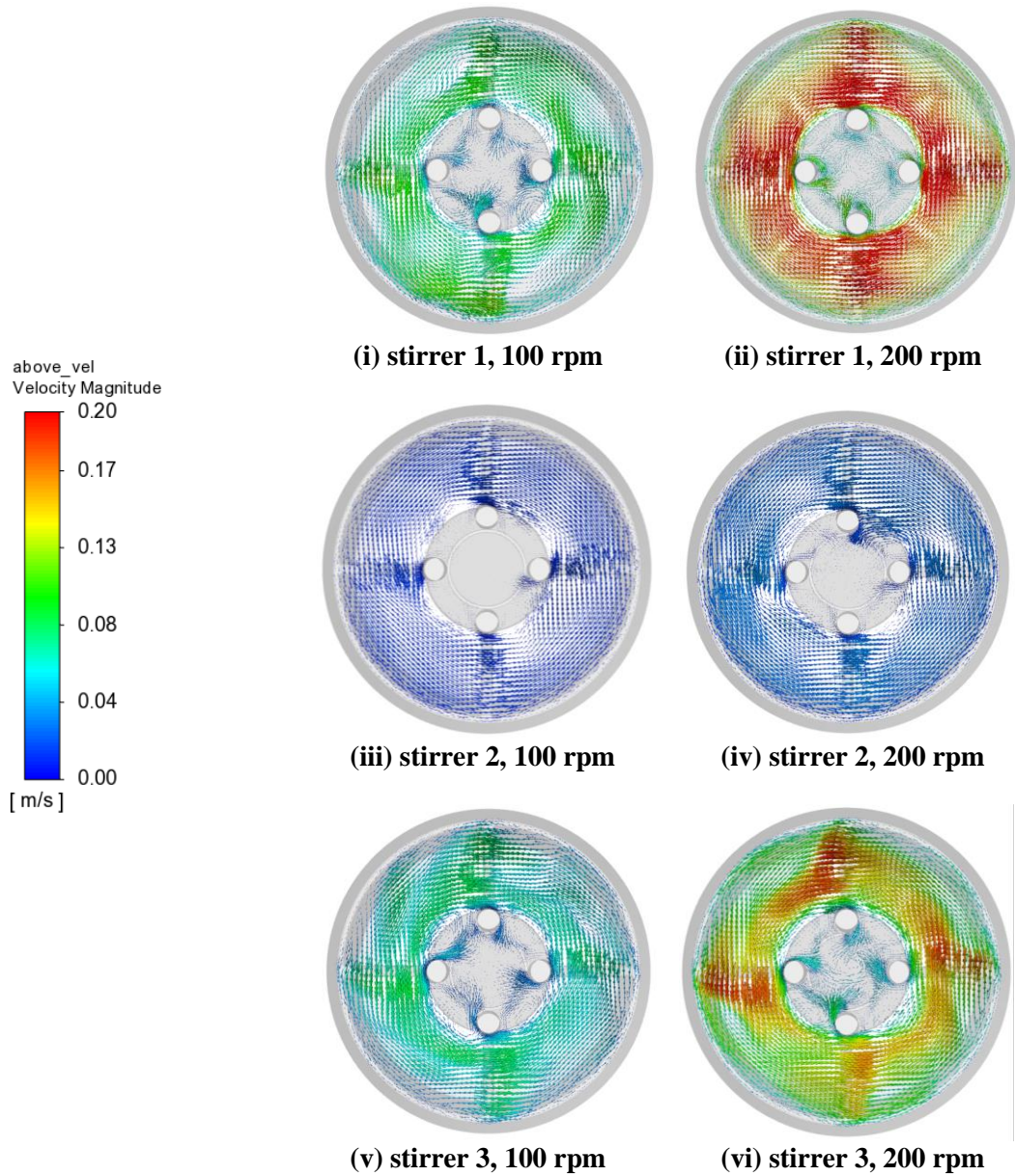
Figure 6.8: CFD predictions of velocity vectors above the tablet for different stirrers at different rotation speeds (100 rpm and 200 rpm) at 20 s.

Fluid strain rate

The patterns of the fluid strain rate are shown in Figure 6.9. The strain rate of the fluid ranges from 0 to 200 s^{-1} while it reaches up to 800 s^{-1} on the tablet, which is in line with the previous predictions of Bai and Armenante [185, 188], and some predicted strain rates for the USP II apparatus shown in Figure 5 of Baxter et al. [193]. The strain rate of the fluid is the highest near the tablet with stirrer 1, while it is the highest near the stirrer with stirrer 2. The strain rate is important as it controls mixing at the small scale and again illustrates the better performance of stirrer 1.

152
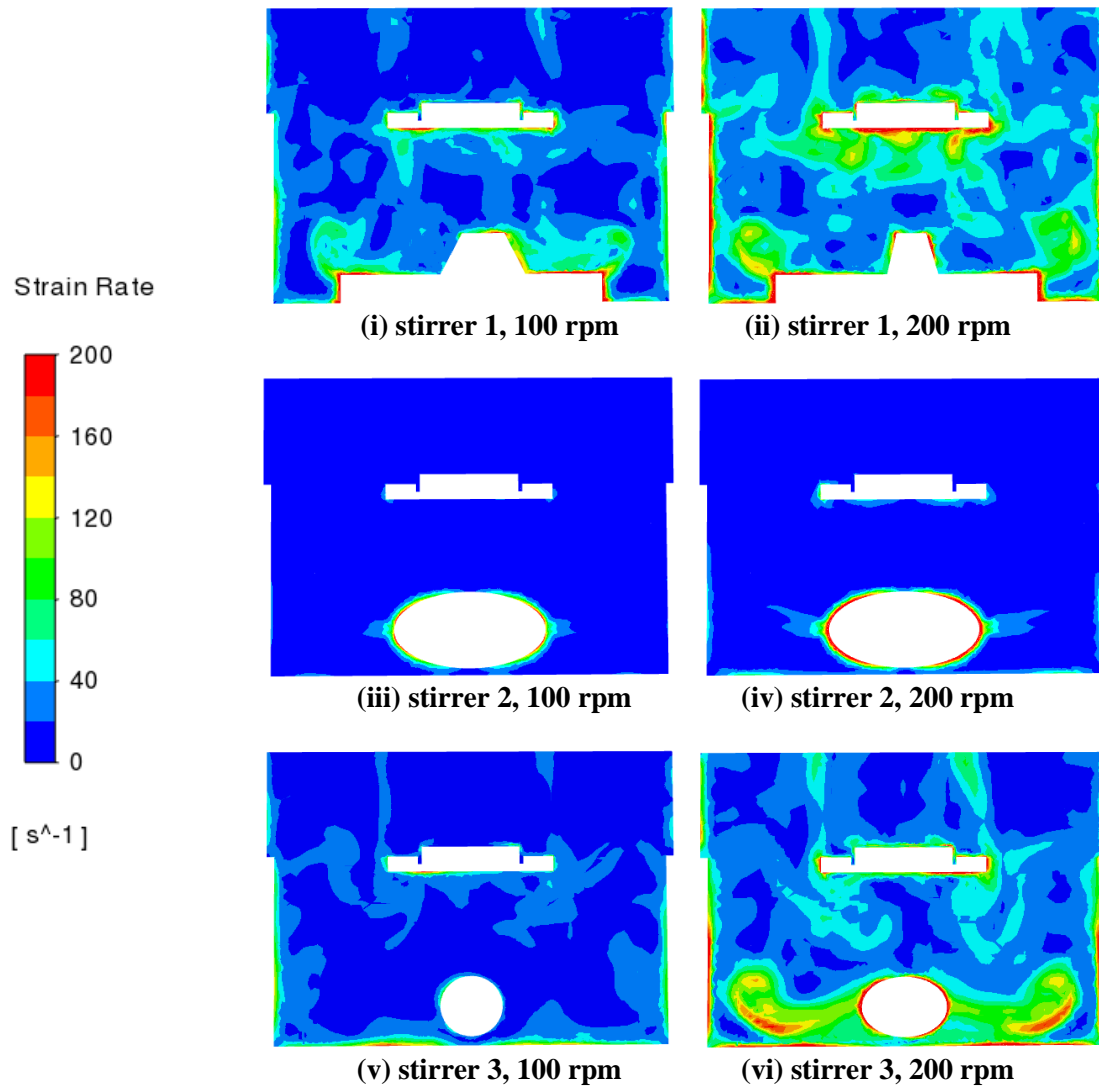
Figure 6.9: CFD predictions of strain rate on the vertical middle cross-section for different stirrers at different rotation speeds (100 rpm and 200 rpm) at 20 s.

Turbulence behaviour

Figure 6.10 shows the wall y^+ value on the tablet and stirrer for stirrer 3 rotating at 200 rpm, which is the case with the highest Reynolds number. The maximum y^+ value in the domain is less than 7 overall and far less than unity on the tablet wall. Therefore, the first point away from the wall is located in the laminar sublayer and the turbulence equations are integrated to the wall rather than a log-law boundary profile being applied. This is important as it means the mass transfer boundary layer is calculated rather than an incorrect log-law being applied at the very low turbulent Reynolds numbers.

yplus
Wall Yplus

■	0.25
	0.22
	0.20
	0.17
	0.15
	0.13
	0.10
	0.08
	0.05
	0.03
■	0.00

yplus
Wall Yplus

■	6.50
	5.85
	5.20
	4.55
	3.90
	3.25
	2.60
	1.95
	1.30
	0.65
■	0.00

(a)   **(b)**
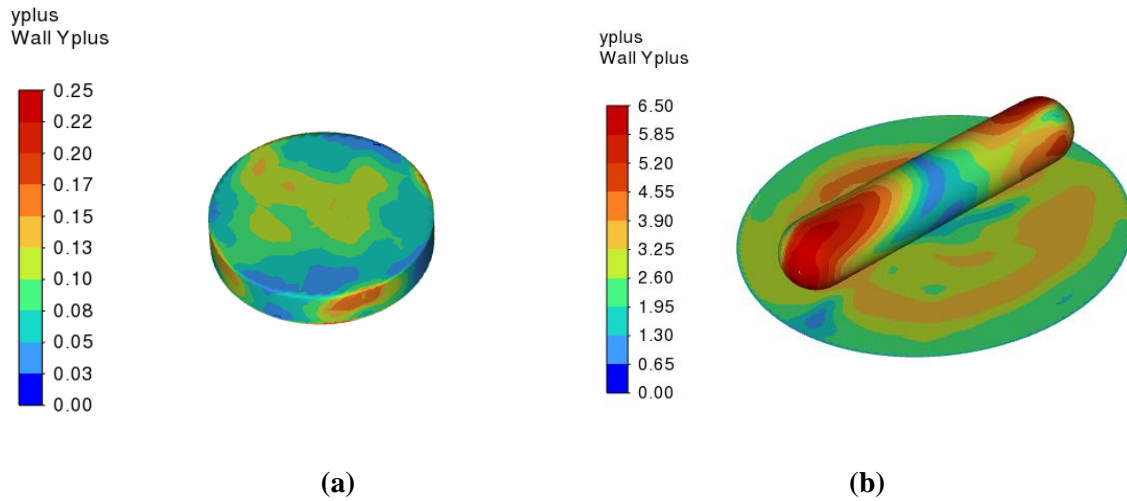
Figure 6.10: CFD predictions of the wall y^+ value on (a) the surface of the tablet; and (b) the surface of the stirrer and the base of the beaker for the stirrer 3 system with a rotation speed of 200 rpm.

Figure 6.11 shows the contours of the turbulent viscosity ratio in the fluid field. The ratio is highest with stirrer 1, followed by stirrer 3 then stirrer 2. With stirrer 1, the highest values are observed above the stirrer. With stirrer 3, the highest values are near the tips of the stirrer. However, in all cases the region around the tablet is unaffected by turbulence.
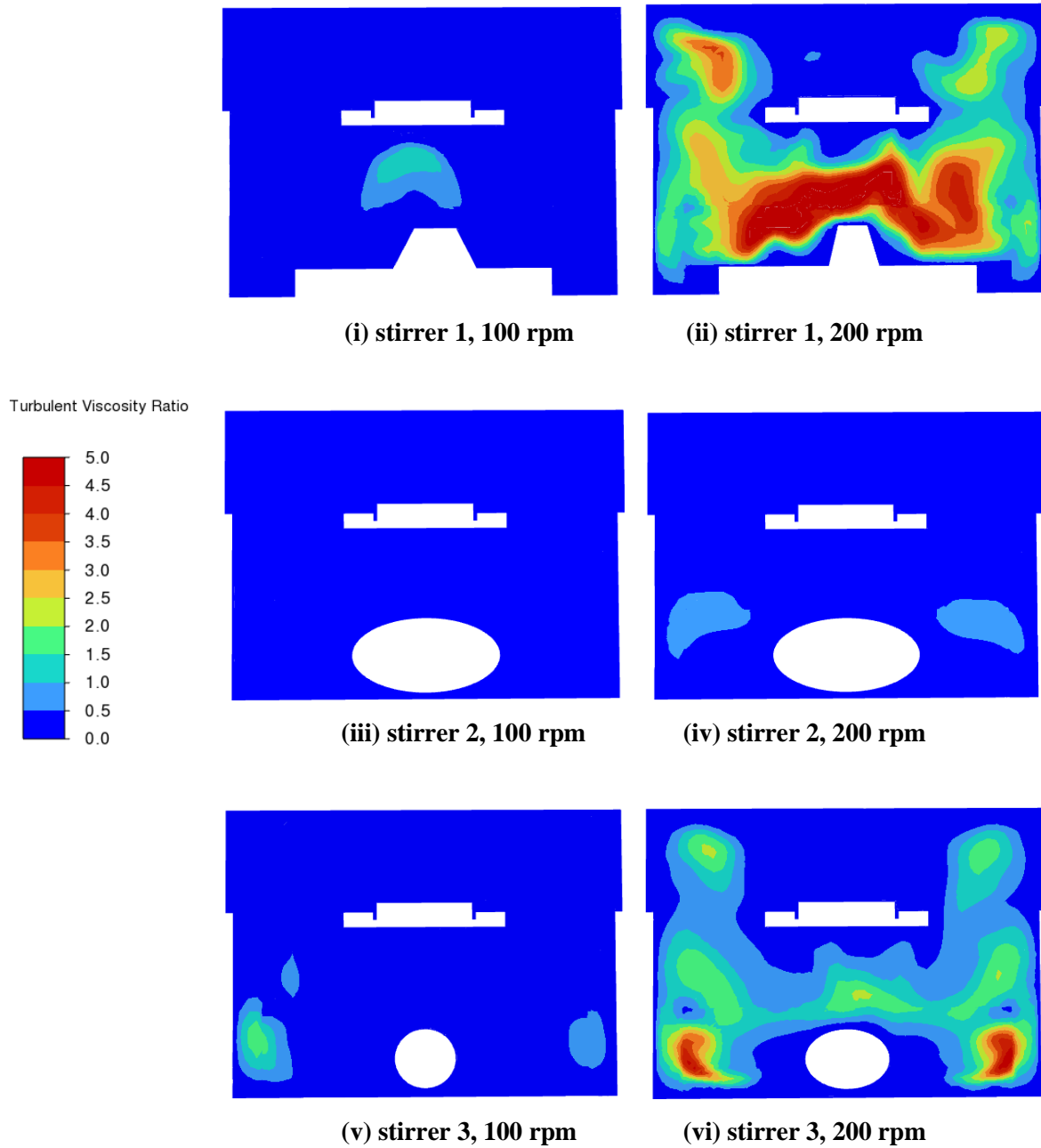
Figure 6.11: CFD predictions of the turbulent viscosity ratio on the vertical middle cross-section for different stirrers at different rotation speeds (100 rpm and 200 rpm) at 20 s.

The turbulence kinetic energy and the turbulent energy dissipation rate in the flow field are shown in Figures 6.12 and 6.13, respectively. The turbulence kinetic energy ranges from 0 to 0.001 m^2 s^{-2} and the turbulent energy dissipation rate range from 0 to 0.1 m^2 s^{-3}. These values are consistent with the values obtained in the previous studies conducted by Bai et al. [185, 189]. When the rotational speed is 100 rpm, the values are small and close to zero. The turbulence levels are higher, consistent with the observed turbulent eddy viscosity ratio, when the rotational speed is 200 rpm and are present mainly in the region above the stirrers. The small spikes at the corners where the rotating and stationary frames meet, seen predominantly

for stirrer 2, are numerical artefacts that arise for some mesh configurations and are hard to avoid.

(i) stirrer 1, 100 rpm   (ii) stirrer 1, 200 rpm

(iii) stirrer 2, 100 rpm   (iv) stirrer 2, 200 rpm

(v) stirrer 3, 100 rpm   (vi) stirrer 3, 200 rpm
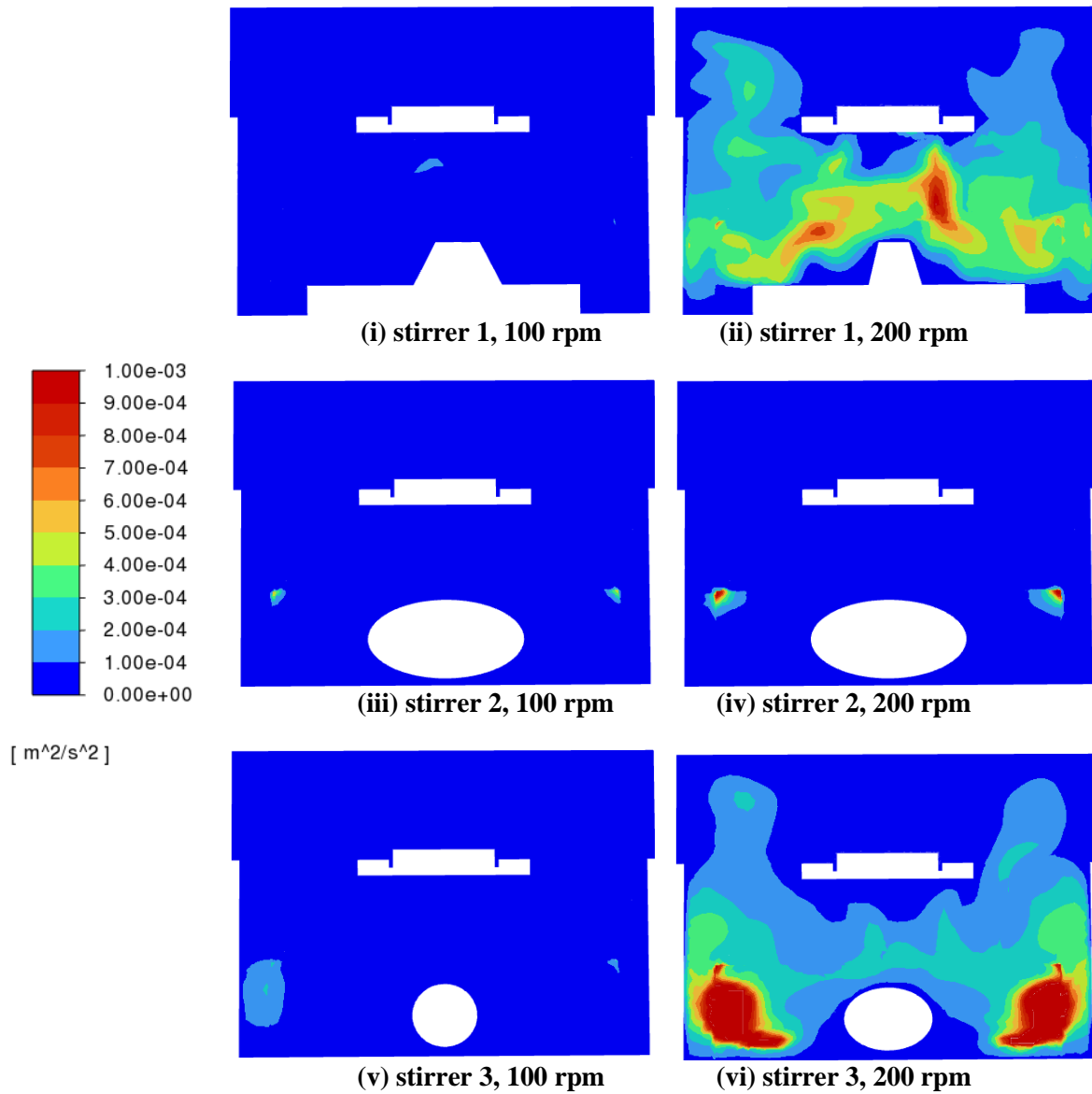
Figure 6.12: CFD predictions of the turbulence kinetic energy on the vertical middle cross-section for different stirrers at different rotation speeds (100 rpm and 200 rpm) at 20 s.
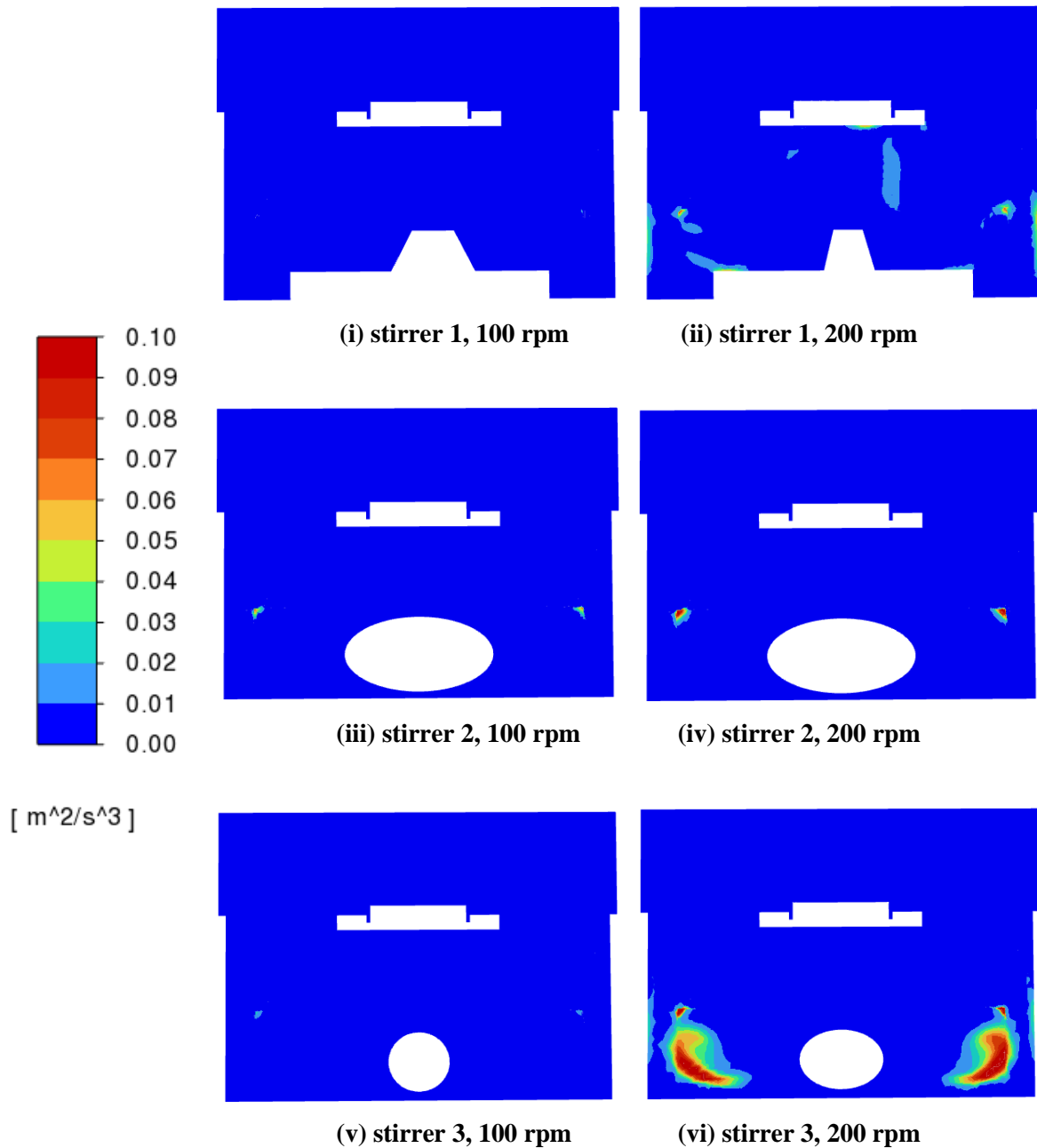
Figure 6.13: CFD predictions of the turbulent energy dissipation rate on the vertical middle cross-section for different stirrers at different rotation speeds (100 rpm and 200 rpm) at 20 s.

It is evident from the results presented above that whilst there is some local turbulence in the vicinity of the stirrer and its discharge, the simulations suggest that mass transfer is occurring in the laminar regime.

6.4.2. Mass-transfer coefficient analysis

From basic mass-transfer theory, the mass-transfer rate is related to the mass transfer area, mass transfer coefficient and the rate of concentration change as defined in equation 6.1.

$$\frac{d\,m_{sol}}{d\,t} = A\,k\,(C_s - C_b) \tag{6.1}$$

where m_{sol} is the mass of benzoic acid transferred from the tablet to the bulk solution, A is the interfacial area between the tablet and solution, taken as the sum of the top and side areas of the tablet here, k is the overall mass-transfer coefficient, C_s is the saturation concentration of benzoic acid at the tablet surface, and C_b is the concentration of benzoic acid in the bulk solution, derived from the simulation results. Data from the last second of the simulation were used to calculate both $\frac{d\,m_{sol}}{d\,t}$ and C_b.

The mass-transfer coefficients are calculated from the simulation results based on equation 6.1 and compared with the experimental results from Langrish et al. [178], as shown in Table 6.1. Both experiment and simulation agree that stirrer 1 provides the highest mass-transfer coefficients, followed by stirrer 3 and then stirrer 2. The values from the simulation are lower than the experimental values overall but within acceptable ranges. The mass-transfer coefficients range from 1.33×10^{-5} to 4.48×10^{-5} m s^{-1} in the experiment and from 6.33×10^{-6} to 2.89×10^{-5} m s^{-1} in the simulation.

Table 6.1: Comparison of estimated mass transfer coefficients (m s^{-1}) between experimental and simulation results. The experimental data are from Langrish et al. [178].

Speed (rpm)	Stirrer 1		Stirrer 2		Stirrer 3	
	Experiment	Simulation	Experiment	Simulation	Experiment	Simulation
0	5.21×10^{-6}, 4.55×10^{-6}	4.11×10^{-6}				
100	3.86×10^{-5}, 3.60×10^{-5}	1.74×10^{-5}	1.56×10^{-5}, 1.33×10^{-5}	6.33×10^{-6}	2.23×10^{-5}, 1.94×10^{-5}	1.40×10^{-5}
200	4.48×10^{-5}, 4.33×10^{-5}	2.89×10^{-5}	1.87×10^{-5}, 1.48×10^{-5}	8.99×10^{-6}	3.47×10^{-5}, 3.44×10^{-5}	2.32×10^{-5}

6.4.3. Dimensional analysis

The mass transfer data are further investigated using dimensional analysis, including the calculation of the Reynolds number, Sherwood number, Schmidt number and power number.

The Reynolds number for the tablet (Re_t) is the ratio of inertial forces to viscous forces in the fluid, defined by:

$$Re_t = \frac{\rho \, u \, L_t}{\mu} = \frac{\rho \, N \, L_s \, L_t}{2\mu} \tag{6.2}$$

where ρ is the density of the solution, μ is the viscosity of the solution, u is the characteristic speed, defined as $N \, L_s/2$ in this study, L_t is the length scale of the tablet which is taken as the tablet diameter (0.013 m), L_s is the length scale of the impeller which is taken as the impeller diameter (0.034 m for stirrer 1, 0.020 m for stirrer 2 and 0.040 m for stirrer 3), and N is the rotational speed of the stirrer (100 rpm or 200 rpm).

The Sherwood number (Sh) is the ratio of mass transfer by convection to the mass transfer by diffusion, defined by:

$$Sh = \frac{k \, L_t}{D} \tag{6.3}$$

where k is the external mass-transfer coefficient, and D is the diffusivity of the benzoic acid in water.

The Schmidt number (Sc) is the ratio of momentum diffusivity (kinematic viscosity) over species diffusivity, defined by:

$$Sc = \frac{\mu}{\rho \, D} \tag{6.4}$$

The Ranz–Marshall correlation [194], which is widely used to predict the Sherwood number from a sphere, was used in Langrish et al. [178] to give a reference value. It is given by

$$Sh = a + b \, Re_t^c \, Sc^{1/3} \tag{6.5}$$

where $a = 2$, $b = 0.6$, and $c = 0.5$.

The correlations between the Reynolds number of the tablet and the Sherwood number for both the simulations and experiments with different stirrers are shown in Figure 6.14. The Sherwood numbers for tablet dissolution are of the same order of magnitude as that for spheres when correlated against the Reynolds number. The simulation results show good agreement with the

experimental data in that they capture the trends for all configurations. Differences can easily be explained by the fact that the magnetic stirrer in the experiment will not rotate perfectly centred on the axis but tend to wobble, causing improved mixing which is consistent with the excellent agreement in the stationary case.
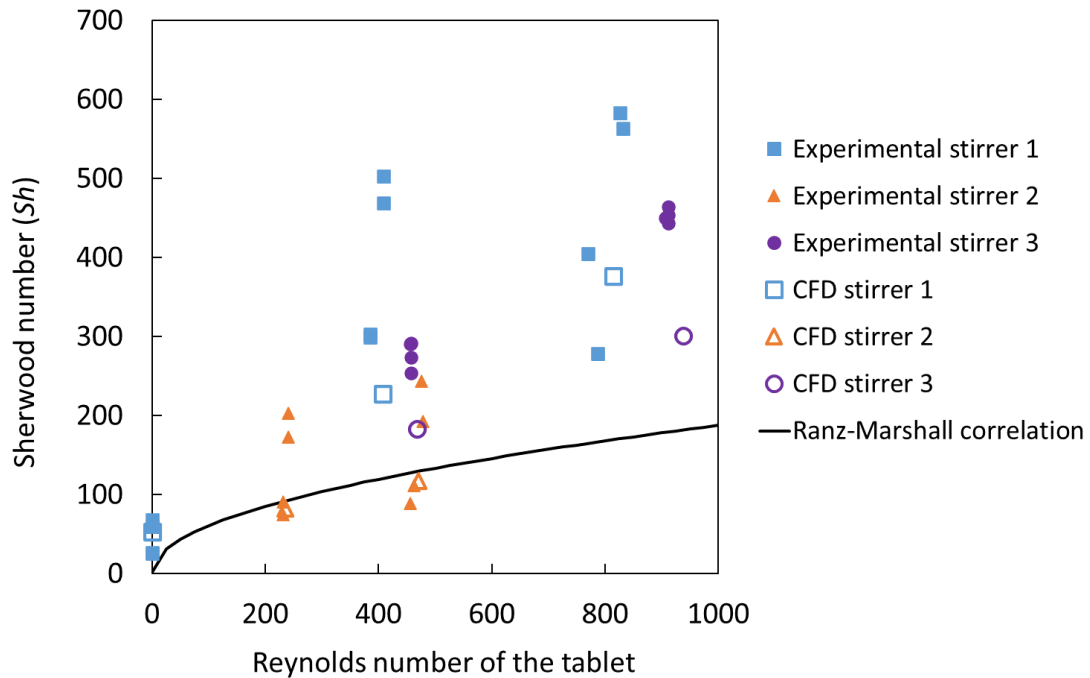
Figure 6.14: The relationship between the Sherwood number and Reynolds number achieved from experiment and simulation results.

The performance of the stirrers can be examined based on the Reynolds number and power number of the impeller [195]. The Reynolds number of the impeller (Re_i) is given by

$$Re_i = \frac{\rho \, N \, L_i^2}{\mu} \tag{6.6}$$

The power number (N_p) is the ratio of external force exerted over the inertial force imparted, defined by:

$$N_p = \frac{P}{\rho \, N^3 \, L_s^5} \tag{6.7}$$

where P is the external power to the stirrer.

The power (P) is determined from the torque (τ) derived from the CFD results based on:

$$P = \tau \cdot 2\pi \cdot N \tag{6.8}$$

160

Figure 6.15 shows the correlation between the Sherwood number and the impeller Reynolds number. It is found that the Sherwood number increases linearly with increasing impeller Reynolds number for different stirrers, meaning that the mass-transfer coefficient increases linearly with the increased rotational speed in this system with different stirrers. Stirrer 1 performs best, whilst stirrers 2 and 3 follow the same trend.
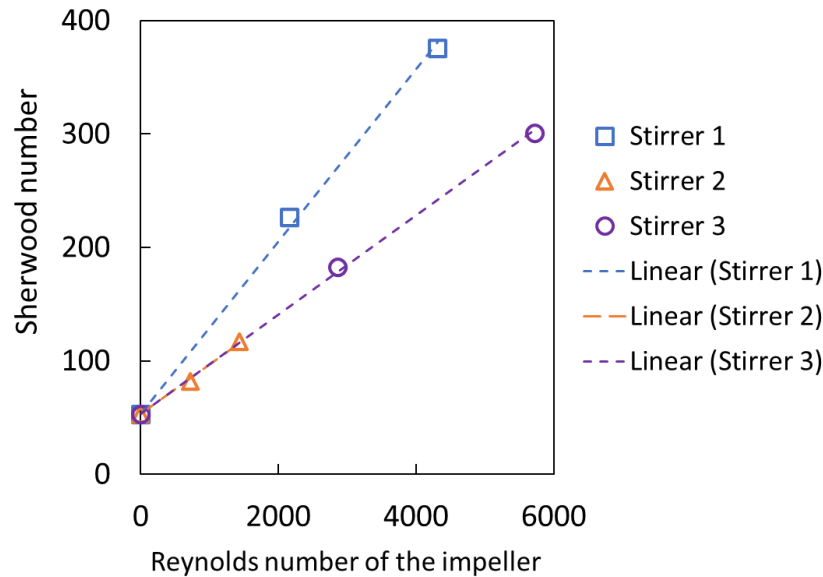
Figure 6.15: Sherwood number as a function of the impeller Reynolds number derived from the simulation results.

Figure 6.16 shows the correlation between the Sherwood number and the average wall shear stress on the tablet, which ranges from 0 to 0.2 Pa for different stirrers and different rotational speeds. Typical correlations show that the Sherwood number increases as the wall shear stress increases and this is evident here too.
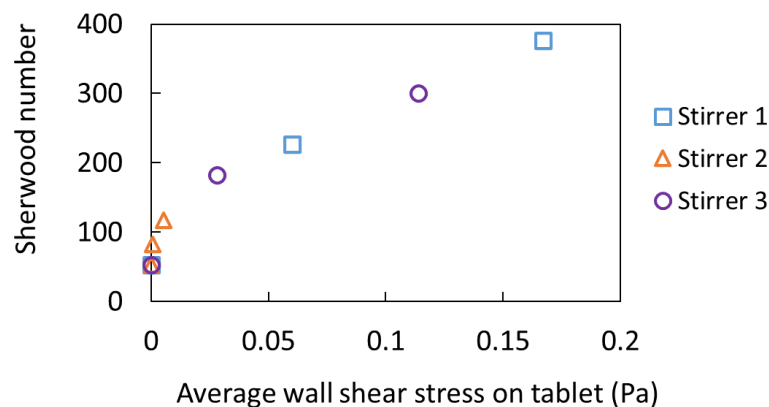
Figure 6.16: Sherwood number as a function of the average wall shear stress derived from the simulation results.

Figure 6.17 shows the relationship between the power number and Reynolds number of the impeller for different stirrers and different rotational speeds. With stirrer 2, the Reynolds numbers are smaller than 2000, and the power number decreases with an increase in the Reynolds number showing laminar flow behaviour. With stirrer 1, the Reynolds numbers are in the range of 2,000 to 4,000 and the power number decreases slowly as the Reynolds number increases. With stirrer 3, the Reynolds numbers range from 3,000 to 6,000 and the power number only changes slightly when the Reynolds number increases. These results are consistent with those expected from compilations of data for many impellers [195].
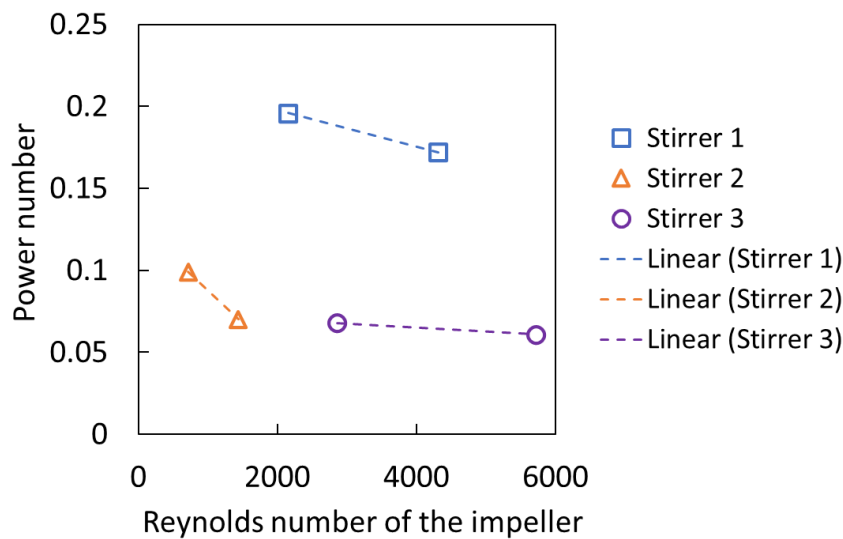
Figure 6.17: Power number as a function of the impeller Reynolds number derived from the simulation results.

6.5. Conclusions

This study presents CFD simulations of an *in vitro* beaker and stirrer system. The estimated mass-transfer coefficients from the simulation match well with the experimental results. Tablet dissolution and mixing behaviour of the system are influenced by both the type of stirrer and the rotation speed. The dimensionless mass-transfer coefficient (Sherwood number) correlates well with the Reynolds numbers and the shear stress on the tablet. The correlations between the power number and the Reynolds number are also presented for different stirrers and follow the expected trends. This work reinforces the utility of CFD simulation to provide additional insights into the digestion process, this time at the food particle scale.

In the next chapter, we return to the comparison of the FVM and SPH approaches, this time addressing buoyancy effects in a real stomach geometry.

Chapter 7. Numerical Simulation of Buoyancy-Driven Flow in a Human Stomach

An early version of work from this chapter was presented at the Australasian Fluid Mechanics Conference held in Sydney, Australia, 5-8 December 2022. A manuscript "X. Liu, S.M. Harrison, D.F Fletcher and P.W. Cleary, Numerical simulation of buoyancy-driven flow in a human stomach geometry: Comparison of SPH and FVM models" was submitted for publication in Applied Mathematical Modelling on 14 February 2023 and is currently under review.

7.1. Introduction

During food ingestion, low-density liquid such as oil floats over the remaining gastric content and forms an upper layer in the stomach, due to buoyancy as shown in Figure 2.10. Oils (or fats), which usually exist in the form of an emulsion, have the slowest emptying rate compared with other food components, such as carbohydrates and protein, from this low-density buoyancy effect because the stomach empties from the bottom [73]. The existence of a buoyant layer at the top of the stomach is not only important for digestion. The floating drug delivery system (FDDS) was developed based on this buoyant behaviour to prolong the gastric residence time [196, 197]. In FDDS, drug carriers have a bulk density lower than gastric fluids and therefore can remain buoyant in the stomach for a prolonged period. The drug is released slowly in the stomach at the desired rate.

In the past two decades, various computational techniques have been applied to model the gastric digestion process in the human stomach numerically [14, 22, 26, 79, 81-84, 112, 114, 115]. Some developed models have implemented gravity [81-84, 112, 114, 115, 198], but none have incorporated buoyancy-driven mixing or de-mixing between different phases despite the importance of density driven stratification to stomach operation.

In this study, a thick oil layer is initially placed below a water layer of equal volume. Once the simulation begins, the buoyancy-driven flow behaviour is observed and analysed. The coupled Biomechanical-Smoothed Particle Hydrodynamics (B-SPH) model developed by Harrison, et al. [83] is used to investigate the buoyancy-driven gastric mixing between the oil and water phases in the human stomach. The multi-density flow was developed and validated using the SPH code in a previous study [124] and therefore the same methodology is applied in this study. A FVM model is also developed for the same mixing system and its solution is used to compare with the SPH results.

The aim of this study is to investigate the flow behaviour of the buoyancy-driven flow process in the stomach, including the initial growth of the flow instability, the separation of the fluid phases, the duration of the separation process, and the velocity of the fluids. Results are shown for both the SPH and FVM models. Sensitivity studies are conducted for both models and their results are compared.

7.2. Numerical models setup

7.2.1. Stomach geometry and gastric content

The geometry used in the models has a generic stomach-shape that has been used previously by Harrison et al. [83] and is shown in Figure 7.1. Gravity acts vertically downwards, as shown in the figure. The modelled stomach has a volume of 580 mL, a total surface area of 0.04 m^2, a fundus diameter of 80 mm and a greater curvature of 320 mm, which is within the range of adult stomach size [12, 199]. The dimensions of the geometry are 122 mm in height, 137 mm in width and 122 mm in depth. The orientation of the geometry is shown in Figure 7.2 and the descriptions are used later in the discussion of the results.
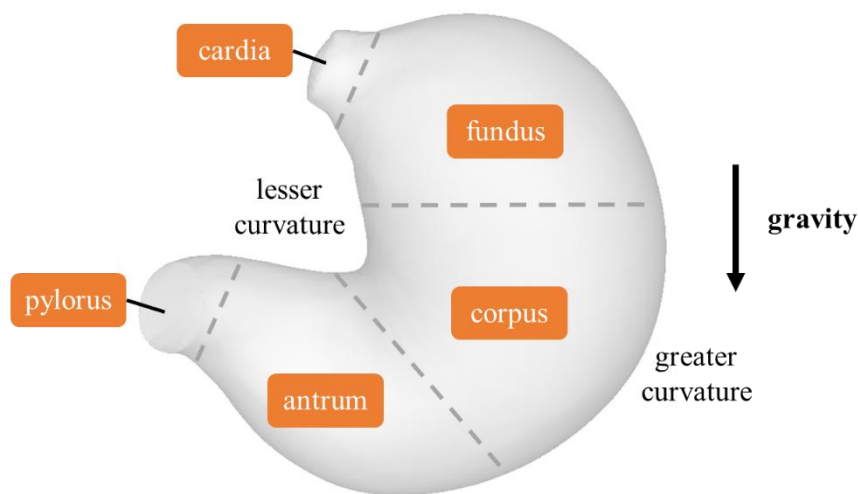
Figure 7.1: The 3D anatomical model of the stomach geometry used in the present simulations.
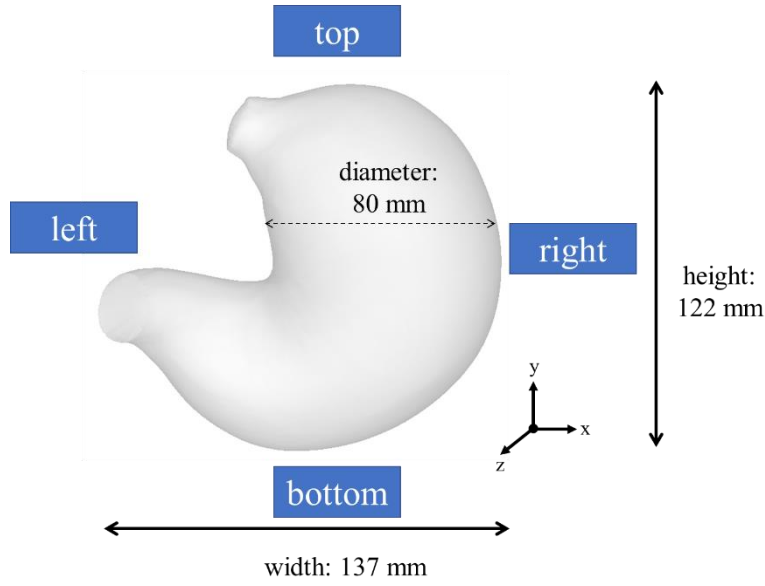
(a) front view
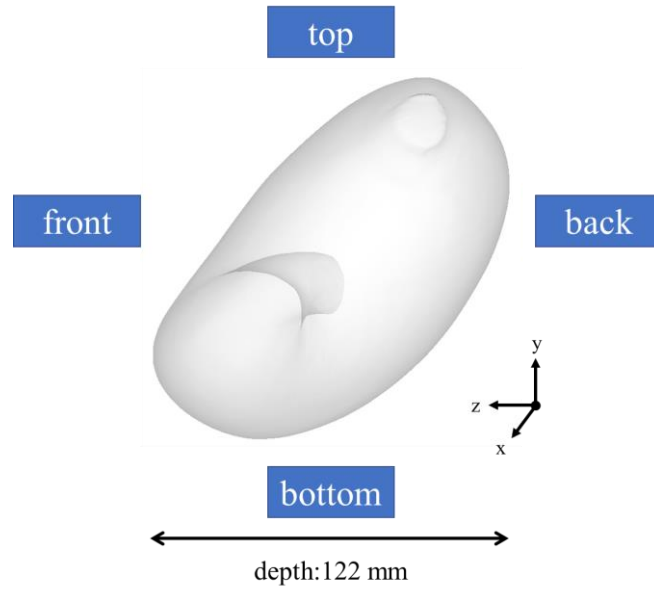
(b) side view

Figure 7.2: Orientations and dimensions of the geometry.

In a real human stomach, the wall can expand, which allows it to enclose a larger volume. The average gastric capacity of a human stomach is measured to be 750 mL [200]. In this study, the stomach wall is assumed to be rigid, and the total volume of the geometry is fixed. The timescale of the density driven flow (finishes with 6 s) is fast compared with the propagation time of an ACW along the stomach length (20 s per cycle) so the deformation and the density driven flow are relatively independent. On this basis the wall deformation was omitted for this study.

The stomach model is initially filled to 80% of its capacity with a total volume of 460 mL, comprising 230 mL oil and 230 mL water. The total height of the fluid is 88 mm, with an oil layer height of 46 mm and a water layer (which is in a wider section of the stomach geometry) with a height of 42 mm as shown in Figure 7.3. The velocity driven by gravity (up to 0.06 m/s as found in this study) is much faster than the velocity of the antral contraction waves (0.0022 to 0.0033 m/s) [109], so this study was deemed to be worthwhile as a first step in combing multiple physics into the stomach model. The Reynolds number of the flow is estimated to be 240, which means the flow is laminar.

Although present in this system, the surface tension force was not included in either simulation. For the FVM, surface tension modelling is available through the continuum force method of Brackbill et al. [201] in which the surface force is converted to volumetric force over a small distance on either side of the interface. However, this method can lead to the production of random velocities, known as spurious velocities or spurious currents at the interface [202]. Attempts to include this force led to unphysical velocities, even when the hexcore grid was used. The effect was small in the region of hexahedral elements but large in the transition layer. Unfortunately, these problems become even worse as the mesh is refined [202]. Although improvements have been made by changing the method of curvature calculation, they cannot be applied to complex geometry [203].

For SPH, a surface tension model is implemented in the code. In this case, it needs good particle resolution to capture the surface curvature [204]. Given the model is not viable in the FVM code and would require some work to test in the SPH code, it was decided to proceed without including surface tension effects explicitly.

The properties of the two fluids are shown in Table 7.1. A modified water viscosity of 0.02 Pa.s is used to avoid the numerical instability of the SPH model (see later for details) and this viscosity is within the characteristic range of viscosity of the typical gastric content (0.01 to 2 Pa.s) [22]. The initial setup of the stomach model is shown in Figure 7.3, with oil placed at the bottom and water placed at the top. The density difference allows the oil to float to the top once the simulation begins. For analysis purposes, the fluid is divided into five layers of the same height. The flow behaviour in each layer is investigated but the layers division has no impact on the actual physical phases of oil and water.

Table 7.1. Properties of two fluid phases.

Phase	Density (kg/m^3)	Viscosity (Pa.s)
Water	1000	0.02
Olive oil	909	0.074
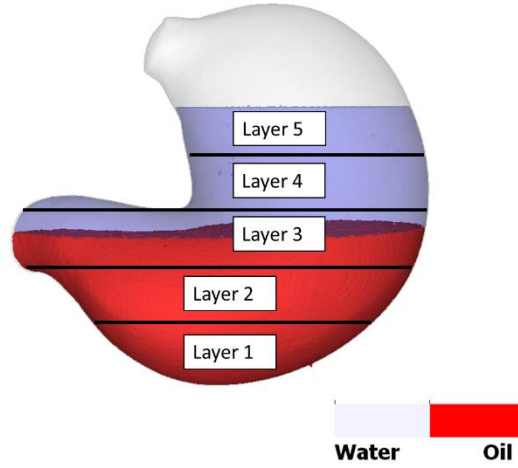
Figure 7.3: The initial layer setup of the gastric content with the water layer coloured in blue and the oil layer coloured in red. The marked layers are used later to capture data for model comparison.

A residual swirling behaviour is observed in the top layer after the fluids have turned over, so data are captured to investigate this using a locally defined cylindrical coordinate system at the centreline of layer 5, as shown in Figure 7.4. The cylindrical coordinates (r, θ) are transformed from the Cartesian coordinate system (x, z) at the free surface.

$$r = \sqrt{(x^2 + y^2)} \tag{7.1}$$

$$\theta = \tan^{-1}\left(\frac{z - z_0}{x - x_0}\right) \tag{7.2}$$

where x_0, and z_0 are the Cartesian coordinates at the midpoint of the free surface.
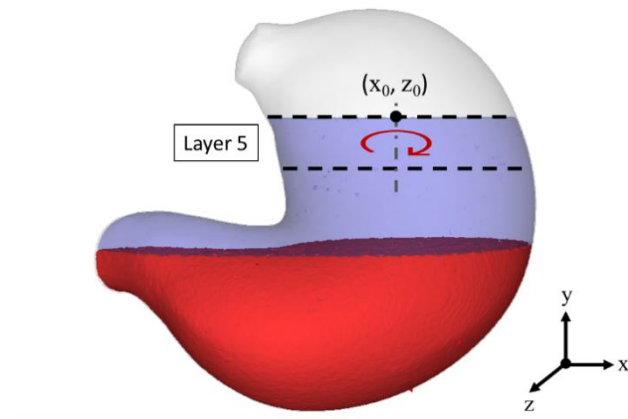
Figure 7.4: Illustration of the radial coordinate system set up in the top layer.

7.2.2. Modelling approaches

The fluid flow is governed by the NSE which apply to a mixture of fluids. Gas mixing occurs on the molecular level, so the NSE can be applied directly to the mixture, with the local composition determined by the species concentrations. However, for a mixture of fluids, such as oil and water, there are macroscopic fluid regions, with the potential for droplets of one fluid to be immersed in another. This situation is treated rather differently in SPH and FVM.

The SPH method treats the fluids as a collection of particles that fill space and Lagrangian equations are solved to track the density, velocity and location of the particles. Each particle has a fixed composition so mass is conserved naturally by the scheme. As the particles move, the interface between the two fluids is moved. With no inherent numerical diffusion, the method is highly suitable for free surface flows.

In the FVM, conservation equations are solved on a finite-size mesh which may contain one single fluid, droplets of one fluid inside another or an interface between the two fluids. To make the NSE suitable for this situation, ensemble averaging is performed and the concept of a volume fraction is introduced, in which the fraction of one fluid in a cell is determined [205]. For a value that is neither 0 nor 1, the cell has both fluids present but no information is available on the topology, i.e., droplets or a sharp interface. Not only is the detailed topology lost but a decision must be made on how to treat the momentum equation. If the problem is one in which there is an interface between two continuous fluids, the homogenous velocity assumption is made and a single velocity field is assumed. This is known as the Volume of Fluid (VOF) method [206] and is widely used for liquid pouring, wave motion and many other free surface

problems. However, if droplets are present in a continuous phase there is no slip between the phases and they cannot separate.

This limitation is avoided, at additional computation cost, by solving separate momentum equations for each phase. This gives a model that applies in theory to any two-fluid situation provided suitable closure relations that are introduced by the phase averaging can be found. A specific version of these equations, known as Multi-fluid-VOF (or MVOF) [207], is used for free surface flows where the two phases can separate but a sharp interface is kept between the phases. The key closure model is the drag law, which is designed to control the velocities of the phases in an optimal manner when they are either mixed or exist as an interface. The MVOF approach is implemented in a test case as a comparison and its effect is discussed later.

7.2.3. SPH model setup

The CSIRO SPH code [90, 134] is used to simulate the oil-water buoyancy problem. The same model equations, with the addition of the gravitational force in the momentum equation, and solution procedure as described in Chapter 3 are applied here. The fluids are treated as being homogeneous and Newtonian, with no special treatment required to handle the two fluid nature of the flow. The weakly-compressible approach to solve the incompressible NSEs are again adopted here. Different from the setup used in Chapter 3, no offset pressure is needed in this study as the pressure is set to zero at the free surface and the hydrostatic pressure gradient ensures that the pressure always remains positive. The cubic-spline kernel is used in this work after assessing the effect of different kernels (see later).

In the base simulation, a particle size of 0.6 mm is used to represent the fluids, resulting in 2.0M SPH particles in total, with 1.0M particles for each fluid phase. The boundary at the stomach wall is represented by a triangulated surface mesh with an approximately equidistant spacing of nodes, as shown in Figure 7.5.
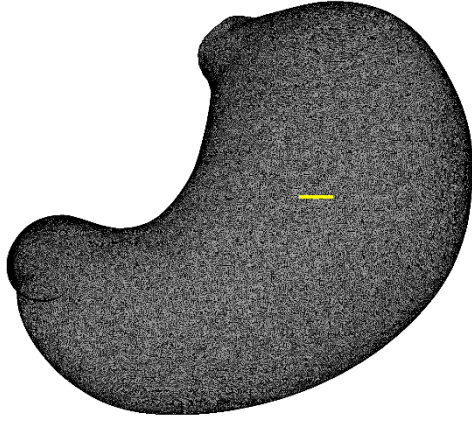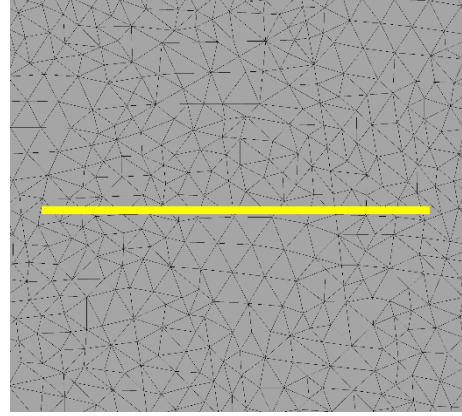
(a) surface mesh   (b) close-up of the mesh

Figure 7.5: Images of the surface mesh used in the SPH base case (the yellow bar is 10 mm long in both images).

7.2.4. FVM model setup

As discussed earlier, the VOF approach [206] is the computationally simplest and cheapest approach to solve the two fluid separation problem when using FVM. In this approach, the two fluids are assumed to be separated by an interface within each cell, so that only one velocity field is needed and the presence of the two phases is tracked using a volume fraction. The conservation equations for mass and momentum for the VOF model are listed below:

$$\frac{\partial \rho_m}{\partial t} + \nabla \cdot (\rho_m \boldsymbol{u}) = 0 \tag{7.3}$$

$$\frac{\partial (\rho_m \boldsymbol{u})}{\partial t} + \nabla \cdot (\rho_m \boldsymbol{u} \otimes \boldsymbol{u}) = -\nabla P + \nabla \cdot \left(\mu_m (\nabla \boldsymbol{u} + \nabla \boldsymbol{u}^T)\right) + \rho_m \boldsymbol{g} \tag{7.4}$$

where $\boldsymbol{u}$ is the fluid velocity, ρ_m is the mixture density, t is time, P is the pressure, μ_m is the mixture viscosity and $\boldsymbol{g}$ is the acceleration due to gravity.

Finally, the mixture properties are calculated from the component properties via

$$\rho_m = \alpha_o \rho_o + \alpha_w \rho_w \tag{7.5}$$

and

$$\mu_m = \alpha_o \mu_o + \alpha_w \mu_w \tag{7.6}$$

The presence of the oil or water is determined using the following advection equation for the oil phase volume fraction

$$\frac{\partial \alpha_o}{\partial t} + \boldsymbol{u} \cdot \nabla \alpha_o = 0 \tag{7.7}$$

where α_o is the volume fraction of oil. The volume fraction of water, α_w, is calculated from the constraint equation

$$\alpha_o + \alpha_w = 1 \tag{7.8}$$

In the MVOF case the conservation equations for mass and momentum become:

$$\frac{\partial \alpha_i \rho_i}{\partial t} + \nabla \cdot (\alpha_i \rho_i \boldsymbol{u}_i) = 0 \tag{7.9}$$

$$\frac{\partial (\alpha_i \rho_i \boldsymbol{u}_i)}{\partial t} + \nabla \cdot (\alpha_i \rho_i \boldsymbol{u}_i \otimes \boldsymbol{u}_i) = -\alpha_i \nabla P + \nabla \cdot \left(\mu_i (\nabla \boldsymbol{u}_i + (\nabla \boldsymbol{u}_i)^T) \right) + \alpha_i \rho_i \boldsymbol{g} + \boldsymbol{F}_{ij} \tag{7.10}$$

where $i = o, w; \quad j = w, o$. Together with the constraint equation (7.10), these form a closed set of equations. There is now one closure relation needed for the drag force per unit volume $\boldsymbol{F}_{ij}$. As the topology of the fluid in a cell is not known this takes a symmetric form that blends smoothly between the limits of the two possible dispersed phases. Details can be found in [208].

The flow domain is reduced in height to contain only the two fluids without an air space above them. Therefore, the top surface is treated as a free-slip wall, meaning that there can be no flow normal to the wall and no stress is applied tangentially to the wall.

Initial work applied a no-slip condition at the stomach wall, but this led to the initial phase in contact with the wall being trapped on the wall in a mesh-dependent manner. The simulated results depended on both the near-wall mesh size and topology. Inflation mesh trapped more fluid than polyhedral mesh at the wall. To remove this sensitivity and to reproduce the behaviour observed in the SPH model, the stomach walls are set to be free-slip. Even though a no-slip boundary condition is used in SPH, it behaves differently in both models. In SPH, the no-slip condition applies only at the wall while the centre mass of the particle, which is located away from the wall, is free to move. In FVM, the no-slip boundary condition is applied at the wall itself and causes fluid to be trapped at the wall.

The initial values for the gauge pressure, x, y and z velocity components are set to zero.

The FVM model is developed using ANSYS Fluent, version 2022R2. The Ansys Fluent Watertight geometry meshing tool is used to generate the fluid mesh. The generated mesh has 126,000 cells and comprises poly-hexcore elements, with a single layer of inflation at the wall and several layers of polyhedral to join these together. The average cell size of the mesh is

1 mm, and the minimum orthogonal quality is 0.41. The individual cell size ranges from 0.003 mm to 6.5 mm. Figure 7.6 shows the computational mesh on the surface and a cross-section through the stomach geometry. The effect of mesh type is discussed later by replacing the poly-hexcore mesh with a polyhedral mesh in a comparison simulation.

<div align="center">(a)   (b)</div>
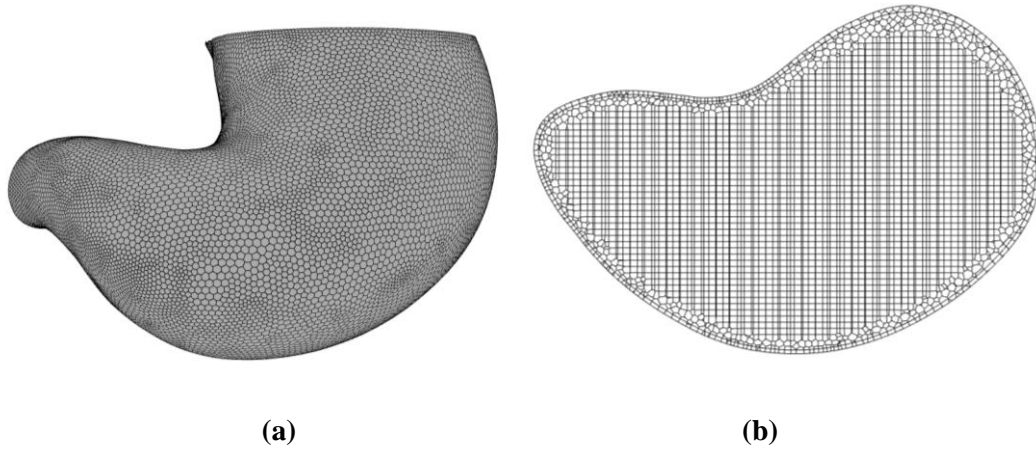
Figure 7.6: Computational mesh on the fluid domain for the FVM,
(a) surface mesh; (b) cross-section of the mesh.

The transient, pressure-based solver is used to solve for laminar flow. To solve for the volume fraction in the VOF model, an explicit formulation is used to track the fluid interface. In this method, the volume fraction is advected in time and then a geometrical reconstruction algorithm is used to distribute the fluid, in any cell where the volume fraction is neither 0 nor 1, to be located next to the adjacent region of the same fluid [209]. The sharp interface option is selected with interfacial anti-diffusion enabled for the advection step in the above algorithm. The implicit body force correction is enabled in the formulation for stability [142], which adds an extra step in the pressure correction formulation to ensure that there is a partial equilibrium of the pressure gradient and gravitational forces [142]. The PISO pressure-velocity coupling scheme [210] is used to solve the flow equations. Time-stepping uses the first-order implicit method [142]. Gradients are determined using the least-squares cell-based option, the pressure is determined using the PRESTO method. The second-order upwind scheme is used for the momentum equations. A time step of 0.005 s is used after conducting a time step independence study, and the total run time for the simulation is 8 s. The maximum iteration number for each time step is set to 30, with 16 iterations typically being needed for convergence. Converged solutions are achieved when normalized residual values for the continuity, x, y, z velocities and volume fraction are below 10^{-3}. The residual values are calculated based on the globally scaled Root Mean Square (RMS) metric.

7.3. Simulation results

7.3.1. SPH

The visualisation of the buoyancy-driven separation process is shown in Figure 7.7 viewed along each of the axes. The simulation begins with the two fluids separated vertically in two quiescent layers. The water is shown in translucent blue, and the oil is shown in opaque red. From 0.0 to 0.5 s, the effect of buoyancy driven by gravity has initiated localized elevation of the less-dense oil to form small peaks at the interface on the left side of the stomach and some larger ripples are present in the middle of the interface.

At 1.0 s, the effect is more pronounced as the small peaks increase in height and the larger ripples grow and form into round topped plumes, which is characteristic of a Rayleigh-Taylor Instability (RTI) [211]. The RTI was first investigated by Rayleigh [212] and Taylor [213], describing the instability of an interface between two fluids with different densities when the heavier fluid is placed above the lighter fluid. Similar RTIs have been captured in other work using SPH models [214-216].

After 1.5 s, the plumes rise and form into strands, and the fluid connecting them to the main body of fluid becomes very thin causing formation of small droplets when they rupture, which then float to the free surface. From 2.0 s, this behaviour continues and some droplets gradually drift to the left. At the same time, a much more extensive bulk flow is observed on the right side, following the pathway of the strands and moves up along the front side of the stomach wall as shown in Figure 7.7(a). From 2.5 to 3.0 s, this large mass of water forming the bulk flow travels up the front of the stomach as shown in Figure 7.7(b), and reaches the free surface, resulting in a swirling flow in the yz-plane. This swirl is created as vertically travelling fluid interacts with the curved walls and the resulting pressure changes the flow direction.

Between 3.0 and 3.5 s, the swirling flow of the liquid continues with most of the oil at the bottom flowing to the top along the front of the stomach wall. Most of the oil accumulates in the top half of the stomach from 4.0 s. After 4.0 s, the remaining oil slowly moves to the top but at a much slower speed. At 5.0 s, the flow is relatively quiescent again with some oil droplets remaining at the front wall and inside the water layer.

(a) front view [video]

174

Time = 0.00 s   Time = 0.50 s   Time = 1.00 s   Time = 1.50 s

Time = 2.00 s   Time = 2.50 s   Time = 3.00 s   Time = 3.50 s

Time = 4.00 s   Time = 4.50 s   Time = 5.00 s   Time = 6.00 s

(b) side view [video]

175
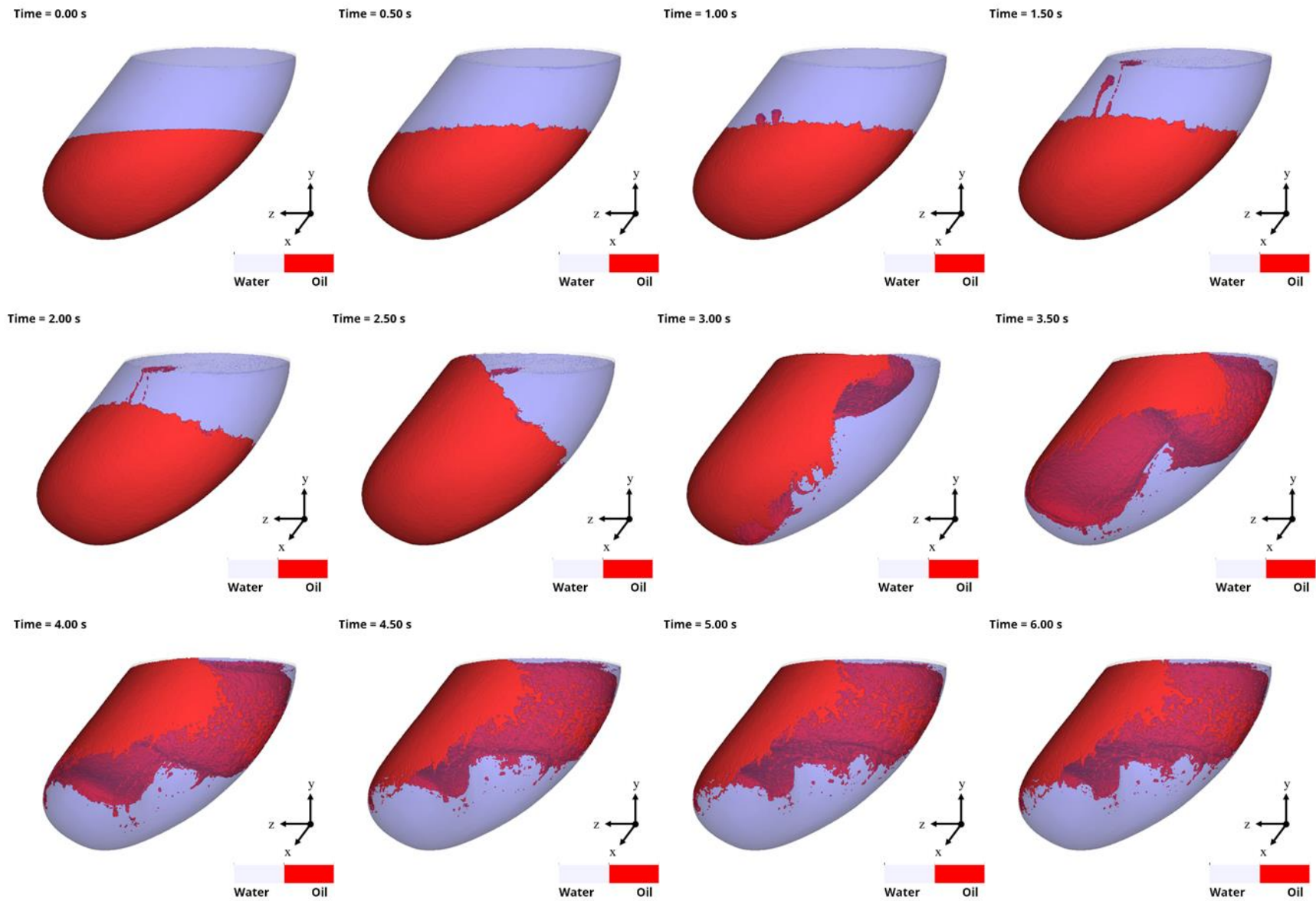
(c) top view [video]

Figure 7.7: Visualisation of the buoyancy-driven separation process of the oil and water in the SPH model.

7.3.2. FVM

The visualisation of the buoyancy-driven separation process in the FVM model is shown in Figure 7.8. In this case, the flow is visualised using the volume rendering option of Ansys EnSight which visualises data throughout the domain rather than colour just one phase as in the SPH graphics. This means that the phase interfaces look much softer compared with the very distinct interfaces in the SPH rendering. The fluid appears to be quiescent until 0.5 s. From 0.5 to 1.5 s, small regions of oil move along the enclosing walls, separate from the bulk fluid. In the meanwhile, some oil starts to rise along the front wall. From 2.0 to 2.5 s, the dispersed oil floats and accumulates at the top and the oil along the front wall is pushed to the back by the curved shape of the wall, resulting in a bulk swirling flow. The remaining oil swirls in the xz-plane in the middle of the stomach during this period. From 2.5 s to 3.5 s, the remaining oil floats to the top and a swirling motion in the yz-plane is observed as in the SPH model, but the strength of the swirling motion seems to be weaker in the FVM. The velocity then gradually dissipates from 3.5 s to 6 s and all the fluid is separated at 6.0 s.
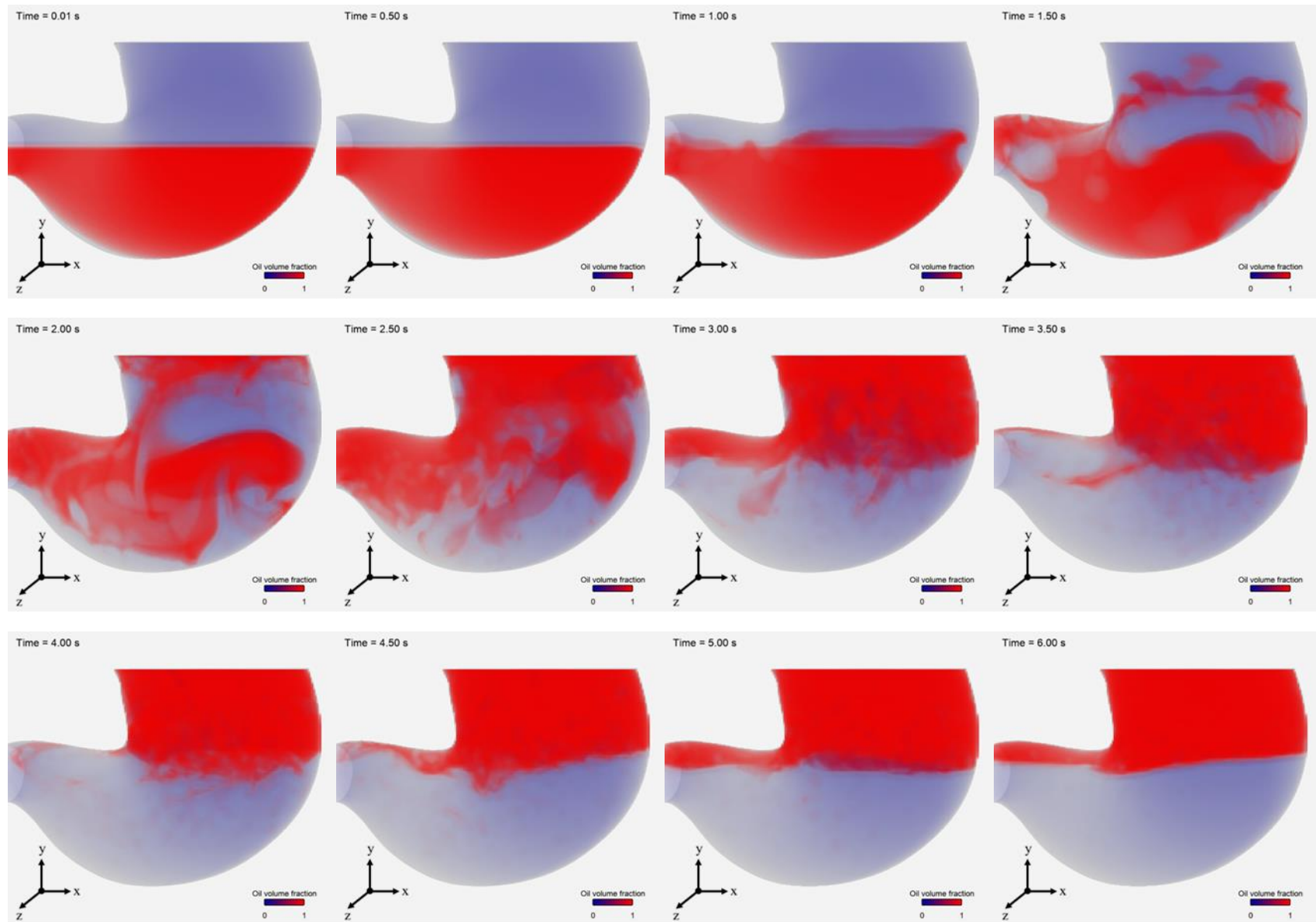
(a) front view [video]

(b) Side view [video]

179
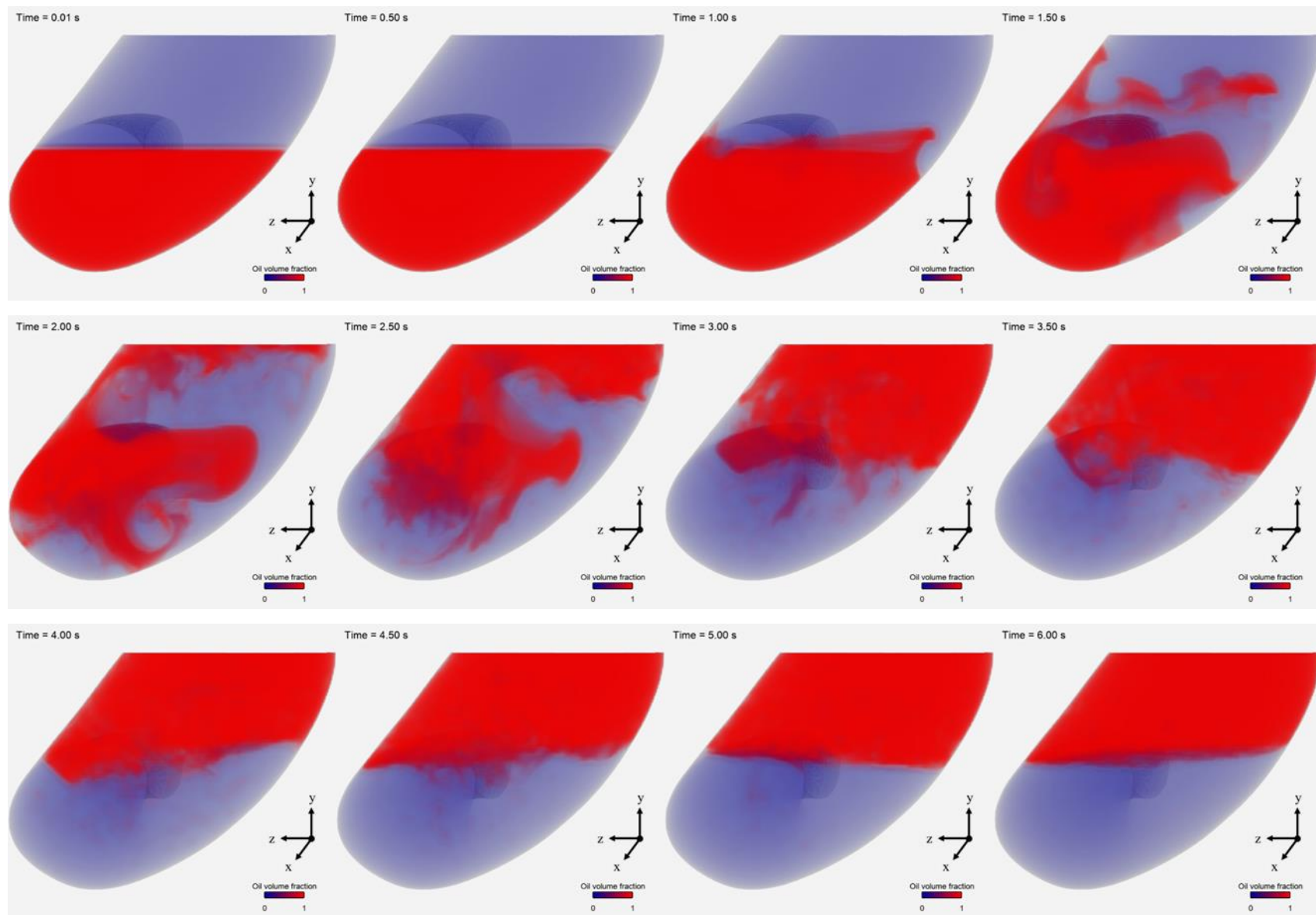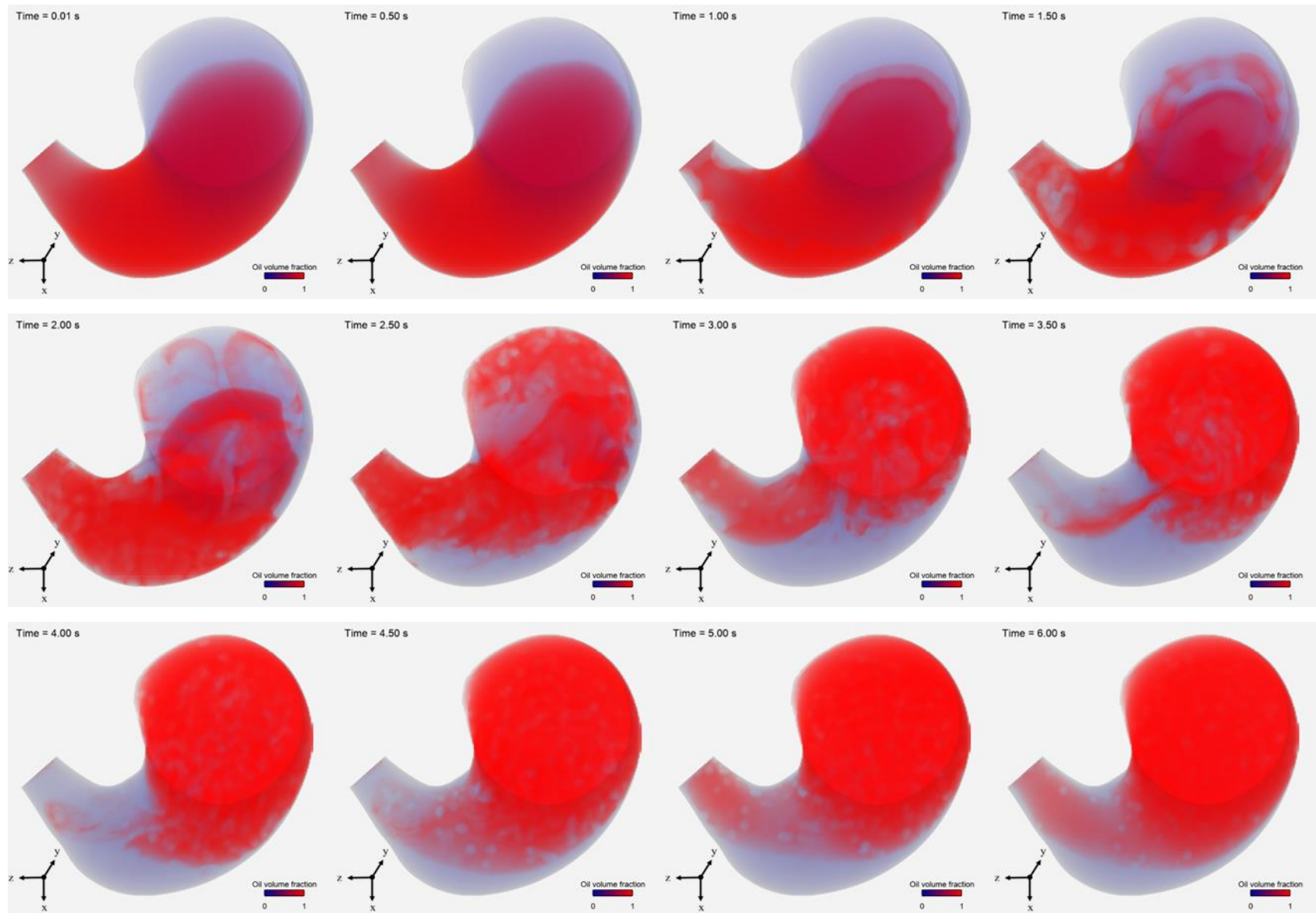
(c) top view [video]

Figure 7.8: Visualisation of the buoyancy-driven separation process of the oil and water in the FVM model.

7.3.3. Comparison

It is evident that the SPH simulation shows a much sharper oil-water interface and captures the buoyant plumes very well. The RTIs observed so clearly in the SPH calculations are absent in the FVM results. Despite the high-accuracy interface capturing scheme used in the FVM the interfaces are much more diffused. However, the FVM model performs better in the asymptotic regime when small residual regions of one fluid are immersed in the other fluid as the separation behaviour of these droplets is more physical, in that they separate in an expected manner. Beyond these differences the nature of the bulk flow that leads to the over-turning of the fluid layers with the oil moving upward as a coherent mass on one side of the stomach is broadly similar.

The flow behaviours in both models are compared quantitatively by considering the time variation of the layer-averaged oil volume fraction, as shown in Figure 7.9. In both models, the growth of the instability becomes visible at around 1.0 s, but the turn-over behaviour in layer 1 occurs more slowly in the SPH simulation than in the FVM. The initiation of flow instabilities is complex, especially for the RTI where there is an initial slow growth of the instability that accelerates rapidly in the non-linear phase. The FVM model introduces perturbations at the interface in the regions of polyhedral mesh which enhance the growth rate, which likely explains the faster formation of the RTI at the interface than was observed in the SPH model. However, the duration of the turn-over event is shorter once this flow behaviour is initiated in SPH, as shown in the layer 1 and 5 plots in Figure 7.9. In layer 2, the oil volume fraction decreases monotonically in the SPH results while some small peaks are observed from 2.5 s to 4.0 s in the FVM plots.

In layer 3, some small peaks are observed from 2.5 s to 4.5 s in SPH. During this time, some fluid continues to rotate until fully settled, which is caused by the effects of inertia. In contrast, for the FVM, there is a sudden increase in oil volume fraction at around 2 s when a large amount of oil enters layer 3, then the oil rapidly floats to the top and the oil volume fraction decreases to 0.3. In layer 4, the SPH change starts later but both methods predict a similar time for the transition from zero oil to being oil dominated.

In layer 5, the behaviour is broadly similar to that of layer 1, except that the SPH result reaches a slightly lower asymptotic limit than that from the FVM. In the SPH model, the oil volume fraction in layer 5 does not reach 100% at the end of the simulation, as shown in Figure 7.9, which means some water particles remain in the top layer. The plot of the summed oil volume

fraction in Figure 7.9 shows that both methods have excellent global mass conservation properties.

In SPH, the smoothed buoyancy force becomes less effective when the width of the fluid fragments is smaller than the kernel width, as the density difference is smoothed over the kernel diameter leading to a smaller magnitude which results in a reduced buoyancy force. The smaller the region of fluid the worse this effect becomes. At the same time, a weak numerically-induced surface tension force is present at the edges of the free surface (where they meet the stomach walls and so have high curvature) which is sufficiently strong to stabilize the motion of the fluid fragments in this region. The buoyancy force exerted by the fluid particles with a smoothed density is then in some cases insufficient to overcome the interface surface tension and therefore some of the fluid particles are not fully settled [204].
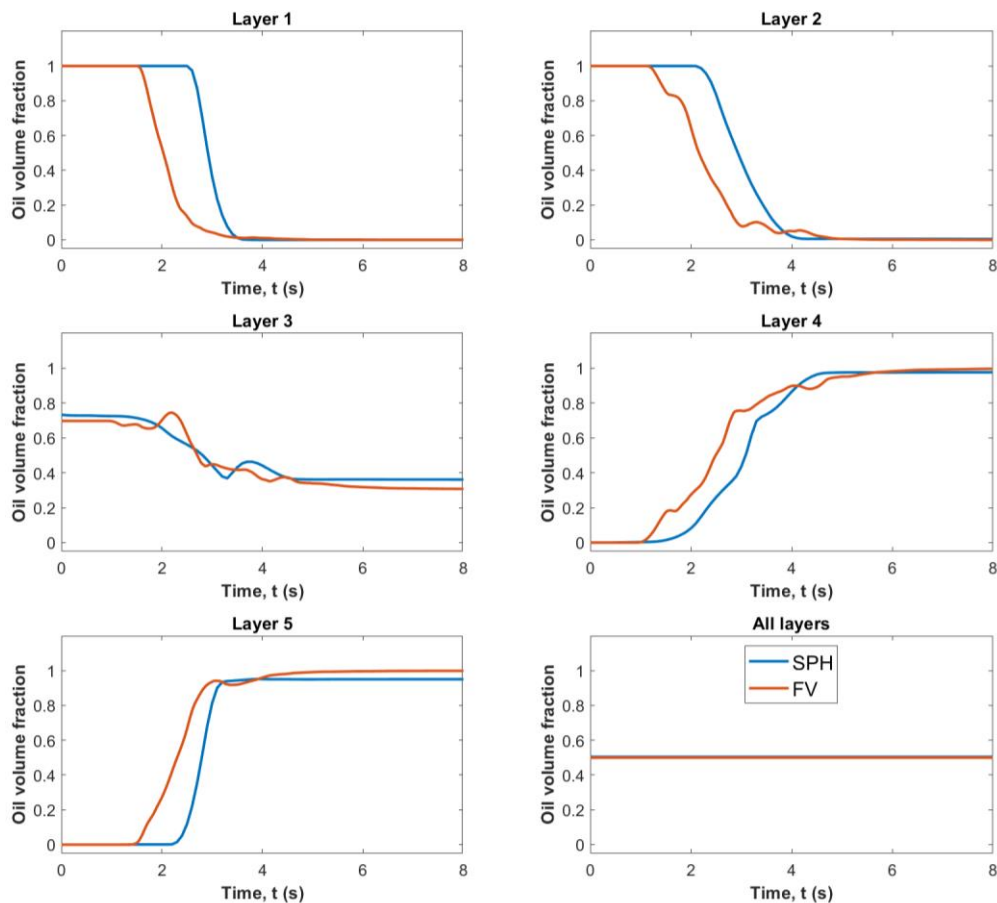
Figure 7.9: Oil volume fraction in each layer as predicted by the SPH and FVM models.

Figure 7.10 shows the average flow speed for each layer as a function of time from both models. The results show similar average speeds in each layer. The maximum speed in both models is around 0.06 m/s and occurs in layer 4. As previously identified, the bulk separation

process in FVM starts earlier than in SPH. As discussed above, the difference in initiation time between the methods is hard to pinpoint as the flow is driven by instability at the interface. As the initial conditions and numerical resolution are different, the initiation and growth phases are necessarily different. The separation process finishes earlier in the SPH results with the FVM model showing some residual motion in layers 1 - 4 at 8 s.
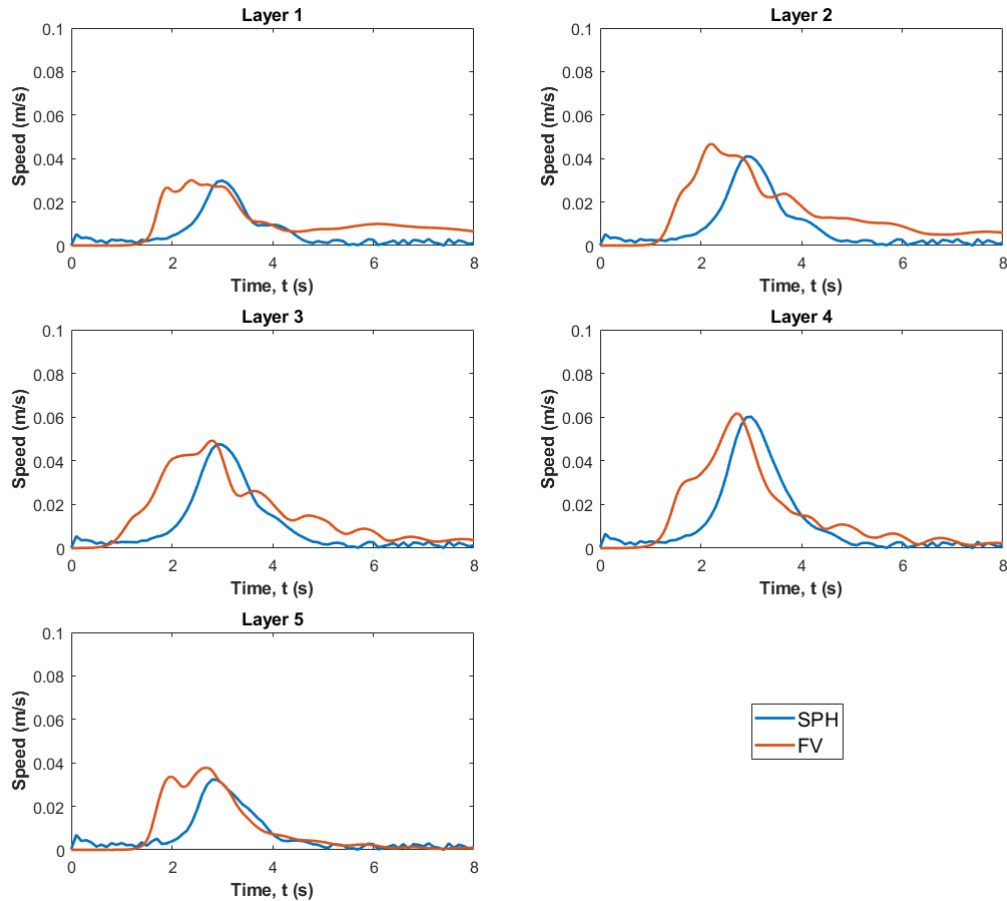
Figure 7.10: Average fluid speed in each layer as predicted by the SPH and FVM models.

A net swirling behaviour is observed in the upper layers of the fluid. This is a consequence of the interaction of the turnover flow interacting with the complex but smoothly varying shape of the stomach wall. To quantify this, the swirling speed in the top layer from both models is shown in Figure 7.11. The swirling behaviour start at around 1.5 s in both simulations. In the SPH model, the first extremum in the swirling speed is at 2.5 s and is positive (resulting from the initial density plumes which are on the front part of the stomach in Figure 7.7(a). From 3.0 s, the swirling motion reverses direction with strong swirling in the negative direction (with a peak speed of around 0.03 m/s at 3.5 s). This is driven by the bulk over-turning motion where a large upwelling of fluid on the front part of the stomach leads to a negative swirl. This swirling motion decays leading to a minor reversal after which the fluid settles and becomes

relatively quiescent. In the FVM, there is no initial positive peak (because of the absence of the early stage fine plumes), but a wider and shallower trough (again resulting from the bulk turnover flow) followed by decaying oscillations. The reduced maximum swirling speed is consistent with the observation that the bulk flow is less pronounced in the FVM.
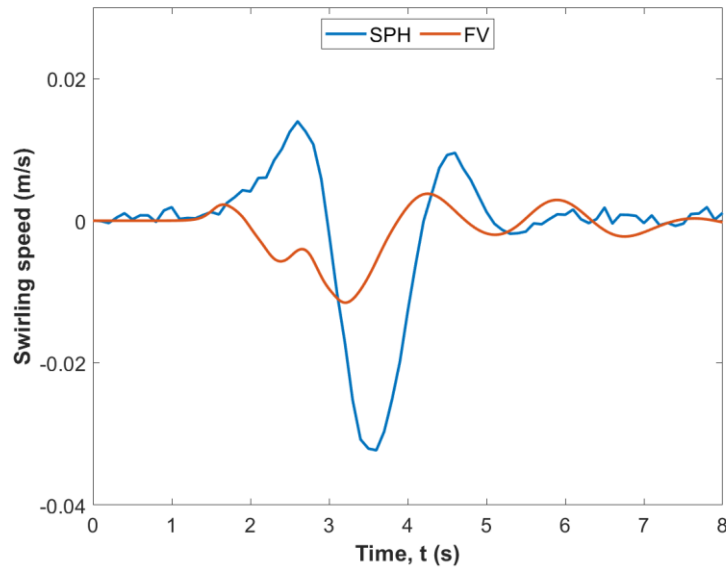
Figure 7.11: Swirling speed in the top layer as predicted by the SPH and FVM models.

7.4. Sensitivity analysis

The effect of numerical parameters is tested and analysed here to examine the sensitivity of both models. In SPH, the results depend on the choice of fluid viscosity, the kernel, and the spatial resolution. In FVM, the effect of fluid viscosity is tested, and a standard check of mesh independence is performed. Variations in parameter values lead to different flow initiations, which is not particularly of interest when conducting sensitivity analysis of the numerical parameters. Therefore, the flow data are shifted so that the starting time of the separation is similar in each comparison, making the comparison of the post-initiation behaviour easier to understand.

7.4.1. SPH

Effect of water viscosity

A study of the effect of water viscosity is reported here for the SPH model. The fluid becomes well-settled when the water viscosity is increased, as can be seen in the results in layer 5 from Figure 7.12. When a water viscosity of 0.001 Pa.s is used, the fluid velocity field is noisy even

after the separation process is finished after 6 s, as shown in Figure 7.13. Importantly, although the peak layer speeds are reduced with increasing viscosity (due to the resulting increased dissipation) the overall patterns are very similar. This requirement for an artificially increased viscosity comes from the need to add more damping to the system in the SPH approach to maintain stability. Therefore, a viscosity of 0.02 Pa.s is used in the base model to provide sufficient minimisation of the noise in the velocity.

Figure 7.12: Oil volume fraction in layers 1, 3 and 5 as predicted by the SPH model for different water viscosities.
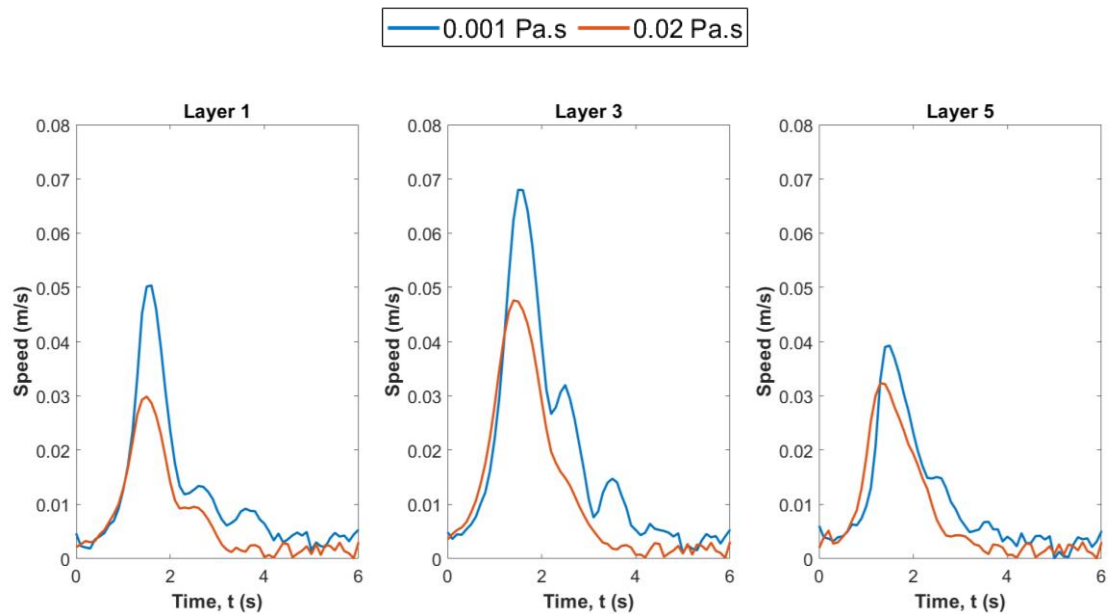
Figure 7.13: Speed in layers 1, 3 and 5 as predicted by the SPH model for different water viscosities.

Effect of kernel choice

Figures 7.14 and 7.15 compare the results achieved using three different kernels: cubic, quartic and Wendland, details of which can be found in Chapter 3, section 3.3.3. Figure 7.14 shows that results for the cubic and Wendland kernels are similar, but there is around 7% of oil remains in layer 1 at the end of the simulation for the quartic kernel. Compared with the other two kernels, the quartic kernel has more difficulty in separating the two phases.

In the case of a multiphase flow, more than one of the fluids are likely to result in the density becoming that of a mixture rather than the pure fluid with the kernel smoothing. The quartic kernel has a larger compact support compared with the other two and therefore the smoothing is over a larger volume, resulting in a lower smoothed density and lower buoyancy force.

Therefore, although the quartic option is the best kernel for the peristalsis problem in Chapter 3 (where enhanced smoothing is beneficial for resolving strong gradients at moderate resolution), it is not the ideal kernel for phase separation (where sharpness of the smoothed density is important). The de-mixing behaviour and the speed in each layer are similar between the cubic and Wendland kernels. However, the swirling behaviour is stronger with Wendland as shown in Figure 7.16, potentially caused by its higher weighting on the nearest particles. In comparison, the cubic kernel is the best for solving the buoyancy-driven flow in this work as it provides the smoothest velocity field and the best phase settling after separation.
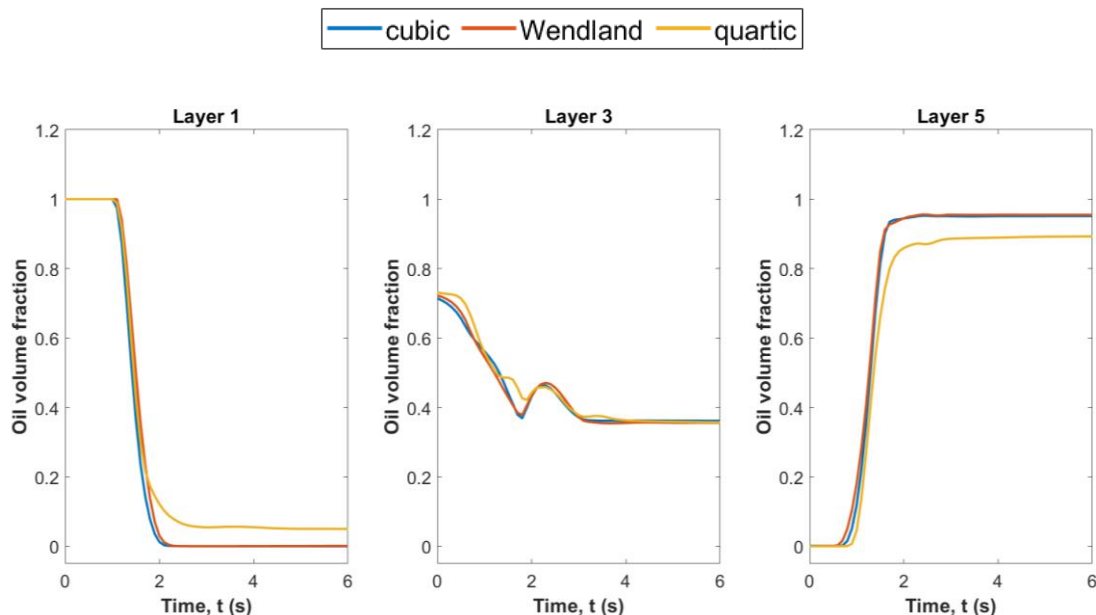
Figure 7.14: Oil volume fraction in layers 1, 3 and 5 as predicted by the SPH model for different kernels.
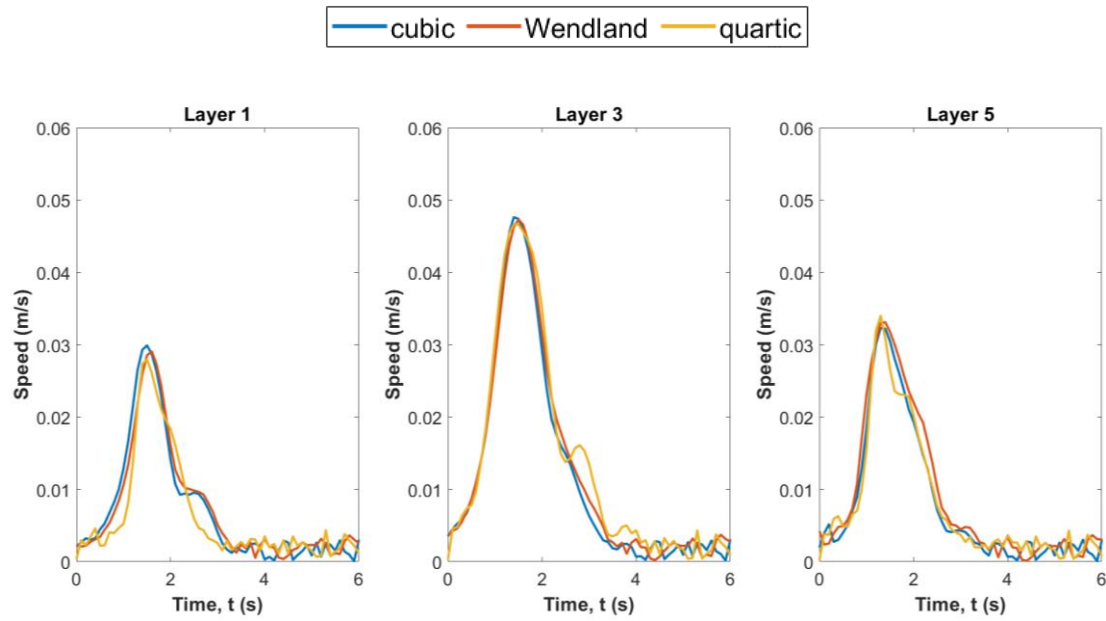
Figure 7.15: Speed in all layers as predicted by the SPH model for different kernels.
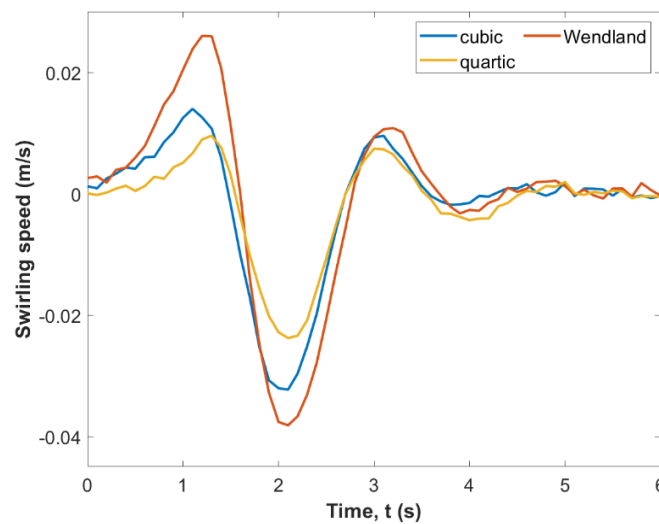
Figure 7.16: Swirling speed as predicted by the SPH model for different kernels.

Effect of spatial resolution

A test of convergence is performed on spatial resolution and the results are shown in Figures 7.17 and 7.18. As the spatial resolution increases, the fluids are settled better in layer 5 and the speed in each layer is less noisy. The results for resolutions of 0.6 mm and 0.5 mm are very close, demonstrating that the 0.6 mm resolution provides a well-converged solution, which is why it was used for the base model.
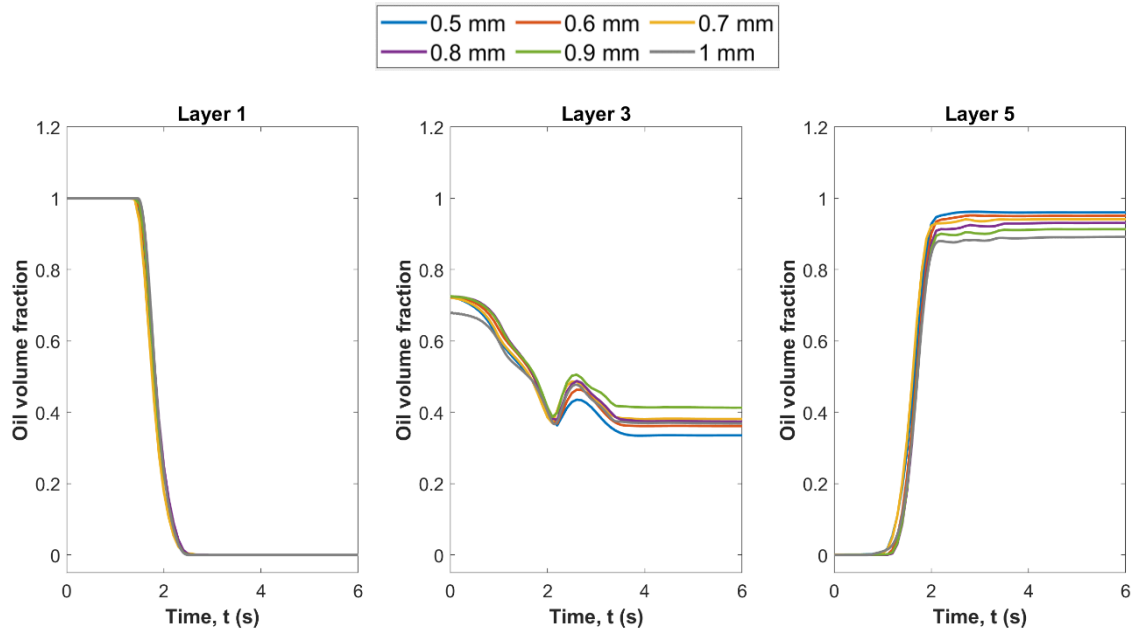
Figure 7.17: Oil volume fraction in layers 1, 3 and 5 as predicted by the SPH model for different resolutions.
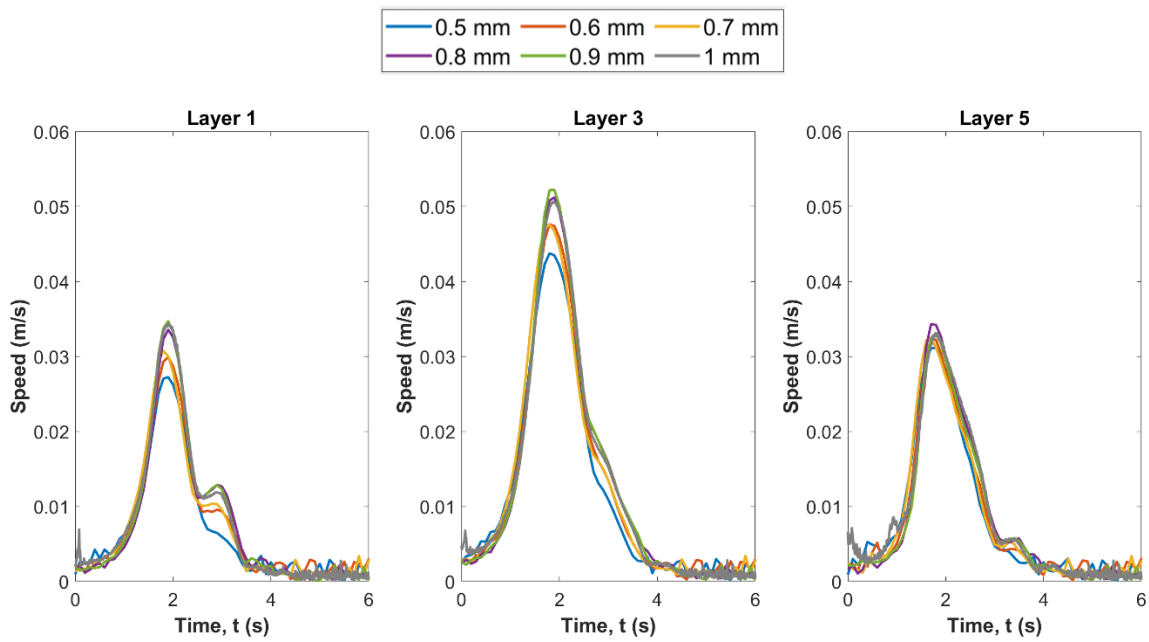
Figure 7.18: Speed in layers 1, 3 and 5 as predicted by the SPH model for different resolutions.

7.4.2. FVM

Effect of water viscosity

The oil volume fraction in layers 1, 3 and 5 are very similar when the water viscosity is changed from 0.001 Pa.s to 0.02 Pa.s in the FVM model, as can be seen in Figure 7.19. The maximum

speed in layer 1 with a water viscosity of 0.001 Pa.s is higher than it is with 0.02 Pa.s but the magnitudes in other layers are very similar, as shown in Figure 7.20. A viscosity of 0.02 Pa.s is used in the base model to match with the SPH model. This invariance of the flow behaviour to this viscosity variation demonstrates that the use of a moderately enhanced viscosity for the purposes of numerical stabilisation has little effect on the dynamics of this system.
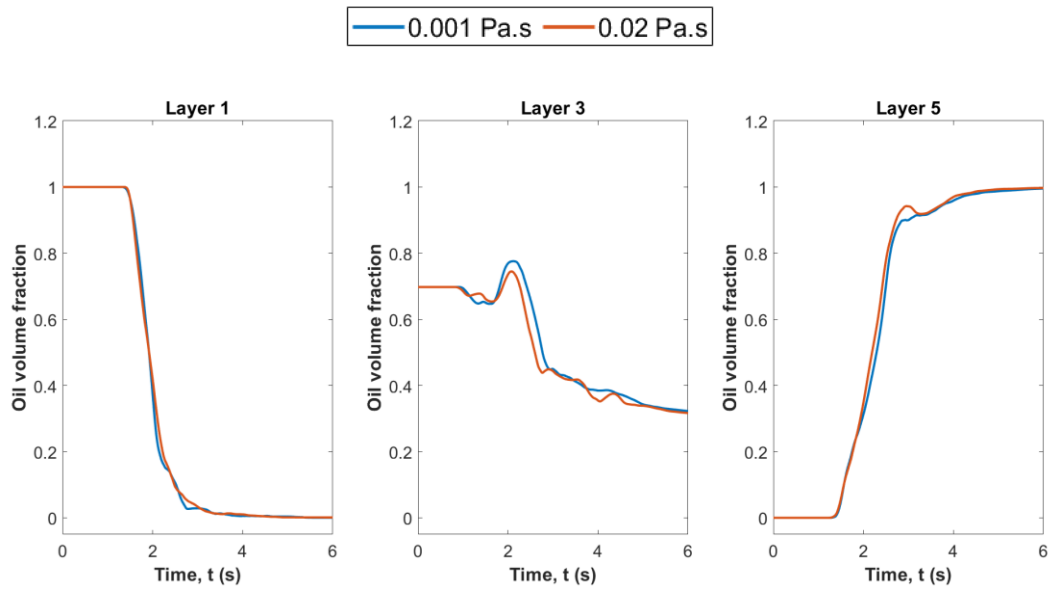
Figure 7.19: Oil volume fraction in layers 1, 3 and 5 as predicted by the FVM model for different water viscosities.
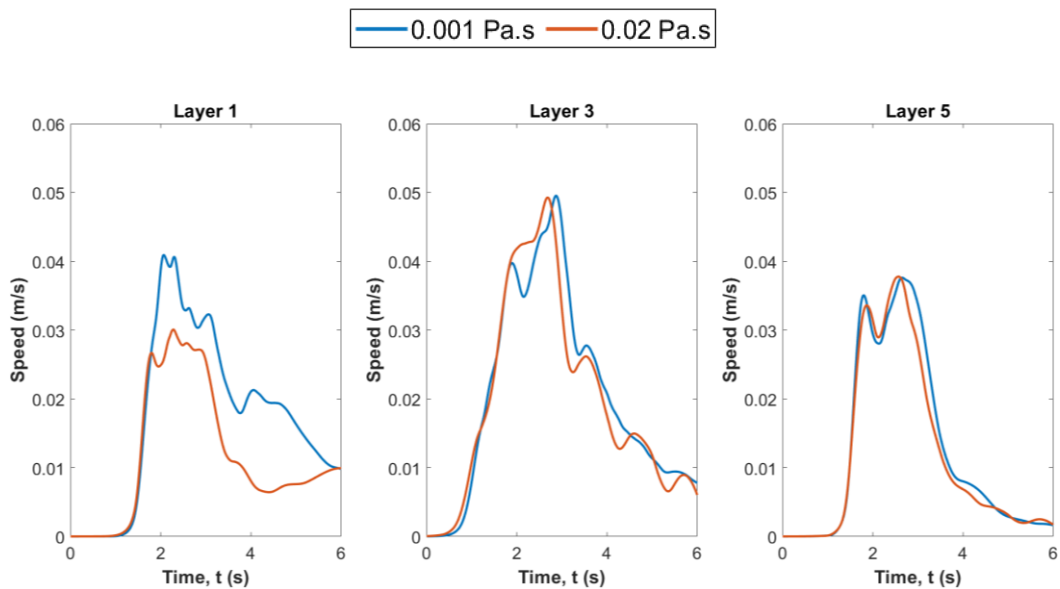
Figure 7.20: Speed in all layers as predicted by the FVM model for different water viscosities.

Mesh independence study

Mesh independence studies are performed to examine the accuracy of the FVM model. Two simulations are made to establish mesh independence, one with a coarser mesh and one with a finer mesh. The coarse mesh has 41,000 cells with an average cell size of 2 mm, the medium mesh has 126,000 cells with an average cell size of 1 mm, and the fine mesh has 377,000 cells with an average cell size of 0.5 mm. Results for these analyses are shown in Figures 7.21 and 7.22. The results from different meshes are very similar but not perfectly aligned, probably due to changes in how well the interface is captured. However, the overall pattern of the oil volume fraction evolution and the speed are very close, meaning that the simulation results achieved are sufficiently independent of the underlying mesh.
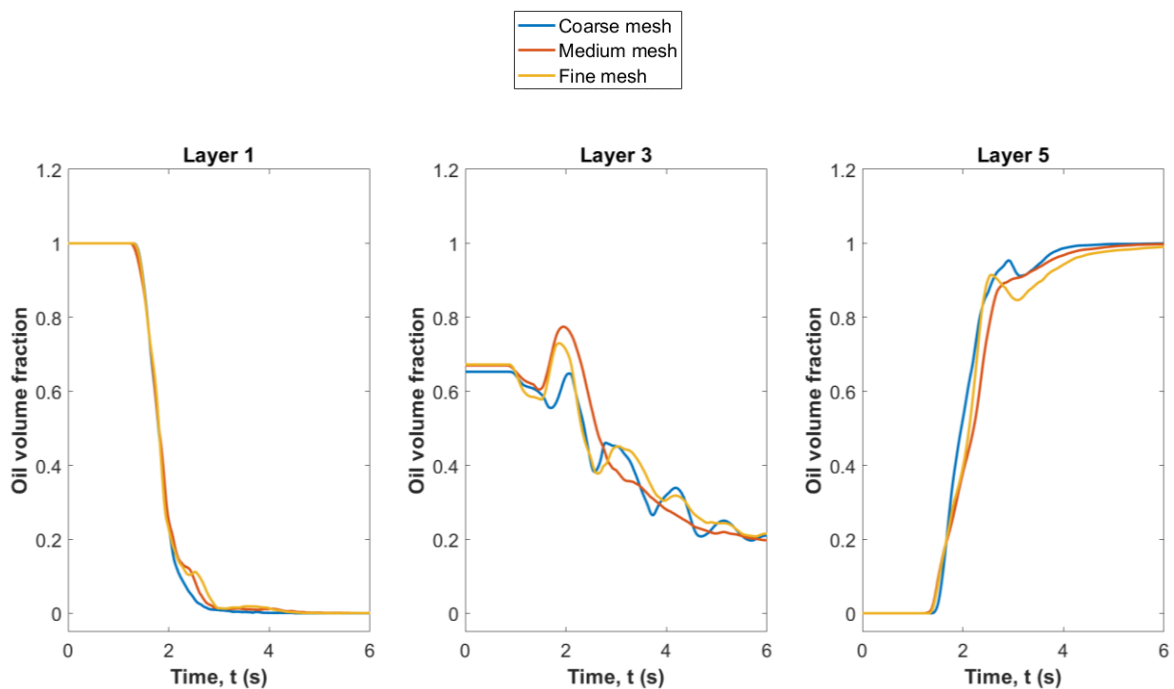
Figure 7.21: Oil volume fraction in layers 1, 3 and 5 as predicted by the FVM model for different mesh resolutions.
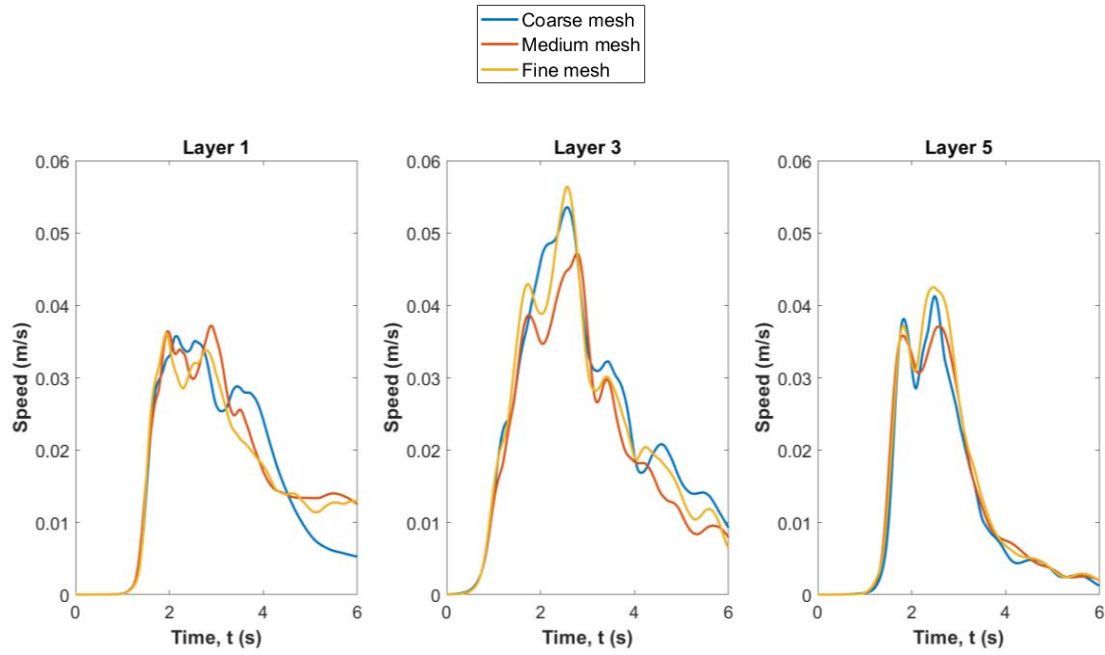
Figure 7.22: Speed in all layers as predicted by the FVM model for different mesh resolutions.

Impact of using the Multi-fluid VOF (MVOF) model

The MVOF approach is applied to the base case model to determine the impact of allowing slip between the oil and water phases. The velocity vectors for both phases are shown in Figure 7.23. At 0.5 s, similar to the VOF model, instability starts to arise near the wall. At 1 s, some oil strands appear, which are not as clearly visible when using the VOF approach. At 5 s, all the fluid is well-separated, and the phase interface is much less diffused than in the VOF results.
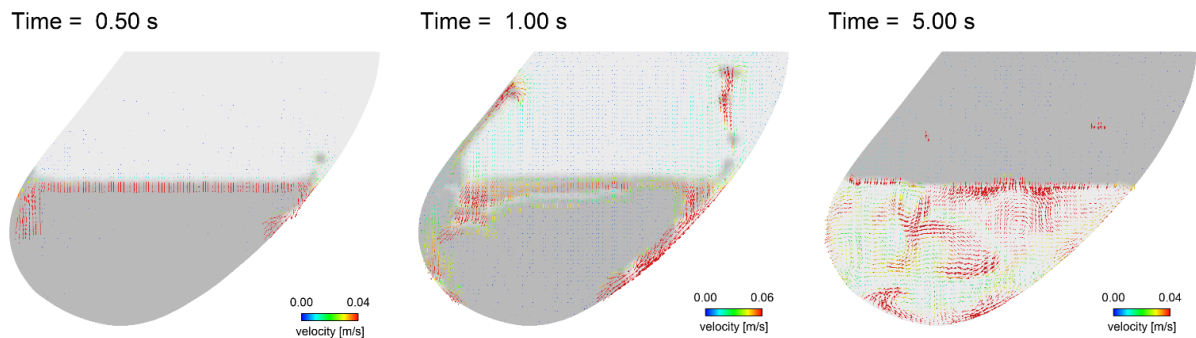
Figure 7.23: Velocity vectors computed using the MVOF model.

Figures 7.24 and 7.25 shows a comparison between the results obtained from the VOF and MVOF approaches. The flow behaviour is very similar for layers 1 and 3. The MVOF model

191

results show a faster separation at layer 5 as the oil volume fraction reaches one and the speed reduces to zero earlier.
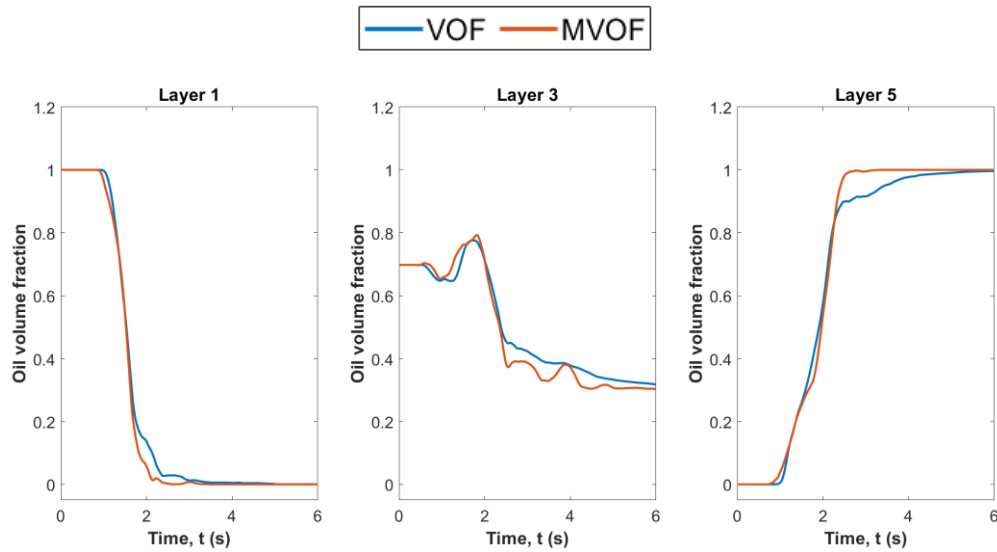
Figure 7.24: Oil volume fraction in layers 1, 3 and 5 as predicted by the FVM model for different VOF approaches.
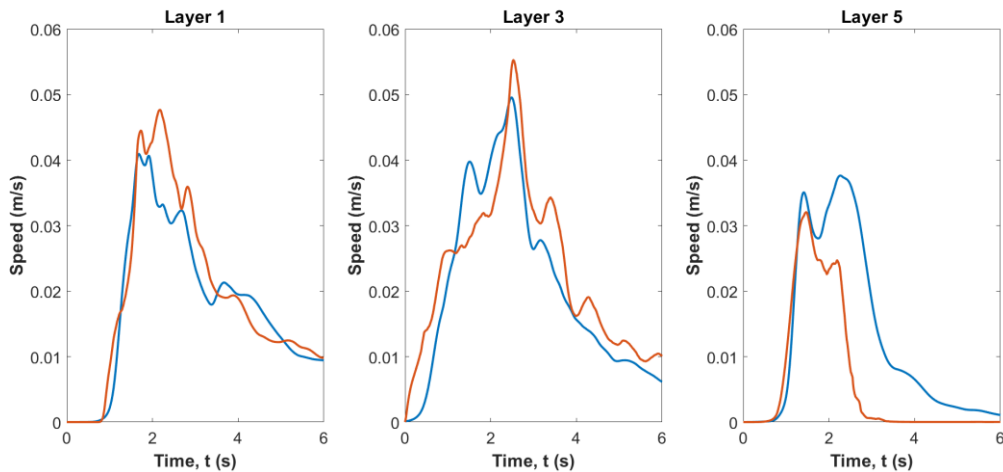
Figure 7.25: Speed in layers 1, 3 and 5 as predicted by the FVM model for different VOF approaches.

Effect of mesh type

In the base model, a poly-hexcore mesh is used to construct the fluid domain. To investigate the effect of the mesh type, a polyhedral mesh with a similar number of elements is used to perform the same analysis. As shown in Figure 7.26, the instability appears near the wall for the poly-hexcore mesh and appears randomly at the interface for the polyhedral mesh at 1.0 s. The location of the instability growth in the FVM is most likely due to the flow being initiated by grid induced errors and the interface then being diffused. Figures 7.27 and 7.28 shows the

comparison between the results obtained using the poly-hexcore and polyhedral meshes. The overall flow behaviour is very similar.

(a) poly-hexcore

(b) polyhedral
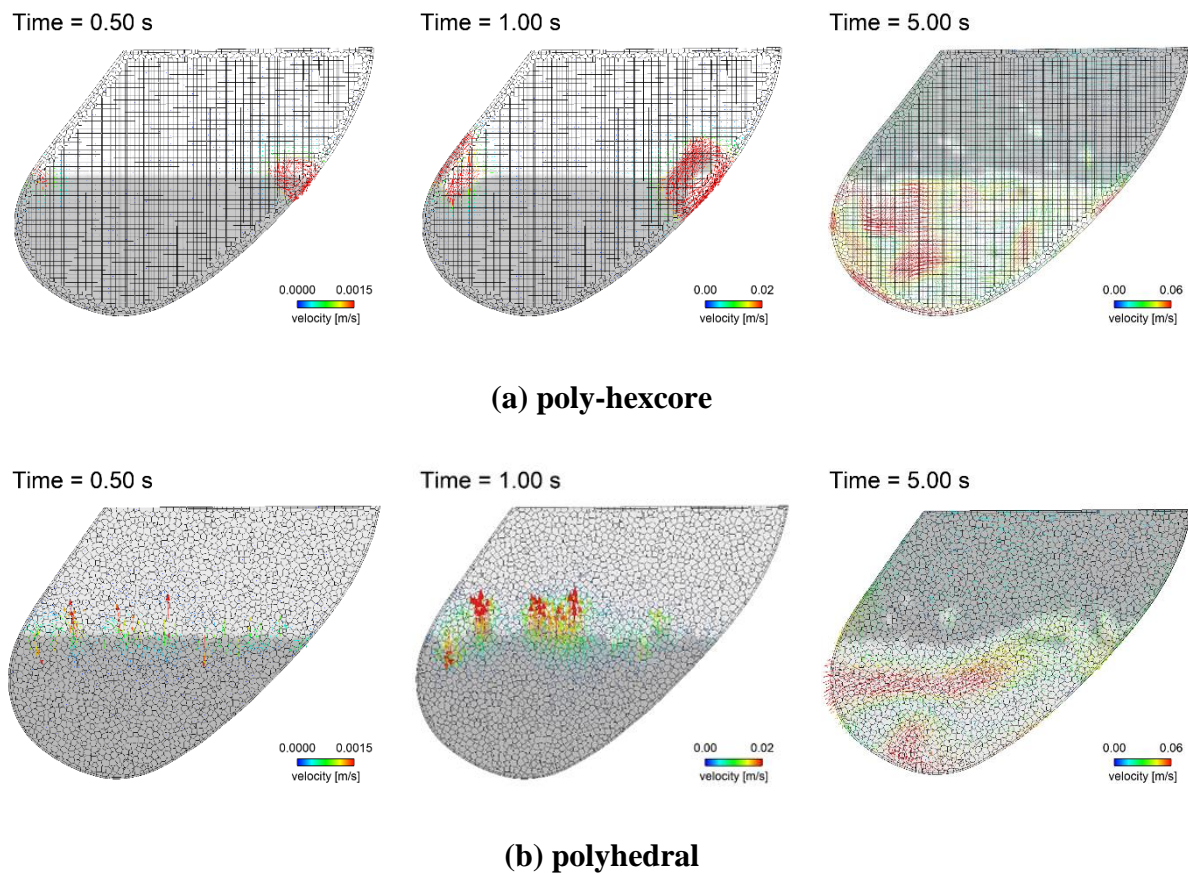
Figure 7.26: Velocity vectors in the VOF model with different mesh types.

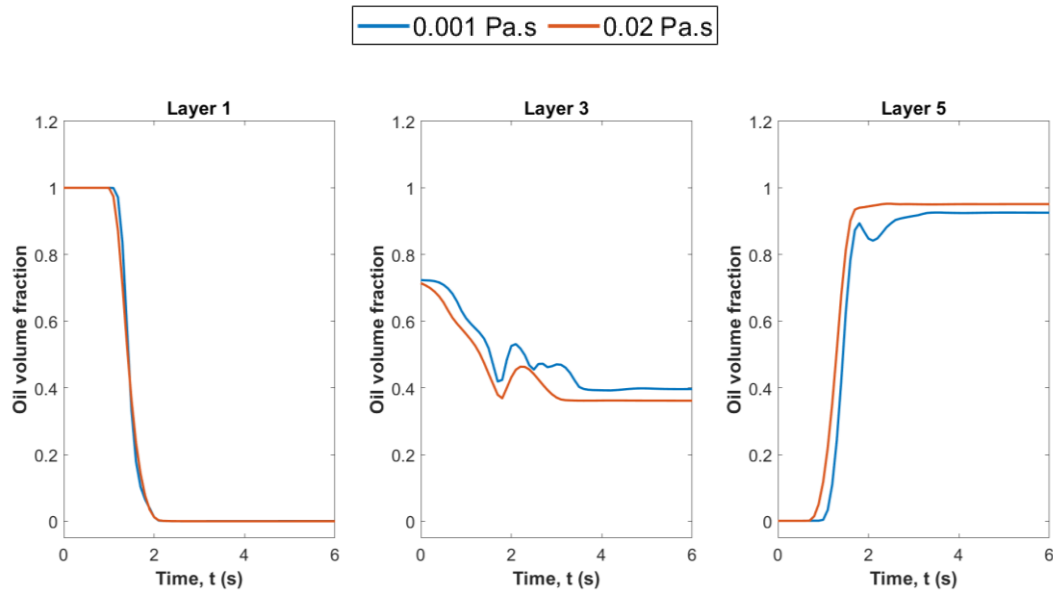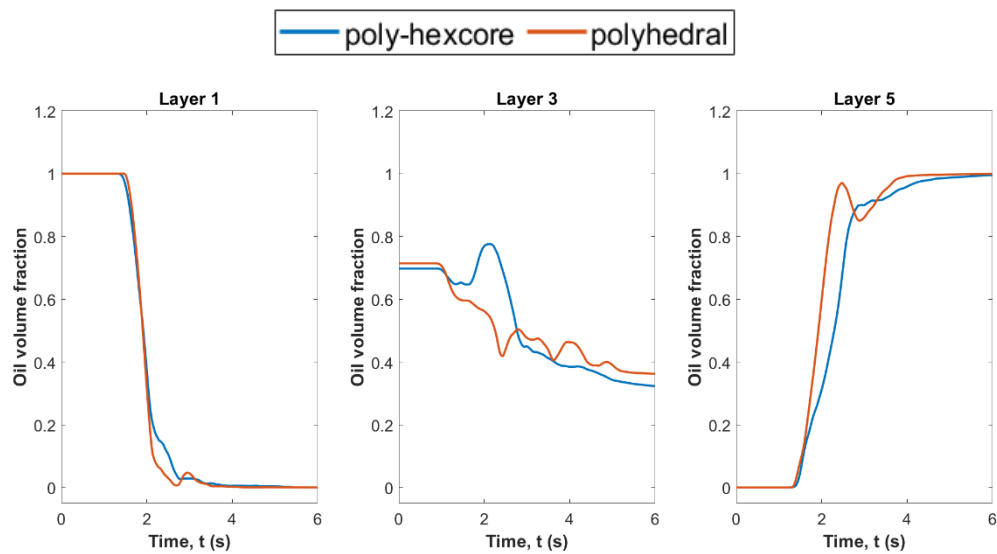**Figure 7.27: Oil volume fraction in layers 1, 3 and 5 as predicted by the FVM model for different mesh types.**
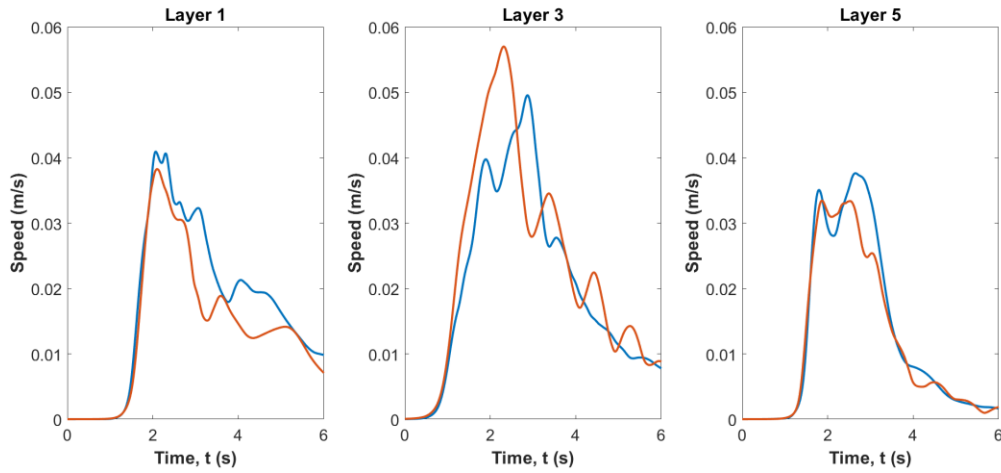
Figure 7.28: Speed in layers 1, 3 and 5 as predicted by the FVM model for different mesh types.

7.5.　Conclusions

Results from two numerical models of buoyancy-driven flow in the stomach have been presented. One is built upon the SPH method and the other is developed using the FVM. The solutions from both models show that the separation process happens rapidly in the stomach geometry. After initial interface instabilities develop there is a fast turnover of the bulk of the fluid and then the system settles into a quasi-steady state.

Some details of the flow behaviours are slightly different between the modelling approaches, including the timing of the growth of the flow instability, the strength of the phase turnover motion, the surface layer swirling speed, and the amount of final separation. However, the speed and the duration of the separation from both models are similar. The capture of the RTI growth is very clear in SPH (with the development of fine plume structures preceding the development of the bulk turnover flow) but not in FVM, most likely due to numerical smearing in the FVM.

Numerical noise in the SPH model is visible and further improvement is desirable to reduce this effect and allow the simulation of lower-viscosity fluids. The implementation of an adaptive resolution refinement method to better resolve small fluid zones and allow their complete separation would be useful.

These simulations have highlighted differences between the results from the two methods, but the complex geometry and the presence of flow instabilities means exact agreement is impossible.

In the next chapter, the successfully developed approach for flow in a non-deforming stomach is applied to a stomach having antral contraction waves with acid release from the wall is modelled and mixing behaviour in the stomach is studied.

Chapter 8. SPH Model Investigations of Gastric Mixing with Acid Diffusion in a Human Stomach

The next stage of the stomach model development following Chapter 7 is to implement contractive waves on the stomach wall, and acid diffusion from the wall. This work was completed in the last stage of the thesis and has not undergone the rigorous verification and validation that was applied in the earlier chapters. The wave propagation model is currently under development, but an initial version was made available by Shouryadipta Ghosh and Simon Harrison, CSIRO for these simulations.

8.1. Introduction

Digestive processes in the stomach can be classified into mechanical digestion and chemical digestion. Mechanical digestion involves processes such as crushing, fracturing and squeezing and is caused by the deformation of the food arising from interaction with the contracting stomach wall and the applied fluid stresses. Chemical digestion involves the secretion of gastric acid from the stomach wall and the interaction between gastric acid and gastric content. These two processes are interconnected. For instance, the mechanical breakdown of a food fragment will expose a new contact area for gastric acid to produce chemical digestion. This can lead to the softening of the food structure, which enables easier mechanical breakdown. Understanding human digestion offers potential treatments for gastric diseases, as well as advice regarding diet selection and drug delivery.

Pal et al. [26] developed a model of the dynamics of the antral contraction wave (ACW) through magnetic resonance imaging (MRI) studies and these dynamics are implemented in most of the developed *in silico* stomach models [14, 22, 77, 81-84, 115]. Most developed stomach models have not considered acid secretion, except Kamaltdinov et al. [78] and Li and Jin [80]. Kamaltdinov et al. [78] developed a multi-component mixture model by incorporating chemical kinetics between species. However, the stomach wall was assumed to be static in the study. Li and Jin [80] use a FVM to simulate gastric secretion from the upper region of the stomach with a moving stomach wall and the pH changes were tracked in the gastric content.

A biomechanical-Smoothed Particle Hydrodynamics (B-SPH) model was developed by Harrison, et al. [83], which was used to investigate fluid mixing and emptying with the ACW dynamics developed by Pal et al. [26]. In the current study, acid diffusion is incorporated into this previous model and the ACW dynamics were improved [217] by implementing the

electrophysiological activity data quantified by Berry et al. [218]. The peristaltic contraction ratios are exported as functions of time and spatial position, and then applied to the stomach boundary [217]. The aim of this study is to investigate the relationship between the acid diffusion process and fluid mixing behaviour in a deforming stomach to better understand how aspects of chemical digestion occur. The effects of several parameters are tested in the study, including the fluid viscosity, acid diffusion coefficient, and the speed of the contraction wave. Their effect on acidity level and fluid mixing are investigated and discussed.

8.2. Numerical model setup

8.2.1. Stomach geometry

The same stomach geometry as used in Chapter 7 is adopted here. The peristaltic waves, known as antral contraction waves or ACWs, are modelled as kinematically prescribed deformations of the stomach wall. They emerge at the proximal antrum and approach the pylorus with a spatially varying amplitude, pulse width and speed [217]. The parameters defining the contraction waves were taken from an experiment by Berry et al. [218], where high-resolution electrophysiological activity data were utilized to quantify the peristaltic waves in fasted stomachs of patients undergoing hepatobiliary or pancreatic surgery [217].

Instead of a stationary mesh, the boundary of the stomach is represented by a sequence of deforming meshes, which represent the temporal variation of the stomach surface position. A constant mesh update period of 0.25 s is used with deformation between mesh updates represented by updates to the position, velocity and normal of each mesh node calculated at each timestep. The pylorus is kept closed for the entire simulation, and therefore gastric emptying is not considered in this model.

8.2.2. Gastric content

The simulation starts with the stomach filled with quiescent fluid at 50% of its capacity, which leads to a total volume of 400 mL. The fluid in the stomach has an initial neutral pH of 7. A boundary condition of a constant pH of 3 is set on the stomach wall, as illustrated in Figure 8.1. Both the fluid and the acid are assumed to have a constant density of 1000 kg m^{-3} and a constant dynamic viscosity of 0.1 Pa.s, which is in line with the representative range of fluid properties found in the stomach. The effective species diffusivity of H$^+$ into water is in the order of 10^{-9} m^2 s^{-1} [80, 219]. In this study, an artificially increased diffusion coefficient of 10^{-7} m^2 s^{-1} is assumed to show a larger extent of diffusion on a shorter timeframe to avoid high simulation

run times, while two lower values (10^{-8} m^2 s^{-1} and 10^{-9} m^2 s^{-1}) are used in a comparative study later.

Figure 8.1: Illustration of the acid diffusion region coloured in red.

The CSIRO SPH code [134] is used to build this model. A SPH particle size of 1 mm is used to represent the fluid, resulting in 0.4 M particles in total. The cubic-spline kernel is used in this model after assessing the effect of different kernels in Chapter 7. The diffusion of the gastric acid in the gastric fluid is simulated using a Fick's diffusion model. The effect of temperature is not considered in this study since the range of temperature variation is fairly small. The species transfer equation used in the SPH model is [220]:

$$\frac{dC_a}{dt} = \sum_b \frac{4m_b}{\rho_a \rho_b} \frac{D_{ma} D_{mb}}{D_{ma} + D_{mb}} \cdot C_{ab} \frac{r_{ab} \cdot \nabla_a W_{ab}}{r_{ab}^2 + \eta^2} \tag{8.1}$$

where, C_a is the concentration of the acid in particle a, C_{ab} is the difference in concentration between particles a and b, D_{ma} and D_{mb} are the mass diffusion coefficients for the materials represented by particles a and b, respectively. The kinematic diffusion coefficient is given by $D_a = D_{ma}/\rho_a$.

The acid concentration is converted into pH by:

$$\text{pH} = -\log_{10}[C_a] \tag{8.2}$$

The initial fluid volume is again divided into five bands with the same height and different colours are ascribed to the particles in each layer, as shown in Figure 8.2. The fluid particles retain their initial colour when the fluid is mixed, allowing the mixing behaviour to be visualised and analysed. The average height of each set of coloured particles is calculated and recorded throughout the simulation. The initial positions of the particles in different colour bands are shown in Figure 8.2.
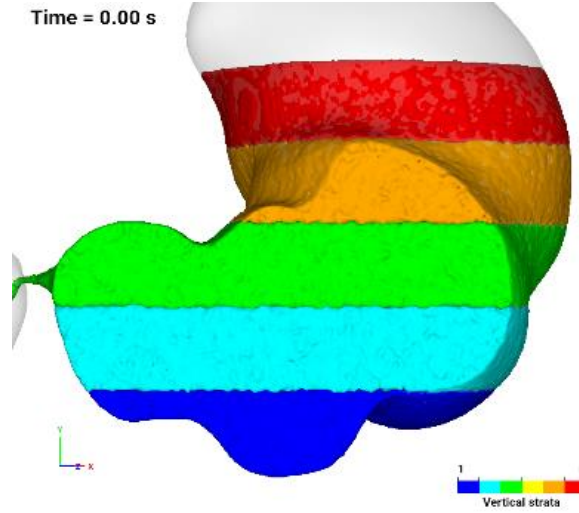
Figure 8.2: Visualisation of the initial fluid bands.

Data for the height and pH of every particle are known at each time step. A mean quantity can be defined at any instant via

$$\bar{\phi} = \frac{1}{N} \sum_i \phi_i \qquad (8.3)$$

where ϕ could be particle height or pH. N is the number of particles in the sum and the subscript i determines the summation range. The summation could be over all particles to obtain the average height or pH, or over a group of particles, say the blue ones, to determine their average height.

A standard deviation can also be calculated via

$$\sigma = \sqrt{\frac{1}{N} \sum_i (\phi_i - \bar{\phi})^2} \qquad (8.4)$$

which can be used to determine the spread of particle heights or acid concentrations about the mean.

8.3. Simulation results

The mixing behaviour of the fluid in the stomach is illustrated in Figure 8.3. Recall, the initial fluid is divided into five colour bands (Figure 8.2). As the ACWs propagate towards the pylorus, the fluid at the bottom coloured in blue, cyan and green is pushed upwards towards the free surface along the greater curvature of the stomach wall. Similarly, some of the fluid in the upper layers, coloured in orange and red, is transported down the back of the stomach. From 15 s to 30 s, some blue particles start to reach the free surface. At the same time, some red and

orange particles remain near the free surface and gradually move to the left. From 45 s to 75 s, some red and orange particles start to move to the bottom of the stomach. During the mixing, the cyan and green particles remain mostly in the middle area. After 75 s, there is already a good level of mixing of all layers of fluid. At 90 s, some orange particles move to the middle area and the fluid near the wall is filled with particles of all layers. From 105 s to 135 s, more orange particles with some blue particles are visible in the middle area while most red particles remain at the top layer. Importantly, the external surface of the fluid at 150 s, which contacts the source of acid, is visibly different to the fluid that was in contact with the stomach wall at the start of the simulation.
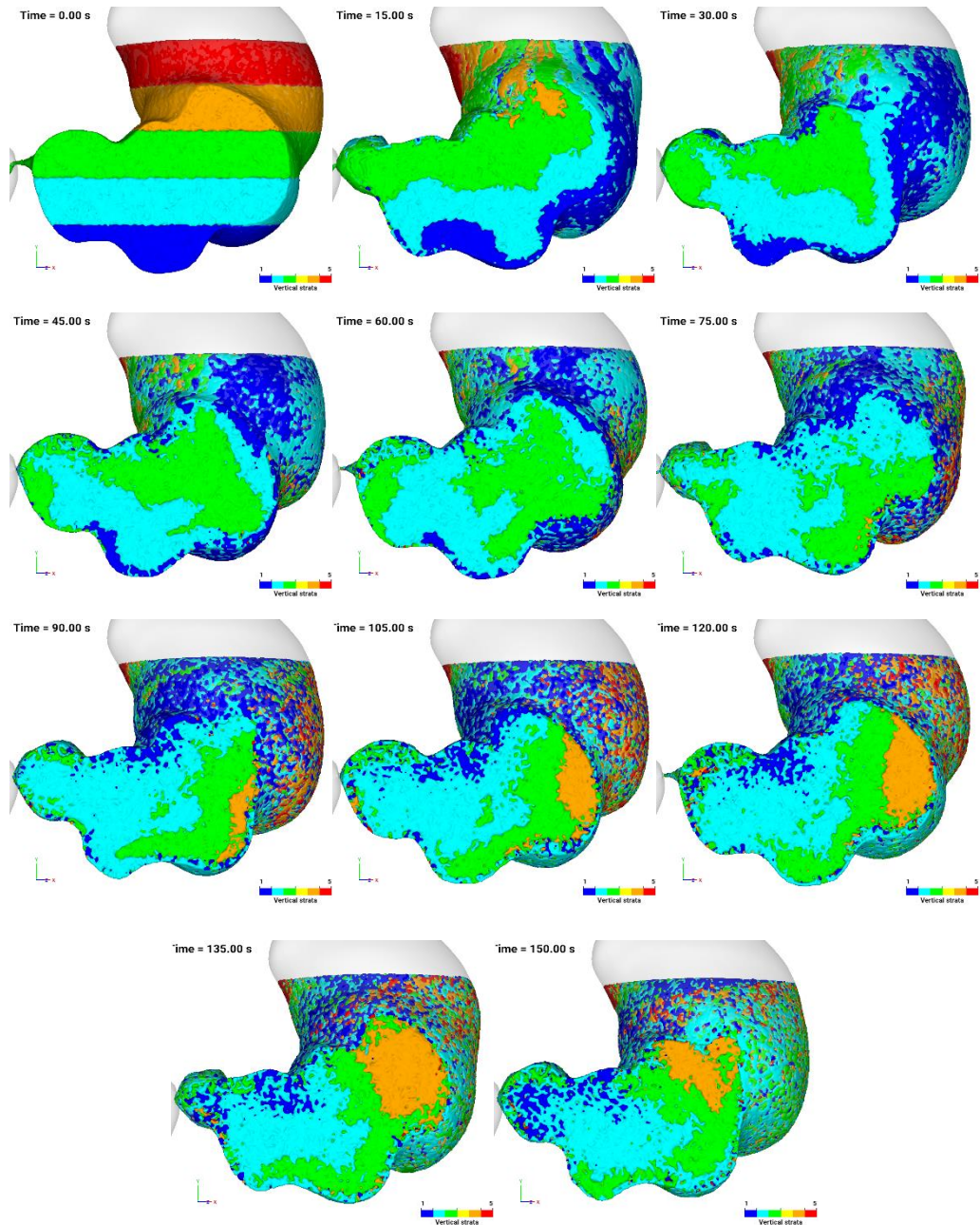
Figure 8.3: Visualisation of the mixing behaviour within the stomach.

The time evolution of the average height of each of the fluid particles of the same colour is shown in Figure 8.4. The average height of all particles is also shown (as a dashed black line) and acts as a comparison. It is not completely flat because of the cyclic vertical translation of the free surface that occurs with the transit of the ACWs. As the average height of each of the colour groups tends towards the overall average with increasing time, this indicates that the fluid is becoming increasingly mixed well. At 100 s, the average height of each colour group becomes relatively stable, but fluctuations still exist, meaning that the fluid is not completely mixed yet and may require a much longer time. The standard deviation of the heights in

different colour bands is used as an additional measure of mixing between fluid bands and is presented in Figure 8.5. The standard deviation of the heights decreases from 27 mm at the start to 7 mm at 90 s, meaning that the fluid is progressively mixed in the stomach by the contractive waves. From 90 s to 150 s, the standard deviation increases back to 10 mm, meaning that the fluid is not completely mixed yet.
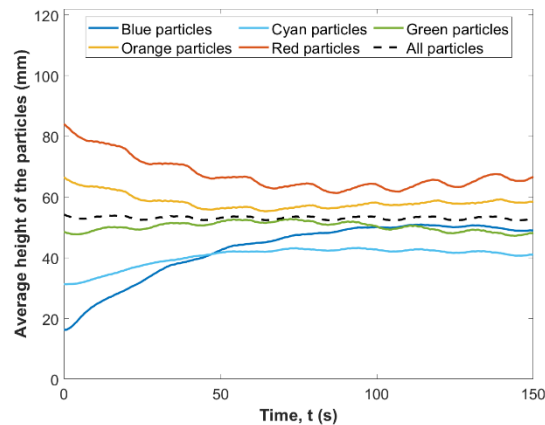
Figure 8.4: The average height of differently coloured particles.
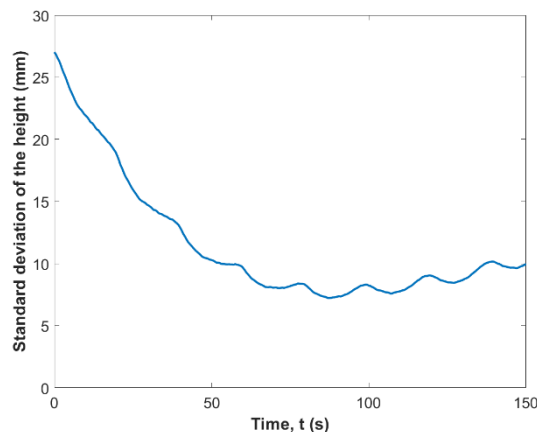
Figure 8.5: Standard deviation of the height of all colour groups.

The change in pH of the fluid in the stomach over time is shown in Figure 8.6. In this figure and all figures showing pH changes in the fluid, the boundary particles used to set the pH are not shown. Only the fluid particles are shown. The pH of the fluid is 7.0 initially, meaning the fluid is pH neutral. As the contractive wave propagates along the stomach wall, the acid that is diffusing into the fluid adjacent to the wall is transported away from the walls and progressively mixed into the bulk of the fluid mainly through advection but also with diffusion. At 15 s, the pH of the fluid near the stomach wall decreases to 3.5, while the pH of the fluid at the free surface decreases to 3.0. This is because the fluid that was in contact with the acid source (coloured orange and yellow in Figure 8.3) has now moved up to the free surface. At 30.0 s,

the pH of the fluid near the boundary becomes almost constant at 3.0 and the pH of the interior fluid decreases smoothly. From 45 s to 150 s, the pH of the fluid continues to decrease, and the pH of most fluid becomes 3 at 150 s.
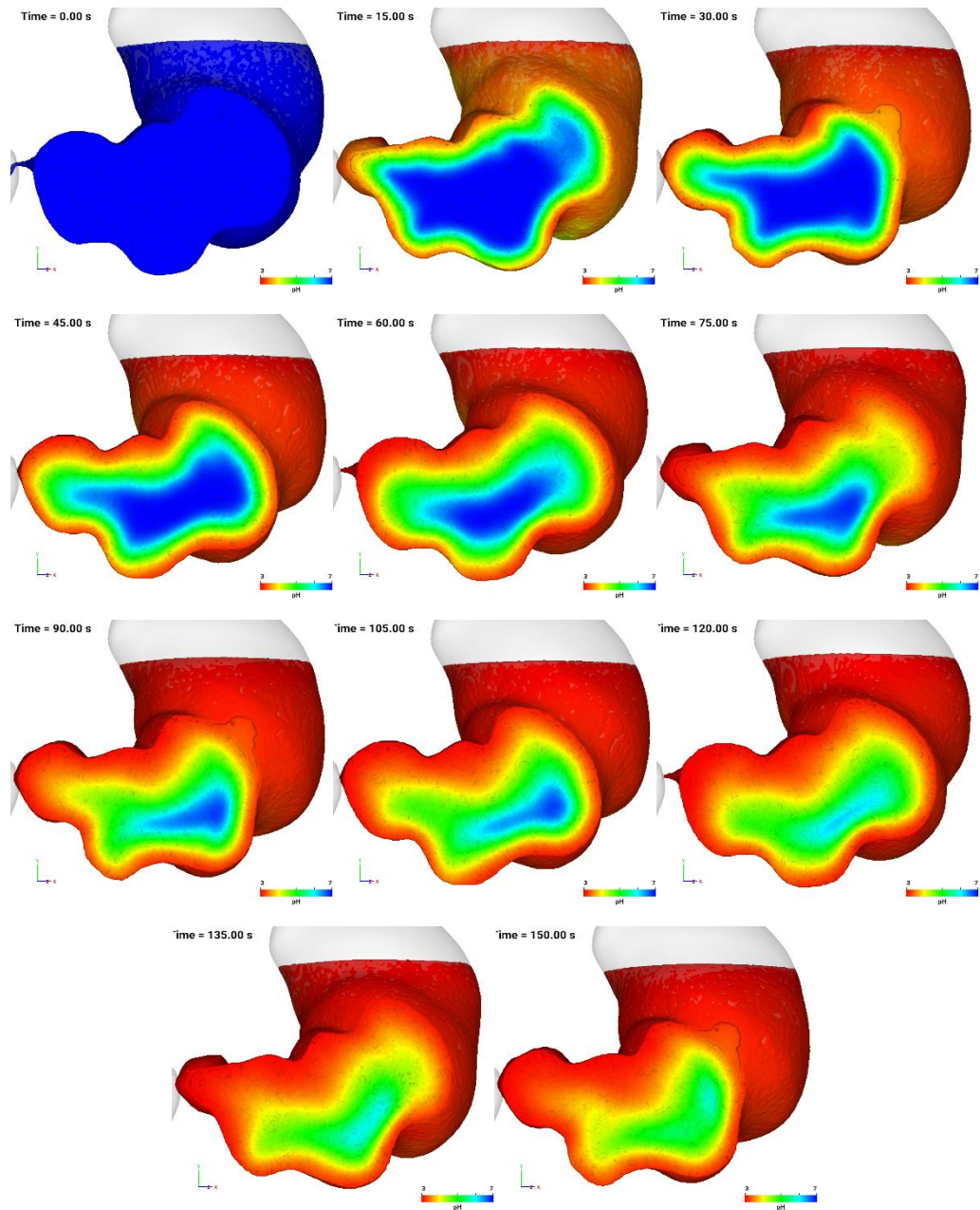
Figure 8.6: Visualisation of the pH changes in the fluid.

The changes in average pH in the fluid over time are shown in Figure 8.7. As the stomach wall continues to move, the acid at the wall initially is transported into the fluid and reduces the average pH gradually. At 150.0 s, the average pH of the fluid has reduced to 3.8.
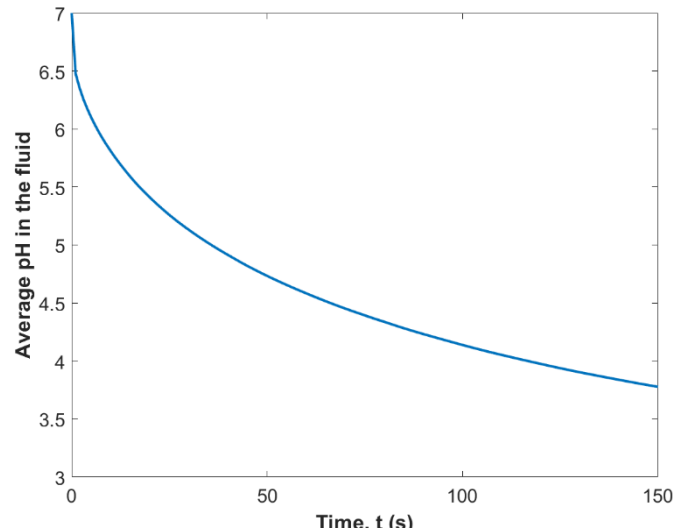
Figure 8.7: The changes of average pH in the fluid over time.

8.4. Parameter variations

Different parameter variations are tested in this study to understand their effect on fluid mixing. Parameters tested include the fluid viscosity, the acid diffusion coefficient, and the contraction wave speed, which are all closely related to food digestion in the stomach.

8.4.1. Effect of fluid viscosity

The effect of fluid viscosity is analysed by comparing the mixing behaviour and pH changes of fluids. Dynamic viscosities of 0.02 Pa.s, 0.1 Pa.s and 0.5 Pa.s are used, which are within the range of viscosity variation of typical gastric content (0.01 to 2 Pa.s) [22].

The mixing behaviour of the fluids with different viscosities is shown in Figure 8.8. With a viscosity of 0.02 Pa.s, the fluid in the stomach mixes rapidly. At 30 s, some blue particles, which are at the bottom originally, have already moved to the free surface when the fluid viscosity is 0.02 Pa.s. With a viscosity of 0.5 Pa.s, the blue particles have not even reached the free surface at 60.0 s. At 150 s, the fluid is filled with particles of all colours both near the wall and internally with the lowest viscosity while the internal fluid is still mostly filled with cyan and green particles with the highest viscosity. Compared with the high-viscosity fluid, the mixing speed of the low-viscosity fluid is much faster. The mixing rate for the interior fluid is slower than the mixing near the walls, and even with the lowest viscosity fluid that has the highest mixing rate, the portions of the cyan and green particles in the internal fluid are still higher than other particles.
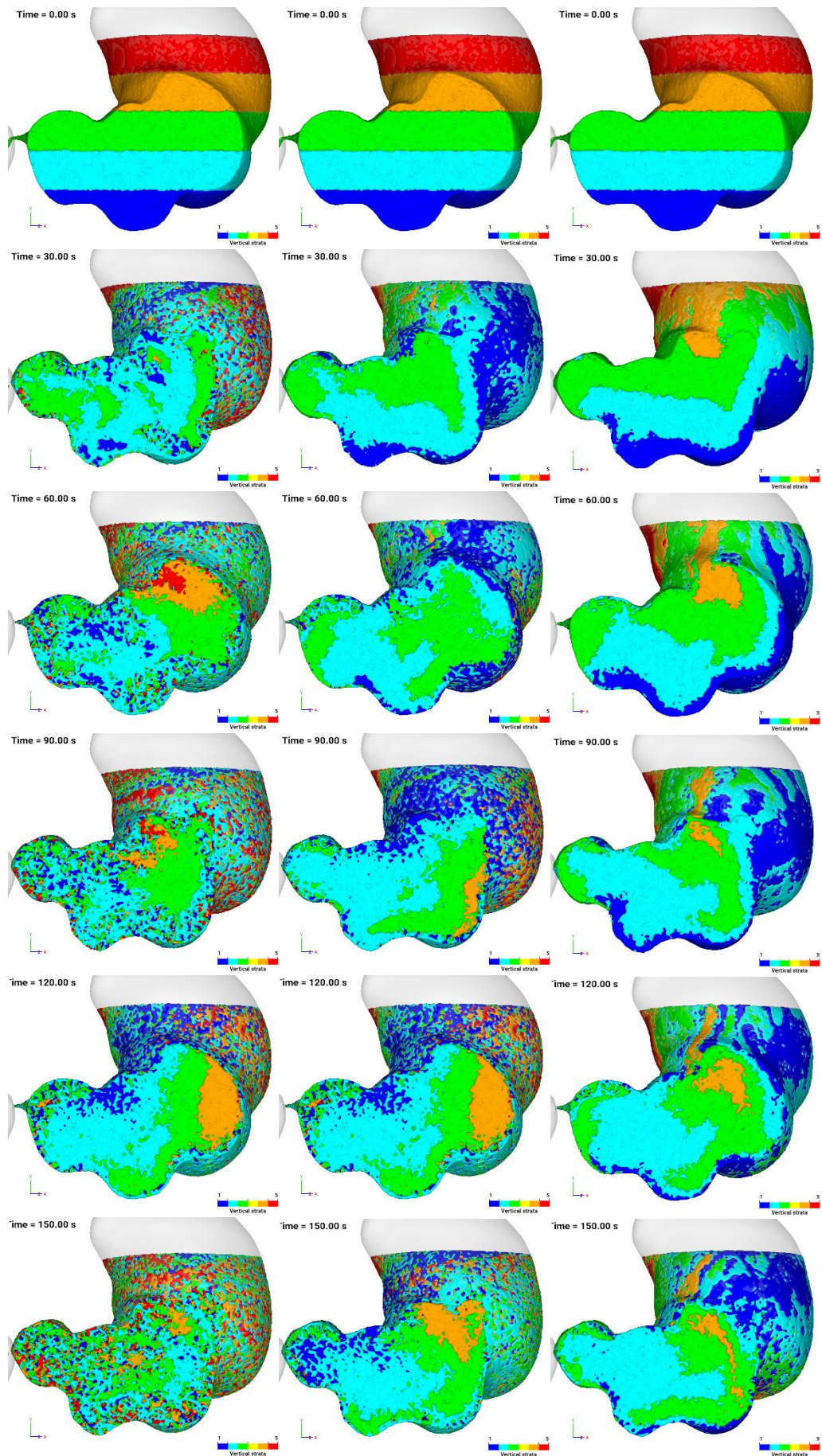
Figure 8.8: Visualisation of mixing within the stomach for different fluid viscosities. (left) 0.02 Pa.s; (middle) 0.1 Pa.s; (right) 0.5 Pa.s.

Figure 8.9 shows the average height of each particle colour group for different fluid viscosities. Figure 8.9(a) shows that with a viscosity of 0.02 Pa.s, some mixing occurs rapidly at the start from 0 to 20.0 s as the average heights of each layer become closer to the average height of all particles. After 20.0 s, the heights do not change significantly except for the red particles, the height of which has an increase between 20 s and 70 s then decreases afterwards. Figure 8.9(b) shows the mixing behaviour of the medium-viscosity fluid. The curves have lower gradients (meaning slower mixing) compared with the low-viscosity fluid results. The heights have not reached steady levels at 150.0 s, meaning that the fluid mixing is continuing. Figure 8.9(c) shows the slopes of the lines are even smoother and flatter with a viscosity of 0.5 Pa.s since the advective transport of fluid is significantly inhibited by the high viscosity. Therefore, as expected, the highest viscosity fluid provides the poorest mixing among the three cases.
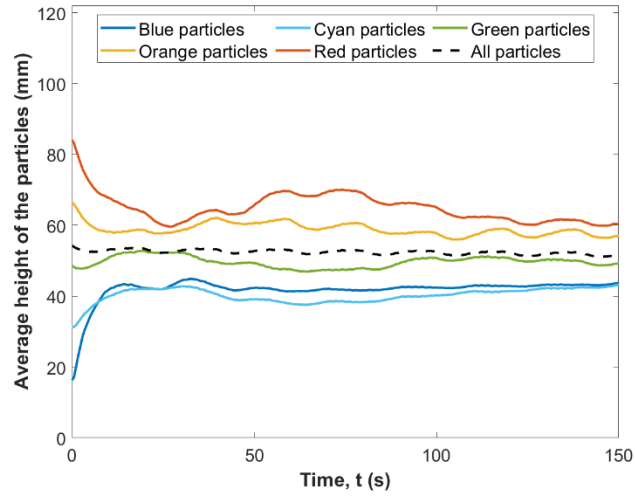
(a) viscosity = 0.02 Pa.s
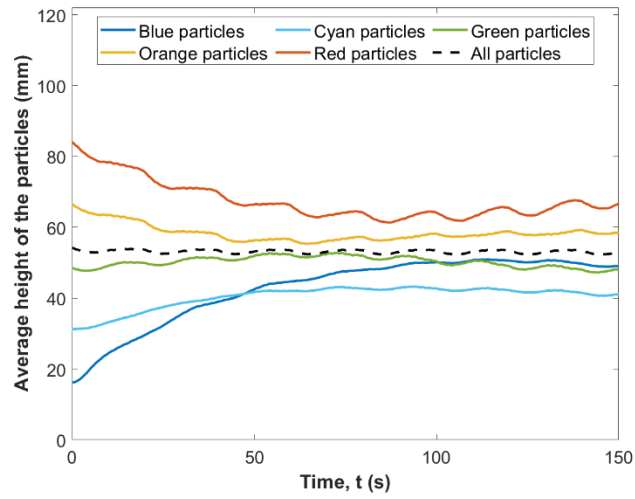
(b) viscosity = 0.1 Pa.s
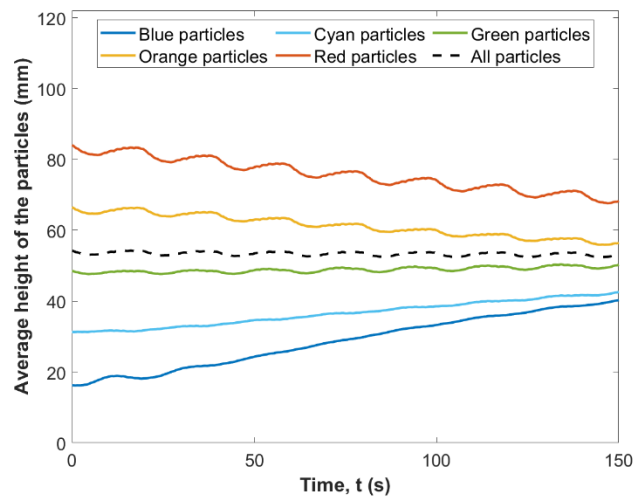
(c) viscosity = 0.5 Pa.s

Figure 8.9: The average height of each coloured particle group for different fluid viscosities.

The standard derivations of the average height for different fluid viscosities are shown in Figure 8.10. The value for 0.02 Pa.s decreases rapidly from 27 mm to 8 mm from 0.0 to 30.0 s, which shows that some mixing happens rapidly. From 20.0 s to 60.0 s, the value increases from 9 mm to 13 mm then decreases back to 8 mm at 150 s. To reach a fully mixed state with a stable standard deviation value, it may require a longer run time. With high viscosity, the fluid mixing is much slower as the standard deviation for the 0.5 Pa.s case has only decreased to 21 mm at 150 s.
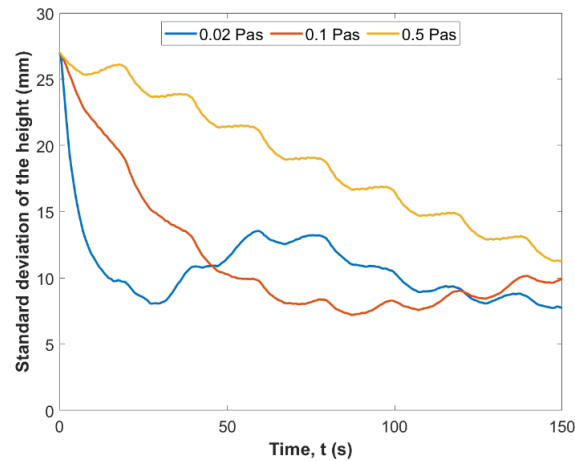
Figure 8.10: The standard deviation of the heights of all colour groups for different fluid viscosities.

The average speed of the fluid for different fluid viscosities is shown in Figure 8.11. With a viscosity of 0.02 Pa.s, the fluid speed rises very rapidly to 0.01 m/s at the start, decreases to 0.004 m/s at 10.0 s and remains relatively constant afterwards. The high-frequency noise arises from the numerical method and is not a physical effect. The average speeds for the medium-viscosity and low-viscosity fluids are around 0.002 m/s and 0.001 m/s, respectively.
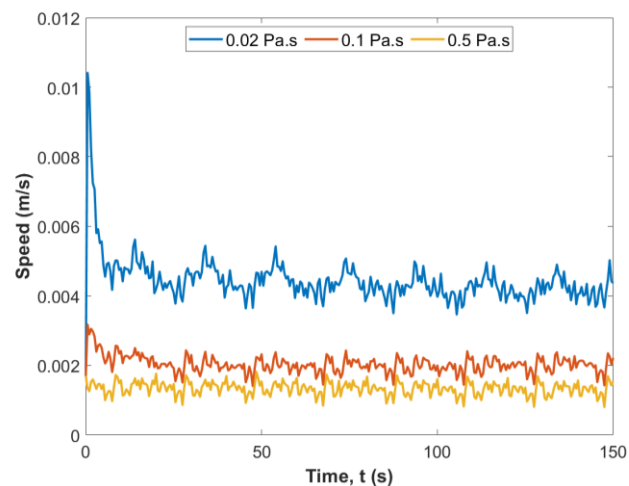
Figure 8.11: The effect of fluid viscosity on the average fluid speed in the stomach.

Table 8.1: The effect of fluid viscosity on the Reynolds, Schmidt and Peclet numbers of the system.

Fluid viscosity	0.02 Pa.s	0.1 Pa.s	0.5 Pa.s
Reynolds number	17.76	1.62	0.21
Schmidt number	200	1,000	5,000
Peclet number	3550	1620	1070

.

shows the Reynolds, Schmidt and Peclet numbers of the fluid for the different viscosities studied. As the viscosity increases, the Reynolds number decreases significantly, and the momentum of the fluid changes from being advection-dominated to viscous-dominated. This is consistent with the observed much poorer mixing at higher viscosity. This decrease in the Reynolds number is accompanied by an increase in the Schmidt number. The Peclet number, the product of the Reynolds and Schmidt numbers, gives the ratio of convective to diffusive mass transfer. This shows that as the fluid viscosity increases the influence of convection is becoming weaker which is consistent with the observed results.

Figure 8.12 shows the visualisation of the pH values of the fluid for different fluid viscosities. As the viscosity decreases, the acid mixes into the internal fluid more quickly. At 90.0 s, the number of fluid particles coloured in red is much higher for smaller viscosities because the fluid mixes more thoroughly.
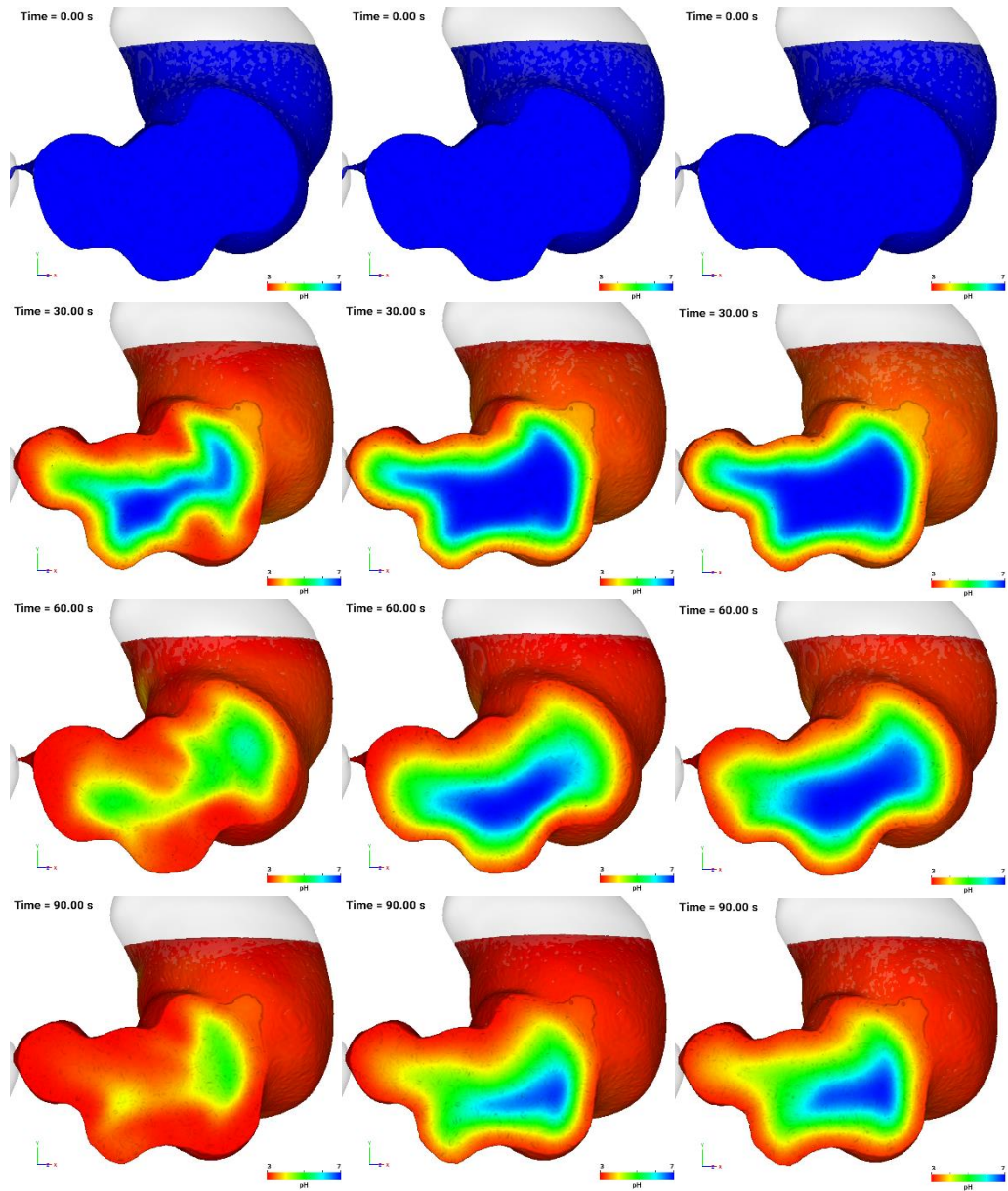
Figure 8.12: Visualisation of pH changes in the fluid for different viscosities. (left) 0.02 Pa.s; (middle) 0.1 Pa.s; (right) 0.5 Pa.s.

The changes in average pH values in the fluid over time for different fluid viscosities are shown in Figure 8.13(a). The pH values decrease monotonically in all three cases. At 150.0 s, the average pH of the lowest viscosity fluid reduces to 3.4, and the pH of the highest viscosity fluid reduces to 4.0. Figure 8.13(b) shows the change in the standard deviation of the pH over time. As the acid starts to diffuse into the fluid, the standard deviation starts to increase from zero. The rate of the increase is the highest with the 0.02 Pa.s fluid from 0 to 10 s, as the lower viscosity allows greater convective fluid motion. From 16 s, the standard deviation of the pH for the 0.02 Pa.s fluid starts to decrease, showing the acid is more uniformly distributed in the stomach. The standard deviations of pH with viscosities of 0.1 Pa.s and 0.5 Pa.s start to

210

decrease from 25 s and 35 s, respectively. The average pH in the fluid should eventually reduce to 3.0 and the standard deviation of the pH should reach zero if the simulation were run for long enough. Therefore, the mass transfer rate between the acid and fluid is much higher in the low-viscosity fluid.

(a)

(b)
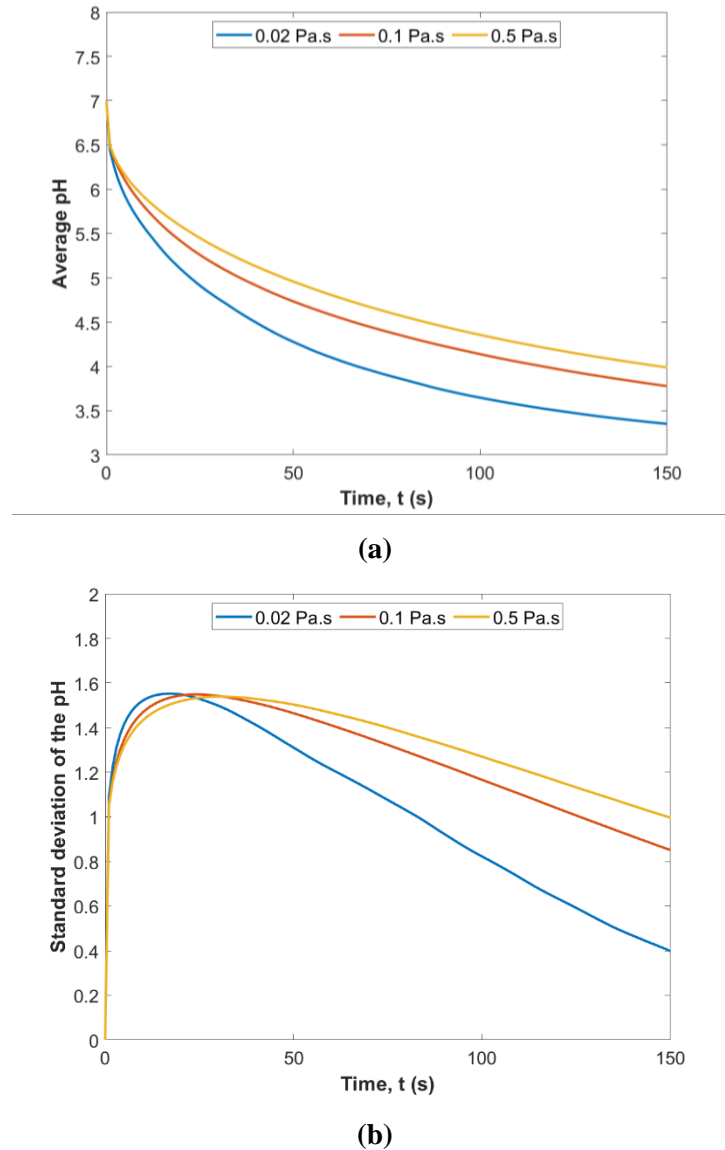
Figure 8.13: The effect of fluid viscosity on pH changes in the stomach (a) average pH; (b) standard deviation of the pH.

8.4.2. Effect of acid diffusion coefficient

The effect of the acid diffusion coefficient is investigated by comparing the results with diffusion coefficients of 10^{-7}, 10^{-8}, and 10^{-9} m^2 s^{-1}. The changing pH over time for the different diffusion coefficients is shown in Figure 8.14. As expected, a higher diffusion coefficient leads to greater acid transport into the stomach.
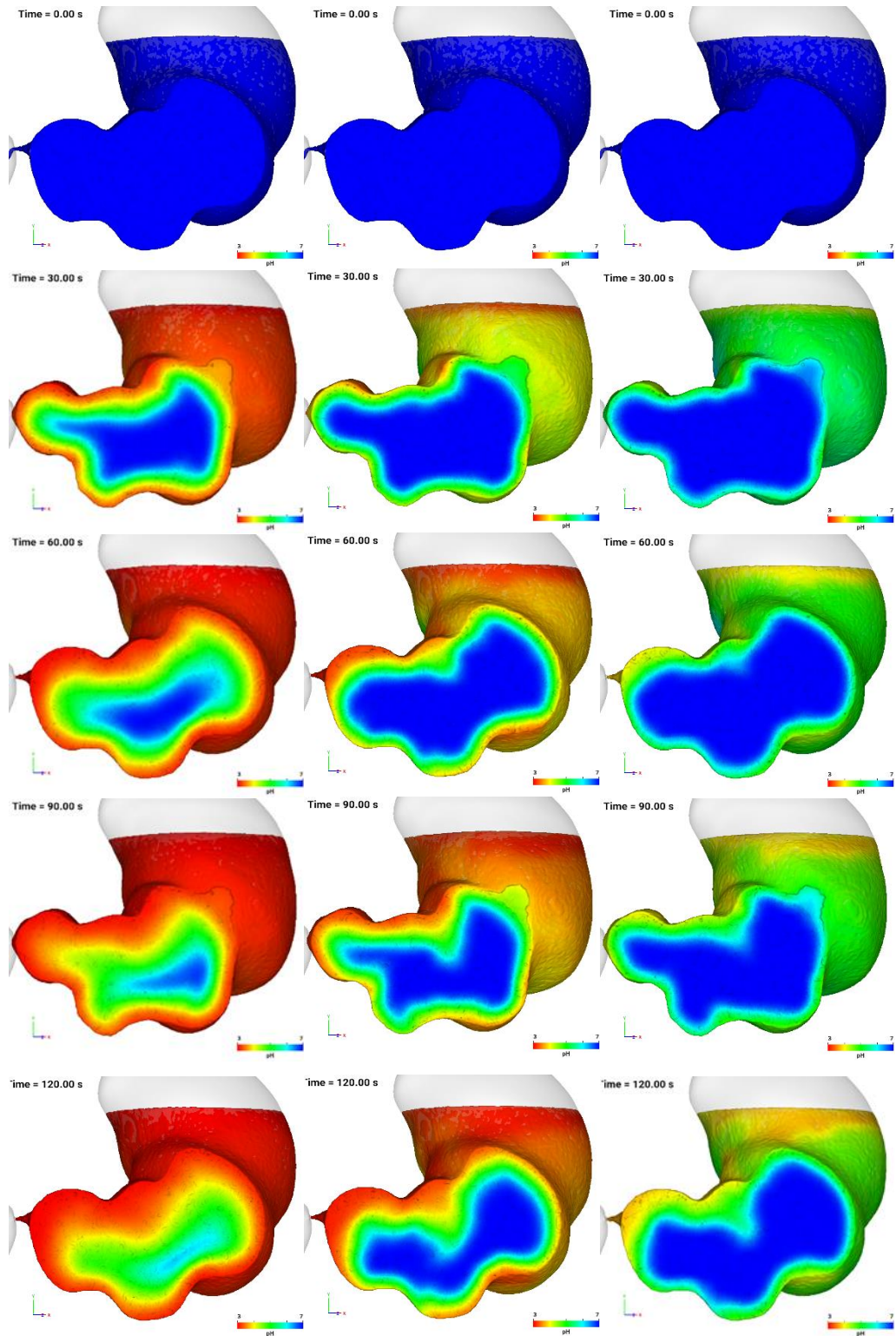
Figure 8.14: Visualisation of pH changes in the fluid for different acid diffusion coefficients. (left) 10^{-7} m^2 s^{-1}; (middle) 10^{-8} m^2 s^{-1}; (right) 10^{-9} m^2 s^{-1}.

The effect of the diffusion coefficients on the average pH is shown in Figure 8.15(a). The average pH decreases much more quickly with a higher diffusion coefficient. The average pH of the fluids starts from 7.0 and decreases to 3.8, 5.0, and 5.9 at 150 s with acid diffusion coefficients of 10^{-7}, 10^{-8}, and 10^{-9} m^2 s^{-1}, respectively. Figure 8.15(b) shows the standard deviations of the acid concentration. The data show that the higher the acid diffusion coefficient, the faster the standard deviation increases initially, as acid enters the stomach. Once there is a significant amount of acid in the stomach, the standard deviation starts to fall and will eventually reach zero, indicating a uniform acid concentration in the stomach.
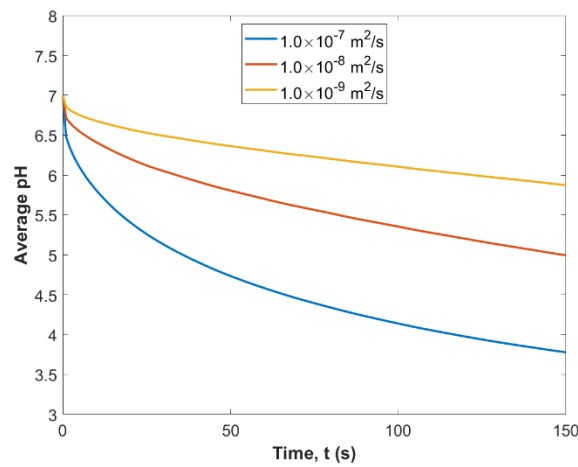
(a)
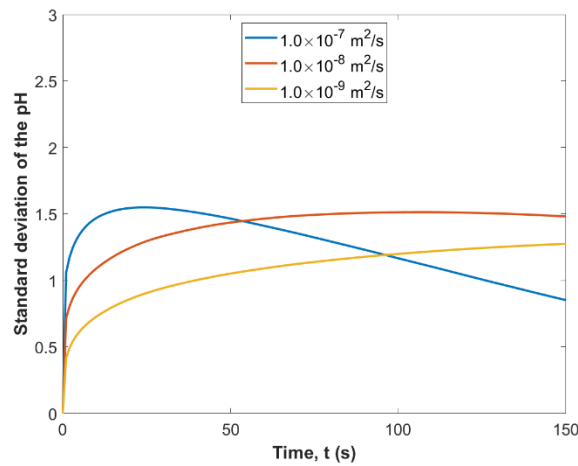
(b)

Figure 8.15: The effect of diffusion coefficient on pH changes in the stomach (a) average pH; (b) standard deviation of the pH.

A sudden drop in pH from 0 to 1 s is observed in all cases as shown in Figure 8.16, which is not correct as the acid should enter smoothly throughout the simulations.

213
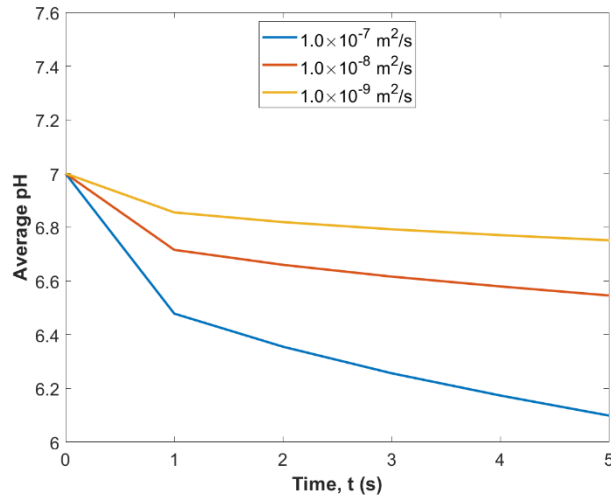
Figure 8.16: Average pH in the first 5 s for different diffusion coefficients.

This can be explained as follows. The thickness of the diffusion boundary layer for a sphere, deemed to be the closed simple shape that can be used to represent the stomach, at time t can be estimated using a first-term approximation to the solution of the diffusion equation [221] as:

$$\delta_C = \pi\sqrt{Dt} \qquad (8.5)$$

For a time of 5 s, equation 8.5 gives thicknesses of 2.2 mm, 0.7 mm, and 0.2 mm for acid diffusion coefficients of 10^{-7}, 10^{-8}, and 10^{-9} m^2 s^{-1}, respectively. It is evident that for a particle size of 1 mm even the 10^{-7} m^2 s^{-1} case is barely resolved and for the two other cases, at this stage in the calculation the concentration boundary layer is certainly not being resolved. Verification tests of simple diffusion problems are needed to determine the best way to model the concentration boundary layer of low diffusivity species (see Future Work).

8.4.3. Effect of moving wall

The effect of the moving stomach wall on the average pH is analysed by comparing the base case results with the results with a static wall. The visualization of the pH changes is shown Figure 8.17 and the effect on the average pH is shown in Figure 8.18. Without the wall motion, the mass transfer from the acid is purely by diffusion and the pH decreases from 7.0 to 4.2. With the wall motion, the pH decreases to 3.8. The effect of the wall motion is important as it increases the acid mass transfer rate by advection significantly, with the Peclet number of this system being 1620 (Table 8.1).

214
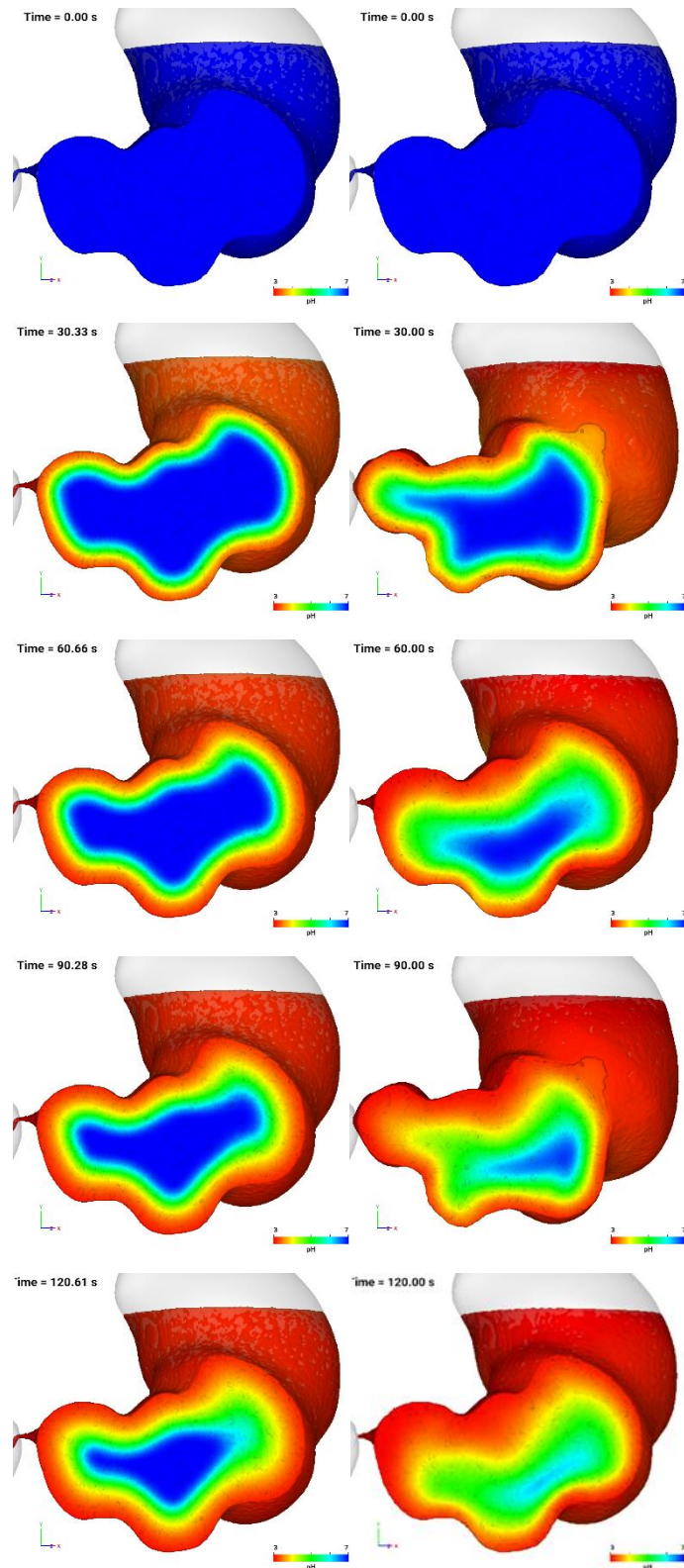
Figure 8.17: Visualization of pH changes in the fluid (left) with a static wall; (right) with deforming wall.
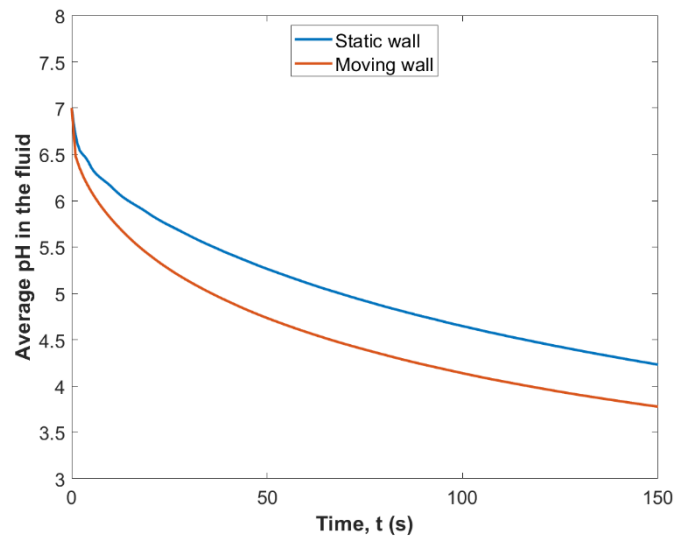
Figure 8.18: The effect of the moving wall on average pH in the stomach.

8.4.4. Effect of contraction wave speed

The speed of the contraction wave is examined by increasing and decreasing the speed by 50%. The mixing behaviour of the colour bands for different contractive wave speeds is shown in Figure 8.19. The average heights of the blue, green, and red particles are shown in Figure 8.20, which shows that the effect of the contraction wave is not significant, for the range of variation considered, on fluid mixing. A higher contraction wave speed provides slightly better mixing as the standard deviation decreases faster with a higher wave speed as shown in Figure 8.21, but the difference is not significant. A larger effect is expected for changes in wave amplitude, but this was not possible at the time of writing this thesis.
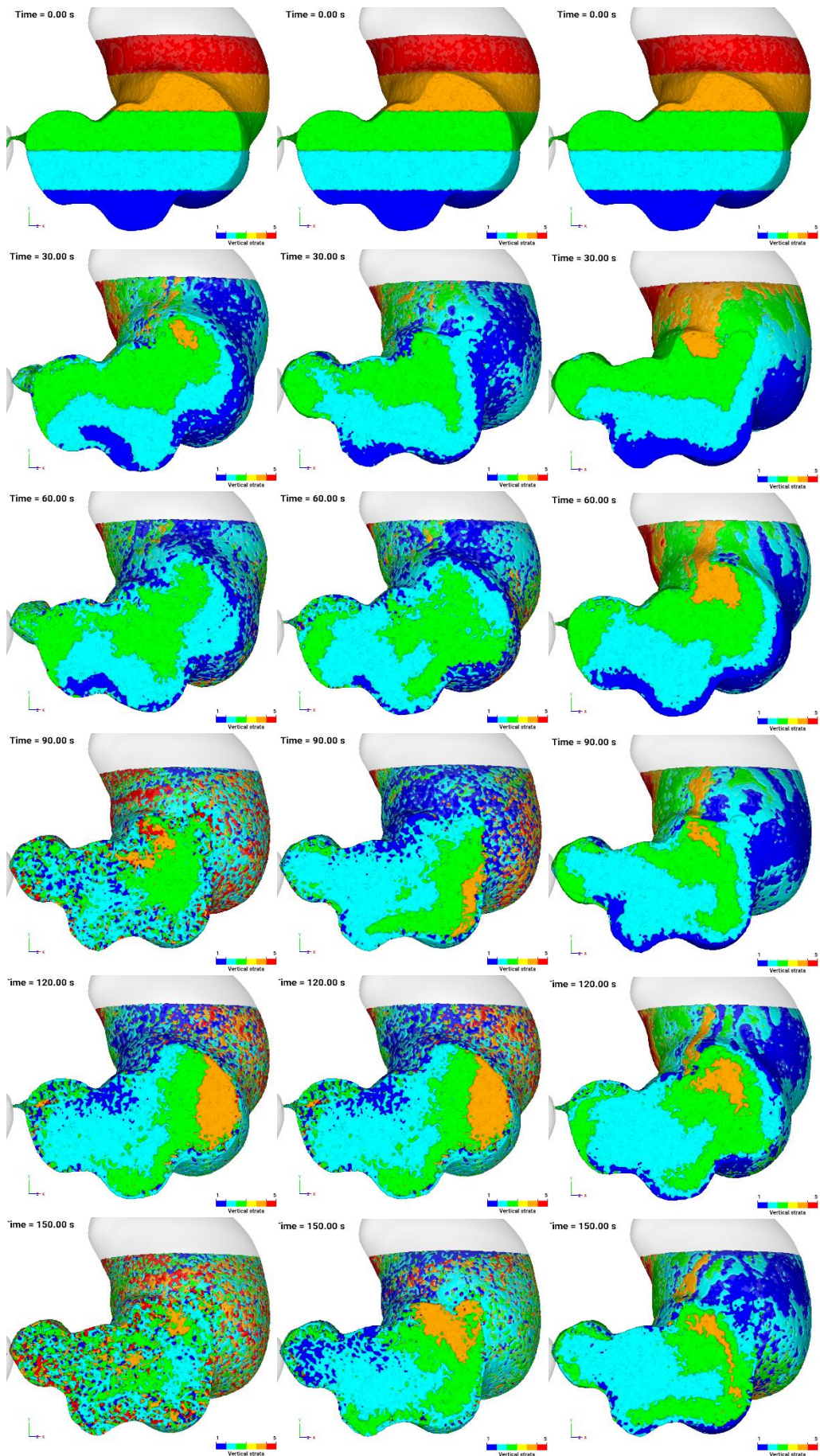
**Figure 8.19: Visualisation of mixing within the stomach for different contraction wave speeds. (left) 1.5×
slower; (middle) normal speed; (right) 1.5× faster.**
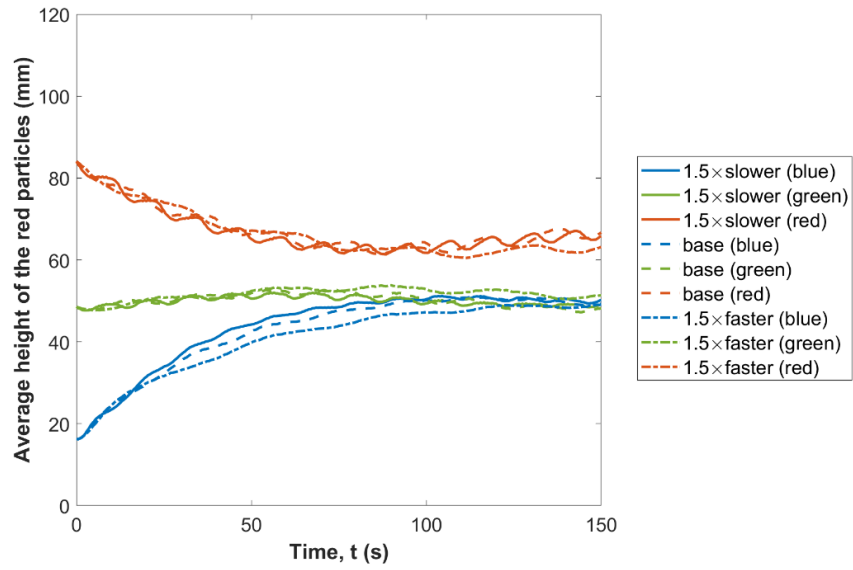
Figure 8.20: The average height of blue, green, and red particle groups for different contractive wave speeds.
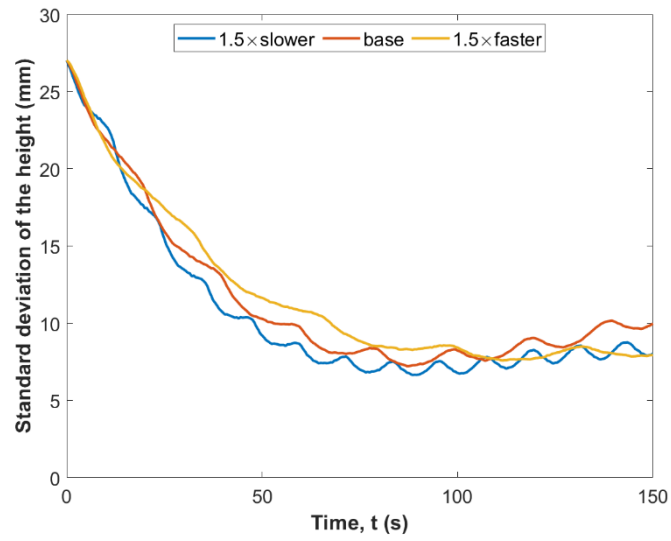
Figure 8.21: The standard deviation of the heights of all colour groups for different contractive wave speeds.

Figure 8.22 shows that its effect on the pH changes is not significant either as the average pH in the fluid is almost the same with different contractive wave speeds.
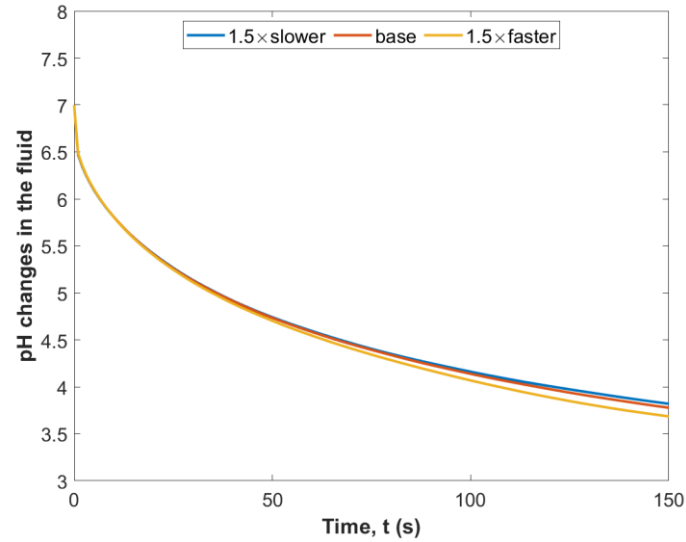
Figure 8.22: The effect of contraction wave speed on average pH in the stomach.

8.4.5. Effect of spatial resolution

A test of spatial resolution is also performed. The effect of spatial resolution on the average and standard deviation of the heights is shown in Figures 8.23 and 8.24, respectively. The average heights are similar while the standard deviations are slightly different. With a lower resolution, the standard deviation decreases slightly faster. The results show a weak dependence on resolution.
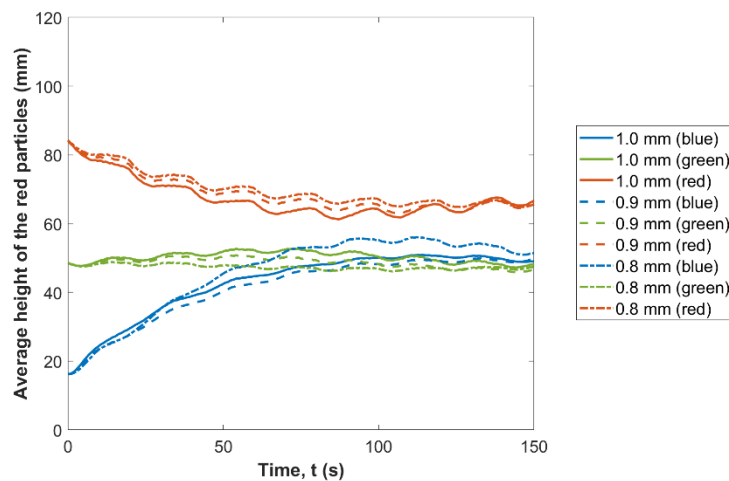
Figure 8.23: The average height of blue, green and red particle groups for different spatial resolutions.
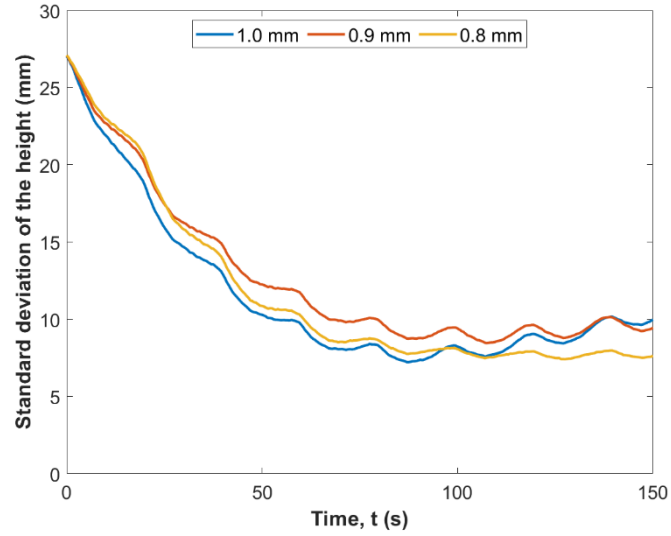
Figure 8.24: The standard deviation of the heights of all colour groups for different spatial resolutions.

Figure 8.25 shows its effect on the average pH and shows that it is not significant either.
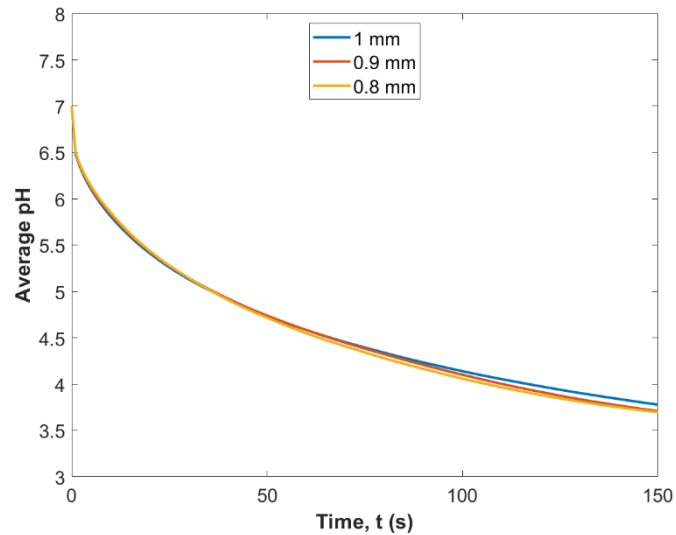
Figure 8.25: The effect of spatial resolution on average pH in the stomach.

8.5. Conclusions

SPH simulations of a closed stomach model in which the wall motion is included have been run to study its effect on the mixing of the fluid in the stomach and the transfer of acid into and within the stomach. Fluid viscosity has a significant effect on pH changes and fluid mixing because of its strong impact on the velocity field. Analysis shows that even for the highest viscosity the mass transfer is advection dominated. The acid diffusion coefficient plays an

important role in determining the pH change in the stomach, as it controls the acid flux at the walls. As for the effect of contraction wave speed, a 50% change does not have a significant effect either on the pH change or the fluid mixing.

A simple boundary layer analysis showed that for the used particle size of 1 mm the concentration boundary layer could not be resolved for physically realistic diffusion coefficients and that even for the base case that uses a diffusion coefficient that has been multiplied by 100, the resolution is barely adequate at the start of the simulation. In addition, the wall boundary condition needs modification to enforce a constant pH value. These issues are discussed in the Future Work presented in the next chapter. The aim of this chapter was to explore the possibility of modelling the acid and the wall contractions and to identity any issues relating to their implementation. This objective has been met.

Chapter 9. Conclusions and future work

In this chapter, the conclusions arising throughout this thesis are consolidated and proposed future work is presented.

9.1.   Conclusions

Gastrointestinal health is essential for human beings as it is closely related to a person's well-being. Gastric diseases, such as obesity, gastritis, gastroparesis, and stomach cancer could potentially be prevented or at least alleviated if we had a better understanding of gastric functions. Gastric digestion has been studied *in vivo*, *in vitro*, and *in silico* for decades. *In vivo* studies require strict ethical approval, and measurements are difficult to collect. *In vitro* models have been widely used but further development is needed to make them more representative of the real stomach. The development of *in silico* models is growing because of the massive improvement in software and computing power recently.

The main purpose of an *in silico* model of the stomach is to replicate the physics and chemistry that happens in a real human stomach. A literature review showed that the developed stomach models to date are capable of simulating fluid flow, a moving stomach wall, acid secretion and small food particles that can be tracked to show the motion of digested food. Food softening and food breakdown have not been simulated *in silico* but have been studied *in vivo* and *in vitro*. Although the current state of art of *in silico* models is still limited, they can provide valuable insight into the physics of the gastric flow, including the velocity field, acid concentration, strain rate and shear stress in the fluid. These data assist in developing a better understanding of fluid mixing and mass transfer in the stomach. Additionally, *in silico* models can be used as a tool to improve the design of *in vitro* models, ensuring that the experiment is as representative as possible of the real stomach. However, it is not evident that the components of the various *in silico* models have undergone sufficient vigorous verification and validation.

Two main modelling approaches have been implemented here in the computational modelling of the stomach, which are the Finite Volume Method (FVM) and Smooth Particle Hydrodynamics (SPH). FVM is a traditional mesh-based method that has been well-established for decades and forms the basis of most commercial CFD software. However, it can be computationally expensive when deforming geometry is involved because remeshing is required to maintain the quality of the mesh. SPH is a particle-based method that has the advantages of accommodating flexible geometry, handling multiphase flow naturally, and

combing fluid with large particles. However, SPH is a more novel approach and requires greater verification and validation for this application. In conclusion, rigorous comparison and validation are required for these two methods to ensure they can be used confidently for this application. The pros and cons of both methods should be considered carefully before they are applied to a particular situation.

The main body chapters of this thesis start with a verification study of a kinematically prescribed peristalsis-like flow in a tube by comparing the performance of SPH and FVM with an analytical solution (Chapter 3). Both models provided accurate results and have been demonstrated to be verified for this application. The FVM model was developed using Ansys Fluent, which is a commercial software package. The sensitivity studies in the FVM model were easy to perform and both mesh and timestep independence studies gave excellent results. The SPH model was developed using the CSIRO SPH code. More investigation was required on the numerical parameters for the SPH model, including the initial particle arrangement, use of an offset pressure to prevent numerical cavitation, and the choices for the kernel, characteristic speed, and particle size, prior to obtaining good agreement with the analytical solution. The results from the SPH model were sensitive to some of these parameters. Careful consideration of these inputs was required when developing the SPH model and therefore a comprehensive understanding of the method is essential. There is very limited documentation on the SPH model, compared with that for commercial software with FVM.

This was followed by a verification study of Fluid Structure Interaction (FSI) modelling of wave propagation in fluid-filled elastic tubes (Chapter 4). This work used a coupling method that combined the FVM and a Finite Element Analysis (FEA) solver. In this case, the Ansys Fluent CFD solver and the Ansys Mechanical FEA solver were coupled using the Ansys System Coupling interface. The propagation wave speed in an elastic tube was tested in this FSI model. Simulation results matched well with theoretical results, proving the model to be accurate. The effect of the wall material, wall thickness, fluid viscosity, tube constraints, and choice of the structural element were investigated and discussed in detail. This verification gave a solid foundation for the *in vitro* comparison conducted in Chapter 5, where a FSI model was utilized. It is an essential study for stomach modelling as well when investigating the interaction between the stomach wall and the gastric content in the future.

A FSI simulation was developed based on an *in vitro* intestinal peristaltic system designed by Professor Timothy Langrish and his PhD student Chao Zhong from the University of Sydney

223

(Chapter 5). The model was built based on the solution methodology verified in Chapter 4. The study aimed to replicate the mixing behaviour in a digestion system. In the *in vitro* study, oscillating pistons were used to generate flow in a flexible elastic tube and the mixing behaviour of the dye injected in the fluid was investigated. A significant amount of work was carried out to obtain stable solutions from the computational model, including the use of a weakly compressible fluid, optimising the parameters in a novel Quasi-Newton stabilisation algorithm, identification of the best means to constrain the model, and the pre-possessing of the input data to remove noise. A reliable and well-converged FSI model was developed, and the simulation results matched well with the base case experimental results. Two additional experimental cases were investigated, which did not match the simulation results so well. The additional experiments were conducted after the COVID interruption, and the experimental environment may have changed. Therefore, further investigation is required. Repeat experiments and improved visualisation techniques are currently being undertaken by the experimental team.

The ultimate goal of the *in vitro* study in Chapter 5 is to investigate tablet dissolution/food breakdown in the digestion system. Prior to that, the same group had collected experimental data for tablet dissolution in a beaker and stirrer system to estimate the mass transfer coefficient in the mixing system. Previous simulations for similar types of apparatus had used a simplified treatment of the stirrer and only studied the hydrodynamics. In Chapter 6, a numerical simulation of an *in vitro* beaker and stirrer system was developed and presented. The latest sliding mesh technique was used to capture the mixer motion. The flow and mass transfer for three different stirrers and two rotational speeds were simulated. The calculated mass transfer rate matched well with the experimental results. The calculated mass transfer rate was well correlated with the calculated Reynolds number and the predicted shear stress on the tablet surface. The relationship between these parameters is closely related to mass transfer in the digestion study as well.

The buoyant separation process of oil and water layers was simulated in a static stomach with SPH and FVM methods and was presented in Chapter 7. The mixing behaviour was visualized and characterised by tracking the oil volume fraction in different layers. Both methods provided similar results. The separation process occurred rapidly in the stomach geometry due to its complex curved shape that resulted in the buoyant motion generating a swirling flow. The growth of the Rayleigh-Taylor instability was well captured in the SPH model but not in the FVM model, most likely due to numerical smearing of the interfaces. However, the final

separation in the SPH model was incomplete while the fluid was fully separated in the FVM model, as expected. In addition, the dynamic viscosity of the water had to be increased artificially in the SPH simulation to reduce noise from the SPH tensile instability. Further improvement is desirable for both models, but the study has demonstrated the capability of both approaches when applied to the buoyancy effect in the stomach.

The motion of the stomach wall and acid mixing were implemented in the SPH stomach model, and the results were presented in Chapter 8. The fluid viscosity was found to have a significant effect on the fluid mixing and pH changes because the mass transfer in the fluid is advection dominated when a deforming wall was used. A 50% change in the contraction wave speed was found to be insignificant in this study. The pH change in the stomach was also affected by the acid diffusion coefficient. For a typical value of $10^{-9}\,\mathrm{m^2\,s^{-1}}$, it appears that the constant particle resolution SPH model was unable to resolve the mass transfer for a reasonable particle size. Possible ways of addressing this issue are presented in the future work.

In conclusion, a wide range of verification and validation studies on FVM, SPH and FSI approaches have been undertaken in this thesis. Traditional FVM has proven to be verified and easy to implement. SPH is a novel approach for these applications that has its advantages, but a comprehensive understanding of the method is required by the user to obtain accurate results with many inputs affecting the results. FSI was easy to utilize in the basic test case but required extensive user input for the complex problem. All three methods would benefit from continuous development to enhance their usability, accuracy and capabilities. Work from this thesis has been used to resolve defects and improve model accuracy in all the software used, stressing the importance of using the latest software versions.

In summary, FSI and FVM models have been developed to assist in the design and investigation of two *in vitro* models. Stomach modelling using SPH has been further explored by incorporating buoyancy-driven flow, a moving wall and acid mixing.

9.2. Future work

There are two main purposes of computational modelling in this thesis: (i) as a tool to assist in the design of *in vitro* experiments, and (ii) to provide more insights into the physics and chemistry of digestion in a human stomach. For the first, work in this thesis has provided support for designing the intestinal peristaltic system and the stirrer system. To further assist the improvement of the peristaltic system the cases that currently show poor agreement with

experimental data need to be revisited. The simulation could be run for laminar flow, as the Reynolds number in the fluid is within the laminar-turbulent transition region for the reduced force and reduced frequency cases. An initial attempt to run a laminar case with the same timestep and one order of magnitude smaller diverged. A highly refined mesh and small timestep will likely be needed to capture the complex jet flow present. In the meanwhile, recalibration of the colour test in the experiment is underway and the continued investigation of *in vitro* model is required as more experimental data become available.

Ansys Fluent has an in-built structural solver that was tested for the validation work done in Chapter 4, but it was not possible to obtain a stable solution. Since then, the feedback provided from the work in this thesis has been used to make improvements. It would be very useful to retest the case, as using only one software package could potentially speed up simulations and make their setup much easier.

The objective of stomach modelling is to provide a reliable and comprehensive understanding of flow and mixing behaviour in the stomach. This thesis has presented a large amount of verification and validation investigation of different numerical approaches and expanded the capabilities of the currently developed SPH method. Further investigation is required in improving the accuracy of the current models and expanding the capabilities even further.

Based on the results from the SPH model for the buoyancy-driven flow, the buoyancy force exerted by the fluid particles with a smoothed density does not lead to full separation. A potential solution to this issue is to implement an adaptive refinement method, which allows particle size modification to capture small fluid fragments. Its use should be considered in future work, if it is desirable to achieve complete separation.

In the acid modelling, a more sophisticated treatment to capture the thin concentration layer close to the wall is required. Use of extremely small particles is impractical. In the FVM, wall functions are used to avoid resolving velocity and concentration boundary layers in turbulent flow. Investigation of ways of adapting this, or a modified approach, for use in SPH is desirable. A staged verification and validation approach, starting with simple boundary layer flow, is required to validate any such implementation.

When comparing FVM and SPH, the major disadvantage of FVM is the need to change the location of every node in the mesh when the domain shape is changed, as occurs for the stomach modelling presented here. Previous work [14, 22] using FVM incorporated a succession of meshes that are read in at each timestep, with data being interpolated onto the new mesh from

the previous solution. This is expensive computationally and not well suited to parallel computing, as repartitioning is needed for each new mesh. A recent study used the dynamic mesh method to adapt the deformation using the open-source CFD program OpenFoam [80]. This technique could be tested in Ansys Fluent given the significant improvements made in dynamic meshing over recent years and from feedback provided as part of this thesis.

An alternative strategy is to create a series of meshes at key points in time that have the same mesh topology and number of elements, and then use an interpolation method between them. Often radial basis functions are used for this task as they provide an efficient method of smooth interpolation [222]. This methodology is embodied in a computer code RBF-MORPH, developed at the University of Rome Tor Vergata, that interfaces with the CFD solver Ansys Fluent used in this thesis. A recent study of the motion of a heart valve [223] demonstrates an application that is very similar to the motion required for the stomach and highlights the ability of the method to maintain good mesh quality. Morphing means the topology of the computational mesh does not change, so no repartitioning is needed between mesh updates. It is recommended that this technique be tried with a mesh of the stomach geometry used in this thesis, which would produce a model that can be compared with the SPH method used here to provide an independent comparison. It would allow all the physical models present in Ansys Fluent, that have undergone extensive verification and validation, to be used in the study of digestion in the stomach.

The development of stomach modelling still requires an extensive amount of work, including the integration of comprehensive models of food breakdown and chyme chemistry. Detailed components that need to be implemented are the inclusion of large undigested food fragments with properly simulated internal and external structures, mass diffusion of acid and other chemical species at the surface of the food, also allowing internal penetration. The different mechanisms of food breakdown with different types of food (carbohydrates, proteins, fats, etc.) need to be investigated as well. Furthermore, the simulation results from the comprehensively developed model need to be validated against *in vivo* or *in vitro* data.

Finally, modelling of the compliant behaviour of the stomach wall should be included. The model needs to include a representation of the multiple layers of the stomach wall, along with their non-linear and anisotropic elastic behaviour and their contraction behaviour balancing internal fluid forces and external supporting forces from surrounding connective tissue. This is a very challenging problem that will need significant code development.

Reference

[1]   World Health Organization. "Obesity and overweight." https://www.who.int/news-room/fact-sheets/detail/obesity-and-overweight (accessed 08/01, 2022).

[2]   D. Dupont *et al.*, "Can dynamic in vitro digestion systems mimic the physiological reality?," *Food Science and Nutrition,* pp. 1-17, 2018, doi: 10.1080/10408398.2017.1421900.

[3]   C. Li, W. Yu, P. Wu, and X. D. Chen, "Current in vitro digestion systems for understanding food digestion in human upper gastrointestinal tract," *Trends in Food Science and Technology,* vol. 96, pp. 114-126, 2020, doi: 10.1016/j.tifs.2019.12.015.

[4]   C. Zhong and T. Langrish, "A comparison of different physical stomach models and an analysis of shear stresses and strains in these system," *Food Research International,* vol. 135, p. 109296, 2020, doi: 10.1016/j.foodres.2020.109296.

[5]   G. M. Bornhorst and R. P. Singh, "Gastric digestion in vivo and in vitro: how the structural aspects of food influence the digestion process," *Annual Review of Food Science and Technology,* vol. 5, pp. 111-32, 2014, doi: 10.1146/annurev-food-030713-092346.

[6]   T. A. G. Langrish, "Multifilm mass transfer and time constants for mass transfer in food digestion: Application to gut-on-chip models," *Applied Biosciences,* vol. 1, no. 2, pp. 101-112, 2022, doi: 10.3390/applbiosci1020007.

[7]   F. Kong and R. P. Singh, "A model stomach system to investigate disintegration kinetics of solid foods during gastric digestion," *Journal of Food Science,* vol. 73, no. 5, pp. E202-10, 2008, doi: 10.1111/j.1750-3841.2008.00745.x.

[8]   J.-L. Urbain, J. Siegel, N. D. Charkes, A. Maurer, L. Malmud, and R. Fisher, "The two-component stomach: effects of meal particle size on fundal and antral emptying," *European Journal of Nuclear Medicine,* vol. 15, no. 5, 1989, doi: 10.1007/bf00257543.

[9]   S. Brandstaeter, S. L. Fuchs, R. C. Aydin, and C. J. Cyron, "Mechanics of the stomach: A review of an emerging field of biomechanics," *GAMM-Mitteilungen,* vol. 42, no. 3, p. e201900001, 2019, doi: 10.1002/gamm.201900001.

[10]   E. A. H. Beckett, C. A. McGeough, K. M. Sanders, and S. M. Ward, "Pacing of interstitial cells of Cajal in the murine gastric antrum: neurally mediated and direct stimulation," *The Journal of Physiology,* vol. 553, no. 2, pp. 545-559, 2003, doi: 10.1113/jphysiol.2003.050419.

[11]   D. A. Owen, "Normal histology of the stomach," *The American Journal of Surgical Pathology,* vol. 10, no. 1, pp. 48-61, Jan 1986, doi: 10.1097/00000478-198601000-00006.

[12]   A. Csendes and A. M. Burgos, "Size, volume and weight of the stomach in patients with morbid obesity compared to controls," *Obesity Surgery,* vol. 15, no. 8, pp. 1133-1136, 2005, doi: 10.1381/0960892055002158.

[13]   K. Schulze, "Imaging and modelling of digestion in the stomach and the duodenum," *Neurogastroenterology and Motility,* vol. 18, no. 3, pp. 172-183, 2006, doi: 10.1111/j.1365-2982.2006.00759.x.

[14] M. J. Ferrua and R. P. Singh, "Modeling the fluid dynamics in a human stomach to gain insight of food digestion," *Journal of Food Science,* vol. 75, no. 7, pp. R151-62, 2010, doi: 10.1111/j.1750-3841.2010.01748.x.

[15] T. Yamada, D. H. Alpers, L. Lain, and N. Kaplowitz, *Textbook of Gastroenterology*. Lippincott Williams & Wilkins, 2003.

[16] L. M. B. S. D. A. H. R. H. J. K. M. L. P. M. K. M.-G. D. Q. a. J. Runyeon, "The digestive system," in *Anatomy & Physiology 1.1 OE*, 2019, ch. 23.

[17] C. H. Huh, M. S. Bhutani, E. B. Farfan, and W. E. Bolch, "Individual variations in mucosa and total wall thickness in the stomach and rectum assessed via endoscopic ultrasound," *Physiological Measurement,* vol. 24, no. 4, pp. N15-N22, 2003, doi: 10.1088/0967-3334/24/4/401.

[18] B. T. Petersen, *Gastrointestinal disease: Pathophysiology, diagnosis, management, 5th ed* (Gastroenterology, no. 3). Philadelphia, Pennsylvania: W. B. Saunders Company, 1994, p. 818.

[19] Z. G. Jia, W. Li, and Z. R. Zhou, "Mechanical characterization of stomach tissue under uniaxial tensile action," *Journal of Biomechanics,* vol. 48, no. 4, pp. 651-658, 2015, doi: 10.1016/j.jbiomech.2014.12.048.

[20] J. Zhao, D. Liao, P. Chen, P. Kunwald, and H. Gregersen, "Stomach stress and strain depend on location, direction and the layered structure," *Journal of Biomechanics,* vol. 41, no. 16, pp. 3441-3447, 2008, doi: 10.1016/j.jbiomech.2008.09.008.

[21] D. Liao, J. Zhao, and H. Gregersen, "Three-dimensional geometry analysis of the stomach in type II diabetic GK rats," *Diabetes Research and Clinical Practice,* vol. 71, no. 1, pp. 1-13, 2006, doi: 10.1016/j.diabres.2005.05.016.

[22] M. J. Ferrua and R. P. Singh, "Understanding the fluid dynamics of gastric digestion using computational modeling," *Procedia Food Science,* vol. 1, pp. 1465-1472, 2011, doi: 10.1016/j.profoo.2011.09.217.

[23] R. R. Seeley, *Essentials of anatomy and physiology*, 4th ed. Boston, Mass: McGraw-Hill, 2002.

[24] F. Azpiroz, "Control of gastric emptying by gastric tone," *Digestive Diseases and Sciences,* vol. 39, no. 12, pp. 18S-19S, 1994, doi: 10.1007/BF02300362.

[25] D. H. A. Tadataka Yamada, Anthony N Kalloo, Neil Kaplowitz, Chung Owyang, Don W. Powell, *Textbook of gastroenterology*, 5th ed. Blackwell Publishing Ltd, 2009.

[26] A. Pal, K. Indireshkumar, W. Schwizer, B. Abrahamsson, M. Fried, and J. G. Brasseur, "Gastric flow and mixing studied using computer simulation," *Proceedings of the Royal Society B: Biological Sciences,* vol. 271, no. 1557, pp. 2587-94, 2004, doi: 10.1098/rspb.2004.2886.

[27] Z. Xue, M. J. Ferrua, and R. P. Singh, "Computational fluid dynamics modeling of granular flow in human stomach," *Alimentos Hoy,* vol. 21, no. 27, pp. 3-14, 2012. [Online]. Available: https://alimentoshoy.acta.org.co/index.php/hoy/article/viewFile/137/131.

[28] P. M. Hellström, P. Grybäck, and H. Jacobsson, "The physiology of gastric emptying," *Best Practice and Research Clinical Anaesthesiology,* vol. 20, no. 3, pp. 397-407, 2006, doi: 10.1016/j.bpa.2006.02.002.

[29] F. Kong and R. P. Singh, "Disintegration of solid foods in human stomach," *Journal of Food Science,* vol. 73, no. 5, pp. R67-R80, 2008, doi: 10.1111/j.1750-3841.2008.00766.x.

[30] M. A. Evans, E. J. Triggs, M. Cheung, G. A. Broe, and H. Creasey, "Gastric emptying rate in the elderly: implications for drug therapy," *Journal of the American Geriatrics Society,* vol. 29, no. 5, pp. 201-205, 1981, doi: 10.1111/j.1532-5415.1981.tb01766.x.

[31] W. C. Klingensmith, K. L. Rhea, E. A. Wainwright, and O. W. Hopper, "The gastric emptying study with oatmeal: Reference range and reproducibility as a function of age and sex," *Journal of Nuclear Medicine Technology,* vol. 38, no. 4, pp. 186-190, 2010, doi: 10.2967/jnmt.110.077065.

[32] A. Caballero-Plasencia, M. Valenzuela-Barranco, J. Martin-Ruiz, J. Herrerias-Gutierrez, and J. Esteban-Carretero, "Are there changes in gastric emptying during the menstrual cycle?," *Scandinavian Journal of Gastroenterology,* vol. 34, no. 8, pp. 772-776, 1999, doi: 10.1080/003655299750025697.

[33] S. Hellmig *et al.*, "Gastric emptying time of fluids and solids in healthy subjects determined by 13C breath tests: influence of age, sex and body mass index," *Journal of Gastroenterol Hepatol,* vol. 21, no. 12, pp. 1832-1838, 2006, doi: 10.1111/j.1440-1746.2006.04449.x.

[34] N. Gainsborough *et al.*, "The association of age with gastric emptying," *Age and Ageing,* vol. 22, no. 1, pp. 37-40, 1993, doi: 10.1093/ageing/22.1.37.

[35] J. G. Moore, C. Tweedy, P. E. Christian, and F. L. Datz, "Effect of age on gastric emptying of liquid-solid meals in man," *Digestive Diseases and Sciences,* vol. 28, no. 4, pp. 340-344, 1983, doi: 10.1007/BF01324951.

[36] L. Bolondi, M. Bortolotti, V. Santi, T. Calletti, S. Gaiani, and G. Labò, "Measurement of gastric emptying time by real-time ultrasonography," *Gastroenterology,* vol. 89, no. 4, pp. 752-759, 1985, doi: 10.1016/0016-5085(85)90569-4.

[37] G. L. Amidon, G. A. DeBrincat, and N. J. Najib, "Effects of gravity on gastric emptying, intestinal transit, and drug absorption," *The Journal of Clinical Pharmacology,* vol. 31, no. 10, pp. 968-973, 1991, doi: 10.1002/j.1552-4604.1991.tb03658.x.

[38] S. Arora, J. Ali, A. Ahuja, R. K. Khar, and S. Baboota, "Floating drug delivery systems: a review," *AAPS PharmSciTech,* vol. 6, no. 3, pp. E372-E390, 2005, doi: 10.1208/pt060347.

[39] G. M. Bornhorst, L. Q. Chang, S. M. Rutherfurd, P. J. Moughan, and R. P. Singh, "Gastric emptying rate and chyme characteristics for cooked brown and white rice meals in vivo," *Journal of the Science of Food and Agriculture,* vol. 93, no. 12, pp. 2900-8, 2013, doi: 10.1002/jsfa.6160.

[40] J. D. Elashoff, T. J. Reedy, and J. H. Meyer, "Analysis of gastric emptying data," *Gastroenterology,* vol. 83, no. 6, pp. 1306-1312, 1982, doi: 10.1016/S0016-5085(82)80145-5.

[41] Y. Shimoyama *et al.*, "High-viscosity liquid meal accelerates gastric emptying," *Neurogastroenterology and Motility,* vol. 19, no. 11, pp. 879-886, 2007, doi: 10.1111/j.1365-2982.2007.00972.x.

[42] Y. Zhu, W. H. Hsu, and J. H. Hollis, "The impact of food viscosity on eating rate, subjective appetite, glycemic response and gastric emptying rate," *PLOS ONE,* vol. 8, no. 6, p. e67482, 2013, doi: 10.1371/journal.pone.0067482.

[43] P. J. Collins, M. Horowitz, A. Maddox, J. C. Myers, and B. E. Chatterton, "Effects of increasing solid component size of a mixed solid/liquid meal on solid and liquid gastric emptying," *American Journal of Physiology-Gastrointestinal and Liver Physiology,* vol. 271, no. 4, pp. G549-G554, 1996, doi: 10.1152/ajpgi.1996.271.4.G549.

[44] R. K. Goyal, Y. Guo, and H. Mashimo, "Advances in the physiology of gastric emptying," *Neurogastroenterology and Motility,* vol. 31, no. 4, p. e13546, 2019, doi: 10.1111/nmo.13546.

[45] J. H. Lavin, S. J. French, and N. W. Read, "Comparison of oral and gastric administration of sucrose and maltose on gastric emptying rate and appetite," *International Journal of Obesity,* vol. 26, no. 1, pp. 80-86, 2002, doi: 10.1038/sj.ijo.0801828.

[46] Y. Jin, P. J. Wilde, Y. Hou, Y. Wang, J. Han, and W. Liu, "An evolving view on food viscosity regulating gastric emptying," *Critical Reviews in Food Science and Nutrition,* pp. 1-17, 2022, doi: 10.1080/10408398.2021.2024132.

[47] G. Camps, M. Mars, C. De Graaf, and P. A. Smeets, "Empty calories and phantom fullness: a randomized trial studying the relative effects of energy density and viscosity on gastric emptying determined by MRI and satiety," *The American Journal of Clinical Nutrition,* vol. 104, no. 1, pp. 73-80, 2016, doi: 10.3945/ajcn.115.129064.

[48] L. Marciani *et al.*, "Gastric response to increased meal viscosity assessed by echo-planar magnetic resonance imaging in humans," *The Journal of Nutrition,* vol. 130, no. 1, pp. 122-127, 2000, doi: 10.1093/jn/130.1.122.

[49] W. M. Sun, L. A. Houghton, N. W. Read, D. G. Grundy, and A. G. Johnson, "Effect of meal temperature on gastric emptying of liquids in man," *Gut,* vol. 29, no. 3, pp. 302-305, 1988, doi: 10.1136/gut.29.3.302.

[50] J. A. Siegel *et al.*, "Biphasic nature of gastric emptying," *Gut,* vol. 29, no. 1, pp. 85-89, 1988. [Online]. Available: https://gut.bmj.com/content/gutjnl/29/1/85.full.pdf.

[51] G. M. Bornhorst, M. J. Ferrua, and R. P. Singh, "A proposed food breakdown classification system to predict food behavior during gastric digestion," *Journal of Food Science,* vol. 80, no. 5, pp. R924-R934, 2015, doi: 10.1111/1750-3841.12846.

[52] J.-L. C. Urbain, J. A. Siegel, N. D. Charkes, A. H. Maurer, L. S. Malmud, and R. S. Fisher, "The two-component stomach: effects of meal particle size on fundal and antral emptying," *European Journal of Nuclear Medicine,* vol. 15, no. 5, pp. 254-259, 1989, doi: 10.1007/BF00257543.

[53] L. Benini *et al.*, "Gastric emptying of solids is markedly delayed when meals are fried," *Digestive Diseases and Sciences,* vol. 39, no. 11, pp. 2288-2294, 1994, doi: 10.1007/BF02087640.

[54] G. M. Bornhorst, M. J. Roman, S. M. Rutherfurd, B. J. Burri, P. J. Moughan, and R. P. Singh, "Gastric digestion of raw and roasted almonds in vivo and in vitro," *Journal of Food Science,* vol. 78, no. 11, pp. H1807-H1813, 2013, doi: 10.1111/1750-3841.12274.

[55] B. Meyer, C. Beglinger, M. Neumayer, and G. A. Stalder, "Physical characteristics of indigestible solids affect emptying from the fasting human stomach," *Gut,* vol. 30, no. 11, pp. 1526-1529, 1989, doi: 10.1136/gut.30.11.1526.

[56] Australian Dietary Guidelines. "Sample meal plan for men." https://www.eatforhealth.gov.au/food-essentials/how-much-do-we-need-each-day/sample-meal-plan-men (accessed 14/03, 2022).

[57] Food Standards Australia New Zealand. Australian Food Composition Database - Release 2.0 [Online] Available: https://www.foodstandards.gov.au/science/monitoringnutrients/afcd/Pages/foodsearch.aspx

[58] J. Hwang *et al.*, "The effect of rheological properties of foods on bolus characteristics after mastication," *Annals of Rehabilitation Medicine,* vol. 36, no. 6, p. 776, 2012, doi: 10.5535/arm.2012.36.6.776.

[59] M.-L. Jalabert-Malbos, A. Mishellany-Dutour, A. Woda, and M.-A. Peyron, "Particle size distribution in the food bolus after mastication of natural foods," *Food Quality and Preference,* vol. 18, no. 5, pp. 803-812, 2007, doi: 10.1016/j.foodqual.2007.01.010.

[60] C. Fuentes *et al.*, "Fractionation and characterization of starch granules using field-flow fractionation (FFF) and differential scanning calorimetry (DSC)," *Analytical and Bioanalytical Chemistry,* vol. 411, no. 16, pp. 3665-3674, 2019, doi: 10.1007/s00216-019-01852-9.

[61] R. M. Faulks and A. L. Bailey, "Digestion of cooked starches from different food sources by porcine α-amylase," *Food Chemistry,* vol. 36, no. 3, pp. 191-203, 1990, doi: 10.1016/0308-8146(90)90054-8.

[62] P. J. Butterworth, F. J. Warren, and P. R. Ellis, "Human α-amylase and starch digestion: An interesting marriage," *Starch,* vol. 63, no. 7, pp. 395-405, 2011, doi: 10.1002/star.201000150.

[63] J. Nadia *et al.*, "Tracking physical breakdown of rice- and wheat-based foods with varying structures during gastric digestion and its influence on gastric emptying in a growing pig model," *Food and Function,* vol. 12, no. 10, pp. 4349-4372, 2021, doi: 10.1039/d0fo02917c.

[64] G. M. Bornhorst, M. Ferrua, S. Rutherfurd, D. Heldman, and R. P. Singh, "Rheological properties and textural attributes of cooked brown and white rice during gastric digestion in vivo," *Food Biophysics,* vol. 8, no. 2, pp. 137-150, 2013, doi: 10.1007/s11483-013-9288-1.

[65] N. Metayer *et al.*, "Meal size and starch content affect gastric emptying in horses," *Equine Veterinary Journal,* vol. 36, no. 5, pp. 436-440, 2004, doi: 10.2746/0425164044868468.

[66] S. A. S. Gropper, *Advanced nutrition and human metabolism*, 6th ed. Belmont, CA: Wadsworth/Cengage Learning, 2013.

[67] A. Nawirska and M. Kwaśniewska, "Dietary fibre fractions from fruit and vegetable processing waste," *Food Chemistry,* vol. 91, no. 2, pp. 221-225, 2005, doi: 10.1016/j.foodchem.2003.10.005.

[68] S. Medhe, M. Anand, and A. K. Anal, "Dietary fibers, dietary peptides and dietary essential fatty acids from food processing by‐products," *Food Processing By‐Products and their Utilization,* pp. 111-136, 2017, doi: 10.1002/9781118432921.ch6.

[69] Y. A. Mennah-Govela and G. M. Bornhorst, "Food buffering capacity: quantification methods and its importance in digestion and health," *Food and Function,* vol. 12, no. 2, pp. 543-563, 2021, doi: 10.1039/d0fo02415e.

[70] Y. A. Mennah-Govela, R. P. Singh, and G. M. Bornhorst, "Buffering capacity of protein-based model food systems in the context of gastric digestion," *Food and Function,* vol. 10, no. 9, pp. 6074-6087, 2019, doi: 10.1039/c9fo01160a.

[71] W. M. N. Ratnayake and C. Galli, "Fat and fatty acid terminology, methods of analysis and fat digestion and metabolism," *Annals of Nutrition and Metabolism,* vol. 55, no. 1-3, pp. 8-43, 2009, doi: 10.1159/000228994.

[72] F. Carriere, J. A. Barrowman, R. Verger, and L. René, "Secretion and contribution to lipolysis of gastric and pancreatic lipases during a test meal in humans," *Gastroenterology,* vol. 105, no. 3, pp. 876-888, 1993, doi: 10.1016/0016-5085(93)90908-u.

[73] L. Lundin, M. Golding, and T. J. Wooster, "Understanding food structure and function in developing food for appetite control," *Nutrition and Dietetics,* vol. 65, no. s3, pp. S79-S85, 2008, doi: 10.1111/j.1747-0080.2008.00266.x.

[74] M. Armand *et al.*, "Physicochemical characteristics of emulsions during fat digestion in human stomach and duodenum," *American Journal of Physiology-Gastrointestinal and Liver Physiology,* vol. 271, no. 1, pp. G172-G183, 1996, doi: 10.1152/ajpgi.1996.271.1.G172.

[75] A. A. Noyes and W. R. Whitney, "The rate of solution of solid substances in their own solutions," *Journal of the American Chemical Society,* vol. 19, no. 12, pp. 930-934, 1897, doi: 10.1021/ja02086a003.

[76] J. Blazek, *Computational Fluid Dynamics*, 3rd ed. Burlington: Butterworth-Heinemann, 2015, p. 466.

[77] H. Kozu, I. Kobayashi, M. Nakajima, K. Uemura, S. Sato, and S. Ichikawa, "Analysis of flow phenomena in gastric contents induced by human gastric peristalsis using CFD," *Food Biophysics,* vol. 5, no. 4, pp. 330-336, 2010, doi: 10.1007/s11483-010-9183-y.

[78] M. R. Kamaltdinov, P. V. Trusov, and N. V. Zaitseva, "Multi-component mixture flow in the stomach and duodenum allowing for functional disorders: Results of numeric modelling for determining acidity," *Russian Journal of Biomechanics,* vol. 21, no. 3, pp. 205-223, 2017, doi: 10.15593/RJBiomech/2017.3.02.

[79] S. Alokaily, K. Feigl, and F. X. Tanner, "Characterization of peristaltic flow during the mixing process in a model human stomach," *Physics of Fluids,* vol. 31, no. 10, pp. 103-105, 2019, doi: 10.1063/1.5122665.

[80] C. Li and Y. Jin, "A CFD model for investigating the dynamics of liquid gastric contents in human-stomach induced by gastric motility," *Journal of Food Engineering,* vol. 296, p. 110461, 2021, doi: 10.1016/j.jfoodeng.2020.110461.

[81] T. Miyagawa, Y. Imai, S. Ishida, and T. Ishikawa, "Relationship between gastric motility and liquid mixing in the stomach," *American Journal of Physiology-*

Gastrointestinal and Liver Physiology, vol. 311, no. 6, pp. G1114-G1121, 2016, doi: 10.1152/ajpgi.00346.2016.

[82]   S. Ishida, T. Miyagawa, G. O'Grady, L. K. Cheng, and Y. Imai, "Quantification of gastric emptying caused by impaired coordination of pyloric closure with antral contraction: a simulation study," *Journal of The Royal Society Interface,* vol. 16, no. 157, 2019, doi: 10.1098/rsif.2019.0266.

[83]   S. M. Harrison, P. W. Cleary, and M. D. Sinnott, "Investigating mixing and emptying for aqueous liquid content from the stomach using a coupled biomechanical-SPH model," *Food and Function,* vol. 9, no. 6, pp. 3202-3219, 2018, doi: 10.1039/c7fo01226h.

[84]   Y. Imai, I. Kobayashi, S. Ishida, T. Ishikawa, M. Buist, and T. Yamaguchi, "Antral recirculation in the stomach during gastric mixing," *American Journal of Physiology-Gastrointestinal and Liver Physiology,* vol. 304, no. 5, pp. G536-G542, 2013, doi: 10.1152/ajpgi.00350.2012.

[85]   R. Eymard, T. Gallouët, and R. Herbin, "Finite volume methods," in *Handbook of Numerical Analysis*, vol. 7: Elsevier, 2000, pp. 713-1018.

[86]   S. Chen and G. D. Doolen, "Lattice boltzmann method for fluid flows," *Annual Review of Fluid Mechanics,* vol. 30, no. 1, pp. 329-364, 1998, doi: 10.1146/annurev.fluid.30.1.329.

[87]   R. A. Gingold and J. J. Monaghan, "Smoothed particle hydrodynamics: theory and application to non-spherical stars," *Monthly Notices of the Royal Astronomical Society,* vol. 181, no. 3, pp. 375-389, 1977, doi: 10.1093/mnras/181.3.375.

[88]   J. J. Monaghan, "Simulating free surface flows with SPH," *Journal of Computational Physics,* vol. 110, no. 2, pp. 399-406, 1994, doi: 10.1006/jcph.1994.1034.

[89]   J. J. Monaghan, "Smoothed particle hydrodynamics," *Reports on Progress in Physics,* vol. 68, p. 1703, 2005.

[90]   P. Cleary, M. Prakash, J. Ha, N. Stokes, and C. Scott, "Smooth particle hydrodynamics: Status and future potential," *Progress in Computational Fluid Dynamics,* vol. 7, pp. 70-90, 2007, doi: 10.1504/PCFD.2007.013000.

[91]   Ting Ye, Dingyi Pan, and M. L. Can Huang, "Smoothed particle hydrodynamics (SPH) for complex fluid flows: Recent developments in methodology and applications," *Physics of Fluids,* vol. 31, no. 1, p. 011301, 2019, doi: 10.1063/1.5068697.

[92]   G. R. Liu and M. B. Liu, *Smoothed Particle Hydrodynamics: A Meshfree Particle Method.* World Scientific Publishing Co Pte Ltd, 2003.

[93]   Z.-B. Wang, R. Chen, H. Wang, Q. Liao, X. Zhu, and S.-Z. Li, "An overview of smoothed particle hydrodynamics for simulating multiphase flow," *Applied Mathematical Modelling,* vol. 40, no. 23, pp. 9625-9655, 2016.

[94]   P. W. Cleary and J. J. Monaghan, "Conduction modelling using smoothed particle hydrodynamics," *Journal of Computational Physics,* vol. 148, no. 1, pp. 227-264, 1999.

[95]   J. J. Monaghan, "SPH without a tensile instability," *Journal of Computational Physics,* vol. 159, no. 2, pp. 290-311, 2000, doi: 10.1006/jcph.2000.6439.

[96]   V. Mehra, C. D. Sijoy, V. Mishra, and S. Chaturvedi, "Tensile instability and artificial stresses in impact problems in SPH," *Journal of Physics: Conference Series,* vol. 377, p. 012102, 2012, doi: 10.1088/1742-6596/377/1/012102.

[97]   K. S. Kim, M. H. Kim, and J.-C. Park, "Development of moving particle simulation method for multiliquid-layer sloshing," *Mathematical Problems in Engineering,* vol. 2014, p. 13, 2014, doi: 10.1155/2014/350165.

[98]   S. R. Idelsohn and E. Oñate, "Finite volumes and finite elements: Two 'good friends'," *International Journal for Numerical Methods in Engineering,* vol. 37, no. 19, pp. 3323-3341, 1994, doi: 10.1002/nme.1620371908.

[99]   K.-J. Bathe, "Finite Element Method," in *Wiley Encyclopedia of Computer Science and Engineering*, B. W. Wah Ed.: John Wiley and Sons, 2007, pp. 1-12.

[100]   S. S. Rao, *The finite element method in engineering*. Butterworth-heinemann, 2017.

[101]   O. C. Zienkiewicz, R. L. Taylor, and J. Z. Zhu, *The finite element method: its basis and fundamentals*. Elsevier, 2005.

[102]   P. A. Cundall and O. D. L. Strack, "A discrete numerical model for granular assemblies," *Géotechnique,* vol. 29, no. 1, pp. 47-65, 1979, doi: 10.1680/geot.1979.29.1.47.

[103]   F. A. Tavarez and M. E. Plesha, "Discrete element method for modelling solid and particulate materials," *International Journal for Numerical Methods in Engineering,* vol. 70, no. 4, pp. 379-404, 2007, doi: 10.1002/nme.1881.

[104]   G. G. Mustoe, "A generalized formulation of the discrete element method," *Engineering Computations,* 1992, doi: 10.1108/eb023857.

[105]   P. W. Cleary and M. L. Sawley, "DEM modelling of industrial granular flows: 3D case studies and the effect of particle shape on hopper discharge," *Applied Mathematical Modelling,* vol. 26, no. 2, pp. 89-111, 2002, doi: 10.1016/S0307-904X(01)00050-6.

[106]   P. W. Cleary, "Large scale industrial DEM modelling," *Engineering Computations,* vol. 21, no. 2/3/4, pp. 169-204, 2004, doi: 10.1016/S0307-904X(01)00050-6.

[107]   P. W. Cleary, "DEM prediction of industrial and geophysical particle flows," *Particuology,* vol. 8, no. 2, pp. 106-118, 2010, doi: 10.1016/j.partic.2009.05.006.

[108]   A. J. C. Ladd, "Numerical simulations of particulate suspensions via a discretized Boltzmann equation. Part 1. Theoretical foundation," *Journal of Fluid Mechanics,* vol. 271, pp. 285-309, 1994, doi: 10.1017/S0022112094001771.

[109]   A. Pal, J. G. Brasseur, and B. Abrahamsson, "A stomach road or Magenstrasse for gastric emptying," *Journal of Biomechanics,* vol. 40, no. 6, pp. 1202-1210, 2007, doi: 10.1016/j.jbiomech.2006.06.006.

[110]   M. R. Kamaltdinov, P. V. Trusov, and N. V. Zaitseva, "A multiphase flow in the antroduodenum: some results of the mathematical modelling and computational simulation," *MATEC Web of Conferences,* vol. 145, p. 04002, 2018, doi: 10.1051/matecconf/201814504002.

[111]   C. G. Skamniotis, C. H. Edwards, S. Bakalis, G. Frost, and M. N. Charalambides, "Eulerian-Lagrangian finite element modelling of food flow-fracture in the stomach to engineer digestion," *Innovative Food Science and Emerging Technologies,* p. 102510, 2020, doi: 10.1016/j.ifset.2020.102510.

[112] C. Li, J. Xiao, X. Dong Chen, and Y. Jin, "Mixing and emptying of gastric contents in human-stomach: A numerical study," *Journal of Biomechanics,* vol. 118, p. 110293, 2021, doi: 10.1016/j.jbiomech.2021.110293.

[113] S. Acharya, S. Halder, W. Kou, P. J. Kahrilas, J. E. Pandolfino, and N. A. Patankar, "A fully resolved multiphysics model of gastric peristalsis and bolus emptying in the upper gastrointestinal tract," *Computers in Biology and Medicine,* vol. 143, p. 104948, 2022, doi: 10.1016/j.compbiomed.2021.104948.

[114] J. H. Lee, S. Kuhar, J. H. Seo, P. J. Pasricha, and R. Mittal, "Computational modeling of drug dissolution in the human stomach: Effects of posture and gastroparesis on drug bioavailability," *Physics of Fluids,* vol. 34, no. 8, p. 081904, 2022, doi: 10.1063/5.0096877.

[115] S. Kuhar, J. HoLee, Jung-HeeSeo, P. J. Pasricha, and R. Mittal, "Effect of stomach motility on food hydrolysis and gastric emptying: Insight from computational models," *Physics of Fluids,* vol. 34, no. 11, p. 111909, 2022, doi: 10.1063/5.0120933.

[116] S. M. Harrison, G. Eyres, P. W. Cleary, M. D. Sinnott, C. Delahunty, and L. Lundin, "Computational modeling of food oral breakdown using Smoothed Particle Hydrodynamics," *Journal of Texture Studies,* vol. 45, no. 2, pp. 97-109, 2014, doi: 10.1111/jtxs.12062.

[117] M. D. Sinnott, P. W. Cleary, and S. M. Harrison, "Peristaltic transport of a particulate suspension in the small intestine," *Applied Mathematical Modelling,* vol. 44, pp. 143-159, 2017, doi: 10.1016/j.apm.2017.01.034.

[118] M. D. Sinnott, P. W. Cleary, and S. M. Harrison, "Multiphase transport in the small intestine," presented at the Eleventh International Conference on CFD in the Minerals and Process Industries, Melbourne, Australia, 2015. [Online]. Available: https://www.cfd.com.au/cfd_conf15/PDFs/131SIN.pdf.

[119] M. D. Sinnott, P. W. Cleary, J. W. Arkwright, and P. G. Dinning, "Investigating the relationships between peristaltic contraction and fluid transport in the human colon using Smoothed Particle Hydrodynamics," *Computers in biology and medicine,* vol. 42, no. 4, pp. 492-503, 2012, doi: 10.1016/j.compbiomed.2012.01.002.

[120] Y. C. Fung and C. S. Yih, "Peristaltic transport," *Journal of Applied Mechanics,* vol. 35, no. 4, pp. 669-675, 1968, doi: 10.1115/1.3601290.

[121] J. G. Brasseur, "A fluid mechanical perspective on esophageal bolus transport," *Dysphagia,* vol. 2, no. 1, pp. 32-39, 1987, doi: 10.1007/BF02406976.

[122] J. D. Huizinga, "Gastrointestinal peristalsis: joint action of enteric nerves, smooth muscle, and interstitial cells of Cajal," *Microscopy Research and Technique,* vol. 47, no. 4, pp. 239-247, 1999, doi: 10.1002/(SICI)1097-0029(19991115)47:4<239::AID-JEMT3>3.0.CO;2-0.

[123] S. J. Hur, B. O. Lim, E. A. Decker, and D. J. J. F. c. McClements, "In vitro human digestion models for food applications," *Food Chemistry,* vol. 125, no. 1, pp. 1-12, 2011, doi: 10.1016/j.foodchem.2010.08.036.

[124] P. W. Cleary *et al.*, "Application of SPH to single and multiphase geophysical, biophysical and industrial fluid flows," *International Journal of Computational Fluid Dynamics,* vol. 35, no. 1-2, pp. 22-78, 2021, doi: 10.1080/10618562.2020.1841897.

[125] M. Sinnott, P. Cleary, J. Arkwright, and P. Dinning, "Modeling colonic motility: How does descending inhibition influence the transport of fluid?," *Gastroenterology,* 2011, doi: 10.1016/S0016-5085(11)63595-6.

[126] J. G. Brasseur, M. A. Nicosia, A. Pal, and L. S. Miller, "Function of longitudinal vs circular muscle fibers in esophageal peristalsis, deduced with mathematical modeling," *World Journal of Gastroenterology,* vol. 13, no. 9, pp. 1335-1346, 2007, doi: 10.3748/wjg.v13.i9.1335.

[127] M. J. Ferrua, F. Kong, and R. P. Singh, "Computational modeling of gastric digestion and the role of food material properties," *Trends in Food Science and Technology,* vol. 22, no. 9, pp. 480-491, 2011, doi: 10.1016/j.tifs.2011.04.007.

[128] P. Du, N. Paskaranandavadivel, T. R. Angeli, L. K. Cheng, and G. O'Grady, "The virtual intestine: in silico modeling of small intestinal electrophysiology and motility and the applications," *Wiley Interdisciplinary Reviews: Systems Biology and Medicine,* vol. 8, no. 1, pp. 69-85, 2016, doi: 10.1002/wsbm.1324.

[129] P. W. Cleary, Harrison, S. M., Sinnott, M. D., "Flow processes occurring within the body but still external to the body's epithelial layer (gastrointestinal and respiratory tracts) " in *Digital Human Modeling and Medicine*, G. Paul, Doweidar, M. , Ed.: Elsevier, 2022, ch. 17.

[130] A. H. Shapiro, M. Y. Jaffrin, and S. L. Weinberg, "Peristaltic pumping with long wavelengths at low Reynolds number," *Journal of Fluid Mechanics,* vol. 37, no. 4, pp. 799-825, 1969, doi: 10.1017/S0022112069000899.

[131] J. C. Burns and T. Parkes, "Peristaltic motion," *Journal of Fluid Mechanics,* vol. 29, no. 4, pp. 731-743, 1967, doi: 10.1017/S0022112067001156.

[132] C. Barton and S. Raynor, "Peristaltic flow in tubes," *The Bulletin of Mathematical Biophysics,* vol. 30, no. 4, pp. 663-680, 1968, doi: 10.1007/BF02476682.

[133] J. J. Monaghan, "Smoothed particle hydrodynamics," *Reports on Progress in Physics,* vol. 68, no. 8, pp. 1703-1759, 2005, doi: 10.1088/0034-4885/68/8/R01.

[134] P. W. Cleary, "Modelling confined multi-material heat and mass flows using SPH," *Applied Mathematical Modelling,* vol. 22, no. 12, pp. 981-993, 1998, doi: 10.1016/S0307-904X(98)10031-8.

[135] S. J. Cummins, T. B. Silvester, and P. W. Cleary, "Three-dimensional wave impact on a rigid structure using smoothed particle hydrodynamics," *International Journal for Numerical Methods in Fluids,* vol. 68, no. 12, pp. 1471-1496, 2012, doi: 10.1002/fld.2539.

[136] H. Wendland, "Piecewise polynomial, positive definite and compactly supported radial functions of minimal degree," *Advances in Computational Mathematics,* vol. 4, no. 1, pp. 389-396, 1995, doi: 10.1007/BF02123482.

[137] J. J. Monaghan and J. C. Lattanzio, "A refined particle method for astrophysical problems," *Astronomy and Astrophysics,* vol. 149, pp. 135-143, 1985. [Online]. Available: https://adsabs.harvard.edu/pdf/1985A%26A...149..135M.

[138] J. J. Monaghan, "Smoothed particle hydrodynamics," *Annual Review of Astronomy and Astrophysics,* vol. 30, pp. 543-574, 1992, doi: 10.1146/annurev.aa.30.090192.002551.

[139] R. Courant, *Supersonic flow and shock waves: A manual on the mathematical theory of non-linear wave motion* (no. 62). Courant Institute of Mathematical Sciences, New York University, 1944, p. 304.

[140] P. W. Cleary, "New implementation of viscosity: tests with Couette flows," in "SPH Technical Note 8," CSIRO, 1996, vol. CSIRO Division of Maths and Stats Technical Report DMS - C 96/32. [Online]. Available: https://publications.csiro.au/rpr/download?pid=procite:ce934b77-8db6-433c-8c12-a58e5bec2e0c&dsid=DS1

[141] J. Monaghan, "On the problem of penetration in particle methods," *Journal of Computational physics,* vol. 82, no. 1, pp. 1-15, 1989, doi: 10.5555/1718329.1718332.

[142] Ansys Inc. "Ansys Fluent 2021R1 Manual." https://ansyshelp.ansys.com/account/secured?returnurl=/Views/Secured/corp/v211/en/flu_th/flu_th.html (accessed 1 December, 2022).

[143] S. V. Patankar, *Numerical heat transfer and fluid flow*. CRC Press, 2018.

[144] J. H. Ferziger, M. Perić, and R. L. Street, *Computational methods for fluid dynamics*. Berlin, Heidelberg: Springer, 2002.

[145] A. I. Moens, *Die Pulscurve*. Leiden: E.J. Brill (in German), 1878, p. 145.

[146] D. Korteweg, "Ueber die Fortpflanzungsgeschwindigkeit des Schalles in elastischen Röhren," (in German), *Annalen der Physik,* vol. 241, no. 12, pp. 525-542, 1878.

[147] P. Lambossy, "Historical and critical review of the problem of the propagation of waves in a compressible liquid enclosed in an elastic tube," *Helvetica physiologica et pharmacologica acta,* vol. 8, no. 2, pp. 209-227, 1950.

[148] J. F. Hale, D. A. McDonald, and J. R. Womersley, "Velocity profiles of oscillating arterial flow, with some calculations of viscous drag and the Reynolds number," *Journal of Physiology,* vol. 128, no. 3, pp. 629-640, 1955, doi: 10.1113/jphysiol.1955.sp005330.

[149] G. W. Morgan and W. R. Ferrante, "Wave propagation in elastic tubes filled with streaming liquid," *Journal of the Acoustical Society of America,* vol. 27, no. 4, pp. 715-725, 1955, doi: 10.1121/1.1908005.

[150] J. R. Womersley, "Method for the calculation of velocity, rate of flow and viscous drag in arteries when the pressure gradient is known," *Journal of Physiology,* vol. 127, no. 3, pp. 553-563, 1955, doi: 10.1113/jphysiol.1955.sp005276.

[151] J. R. Womersley, "Oscillatory motion of a viscous liquid in a thin-walled elastic tube — The linear approximation for long waves," *The London, Edinburgh, and Dublin Philosophical Magazine and Journal of Science,* vol. 46, no. 373, pp. 199-221, 1955, doi: 10.1080/14786440208520564.

[152] J. R. Womersley, "Oscillatory flow in arteries: the constrained elastic tube as a model of arterial flow and pulse transmission," *Physics in Medicine and Biology,* vol. 2, no. 2, pp. 178-187, 1957, doi: 10.1088/0031-9155/2/2/305.

[153] J. R. Womersley, "An elastic tube theory of pulse transmission and oscillatory flow in mammalian arteries," Aerospace Research Labs Wright-Patterson AFB OH, 1957. [Online]. Available: https://apps.dtic.mil/sti/pdfs/ADB295267.pdf

[154]   D. H. Bergel, "The visco-elastic properties of the arterial wall," Doctor of Philosophy, University of London, London, 1960. [Online]. Available: https://core.ac.uk/download/pdf/30695496.pdf

[155]   D. H. Bergel, "The dynamic elastic properties of the arterial wall," *Journal of Physiology,* vol. 156, no. 3, pp. 458-469, 1961, doi: 10.1113/jphysiol.1961.sp006687.

[156]   D. H. Bergel, "The static elastic properties of the arterial wall," *Journal of Physiology,* vol. 156, no. 3, pp. 445-457, 1961, doi: 10.1113/jphysiol.1961.sp006686.

[157]   E. B. Wylie, V. L. Streeter, and L. Suo, *Fluid transients in systems*. Prentice Hall Englewood Cliffs, NJ, 1993.

[158]   I. S. Pearsall, "The velocity of water hammer waves," in *Proceedings of the Institution of Mechanical Engineers*, 1965, vol. 180, no. 5: SAGE Publications Sage UK: London, England, pp. 12-20, doi: 10.1243/PIME_CONF_1965_180_160_02.

[159]   J. Twyman, "Wave speed calculation for water hammer analysis," *Obras y Proyectos,* no. 20, pp. 86-92, 2018, doi: 10.4067/S0718-28132016000200007.

[160]   G. Z. Watters, *Modern analysis and control of unsteady flow in pipelines*. Michigan: Ann Arbor Science, 1984.

[161]   A. R. Halliwell, "Velocity of a water-hammer wave in an elastic pipe," *Journal of the Hydraulics Division,* vol. 89, no. 4, pp. 1-21, 1963, doi: 10.1061/JYCEAJ.0000897.

[162]   T. Kobori, S. Yokoyama, H. Miyashiro, and H. Seisakujo, *Propagation velocity of pressure wave in pipe line*. Kameari Works, Hitachi, 1955.

[163]   J. E. Akin, *Finite element analysis concepts: via SolidWorks*. World Scientific, 2010.

[164]   Ansys Inc, "SOLSH190," in *Mechanical APDL User's Guide, Release 2021 R2*, 2021.

[165]   Ansys Inc, "Selecting elements for your analysis," in *Mechanical APDL User's Guide, Release 2021 R2*, 2021.

[166]   Y. C. Fung, *Foundation of solid mechanics*. Englewood: Prentice-Hall, 1965.

[167]   J. Degroote, R. Haelterman, S. Annerel, P. Bruggeman, and J. Vierendeels, "Performance of partitioned procedures in fluid–structure interaction," *Computers and Structures,* vol. 88, no. 7, pp. 446-457, 2010, doi: 10.1016/j.compstruc.2009.12.006.

[168]   M. A. Kwiatek *et al.*, "Quantification of distal antral contractile motility in healthy human stomach with magnetic resonance imaging," *Journal of Magnetic Resonance Imaging,* vol. 24, no. 5, pp. 1101-1109, 2006, doi: 10.1002/jmri.20738.

[169]   G. M. Bornhorst, S. M. Rutherfurd, M. J. Roman, B. J. Burri, P. J. Moughan, and R. P. Singh, "Gastric pH distribution and mixing of soft and rigid food particles in the stomach using a dual-marker technique," *Food Biophysics,* vol. 9, no. 3, pp. 292-300, 2014, doi: 10.1007/s11483-014-9354-3.

[170]   F. Kong and R. P. Singh, "A human gastric simulator (HGS) to study food digestion in human stomach," *Journal of Food Science,* vol. 75, no. 9, pp. E627-35, 2010, doi: 10.1111/j.1750-3841.2010.01856.x.

[171]   E. Barroso, C. Cueva, C. Peláez, M. C. Martínez-Cuesta, and T. Requena, "The computer-controlled multicompartmental dynamic model of the gastrointestinal system simgi," in *The impact of food bioactives on health: In vitro and ex vivo models*, K. Verhoeckx *et al.* Eds.: Springer International Publishing, 2015, pp. 319-327.

[172] M. Minekus, "The TNO gastro-intestinal model (TIM)," in *The impact of food bioactives on health: In vitro and ex vivo models*, K. Verhoeckx *et al.* Eds.: Springer International Publishing, 2015, pp. 37-46.

[173] E. C. Thuenemann, G. Mandalari, G. T. Rich, and R. M. Faulks, "Dynamic gastric model (DGM)," in *The impact of food bioactives on health: In vitro and ex vivo models*, K. Verhoeckx *et al.* Eds.: Springer International Publishing, 2015, pp. 47-59.

[174] L. Chen *et al.*, "Gastric emptying and morphology of a 'near real' in vitro human stomach model (RD-IV-HSM)," *Journal of Food Engineering,* vol. 183, pp. 1-8, 2016, doi: 10.1016/j.jfoodeng.2016.02.025.

[175] I. Kobayashi, H. Kozu, Z. Wang, H. Isoda, and S. Ichikawa, "Development and fundamental characteristics of a human gastric digestion simulator for analysis of food disintegration," *Japan Agricultural Research Quarterly,* vol. 51, no. 1, pp. 17-25, 2017, doi: 10.6090/jarq.51.17.

[176] F. R. Menter, "Two-equation eddy-viscosity turbulence models for engineering applications," *AIAA Journal,* vol. 32, no. 8, pp. 1598-1605, 1994, doi: 10.2514/3.12149.

[177] A. La Spina, C. Förster, M. Kronbichler, and W. A. Wall, "On the role of (weak) compressibility for fluid‐structure interaction solvers," *International Journal for Numerical Methods in Fluids,* vol. 92, no. 2, pp. 129-147, 2020, doi: 10.1002/fld.4776.

[178] T. A. G. Langrish, C. Zhong, and L. Sun, "Probing differences in mass-transfer coefficients in beaker and stirrer digestion systems and the USP dissolution apparatus 2 using benzoic acid tablets," *Processes,* vol. 9, no. 12, p. 2168, 2021, doi: 10.3390/pr9122168.

[179] W. F. Koch and B. Ma, "The US Pharmacopeia: interfacing chemical metrology with pharmaceutical and compendial science," *Accreditation and Quality Assurance,* vol. 16, no. 1, pp. 43-51, 2011, doi: 10.1007/s00769-010-0718-1.

[180] D. M. D'Arcy, B. Liu, G. Bradley, A. M. Healy, and O. I. Corrigan, "Hydrodynamic and Species Transfer Simulations in the USP 4 Dissolution Apparatus: Considerations for Dissolution in a Low Velocity Pulsing Flow," *Pharmaceutical Research,* vol. 27, no. 2, pp. 246-258, 2010, doi: 10.1007/s11095-009-0010-4.

[181] M. Vardakou, A. Mercuri, S. A. Barker, D. Q. M. Craig, R. M. Faulks, and M. S. J. Wickham, "Achieving antral grinding forces in biorelevant in vitro models: Comparing the usp dissolution apparatus ii and the dynamic gastric model with human in vivo data," *AAPS PharmSciTech,* vol. 12, no. 2, pp. 620-626, 2011, doi: 10.1208/s12249-011-9616-z.

[182] L. G. McCarthy, C. Kosiol, A. M. Healy, G. Bradley, J. C. Sexton, and O. I. Corrigan, "Simulating the hydrodynamic conditions in the United States Pharmacopeia paddle dissolution apparatus," *AAPS PharmSciTech,* vol. 4, no. 2, pp. 83-98, 2003, doi: 10.1208/pt040222.

[183] L. G. McCarthy, G. Bradley, J. C. Sexton, O. I. Corrigan, and A. M. Healy, "Computational fluid dynamics modeling of the paddle dissolution apparatus: Agitation rate, mixing patterns, and fluid velocities," *AAPS PharmSciTech,* vol. 5, no. 2, pp. 50-59, 2004, doi: 10.1208/pt050231.

[184] D. M. D'Arcy, A. M. Healy, and O. I. Corrigan, "Towards determining appropriate hydrodynamic conditions for in vitro in vivo correlations using computational fluid

dynamics," *European Journal of Pharmaceutical Sciences,* vol. 37, no. 3, pp. 291-299, 2009, doi: 10.1016/j.ejps.2009.02.016.

[185] G. Bai and P. M. Armenante, "Velocity Distribution and Shear Rate Variability Resulting from Changes in the Impeller Location in the USP Dissolution Testing Apparatus II," *Pharmaceutical Research,* vol. 25, no. 2, pp. 320-336, 2008, doi: 10.1007/s11095-007-9477-z.

[186] P. Armenante and F. Muzzio, "Inherent method variability in dissolution testing: the effect of hydrodynamics in the USP II apparatus," A Technical Report Submitted to the Food and Drug Administration, 2005. [Online]. Available: https://www.researchgate.net/profile/Piero-Armenante/publication/237384728_Inherent_Method_Variability_in_Dissolution_Testing_The_Effect_of_Hydrodynamics_in_the_USP_II_Apparatus_A_Technical_Report_Submitted_to_the_Food_and_Drug_Administration/links/02e7e5258269895e09000000/Inherent-Method-Variability-in-Dissolution-Testing-The-Effect-of-Hydrodynamics-in-the-USP-II-Apparatus-A-Technical-Report-Submitted-to-the-Food-and-Drug-Administration.pdf

[187] G. Bai, Y. Wang, and P. M. Armenante, "Velocity profiles and shear strain rate variability in the USP Dissolution Testing Apparatus 2 at different impeller agitation speeds," *International Journal of Pharmaceutics,* vol. 403, no. 1, pp. 1-14, 2011, doi: 10.1016/j.ijpharm.2010.09.022.

[188] G. Bai and P. M. Armenante, "Hydrodynamic, mass transfer, and dissolution effects induced by tablet location during dissolution testing," *Journal of Pharmaceutical Sciences,* vol. 98, no. 4, pp. 1511-1531, 2009, doi: 10.1002/jps.21512.

[189] G. Bai, P. M. Armenante, R. V. Plank, M. Gentzler, K. Ford, and P. Harmon, "Hydrodynamic investigation of USP dissolution test apparatus II," *Journal of Pharmaceutical Sciences,* vol. 96, no. 9, pp. 2327-2349, 2007, doi: 10.1002/jps.20818.

[190] D. M. D'Arcy, O. I. Corrigan, and A. M. Healy, "Evaluation of hydrodynamics in the basket dissolution apparatus using computational fluid dynamics—Dissolution rate implications," *European Journal of Pharmaceutical Sciences,* vol. 27, no. 2, pp. 259-267, 2006, doi: 10.1016/j.ejps.2005.10.007.

[191] D. M. D'Arcy, O. I. Corrigan, and A. M. Healy, "Hydrodynamic simulation (computational fluid dynamics) of asymmetrically positioned tablets in the paddle dissolution apparatus: impact on dissolution rate and variability," *Journal of Pharmacy and Pharmacology,* vol. 57, no. 10, pp. 1243-1250, 2010, doi: 10.1211/jpp.57.10.0002.

[192] S. Irandoust and B. Andersson, "Concentration-dependent diffusivity of benzoic acid in water and its influence on the liquid–solid mass transfer," *The Canadian Journal of Chemical Engineering,* vol. 64, no. 6, pp. 954-959, 1986, doi: 10.1002/cjce.5450640611.

[193] J. L. Baxter, J. Kukura, and F. J. Muzzio, "Hydrodynamics-induced variability in the USP apparatus II dissolution test," *International Journal of Pharmaceutics,* vol. 292, no. 1-2, pp. 17-28, 2005, doi: 10.1016/j.ijpharm.2004.08.003.

[194] W. E. Ranz, "Evaporation from drops : Part II," *Chemical Engineering Progress,* vol. 48, pp. 173-180, 1952.

[195] R. R. Hemrajani and G. B. Tatterson, "Mechanically stirred vessels," in *Handbook of Industrial Mixing*, 2003, pp. 345-390.

[196] R. A. Ishak, "Buoyancy-generating agents for stomach-specific drug delivery: an overview with special emphasis on floating behavior," *Journal of Pharmacy and Pharmaceutical Sciences,* vol. 18, no. 1, pp. 77-100, 2015, doi: 10.18433/j3602k.

[197] B. N. Singh and K. H. Kim, "Floating drug delivery systems: an approach to oral controlled drug delivery via gastric retention," *Journal of Controlled Release,* vol. 63, no. 3, pp. 235-259, 2000, doi: 10.1016/S0168-3659(99)00204-7.

[198] P. W. Cleary, Harrison, S. M., Sinnott, M. D., "Flow and remodeling processes occurring within the body proper," in *Digital Human Modeling and Medicine*, G. Paul, Doweidar, M. Ed., 1st ed.: Elsevier, 2022, ch. 24.

[199] S. H. Kim *et al.*, "Stomach volume assessment using three-dimensional computed tomography gastrography for bariatric treatment," *Obesity Surgery,* vol. 30, no. 2, pp. 401-406, 2020, doi: 10.1007/s11695-019-04189-5.

[200] A. Geliebter and S. A. Hashim, "Gastric capacity in normal, obese, and bulimic women," *Physiology and Behavior,* vol. 74, no. 4, pp. 743-746, 2001, doi: 10.1016/s0031-9384(01)00619-9.

[201] J. U. Brackbill, D. B. Kothe, and C. Zemach, "A continuum method for modeling surface tension," *Journal of Computational Physics,* vol. 100, no. 2, pp. 335-354, 1992, doi: 10.1016/0021-9991(92)90240-Y.

[202] D. J. Harvie, M. Davidson, and M. Rudman, "An analysis of parasitic current generation in volume of fluid simulations," *Applied Mathematical Modelling,* vol. 30, no. 10, pp. 1056-1066, 2006, doi: 10.1016/j.apm.2005.08.015.

[203] Z. Guo, D. F. Fletcher, and B. S. Haynes, "Implementation of a height function method to alleviate spurious currents in CFD modelling of annular flow in microchannels," *Applied Mathematical Modelling,* vol. 39, no. 16, pp. 4665-4686, 2015, doi: 10.1016/j.apm.2015.04.022.

[204] P. W. Cleary, Personal Communication, 30 Nov 2022.

[205] T. H. Mamoru Ishii *Thermo-fluid dynamics of two-phase flow*. Springer New York, NY, 2006.

[206] C. W. Hirt and B. D. Nichols, "Volume of fluid (VOF) method for the dynamics of free boundaries," *Journal of Computational Physics,* vol. 39, no. 1, pp. 201-225, 1981, doi: 10.1016/0021-9991(81)90145-5.

[207] Ansys Inc. "Part III: Solution mode." https://ansyshelp.ansys.com/account/secured?returnurl=/Views/Secured/corp/v222/en/flu_ug/pt03.html (accessed 28 December, 2022).

[208] Ansys Inc. "Interphase Exchange Coefficients." https://ansyshelp.ansys.com/account/secured?returnurl=/Views/Secured/corp/v222/en/flu_th/flu_th_sec_eulermp_theory_exchange.html%23flu_th_eq_eulermp_cd_symmetric_tau (accessed 5 January, 2023).

[209] D. L. Youngs, "Time-dependent multi-material flow with large fluid distortion," *Numerical Methods for Fluid Dynamics,* 1982.

[210] R. I. Issa, "Solution of the implicitly discretised fluid flow equations by operator-splitting," *Journal of Computational Physics,* vol. 62, no. 1, pp. 40-65, 1986, doi: 10.1016/0021-9991(86)90099-9.

[211] D. H. Sharp, "An overview of Rayleigh-Taylor instability," *Physica D: Nonlinear Phenomena,* vol. 12, no. 1-3, pp. 3-18, 1984, doi: 10.1016/0167-2789(84)90510-4.

[212] Lord Rayleigh, "Investigation of the character of the equilibrium of an incompressible heavy fluid of variable density," *Proceedings of the London Mathematical Society,* vol. s1-14, no. 1, pp. 170-177, 1882, doi: 10.1112/plms/s1-14.1.170.

[213] G. Taylor, "The instability of liquid surfaces when accelerated in a direction perpendicular to their planes. I," *Proceedings of the Royal Society of London. Series A. Mathematical and Physical Sciences,* vol. 201, no. 1065, pp. 192-196, 1950, doi: 10.1098/rspa.1950.0052.

[214] M. S. Shadloo, A. Zainali, and M. Yildiz, "Simulation of single mode Rayleigh–Taylor instability by SPH method," *Computational Mechanics,* vol. 51, no. 5, pp. 699-715, 2013, doi: 10.1007/s00466-012-0746-2.

[215] Z. Chen, Z. Zong, M. B. Liu, L. Zou, H. T. Li, and C. Shu, "An SPH model for multiphase flows with complex interfaces and large density differences," *Journal of Computational Physics,* vol. 283, pp. 169-188, 2015, doi: 10.1016/j.jcp.2014.11.037.

[216] S. J. Cummins and M. Rudman, "An SPH projection method," *Journal of Computational Physics,* vol. 152, no. 2, pp. 584-607, 1999, doi: 10.1006/jcph.1999.6246.

[217] S. Ghosh, "Deforming stomach model workflow," Personal Communication, 29 Nov 2022.

[218] R. Berry *et al.*, "Functional physiology of the human terminal antrum defined by high-resolution electrical mapping and computational modeling," *American Journal of Physiology-Gastrointestinal and Liver Physiology,* vol. 311, no. 5, pp. G895-G902, 2016, doi: 10.1152/ajpgi.00255.2016.

[219] B. Abrahamsson, A. Pal, M. Sjöberg, M. Carlsson, E. Laurell, and J. G. Brasseur, "A novel in vitro and numerical analysis of shear-induced drug release from extended-release tablets in the fed stomach," *Pharmaceutical Research,* vol. 22, no. 8, pp. 1215-1226, 2005, doi: 10.1007/s11095-005-5272-x.

[220] S. M. Harrison, P. W. Cleary, G. Eyres, M. D. Sinnott, and L. Lundin, "Challenges in computational modelling of food breakdown and flavour release," *Food and Function,* vol. 5, no. 11, pp. 2792-2805, 2014.

[221] F. P. Incropera, D. P. DeWitt, T. L. Bergman, and A. S. Lavine, *Fundamentals of heat and mass transfer*. Wiley New York, 1996.

[222] M. E. Biancolini and P. P. Valentini, "Virtual human bone modelling by interactive sculpting, mesh morphing and force-feedback," *International Journal on Interactive Design and Manufacturing (IJIDeM),* vol. 12, no. 4, pp. 1223-1234, 2018, doi: 10.1007/s12008-018-0487-3.

[223] L. Geronzi *et al.*, "High fidelity fluid-structure interaction by radial basis functions mesh adaption of moving walls: A workflow applied to an aortic valve," *Journal of Computational Science,* vol. 51, p. 101327, 2021, doi: 10.1016/j.jocs.2021.101327.